NUREG/CR-4307
Vol. 3
HEDL-TME 86-2

LWR Pressure Vessel Surveillance Dosimetry Improvement Program:

NUREG/CR--4307-Vol.3
TI87 009044

1986 Annual Report
October 1985 - September 1986

Manuscript Completed: February 1987
Date Published: April 1987

Prepared by:
W. N. McElroy

Hanford Engineering Development Laboratory
Operated by Westinghouse Hanford Company
P.O. Box 1970
Richland, WA 99352

Prepared for:
Division of Engineering Technology
Office of Nuclear Regulatory Research
U.S. Nuclear Regulatory Commission
Washington, D.C. 20555
NRC FIN B5988

REPORTS IN LWR-PV-SDIP SERIES

NUREG/CR-0038	HEDL-TME 78-4	July 1977 - September 1977
NUREG/CR-0127	HEDL-TME 78-5	October 1977 - December 1977
NUREG/CR-0285	HEDL-TME 78-6	January 1978 - March 1978
NUREG/CR-0050	HEDL-TME 78-7	April 1978 - June 1978
NUREG/CR-0551	HEDL-TME 78-8	July 1978 - September 1978
NUREG/CR-0720	HEDL-TME 79-18	October 1978 - December 1978
NUREG/CR-1240, Vol. 1	HEDL-TME 79-41	January 1979 - March 1979
NUREG/CR-1240, Vol. 2	HEDL-TME 80-1	April 1979 - June 1979
NUREG/CR-1240, Vol. 3	HEDL-TME 80-2	July 1979 - September 1979
NUREG/CR-1240, Vol. 4	HEDL-TME 80-3	October 1979 - December 1979
NUREG/CR-1291	HEDL-SA-1949	October 1978 - December 1979*
NUREG/CR-1241, Vol. 1	HEDL-TME 80-4	January 1980 - March 1980
NUREG/CR-1241, Vol. 2	HEDL-TME 80-5	April 1980 - June 1980
NUREG/CR-1747	HEDL-TME 80-73	October 1979 - December 1980*
NUREG/CR-1241, Vol. 3	HEDL-TME 80-6	October 1980 - December 1980
NUREG/CR-2345, Vol. 1	HEDL-TME 81-33	January 1981 - March 1981
NUREG/CR-2345, Vol. 2	HEDL-TME 81-34	April 1981 - June 1981
NUREG/CP-0029	HEDL-SA-2546	October 1980 - September 1981*
NUREG/CR-2345, Vol. 4	HEDL-TME 81-36	October 1981 - December 1981
NUREG/CR-2805, Vol. 1	HEDL-TME 82-18	January 1982 - March 1982
NUREG/CR-2805, Vol. 2	HEDL-TME 82-19	April 1982 - June 1982
NUREG/CR-2805, Vol. 3	HEDL-TME 82-20	October 1981 - September 1982*
NUREG/CR-2805, Vol. 4	HEDL-TME 82-21	October 1982 - December 1982
NUREG/CR-3391, Vol. 1	HEDL-TME 83-21	January 1983 - March 1983
NUREG/CR-3391, Vol. 2	HEDL-TME 83-22	April 1983 - June 1983
NUREG/CR-3391, Vol. 3	HEDL-TME 83-23	October 1982 - September 1983*
NUREG/CR-3391, Vol. 4	**	October 1983 - December 1983
NUREG/CR-3746, Vol. 1	HEDL-TME 84-20	October 1983 - March 1984
NUREG/CR-3746, Vol. 2	HEDL-TME 84-21	April 1984 - September 1984
NUREG/CR-3746, Vol. 3	HEDL-TME 84-31	October 1983 - September 1984*
NUREG/CR-4307, Vol. 1	HEDL-TME 85-14	October 1984 - September 1985*
NUREG/CR-4307, Vol. 2	HEDL-7601	October 1984 - September 1985***
NUREG/CR-4307, Vol. 3	HEDL-TME 86-2	October 1985 - September 1986*
NUREG/CR-4307, Vol. 4	HEDL-7634	October 1985 - September 1986***

---

*Annual Reports.

**No HEDL-TME number assigned because this progress report contains only an NBS contribution on "Compendium of Benchmark Neutron Fields for Pressure Vessel Surveillance Dosimetry."

***HEDL Summary Annual Report.

FOREWORD

The Light Water Reactor Pressure Vessel Surveillance Dosimetry Improvement Program (LWR-PV-SDIP) has been established by the U.S. Nuclear Regulatory Commission (NRC) to improve, test, verify, and standardize the physics-dosimetry-metallurgy, damage correlation, and associated reactor analysis methods, procedures and data used to predict the integrated effect of neutron exposure to LWR PVs and their support structures. A vigorous research effort attacking the same measurement and analysis problems exists worldwide, and strong cooperative links between the U.S. NRC-supported activities at HEDL, ORNL, NBS, and MEA and those supported by CEN/SCK (Mol, Belgium), EPRI (Palo Alto, USA), KFA (Jülich, Germany), and several United Kingdom laboratories have been extended to a number of other countries and laboratories. These cooperative links are strengthened by the active membership of the scientific staff from many participating countries and laboratories in the ASTM E10 Committee on Nuclear Technology and Applications. Several subcommittees of ASTM E10 are responsible for the preparation of LWR surveillance standards.

The primary objective of this multilaboratory program is to prepare an updated and improved set of physics-dosimetry-metallurgy, damage correlation, and associated reactor analysis ASTM standards for LWR PV and support structure irradiation surveillance programs. Supporting this objective are a series of analytical and experimental validation and calibration studies in "Standard, Reference, and Controlled Environment Benchmark Fields," research reactor "Test Regions," and operating power reactor "Surveillance Positions."

These studies will establish and certify the precision and accuracy of the measurement and predictive methods recommended in the ASTM Standards and used for the assessment and control of the present and EOL condition of PV and support structure steels. Consistent and accurate measurement and data analysis techniques and methods, therefore, will be developed, tested and verified along with guidelines for required neutron field calculations used to correlate changes in material properties with the characteristics of the neutron radiation field. Application of established ASTM standards is expected to permit the reporting of measured materials property changes and neutron exposures to an accuracy and precision within bounds of 10% to 30%, depending on the measured metallurgical variable and neutron environment.

The assessment of the radiation-induced degradation of material properties in a power reactor requires accurate definition of the neutron field from the outer region of the reactor core to the outer boundaries of the PV. The accuracy of measurements on neutron flux and spectrum is associated with two distinct components of LWR irradiation surveillance procedures: 1) proper application of calculational estimates of the neutron exposure at in- and ex-vessel surveillance positions, various locations in the vessel wall and ex-vessel support structures and 2) understanding the relationship between material property changes in reactor vessels and their support structures, in metallurgical test specimens irradiated in test reactors and at accelerated neutron flux positions in operating power reactors.

The first component requires verification and calibration experiments in a variety of neutron irradiation test facilities including LWR-PV mockups, power reactor surveillance positions, and related benchmark neutron fields.

The benchmarks serve as a permanent reference measurement for neutron flux and fluence detection techniques, which are continually under development and are widely applied by laboratories with different levels of capability. The second component requires a serious extrapolation of an observed neutron-induced mechanical property change from research reactor "Test Regions" and operating power reactor "Surveillance Positions" to locations inside the body of the PV wall and to ex-vessel support structures. The neutron flux at the vessel inner wall is up to one order of magnitude lower than at surveillance specimen positions and up to two orders of magnitude lower than for test reactor positions. At the vessel outer wall, the neutron flux is one order of magnitude or more lower than at the vessel inner wall. Further, the neutron spectra at, within, and leaving the vessel are substantially different.

To meet reactor PV radiation monitoring requirements, a variety of neutron flux and fluence detectors are employed, most of which are passive. Each detector must be validated for application to the higher flux and harder neutron spectrum of the research reactor "Test Region" and to the lower flux and degraded neutron spectrum at "Surveillance Positions." Required detectors must respond to neutrons of various energies so that multigroup spectra can be determined with accuracy sufficient for adequate damage response estimates. Detectors being used, developed, and tested for the program include radiometric sensors, helium accumulation fluence monitor sensors, solid state track recorder sensors, and damage monitor sensors.

The necessity for PV mockup facilities for physics-dosimetry investigations and for irradiation of metallurgical specimens was recognized early in the formation of the NRC program. Experimental studies associated with high- and low-flux versions of a PWR PV mockup are in progress in the US, Belgium, UK, and France. The US low-flux version is known as the Poolside Critical Assembly (PCA) and the high-flux version is known as the Oak Ridge Research Reactor Poolside Facility (ORR PSF), both located at Oak Ridge, TN. As specialized benchmarks, these facilities provide well-characterized neutron environments where active and passive neutron dosimetry, various types of LWR-PV and support structure neutron field calculations, and temperature-controlled metallurgical specimen exposures are brought together.

The two key low-flux PV mockups in Europe are known as the Mol-Belgium-VENUS and Winfrith-United Kingdom-NESDIP facilities. The VENUS Facility is being used for PWR core source and azimuthal lead factor studies, while NESDIP is being used for PWR cavity and azimuthal lead factor studies. A third and important low-fluence PV mockup in Europe is identified with a French PV-simulator at the periphery of the Triton reactor. It served as the irradiation facility for the DOMPAC dosimetry experiment for studying surveillance capsule perturbations and through-PV-wall radial fluence and damage profiles (gradients) for PWRs of the Fessenheim 1 type.

Results of measurement and calculational strategies outlined here will be made available for use by the nuclear industry as ASTM standards. Federal Regulations 10 CFR 50 (Cf83) already requires adherence to several ASTM standards that establish a surveillance program for each power reactor and incorporate metallurgical specimens, physics-dosimetry flux-fluence monitors, and neutron field evaluation. Revised and new standards in preparation will be carefully updated, flexible, and, above all, consistent.

ACKNOWLEDGMENTS

Acknowledgment is due to R. L. Knecht and H. H. Yoshikawa of HEDL for their constructive comments and help related to program direction and review of program documentation. Very special acknowledgment is given to Senior Technical Editor N. E. Kenny, who edited this document; to D. C. Smith of the NRC/NRDC Program Office; and to the HEDL Technical Publications, Word Processing, Graphics, and Duplicating personnel, who contributed to its preparation. A. Taboada is the NRC program manager for the LWR-PV-SDIP and his help and encouragement are gratefully acknowledged.

CONTENTS

CONTENTS (Cont'd)

FIGURES

FIGURES

FIGURES

FIGURES

FIGURES

TABLES

TABLES (Cont'd)

TABLES (Cont'd)

TABLES (Cont'd)

TABLES (Cont'd)

ACRONYMS

ASTM	American Society for Testing and Materials
BSR	Bulk Shielding Reactor
BWR	Boiling Water Reactor
C/E	Calculated-to-Experimental Ratio
CEN/SCK	Centre d' Etude de l' Energie Nucleaire - Studiecentrum Voor Kernenergie (Mol, Belgium)
CFR	Code of Federal Regulations
DM	Damage Monitor
DOMPAC	Triton Reactor Thermal Shield and Pressure Vessel Mockup
ENDF	Evaluated Nuclear Data File
ENSA	Engineering Services Associates
EOL	End of Life
EPRI	Electric Power Research Institute
ESP	Emulsion Scanning Processor (System)
FTR	Fast Test Reactor
HAFM	Helium Accumulation Fluence Monitor
HEDL	Hanford Engineering Development Laboratory
KFA	Kernforschungsanlage Jülich Gmbh (Federal Republic of Germany)
LE	Lateral Expansion
LWR	Light Water Reactor
MEA	Materials Engineering Associates
NBS	National Bureau of Standards
NESDIP	NESTOR Shielding and Dosimetry Improvement Program (UK)
NRC	Nuclear Regulatory Commission
NRDC	National Reactor Dosimetry Center
NRE	Nuclear Research Emulsion
ORR	Oak Ridge Research Reactor (ORNL)
PCA	Poolside Critical Assembly
PSF	Poolside Facility (ORNL)
PV	Pressure Vessel
PVF	Pressure Vessel Face
PVS	Pressure Vessel Simulator

ACRONYMS (Cont'd)

PWR	Pressurized Water Reactor
RM	Radiometric Monitor
SDIP	Surveillance Dosimetry Improvement Program
SPVC	Simulated Pressure Vessel Capsule
SSTR	Solid-State Track Recorder
TSB	Thermal Shield Back
USE	Upper Shelf Energy
VENUS	Vulcain Experimental Nuclear Study (a critical facility at CEN/SCK in Mol, Belgium)

EXECUTIVE SUMMARY

A list of planned NUREG reports is presented in Table S-1. These reports address individual and combined pressurized water reactor (PWR) and boiling water reactor (BWR) physics-dosimetry-metallurgy issues. These will provide a reference base of information to support the preparation of the new set of LWR ASTM Standards (Figures S-1 and S-2).

HANFORD ENGINEERING DEVELOPMENT LABORATORY

Nuclear research emulsions (NRE) irradiations in the VENUS PWR benchmark are described. Six VENUS NRE have been scanned in the integral mode. Absolute proton-recoil reaction rates (I-integral and J-integral) results from these six NRE are presented and compared to proton-recoil reaction rates predicted by theory. It is difficult to interpret these comparisons between theory and experiment because of the limited number of energy groups (only 17) used in the neutron transport calculations. Nevertheless, these comparsions do suggest that difficulties arise in the calculation of neutron transport as one approaches the edge of the core corner.

A calculation was performed using neutron transport theory to evaluate the neutron flux-spectrum within the Buffalo Reactor core region. In addition, a dosimetry irradiation was carried out under carefully controlled conditions using a mockup of an actual metallurgical assembly. Comparisons of the calculation and measurements indicate good agreement, and the combination of the two can be used to determine exposure parameter values to accuracies of 10% to 15%. Systematic differences between measurement and calculation, however, indicate the importance of continued dosimetry measurements for accurate flux fluence evaluation.

The existence of some very simple PV in-wall exposure parameter extrapolation relations are uncovered through a comparative analysis of PCA and PSF benchmark data. Implications of these simple relationships for the description of radiation-induced LWR-PV embrittlement are discussed. The coefficients in the exposure parameter representations are material independent, but the embrittlement models show a significant material-dependent variation.

International participation in the PSF benchmark has been used to assess the worldwide status of RM neutron dosimetry for LWR-PV surveillance. In the first two of these PSF experiments, involving mainly U.S. laboratories, agreement was generally satisfactory, with nonfissile dosimeter results generally falling with ±5% (1σ) and the fissionable dosimeter results falling within ±10% (1σ). Improved agreement was attained in the third PSF experiment, involving mainly European laboratories, wherein nonfissile RM monitors generally agreed better than 2% (1σ) and fission monitors generally agreed to better than 5% (1σ).

A difference in transition temperature and upper-shelf energy has been reported between specimens irradiated on the left- and right-hand sides of the PSF metallurgical assembly. These metallurgical experiments were reviewed to determine whether left/right asymmetries in the irradiation

environment could be responsible for the observed left/right differences. This review concludes that environmental variables are, in all probability, responsible for the observed left/right differences. For the transition temperature measurements, differences in the in-situ irradiation temperature exist. In the case of the upper-shelf energy measurements, a systematic variation in exposure underlies the observed asymmetry.

Various mathematical representations of the nucleation and growth of precipitates in irradiated LWR pressure vessel steels have been studied and reviewed. Emphasis is placed on nucleation sites and copper-rich clusters and their fluence and flux level dependencies. The validity of certain assumptions and boundary conditions that are associated with the mathematical formulation of the problem of developing model equations are addressed. It is concluded that any set of assumptions can be made regarding the nucleation and growth, and in some cases, solutions may be obtained in closed form, but the accuracy will depend on the assumptions. For practical fits of Charpy data, simple formulas involving fluence raised to a power give results that are remarkably in conformity to the more complex realities of the world.

Summary information on ASTM and ASTM-EURATOM papers prepared by HEDL is provided.

By conducting neutron spectrometry at different locations, one obtains the variation of the differential neutron spectrum through the PV, which can be used to validate calculations. This spatial variation is an especially powerful probe for examining trends between theory and experiment, thereby furnishing greater insight into any observed differences. During the fall 1981 PCA irradiations, proton recoil proportional counter neutron spectrometry was conducted in the 4/12 configuration. Preliminary neutron spectral results have now been obtained for the 1/4-T and VB locations. These preliminary spectra cover the energy region from roughly 0.05 to 2.0 MeV.

Information is provided on the status of work to measure the boron and helium (B/He) content of irradiated PV steels to help determine the effect of the He generation rate (as one of the contributing environmental variables) in the calculation of plant specific end-of-life and life-extension range material-dependent trend curves.

Six different PSF-irradiated alloy Cv specimens were received by B&W from ORNL. Chemical analysis of the prepared samples was accomplished using emission spectrographic techniques. Equipment calibration was achieved by analysis of NBS SRM low-alloy steel samples. Chemical anlysis results for 14 elements are reported.

NATIONAL BUREAU OF STANDARDS

The masses of 32 SSTR fission deposits belonging to HEDL have been validated by comparison to the known masses of NBS fission deposits. The importance of this mass verification work is that the HEDL SSTRs have been and are being used to characterize the neutron fields in a number of LWR-PV-SDIP benchmark fields, namely PCA, NESDIP, and VENUS.

Comparison of SSTR measurements for ^{237}Np and ^{238}U fission-rate with corresponding measurements made in the PCA block with the NBS double fission chamber have shown a discrepancy of about 10%. It has been concluded that this is a perturbation effect created by the introduction of the fission chamber into the PV environment. More specifically, the void introduced by the fission chamber during measurements in the PCA block produces approximately a 10% perturbation (increase) in the measured fission rates. Previously published consensus fission rates for ^{238}U and ^{237}Np in the PCA must now be revised. Furthermore, the uncertainty will be reduced but this will depend upon the data set (PCA configuration) under consideration because, for some configurations, considerably more of one type of data exists than for another. These changes in the PCA experimental results have direct bearing on the PCA Blind Test results. The basis for the Blind Test evaluations was the C/E ratios. This change in ^{238}U and ^{237}Np fission rates will increase the averaged C/E ratios by $\sim$5%. FERRET-SAND-II least-squares' analyses will be performed with these revised fission rates.

The 1986 version of the Compendium of Neutron Fields for Benchmarking LWR-PV Surveillance Dosimetry was published as NBSIR-85-3151. In parallel with development of this compendium and in support of the LWR-PV-SDIP development of engineering types of benchmark fields or facilities, a new ASTM standard guide entitled "Benchmark Testing of Reactor Vessel Dosimetry" will be reviewed at the ASTM E10.05 meeting in Tampa, FL, January 26-28, 1987.

WESTINGHOUSE - NUCLEAR TECHNOLOGY DIVISION

A report was prepared by W-NTD in support of the NRC-sponsored LWR-PV-SDIP. Results are given of a 1-D discrete ordinates neutron transport analysis of the Gundremmingen BWR geometry. Neutron exposure parameter values ($E > 1.0$ MeV), ($E > 0.1$ MeV) and dpa in iron are listed for a location one inch from the outer radius of the core shroud as well as at the cladding/vessel wall. Also presented at each location are the ratios of fluence ($E > 0.1$ MeV) and dpa to fluence ($E > 1.0$ MeV). These ratios provide insight into the spectral shift toward lower energies that occurs with penetration into the PV and are an indicator of the different attenuation slopes at six locations within the reactor exhibited by the three exposure parameters. Calculated neutron spectra at six locations within the reactor geometry are also given. These spectra are suitable for use as input to adjustment codes or for direct determination of spectrum-averaged cross sections to be used in dosimetry evaluations for the PV. Since surveillance capsule perturbation effects have not been addressed, caution should be exercised in the use of these data for damage or dosimetry assessments.

In a cooperative LWR-PV-SDIP program, neutron dosimetry measurements were made for the H. B. Robinson plant during Cycle 9. The dosimetry was contained both at a replacement physics-dosimetry surveillance capsule location and in the reactor cavity outside the vessel. Excellent experimental results were obtained that can be used to benchmark calculations of neutron transport through the reactor vessel for H. B. Robinson and other similar reactors. Calculations performed by Westinghouse show good agreement with measured flux

shapes, but the flux magnitude is underpredicted by 15% to 20% at both the surveillance and reactor cavity measurement locations. Reasonable agreement with measured spectral shape is also attained. By using a combination of the calculations and measurements, the fluence at all points in the reactor vessel can be determined to a high degree of accuracy. Work will continue to link NESDIP and VENUS into the LWR-SDIP series of benchmarks and place them in context with the studies being or already carried out in PCA, PSF and a selected number of existing PWR and BWR power plants. The establishment of H. B. Robinson as one of the PWR benchmarks is, therefore, an important accomplishment. Detailed results of the H. B. Robinson measurements and calculations are reported in WCAP-11104, NUREG/CR-4827 (Li85).

A report was prepared by W-NTD in support of the NRC-sponsored LWR-PV-SDIP. This report describes the analysis of neutron and gamma-ray fluxes in the VENUS PWR engineering mockup benchmark experiment (SCK/CEN - Mol, Belgium). The full report is available as WCAP-11173, NUREG/CR-4827, January 1987. Results will also be included in NUREG/CR-3323, see Table S-1.

INSTITUT FÜR KERNENERGETIK UND ENERGIESYSTEME (IKE)

A report was prepared by IKE in support of the NRC-sponsored LWR-PV-SDIP. A 3-D neutron spectrum analysis was performed by Institut für Kernenergetik und Energiesysteme, Universitat Stuttgart (IKE). The objective of this work is to determine the neutron exposure of several trepans taken from the pressure vessel of the nuclear power plant Gundremmingen Block A (KRB-A). The work, funded by the U.S. NRC, is part of the KRB-A program analyzing through-vessel-wall embrittlement of a real reactor vessel at the end of operation. This progress report describes the method used, summarizes important input data, and gives first results of fluence ($E > 1.0$ MeV) values. Calculated and measured ^{54}Mn activities will be compared. A detailed analysis of all transport-calculation results, especially neutron spectrum variation within the vessel, is underway. Further comparison with available dosimetry results will be performed.

TABLE S-1

PROGRAM REFERENCE REPORTS AND DOCUMENTATION SCHEDULE

NRC Report No.	Vol No.	Lab Report No.	LWR-PV-SDIP Program No.*	Issue Date	Revised 12/3/86 Editors and/or Coordinators
NUREG/CR-1861 (PCA Physics-Dosimetry)		HEDL-TME 80-87	NUREG 1-1	July 1981	WN McElroy
NUREG/CR-3295 (PSF Metallurgy)	Vol 1	MEA-2017, Vol 1	NUREG 13-1	April 1984	JR Hawthorne
	Vol 2	MEA-2017, Vol 2	NUREG 13-2	April 1984	JR Hawthorne
NUREG/CR-3318** (PCA Physics-Dosimetry)	--	HEDL-TME 84-1	NUREG 1-2	September 1984 (Revised 9/87)	WN McElroy
NUREG/CR-3319** (Power Reactor Physics-Dosimetry)	--	HEDL-TME 85-3	NUREG 4	August 1985 (Revised 4/87)	WN McElroy
NUREG/CR-3320 (PSF SSC/SPVC Experiments & Blind Test)	Vol 1**	HEDL-TME 86-8	NUREG 3	July 1986	WN McElroy
	Vol 2**	HEDL-TME 86-9	NUREG 2	May 1987	WN McElroy
	Vol 3**	HEDL-TME 86-10	NUREG 5	February 1987	R. Gold
	Vol 4**	HEDL-TME 87-XX	NUREG 6-1	March 1987	
	Vol 5	EPRI NP-4630	NUREG 6-4	August 1986	JS Perrin T. Griesbach
	Vol 6	CEN/SCK-XX	NUREG 6-2	September 1987	Ph VanAsbroeck JR Hawthorne A. Fabry
NUREG/CR-3321** (SDMF Physics-Dosimetry)	--	HEDL-TME 87-XX	NUREG 7	September 1987	WN McElroy R. Gold ED McGarry
NUREG/CR-3323 (VENUS Physics-Dosimetry)	Vol 1	CEN/SCK-XX	NUREG 9-1	January 1987	A. Fabry WN McElroy
	Vol 2	CEN/SCK-XX	NUREG 9-2	September 1987	R. Gold
NUREG/CR-3324 (NESDIP Experiments & Blind Test)	Vol 1	AEEW-R 1736	NUREG 10-1	January 1984	J. Butler
	Vol 2	AEEW-R XXXX	NUREG 10-2	July 1987	J. Butler
	Vol 3	AEEW-R XXXX	NUREG 10-3	December 1987	I. Curl
	Vol 4	AEEW-R XXXX	NUREG 10-4	July 1988	R. Gold
	Vol 5	AEEW-R XXXX	NUREG 10-5	September 1988	WN McElroy
	Vol 6	AEEW-R XXXX	NUREG 10-6	April 1988	P. Miller

*Attachment 1 of (Mc85g) provides additional information on the expected contents of tne 20 NUREG reports. Vols 4, 5 and 6 of NUREG/CR-3324 have been renumbered so that Vols 4, 5 and 6 are now designated as Vols 6, 4 and 5, respectively.
**These program numbers are not to be used on final reports.
***Loose-leaf document.

TABLE S-1 (Cont'd)

NUREG/CR-1861 (Issue Date: July 1981)
PCA Experiments and Blind Test - W. N. McElroy, Editor

This document provides the results of calculations and active and passive physics-dosimetry measurements for the PCA 8/7 and 12/13 configurations X/Y: water gaps (in cm) from the core edge to the thermal shield (X) and from the thermal shield to the vessel wall (Y). The focus of the document is on an international Blind Test of transport theory methods in LWR-PV applications involving eleven laboratories, including reactor vendors.

NUREG/CR-3295
PSF Metallurgy - J. R. Hawthorne, Editor

Vol. 1 (Issue Date: April 1984)
Notch Ductility and Fracture Toughness Degradation of A302-B & A533-B Reference Plate from PSF Simulated Surveillance and Through-Wall Irradiation Capsules

Beyond scope of title, this document supports the analysis of the PSF Blind Test and provides as-built documentation and final PSF A302-B and A533-B reference plate metallurgical results for SSC and SPVC.

Vol. 2 (Issue Date: April 1984)
Postirradiation Notch Ductility and Tensile Strength Determinations for PSF Simulated Surveillance and Through-Wall Specimen Capsules

Beyond scope of title, this document supports the analysis of the PSF Blind Test and provides as-built documentation and final PSF (NRC, EPRI, RR&A, CEN/SCK, and KFA) steel metallurgical results generated by MEA for SSC and SPVC.

NUREG/CR-3318 (Issue Date: September 1984, Revised September 1987)
PCA Dosimetry in Support of the PSF Physics-Dosimetry-Metallurgy Experiments (4/12, 4/12 SSC configurations and update of 8/7 and 12/13 configurations) - W. N. McElroy, Editor

Beyond scope of title, this document supports the analysis of the PSF Blind Test and updates NUREG/CR-1861, "PCA Experiments and Blind Test," (Mc81).

NUREG/CR-3319 (Issue Date: August 1985, Revised April 1987)
LWR Power Reactor Surveillance Physics-Dosimetry Data Base Compendium - W. N. McElroy, Editor

In loose-leaf form this document provides new or reevaluated exposure parameter values [total, thermal, and fast (E > 1.0 MeV) fluences, dpa, etc.] for individual surveillance capsules removed from operating PWR and BWR power plants. As surveillance reports are reevaluated with FERRET-SAND, this document should be revised. The corresponding metallurgical data base is provided in the loose-leaf EPRI NP-2428 (Mc82c). A new (NRC) embrittlement data base (EDB), tailored for use on the IBM-PC, and related trend curves are in preparation by ORNL and HEDL.

TABLE S-1 (Cont'd)

NUREG/CR-3220
PSF Physics-Dosimetry-Metallurgy Experiments:

Vol. 1 (Issue Date: July 1986)
PSF Experiments Summary and Blind Test Results - W. N. McElroy, Editor

This document provides PSF experiment summary information and the results of the comparison of measured and predicted physics-dosimetry-metallurgy results for the PSF experiment. This document also contains (in an appendix) each participants' final report.

Vol. 2 (Issue Date: May 1987)
PSF Startup Experiment - W. N. McElroy and R. Gold, Editors

Beyond scope of title, this document will support analysis of the PSF Blind Test and provides experimental conditions, as-built documentation, and final PSF physics-dosimetry results for the startup experiment.

Vol. 3 (Issue Date: February 1987)
PSF Physics-Dosimetry Program - W. N. McElroy and R. Gold, Editors

Beyond scope of title, this document will support analysis of the PSF Experiment and Blind Test and provides experimental conditions, as-built documentation, and final PSF physics-dosimetry results for SSC, SPVC and SVBC.

Vol. 4 (Issue Date: March 1987)
PSF Metallurgy Program - W. N. McElroy and R. Gold, Editors

Beyond scope of title, this document will support analysis of the PSF Experiments and Blind Test and provides experimental conditions, as-built documentation, and final metallurgical data on measured property changes in different PV steels for SSC-1 and -2 positions, and the (SPVC) simulated PV locations at the 0-T (inner surface), 1/4-T, and 1/2-T positions of the 4/12 PWR PV wall mockup. The corresponding SSC-1, SSC-2, and SPVC locations' neutron exposures are $\sim 2 \times 10^{19}$, $\sim 4 \times 10^{19}$, $\sim 4 \times 10^{19}$, $\sim 2 \times 10^{19}$, and $\sim 1 \times 10^{19}$ n/cm^2, respectively, for a ~550°F irradiation temperature. It will also contain and/or reference available damage analysis results for SVBC using the Vol. 5 metallurgical data base.

Vol. 5 (Issue Date: August 1986)
PSF Simulated Void Box Capsule (SVBC) Charpy and Tensile Metallurgical Test Results - J. S. Perrin, Editor

Beyond scope of title, this document provides the experimental conditions, as-built documentation, and final Charpy and tensile specimen measured property changes in PV support structure and reference steels for the ex-vessel SVBC simulated cavity (void box) for a neutron exposure on the order of 10^{16} n/cm^2 (E > 1.0 MeV) for ~95°F irradiation temperature. This estimate is based on preliminary ORNL calculations, as yet unsubstantiated by measurements.

TABLE S-1 (Cont'd)

Vol. 6 (Issue Date: September 1987)
PSF Simulated Surveillance Capsule (SSC) Results - CEN/SCK/MEA - Ph. Van Asbroech, A. Fabry, and R. Hawthorne, Editors

This document, to be issued by CEN/SCK, will provide CEN/SCK/MEA metallurgical data and results from the Mol, Belgium PV steel irradiated in the SSC position for the ORR-PSF physics-dosimetry-metallurgy experiments.

NUREG/CR-3321 (Issue Date: September 1987)
Service Laboratory Procedure Verification and Surveillance Capsule Perturbations - W. N. McElroy, R. Gold, and E. D. McGarry, Editors

This loose-leaf volume will provide results to certify the accuracy of service laboratory procedures to determine exposure parameter and perturbation effects for surveillance capsules removed from PWR and BWR power plants. It will also contain and/or reference sensor benchmarking results related to the use of RM, HAFM, SSTR, and DM monitors.

NUREG/CR-3323
VENUS PWR Core Source and Azimuthal Lead Factor Experiments and Calculational Tests:

Vol. 1 (Issue Date: January 1987)
Clean (^{235}U) Core Configuration - A. Fabry et al., Editors

Vol. 2 (Issue Date: September 1987)
Burnt (^{235}U and ^{239}Pu) Core Configuration - A. Fabry et al., Editors

These two documents, to be prepared by CEN/SCK and other participants, will provide VENUS-derived reference physics-dosimetry data on active, passive, and calculational dosimetry studies involving CEN/SCK, HEDL, NBS, ORNL, and other LWR program participants for a clean (^{235}U) and a burnt (^{235}U + ^{239}Pu) core configuration.

NUREG/CR-3324
NESDIP PWR Cavity and Azimuthal Lead Factor Experiments and Calculational Tests:

Vol. 1 (Issue Date: January 1984)
PCA Replica Experiments: Part I - Winfrith Measurements and Calculations - J. Butler, Editor

Vol. 2 (Issue Date: July 1987)
PCA Replica Experiments: Part II - Further Analysis Including Measurements by HEDL - J. Butler et al., Editors

These two documents, to be prepared by Winfrith-RR&A and other participants, will provide NESDIP-PCA replica-derived reference physics-dosimetry data on active, passive, and calculational dosimetry studies involving Winfrith, CEN/SCK, HEDL, NBS, and other LWR program participants.

TABLE S-1 (Cont'd)

Vol. 3 (Issue Date: December 1987)
NESTOR Dosimetry Improvement Programme (NESDIP): Radial Shield Experiments - J. Butler et al., Editors

This document will provide NESDIP cavity-derived reference physics-dosimetry data based on the Winfrith startup program and Winfrith and LWR-PV-SDIP participants' calculational results for the ASPIS-PCA Slab Geometry Benchmarks (29.4-cm cavity).

Vol. 4 (Issue Date: July 1988)
NESTOR Dosimetry Improvement Programme (NESDIP): 21-cm Cavity Benchmark - J. Butler et al., Editors

This document will provide NESDIP 21-centimeter cavity-derived reference physics-dosimetry data on active, passive, and calculational dosimetry studies involving Winfrith, HEDL, ORNL, and other LWR program participants.

Vol. 5 (Issue Date: September 1988)
NESTOR Dosimetry Improvement Programme (NESDIP): Nozzle and Coolant Duct Benchmark - J. Butler et al., Editors

This document will provide NESDIP nozzle and coolant duct derived reference physics-dosimetry data on active, passive, and calculational dosimetry studies by Winfrith.

Vol. 6 (Issue Date: April 1988)
NESTOR Dosimetry Improvement Programme (NESDIP): NESDIP Cavity Experiment and Blind Test Results - J. Butler, W. N. McElroy, R. Gold, P. Miller, and I. Curl, Editor(s) TBD

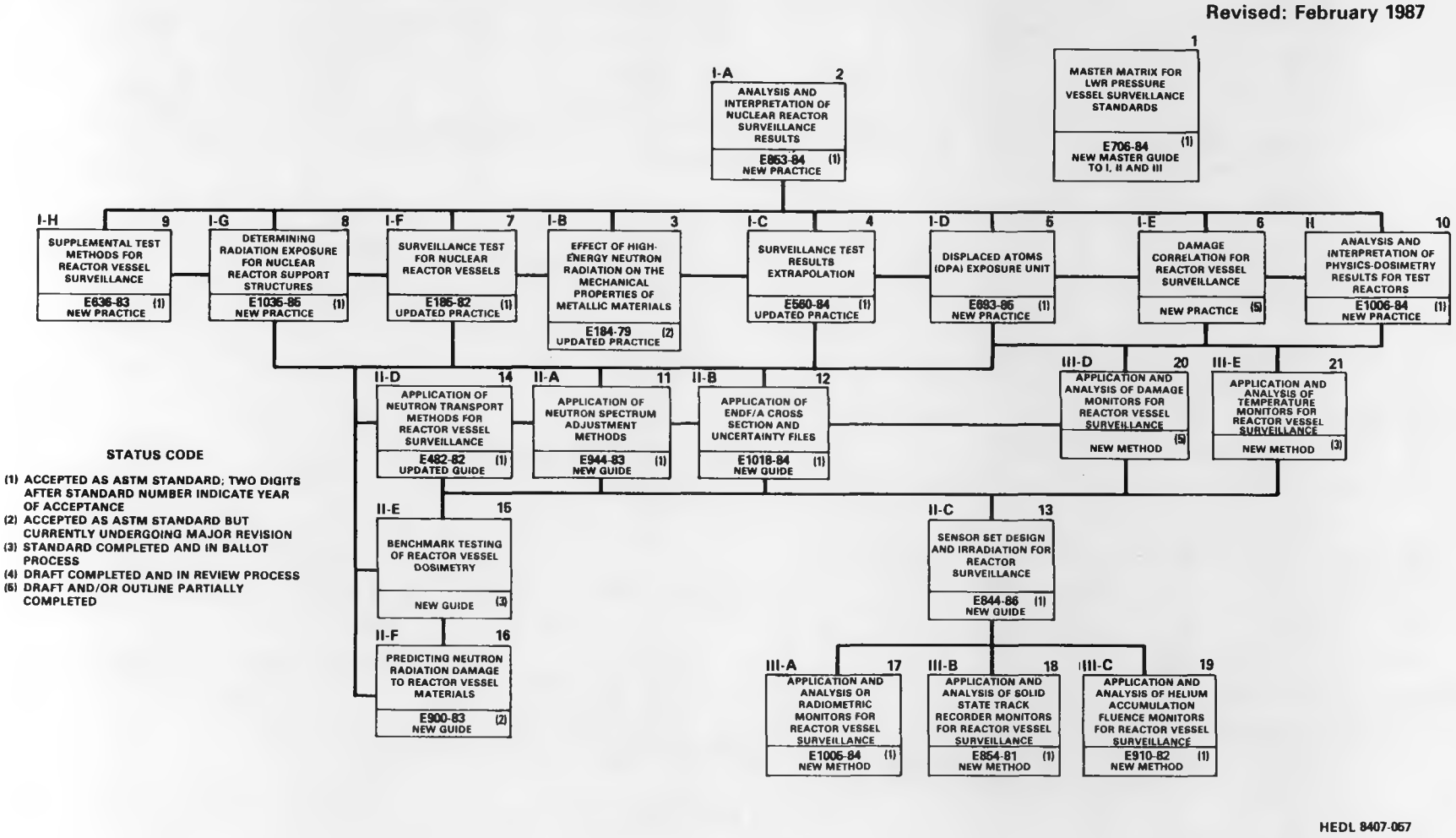

FIGURE S-1. ASTM Standards for Surveillance of LWR Nuclear Reactor Pressure Vessels and Their Support Structures.

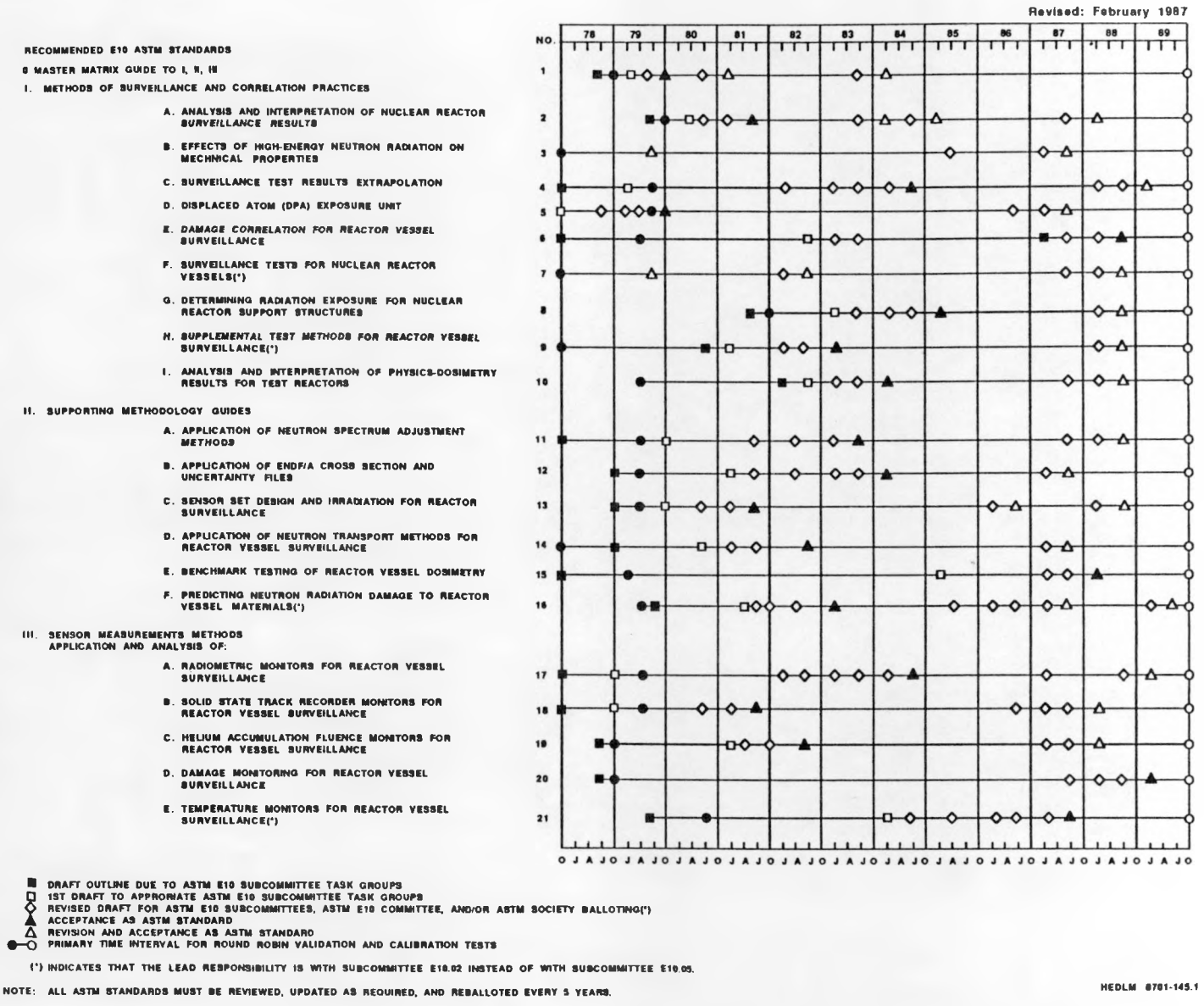

FIGURE S-2. Preparation, Validation, and Calibration Schedule for LWR Nuclear Reactor Pressure Vessels and Their Support Structure Surveillance Standards.

HANFORD ENGINEERING DEVELOPMENT LABORATORY

A. VENUS NUCLEAR EMULSION MEASUREMENTS

Raymond Gold and C. C. Preston (HEDL) and J. H. Roberts (MC^2)

Objective

Nuclear research emulsions (NREs) can be used to establish key absolute neutron spectral data in the energy region above approximately 0.4 MeV. The objective of this work is to obtain such NRE data for the VENUS PWR benchmark.

Summary

Nuclear research emulsions (NREs) irradiations in the VENUS PWR benchmark are described. Six VENUS NRE have been scanned in the integral mode. Absolute proton-recoil reaction rates (I-integral and J-integral) results from these six NRE are presented and compared to proton-recoil reaction rates predicted by theory. It is difficult to interpret these comparisons between theory and experiment because of the limited number of energy groups (only 17) used in these neutron transport calculations. Nevertheless, these comparsions do suggest that difficulties arise in the calculation of neutron transport as one approaches the edge of the core corner.

Accomplishments and Status

1.0 Introduction

Neutron dosimetry plays a crucial role in understanding the limitations of light water reactor pressure vessels (LWR-PVs). The energy dependence of damage produced by neutrons in LWR-PV steel has been recognized for some time now. However, inherent limitations prevent differential measurement of neutron energy spectra in power reactor environments (Go77c). Integral measurements that can be conducted in power reactors, such as with radiometric (RM), solid-state track recorder (SSTR), or helium accumulation fluence monitor (HAFM) dosimeters, possess very limited energy resolution. Of even greater significance is that neutron-induced radiation damage in iron is non-negligible in the 0.1 MeV to 1.0 MeV energy region for these LWR-PV environments. Unfortunately, these passive high power techniques offer little coverage in this energy region. Hence, it is important to develop techniques that extend the applicability and accuracy of these integral methods.

It is possible to use nuclear research emulsions (NREs) to obtain both differential and integral spectral information in part of the 0.1 MeV to 1.0 MeV energy region. Through proper selection and careful processing, NREs can be used down to approximately 0.4 MeV. While NRE measurements have been customarily carried out in the differential mode (Ro53,Ro57,Ro68), the practical utility of integral NRE measurements has only recently been recognized (Go81d,Go81e,Ro83b).

In the integral mode, NREs provide absolute integral reaction rates that can be used in spectral and least-squares adjustment codes. In the past, such

adjustment codes have not used integral reaction rates based on emulsions (Cu79). The advantage of emulsion integral reaction rates is their tie to the elastic scattering cross section of hydrogen. This $\sigma_{n,p}(E)$ cross section is universally accepted as a standard cross section and is known to an accuracy of roughly 1%. Hence, emulsion integral reaction rates add a significant new dimension to the neutron dosimetry data base for the VENUS PWR mockup.

2.0 Emulsion Irradiations in VENUS

VENUS emulsion irradiations were conducted in sequence from Run 83/04 through Run 83/11 in early February 1983. The power-time history and run-to-run monitoring data for these NRE irradiations have already been summarized in Table 2.3.1 of NUREG/CR-3323, Vol. 1. Both Fuiji and Ilford (L4) type emulsions were used. These emulsions were 200 μ and 400 μ thick, mounted on glass backing. The 200 μ and 400 μ NRE of each type were exposed back-to-back inside cylindrical cadmium boxes, 0.93 cm in diameter by 0.25 cm high with 0.10 cm wall thickness. The locations used for the NREs in all these irradiations are shown in Figure HEDL-1. Further details for each of these NRE irradiations are given in Tables HEDL-1 through HEDL-8.

Irradiations 83/04 through 83/07 were used to obtain NRE exposures throughout the range of available radial and azimuthal experimental locations in VENUS. Irradiations 83/08 through 83/11 were used to investigate special effects. To minimize the perturbation created by the cadmium-covered NRE, all experimental tubes used for NRE exposures were completely backfilled with either plexiglas® or steel. Plexiglass was used for the backfill material in water locations and steel at all other locations (see Tables HEDL-1 through HEDL-8).

Irradiations 83/08 and 83/09 were conducted to investigate the angular neutron flux at locations V2 and V3, respectively. In earlier NRE exposures at these locations, the emulsions were positioned horizontally, whereas for irradiations 83/08 and 83/09, the NREs were aligned vertically. In contrast with all other in-situ neutron spectrometry methods, NREs possess the unique capability of detecting variations in angular neutron flux. In fact, NREs were used to detect the angular anisotropy of the neutron flux in the fast test reactor (FTR), which was the very first observation of angular anisotropy in an in-core reactor neutron field (Go81,Ro81).

Irradiations 83/10 and 83/11 were carried out at locations V2 and V3, respectively, to investigate the possible perturbation created by the presence of the 1-in. spherical proportional counter when conducting (n,p) neutron spectrometry. Thereford, NREs were exposed in a dummy 1-in. proportional counter at V2 and V3 for comparison with earlier NRE irradiations at these locations. The creation of such perturbations by detectors of comparable size in LWR-PV environments has already been confirmed. The NBS fission chamber creates a perturbation that increases the threshold fission rates of both ^{238}U and ^{237}Np by ∿10% within the PV (Mc86c). The Janus probe, which is used for γ-ray dosimetry and spectrometry, produces a perturbation that varies from ∿10% to 30%, depending on both location and LWR-PV configuration (Go84d).

®Plexiglas is a registered trademark of Rohm & Haas, Pelham Manor, NY.

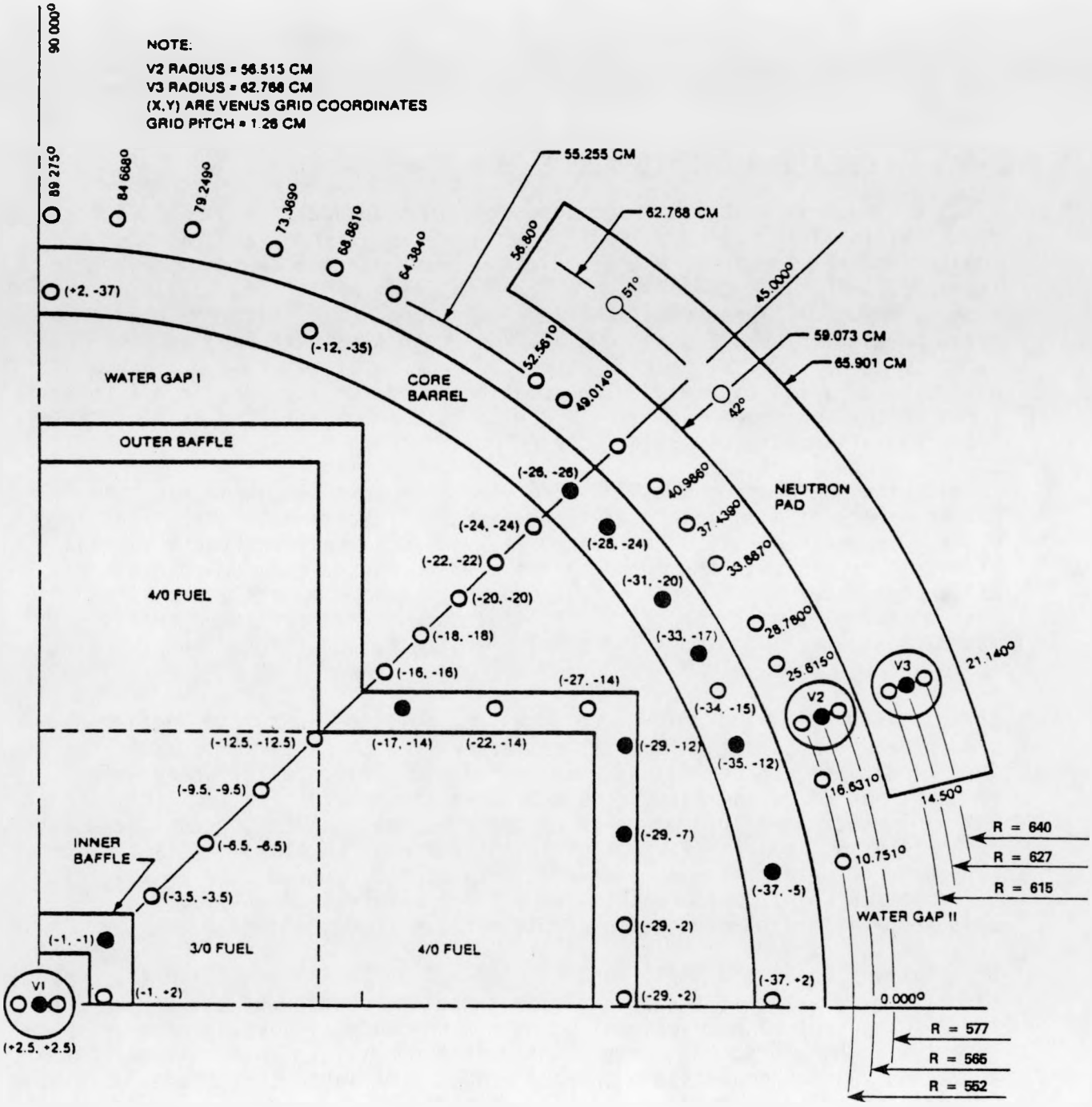

FIGURE HEDL-1. Overhead View of the VENUS PWR Engineering Benchmark Showing Key Dimensions and the Available Locations for Experimental Measurements. NRE were irradiated at the darkened experimental locations.

TABLE HEDL-1

NRE EXPOSED IN VENUS AT CORE CENTER AND INNER BAFFLE
FOR IRRADIATION 83/04

Cadmium Box No.	NRE Type[b]	NRE ID No.	Location[a] X,Y	Location[a] Axial[c] (cm)	Location[a] Backfill
1	F-200 F-400	22 24	2.5, 2.5 (V1)	-2.5	Plexiglas
2	I-200 I-400	17 20	2.5,2.5 (V1)	+2.5	Plexiglas
3	F-200 F-400	23 8	-1,-1	-2.5	Steel
4	I-200 I-400	15 15	-1,-1	+2.5	Steel

(a) See Figure HEDL-1 for a general orientation.
(b) F-200 and F-400 are Fuiji 200-μ and 400-μ thick emulsions; I-200 and I-400 are Ilford 200-μ and 400-μ thick emulsions.
(c) Distance above (+) and below (-) midplane.

TABLE HEDL-2

NRE EXPOSED IN VENUS LOCATIONS V2 AND V3 FOR IRRADIATION 83/05

Cadmium Box No.	NRE Type[b]	NRE ID No.	Location[a] R,θ	Location[a] Axial[c] (cm)	Location[a] Backfill
5	F-200 F-400	21 2	56.5, 21° (V2)	-2.5	Plexiglas
6	I-200 I-400	12 9	56.5, 21° (V2)	+2.5	Plexiglas
7	F-200 F-400	16 15	62.7,21° (V3)	-2.5	Steel
8	I-200 I-400	7 2	62.7,21° (V3)	+2.5	Steel

(a) See Figure HEDL-1 for a general orientation.
(b) F-200 and F-400 are Fuiji 200-μ and 400-μ thick emulsions; I-200 and I-400 are Ilford 200-μ and 400-μ thick emulsions.
(c) Distance above (+) and below (-) midplane.

TABLE HEDL-3

NRE EXPOSED IN VENUS AT THE CORE BARREL AND LOCATION V2
FOR IRRADIATION 83/06

Cadmium Box No.	NRE Type[b]	NRE ID No.	Location[a] X,Y	Location[a] Axial[c] (cm)	Backfill
9	F-200 F-400	13 6	-35,-12	-2.5	Steel
10	I-200 I-400	8 6	-35,-12	+2.5	Steel
11	F-200 F-400	1 14	-37,-5	-2.5	Steel
12	I-200 I-400	1 17	-37,-5	+2.5	Steel
13	F-200 F-400	10 3	-33,-17	-2.5	Steel
14	I-200 I-400	9 13	-33,-17	+2.5	Steel
15	F-200 F-400	14 10	-28,-24	-2.5	Steel
16	I-200 I-400	2 16	-28,-24	+2.5	Steel
17	F-200 F-400	4 11	-26,-26	-2.5	Steel
18	I-200 I-400	4 18	-26,-26	+2.5	Steel
19	F-200 F-400	3 12	-31,-20	-2.5	Steel
20	I-200 I-400	18 5	-31,-20	+2.5	Steel
21	F-200 F-400	18 13	R=55.2,θ=21° (V2)	-2.5	Plexiglas
22	I-200 I-400	13 4	R=55.2,θ=21° (V2)	+2.5	Plexiglas

(a) See Figure HEDL-1 for a general orientation.
(b) F-200 and F-400 are Fuiji 200-μ and 400-μ thick emulsions; I-200 and I-400 are Ilford 200-μ and 400-μ thick emulsions.
(c) Distance above (+) and below (-) midplane.

TABLE HEDL-4

NRE EXPOSED IN VENUS AT THE OUTER BAFFLE
FOR IRRADIATION 83/07

Cadmium Box No.	NRE Type[b]	NRE ID No.	Location[a] X,Y	Location[a] Axial[c] (cm)	Location[a] Backfill
23	F-200	20	-29,-7	-2.5	Steel
	F-400	17			
24	I-200	5	-29,-7	+2.5	Steel
	I-400	11			
1	F-200	17	-29,-12	-2.5	Steel
	F-400	25			
2	I-200	10	-29,-12	+2.5	Steel
	I-400	3			
3	F-200	15	-17,-14	-2.5	Steel
	F-400	5			
4	I-200	11	-17,-14	+2.5	Steel
	I-400	14			

(a) See Figure HEDL-1 for a general orientation.
(b) F-200 and F-400 are Fuiji 200-μ and 400-μ thick emulsions; I-200 and I-400 are Ilford 200-μ and 400-μ thick emulsions.
(c) Distance above (+) and below (-) midplane.

TABLE HEDL-5

NRE EXPOSED IN VENUS AT LOCATION V2 FOR IRRADIATION 83/08[a]

Cadmium Box No.	NRE Type[c]	NRE ID No.	Location[b] R,θ	Location[b] Axial[d] (cm)	Location[b] Backfill
5	F-200	9	56.5,21°	-2.5	Plexiglas
	F-400	26	(V2)		
6	I-200	6	56.5,21°	+2.5	Plexiglas
	I-400	1	(V2)		

(a) Angular flux measurement in V2; NRE aligned vertically facing core center.
(b) See Figure HEDL-1 for a general orientation.
(c) F-200 and F-400 are Fuiji 200-μ and 400-μ thick emulsions; I-200 and I-400 are Ilford 200-μ and 400-μ thick emulsions.
(d) Distance above (+) and below (-) midplane.

TABLE HEDL-6

NRE EXPOSED IN VENUS AT LOCATION V3 FOR IRRADIATION 83/09[a]

Cadmium Box No.	NRE Type[c]	NRE ID No.	Location[b] R,θ	Location[b] Axial[d] (cm)	Backfill
7	F-200 F-400	2 23	62.7,21° (V3)	-2.5	Steel
8	I-200 I-400	14 7	62.7,21° (V3)	+2.5	Steel

[a] Angular flux measurement in V3; NRE aligned vertically facing core center.
[b] See Figure HEDL-1 for a general orientation.
[c] F-200 and F-400 are Fuiji 200-μ and 400-μ thick emulsions; I-200 and I-400 are Ilford 200-μ and 400-μ thick emulsions.
[d] Distance in centimeters above (+) and below (-) midplane.

TABLE HEDL-7

NRE EXPOSED IN VENUS AT LOCATION V2 FOR IRRADIATION 83/10[a]

Cadmium Box No.	NRE Type[c]	NRE ID No.	Location[b] R,θ	Location[b] Axial[d] (cm)	Backfill
9	I-200 I-400	3 8	56.5,21° (V2)	-2.5	Plexiglas

[a] Proportional counter perturbation measurement at V2; NRE aligned vertically facing core center inside spherical proportional counter shell.
[b] See Figure HEDL-1 for a general orientation.
[c] F-200 and F-400 are Fuiji 200-μ and 400-μ thick emulsions; I-200 and I-400 are Ilford 200-μ and 400-μ thick emulsions.
[c] Distance above (+) and below (-) midplane.

TABLE HEDL-8

NRE EXPOSED IN VENUS AT LOCATION V3 FOR IRRADIATION 83/11[a]

Cadmium Box No.	NRE Type[c]	NRE ID No.	Location[b] R,θ	Location[b] Axial[d] (cm)	Location[b] Backfill
10	I-200 I-400	20	62.7,21° (V3)	-2.5	Steel

[a] Proportional counter perturbation measurement at V3; NRE aligned vertically facing core center inside spherical proportional counter shell.
[b] See Figure HEDL-1 for a general orientation.
[c] F-200 and F-400 are Fuiji 200-μ and 400-μ thick emulsions; I-200 and I-400 are Ilford 200-μ and 400-μ thick emulsions.
[d] Distance above (+) and below (-) midplane.

On this basis, one can anticipate that proportional counters used in (n,p) neutron spectrometry also create measurable perturbations. Hence, it is important to quantify such perturbations and to determine their effect upon neutron spectrometry.

3.0 Experimental Method

All VENUS NREs have been processed and possess acceptable clarity, contrast and track density for scanning on the HEDL interactive computer-based Emulsion Scanning Processor (ESP) system (Go83). Comparison of the Fuiji and Ilford emulsions revealed comparable quality. Hence, it was decided that only the Ilford emulsions should be scanned in view of extensive earlier work conducted to characterize Ilford NRE (Ba63,Ro57,Ro68).

Scanning on the ESP system has been performed in the integral mode, which provides two different integral (n,p) reaction rates. The first integral measurement follows directly the integral relation between the neutron spectrum and the observed proton spectrum. This relation can be written in the form

$$M(E_T) = n_p \cdot t \int_{E_T}^{\infty} \frac{\sigma_{np}(E)\phi(E)}{E} dE \qquad (1)$$

where

$\phi(E)$ = Neutron flux (neutrons/cm²/MeV/s)
t = Exposure time (s)
E = Neutron or proton energy (MeV)
n_p = Atomic hydrogen density (emulsion in atoms/cm³)
$M(E_T)$ = Proton spectrum (proton tracks/MeV/cm³) observed in the emulsion at energy E_T.

The integral in Eq. (1) can be defined as

$$I(E_T) = \int_{E_T}^{\infty} \frac{\sigma_{np}(E)}{E} \phi(E)\, dE \quad . \qquad (2)$$

Here $I(E_T)$ possesses units of protons/(MeV-s)/hydrogen atom. Clearly $I(E_T)$ is a function of the lower proton energy cutoff (E_T) used to analyze the emulsion data. Using Eq. (2) in Eq. (1), one finds the integral relation:

$$I(E_T) = \frac{M(E_T)}{n_p \cdot t} \quad . \qquad (3)$$

$I(E_T)$ is evaluated by using a least-squares fit of the NRE scanning data in the neighborhood of $E = E_T$. Alternatively, since:

$$M(E_T) = M(R_T) \frac{dR}{dE} \quad , \qquad (4)$$

where dR/dE is known from the proton range-energy relation in emulsions, one need only determine $M(R_T)$ in the neighborhood of $R = R_T$. Here $M(R)$ is the proton-recoil range distribution in units of proton-recoil tracks/μm/cm³ observed in the emulsion. Consequently, scanning efforts can be concentrated in the neighborhood of $R = R_T$ in order to determine $I(E_T)$. In this manner, the accuracy attained in $I(E_T)$ is comparable to the accuracy of the differential determination of $\phi(E)$, as derived from Eq. (1), but with a significantly reduced scanning effort.

The second integral can be obtained by integration of the observed proton spectrum $M(E_T)$. From Eq. (1), one has

$$\int_{E_{min}}^{\infty} M(E_T)\, dE_T = (n_p \cdot t) \cdot \int_{E_{min}}^{\infty} dE_T \cdot \int_{E_T}^{\infty} \frac{\sigma_{np}(E)}{E} \phi(E)\, dE, \qquad (5)$$

where E_{min} is the lower proton energy cutoff used to analyze the emulsion data. Introducing into Eq. (5) the definitions:

$$\mu(E_{min}) = \int_{E_{min}}^{\infty} M(E_T)\, dE_T \quad , \tag{6}$$

and

$$J(E_{min}) = \int_{E_{min}}^{\infty} dE_T \int_{E_T}^{\infty} \frac{\sigma_{np}(E)}{E}\, \phi(E)\, dE \quad , \tag{7}$$

one has

$$J(E_{min}) = \frac{\mu(E_{min})}{n_p \cdot t} \quad . \tag{8}$$

Hence, the second integral relation, namely Eq. (8), can be expressed in a form analyogous to the first integral relation, namely Eq. (3). Here, $\mu(E_{min})$ is the integral number of proton-recoil tracks/cm³ observed above an energy E_{min} in the emulsion. Consequently, the integral $J(E_{min})$ possesses units of tracks/s/hydrogen atom.

The integral $J(E_{min})$ can be reduced to the form

$$J(E_{min}) = \int_{E_{min}}^{\infty} \frac{\left(1 - \frac{E_{min}}{E}\right)}{E}\, \sigma_{np}(E)\, \phi(E)\, dE \quad . \tag{9}$$

In addition, by using Eq. (4), the observable $\mu(E_{min})$ can be expressed in the form

$$\mu(E_{min}) = \int_{R_{min}}^{\infty} M(R)\, dR \quad . \tag{10}$$

Hence, to determine the second integral relationship, one need only count proton-recoil tracks above $R = R_{min}$. Tracks considerably longer than R_{min} need not be measured, but simply counted. However, for tracks in the neighborhood of $R = R_{min}$, track length must be measured so that an accurate lower bound R_{min} can be effectively determined.

It is of interest to compare the differential energy responses available from these two integral relations. From Eqs. (2) and (9), one finds responses of the form $\sigma_{np}(E)/E$ and $(1 - E_{min}/E)\sigma_{np}(E)$ for the first and

second integral relations, respectively. [Note that the integrals $I(E_T)$ and $J(E_{min})$ possess different units, namely protons/MeV-s and protons/s, respectively.] Here, the hydrogen scattering cross section $\sigma_{n,p}(E)$ is given by (Ba73,Ga61)

$$\sigma_{n,p}(E) = 3\pi\left[1.206\ E_n + \left(-1.860 + 0.0941491\ E_n + 0.000130658\ E_n^{\,2}\right)^2\right]^{-1} + \pi\left[1.206\ E_n + \left(0.4223 + 0.1300\ E_n\right)^2\right]^{-1} \qquad (11)$$

where: E is in MeV and $\sigma_{n,p}$ is in barns.

These two responses are compared in Figure HEDL-2 using a common cutoff of 0.5 MeV for both E_T and E_{min}. Since these two responses are substantially different, simultaneous application of these two integral relations is not only possible, but highly advantageous.

Sources of systematic uncertainty for absolute neutron dosimetry with NREs are summarized in Table HEDL-9. Since these sources of uncertainty are essentially independent, the quadrature uncertainty for all systematic effects comes to roughly 5%. It should be stressed that Table HEDL-9 does not include uncertainties arising from the in-situ irradiation, such as exist in exposure time t as well as in absolute power level.

Uncertainties in the absolute reaction rates $I(E_T)$ and $J(E_{min})$ follow from Eqs. (3) and (8), respectively. The relative variances for these absolute reaction rates are given by

$$\left(\frac{\delta I}{I}\right)^2 = \left(\frac{\delta M}{M}\right)^2 + \left(\frac{\delta n_p}{n_p}\right)^2 + \left(\frac{\delta t}{t}\right)^2 \qquad (12)$$

and

$$\left(\frac{\delta J}{J}\right)^2 = \left(\frac{\delta \mu}{\mu}\right)^2 + \left(\frac{\delta n_p}{n_p}\right)^2 + \left(\frac{\delta t}{t}\right)^2 \qquad (13)$$

4.0 Experimental Results

To date, six NREs exposed in the VENUS PWR mockup have been scanned in the integral mode on the ESP system. Table HEDL-10 summarizes irradiation and location information for these six NRE. All six NREs were the Ilford L-4 type emulsion, 400 μ thick. Approximately 10^3 proton-recoil tracks have been observed in each of these NREs. To illustrate the quality of these data, Figures HEDL-3 and -4 show the I-integral and J-integral track data, respectively, for the NREs exposed at the V1 location in Venus irradiation 83/04.

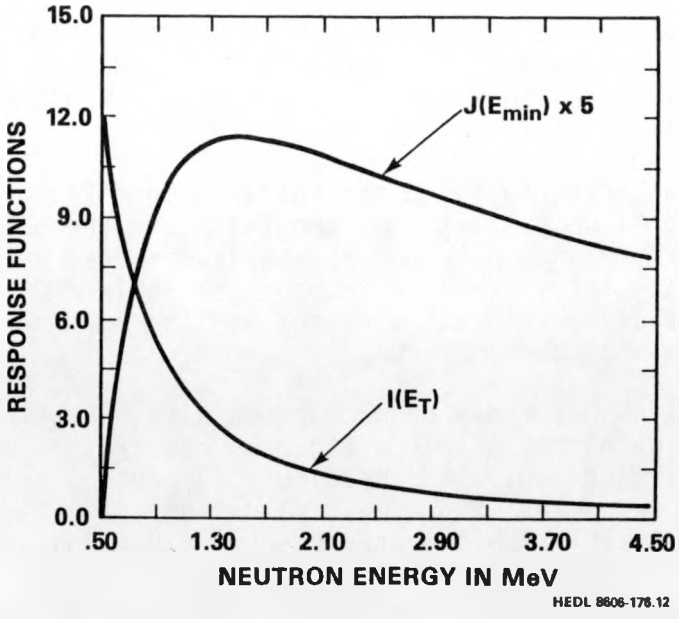

FIGURE HEDL-2. Response Factors for the Integral Reaction Rates $I(E_T)$ and $J(E_{min})$. $I(E_T)$ possesses units of barns/MeV and $J(E_{min})$ possesses units of barns.

TABLE HEDL-9

UNCERTAINTY ESTIMATES FOR ABSOLUTE NEUTRON SPECTROMETRY WITH NUCLEAR RESEARCH EMULSIONS

Source of Uncertainty	Approximate Relative Uncertainty (1σ)
Proton range straggling	2%
Proton energy based on range-energy relation	2%
Range measurements	2%
Volume of emulsion scanned	2%
Hydrogen density in the emulsion	3%
Hydrogen $\sigma_{np}(E)$ cross section	1%

I-integral and J-integral proton-recoil reaction rates obtained from the scanning data for these six NRE are summarized in Tables HEDL-11 through HEDL-16. A set of neutron energy thresholds was used to obtain I-integral results from the proton-recoil scanning data. A set of J-integral results was obtained by analyzing the same proton-recoil scanning data, except that the set of neutron energy thresholds was different than the set used for the I-integral results.

The experimental uncertainty given for the J-integral results is ∿6% at the 1σ level. The 1σ uncertainty for the I-integral results is larger and varies from ∿7% to 10%. The uncertainties reported here include systematic uncertainties in the NRE method (see Table HEDL-9), statistical uncertainties that arise in track scanning and the 1σ uncertainty in scaling results to the reference run.

These experimental results have been compared with CEN/SCK 17-group neutron energy spectra calculations (Fa87)*. To make comparisons with NRE results scaled to the reference run, CEN/SCK-calculated neutron spectra were also scaled to the reference run with a multiplicative scale factor of 2.00673E+14. The FERRET-SAND computer code (Be67b,Sc79) was used to calculate the I-integral and J-integral proton recoil reaction rates. Group cross sections were constructed to carry out the integration in the FERRET-SAND II code. For energy groups above the threshold, the group-averaged cross section for the I-integral is given by

$$\bar{\sigma}_i = \int_{E_1}^{E_2} \frac{\sigma_{np}}{E}\,\phi(E)dE \Bigg/ \int_{E_1}^{E_2} \phi(E)\,dE \quad , \qquad (14)$$

where E_1 and E_2 are the energy boundaries of group i and σ_{np} is the hydrogen (n,p) scattering cross section, which has already been given in Eq. (11). The I-integral is then calculated by summing $\sigma_i\phi_i$ over all groups (similar to the other reaction rates). Integration (summation) is carried out using the SAND II 620-group structure. The corresponding J-integral group averaged cross section is

$$\bar{\sigma}_j = \int_{E_1}^{E_2} \frac{\sigma_{np}}{E}\,(E - E_{th})\,\phi(E)dE \Bigg/ \int_{E_1}^{E_2} \phi(E)\,dE \qquad (15)$$

where E_{th} is the energy threshold. For groups below the threshold, $\bar{\sigma}_j = 0$ and for the group including the threshold a suitable interpolation is used.

*A. Fabry, W. N. McElroy and E. D. McGarry, eds., LWR-PV-SDIP: VENUS PWR Core Source and Azimuthal Lead Factor Experiments and Calculational Tests, NUREG/CR-3323, NRC, Washington, DC, (to be published).

TABLE HEDL-10

VENUS NRE INTEGRAL MODE SCANNING STATUS

VENUS Irradiation	NRE Location	Observed Tracks
83/04	V1 (X=2.5,Y=2.5)	947
83/05	V3 (R=62.7,θ=21°)	1074
83/06	Barrel (X=-35,Y=-12)	1085
83/06	Barrel (X=-28,Y=-24)	996
83/07	Outer Baffle (X=-17,Y=-14)	1017
83/07	Outer Baffle (X=-29,Y=-12)	1004

Calculated and observed proton-recoil reaction rates are compared by location in Tables HEDL-17 through HEDL-22. Calculated-to-experimental (C/E) ratios range from a low of ∿0.9 to a high of approximately 1.7. At each location, the C/E values for the J-integral are generally closer to unity than the C/E values for the I-integral. At two locations, the agreement between theory and experiment is good, namely for the I- and J-integral comparisons at location V1 as well as for the J-integral comparisons in the barrel at 41°. At other locations agreement is marginal, such as at location V3 as well as in the outer baffle at 42°. Finally, disagreement clearly exists at the 21° location in the barrel at the 24° location in the outer baffle.

A pattern emerges from these comparisons that implies that the deviation of the C/E ratio from unity increases the closer one comes to the edge of the core corner at approximately 28°. There is acceptable agreement at both core center (V1) and in the neutron pad (V3), which are both far from the edge of the core corner. The agreement is marginal at 41° in the barrel and at 42° in the outer baffle, which both lie closer to the edge of the core corner. At the closest positions to the edge of the core corner, namely at 21° in the barrel and at 24° in the outer baffle, there is evident disagreement.

This behavior pattern suggests that difficulty arises in the calculational treatment of neutron transport near the edge of the core corner. The limited structure of these 17-group calculations may also contribute to the differences observed between theory and experiment. In particular, Group 8

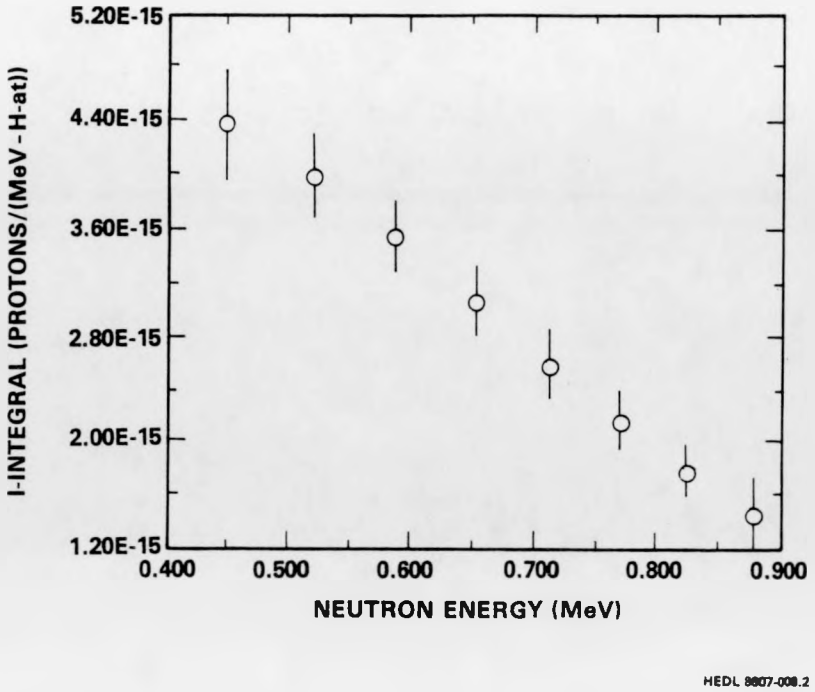

FIGURE HEDL-3. I-Integral Proton-Recoil Track Data Obtained from Integral Mode Scanning of the NRE Exposed at Location V1 During VENUS Irradiation 83/04 and Normalized to the VENUS Reference Run. (See Table HEDL-1.)

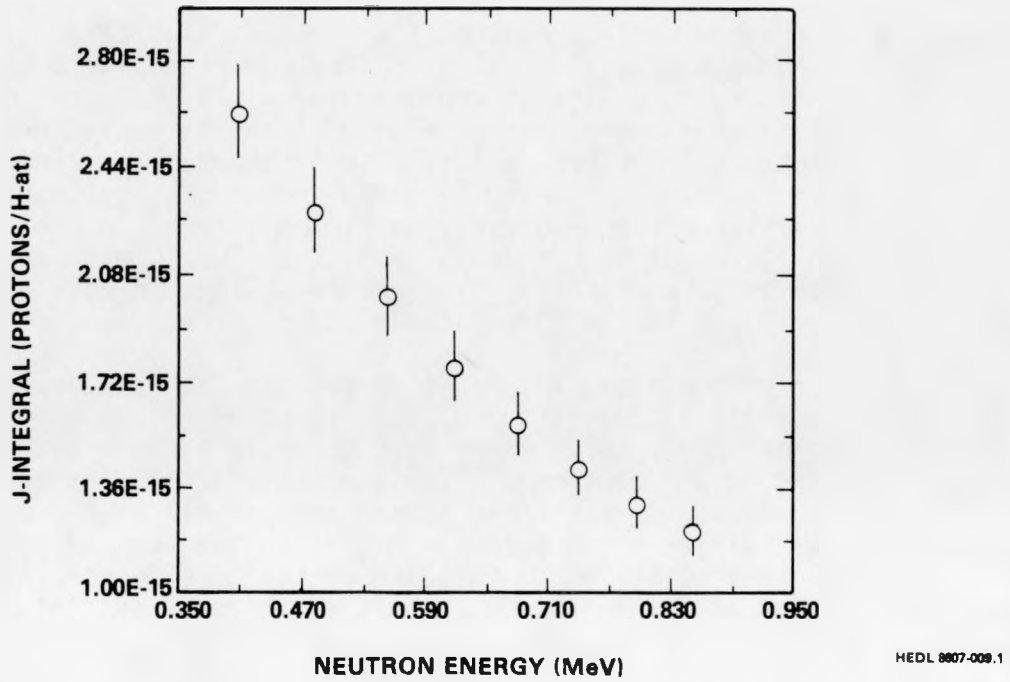

FIGURE HEDL-4. J-Integral Proton-Recoil Track Data Obtained from Integral Mode Scanning of the NRE Exposed at Location V1 During VENUS Irradiation 83/04 and Normalized to the VENUS Reference Run. (See Table HEDL-1.)

TABLE HEDL-11

PROTON-RECOIL REACTION RATES FOR NRE EXPOSED
IN VENUS AT LOCATION V1 FOR IRRADIATION 83/04

Neutron Energy (MeV)		Observed Reaction Rate	Reaction Rate Scaled to Reference Run[c]	Total (%) Uncertainty[d]
I[a]	0.4467	2.977E-16	4.381E-15	8.7
I	0.5198	2.713E-16	3.993E-15	7.3
I	0.5877	2.407E-16	3.542E-15	7.1
I	0.6515	2.085E-16	3.068E-15	8.2
I	0.7119	1.767E-16	2.601E-15	9.3
J[b]	0.4073	1.784E-16	2.626E-15	5.8
J	0.4837	1.557E-16	2.291E-15	5.9
J	0.5540	1.366E-16	2.011E-15	6.0
J	0.6197	1.208E-16	1.778E-15	6.1

(a) Units of protons/(MeV•s).
(b) Units of protons/s.
(c) Scale factor obtained from Run 83/04 of Table HEDL-2.3.1 (NUREG/CR-3323, Vol. 1) is 14.72.
(d) Total uncertainty is given at the 1σ level.

TABLE HEDL-12

PROTON-RECOIL REACTION RATES FOR NRE EXPOSED
IN VENUS AT LOCATION V3 FOR IRRADIATION 83/05

Neutron Energy (MeV)		Observed Reaction Rate	Reaction Rate Scaled to Reference Run[c]	Total (%) Uncertainty[d]
I[a]	0.4467	1.927E-16	3.785E-17	8.1
I	0.5198	1.765E-16	3.466E-17	6.7
I	0.5877	1.553E-16	3.051E-17	6.7
I	0.6515	1.305E-16	2.564E-17	7.6
I	0.7119	1.031E-16	2.025E-17	8.6
J[b]	0.4073	1.009E-16	1.982E-17	5.7
J	0.4837	8.624E-17	1.694E-17	5.8
J	0.5540	7.382E-17	1.450E-17	5.9
J	0.6197	6.364E-17	1.250E-17	6.0

(a) Units of protons/(MeV•s).
(b) Units of protons/s.
(c) Scale factor obtained from Run 83/05 of Table HEDL-2.3.1 (NUREG/CR-3323, Vol. 1) is 0.1964.
(d) Total uncertainty is given at the 1σ level.

TABLE HEDL-13

PROTON-RECOIL REACTION RATES FOR NRE EXPOSED IN
VENUS BARREL AT 21°, (X=-35,Y=-12) FOR IRRADIATION 83/06

Neutron Energy (MeV)		Observed Reaction Rate	Reaction Rate Scaled to Reference Run[c]	Total (%) Uncertainty[d]
I[a]	0.4467	2.050E-16	2.961E-16	8.3
I	0.5198	1.575E-16	2.275E-16	7.1
I	0.5877	1.213E-16	1.752E-16	8.6
I	0.6515	9.674E-17	1.397E-16	9.4
I	0.7119	8.178E-17	1.181E-16	9.5
J[b]	0.4073	9.688E-17	1.399E-16	5.6
J	0.4837	8.123E-17	1.173E-16	5.8
J	0.5540	7.015E-17	1.013E-16	5.9
J	0.6197	6.219E-17	8.981E-17	5.9

[a]Units of protons/(MeV•s).
[b]Units of protons/s.
[c]Scale factor obtained from Run 83/06 of Table HEDL-2.3.1 (NUREG/CR-3323, Vol. 1) is 1.444.
[d]Total uncertainty is given at the 1σ level.

TABLE HEDL-14

PROTON-RECOIL REACTION RATES FOR NRE EXPOSED IN
VENUS BARREL AT 41°, (X=-28,Y=-24) FOR IRRADIATION 83/07

Neutron Energy (MeV)		Observed Reaction Rate	Reaction Rate Scaled to Reference Run[c]	Total (%) Uncertainty[d]
I[a]	0.4467	9.404E-17	1.358E-16	8.9
I	0.5198	8.455E-17	1.221E-16	7.4
I	0.5877	7.430E-17	1.073E-16	7.0
I	0.6515	6.416E-17	9.266E-17	7.9
I	0.7119	5.499E-17	7.941E-17	9.1
J[b]	0.4073	6.344E-17	9.162E-17	5.8
J	0.4837	5.628E-17	8.127E-17	5.8
J	0.5540	5.034E-17	7.269E-17	5.9
J	0.6197	4.545E-17	6.564E-17	6.0

[a]Units of protons/(MeV•s).
[b]Units of protons/s.
[c]Scale factor obtained from Run 83/06 of Table HEDL-2.3.1 (NUREG/CR-3323, Vol. 1) is 1.444.
[d]Total uncertainty is given at the 1σ level.

TABLE HEDL-15

PROTON-RECOIL REACTION RATES FOR NRE EXPOSED
IN VENUS OUTER BAFFLE AT 42°, (X=-17,Y=-14) FOR IRRADIATION 83/07

Neutron Energy (MeV)		Observed Reaction Rate	Reaction Rate Scaled to Reference Run[c]	Total (%) Uncertainty[d]
I[a]	0.4467	6.964E-16	3.843E-15	8.4
I	0.5198	6.389E-16	3.526E-15	7.0
I	0.5877	5.711E-16	3.152E-15	6.8
I	0.6515	4.990E-16	2.754E-15	7.5
I	0.7119	4.269E-16	2.356E-15	8.4
J[b]	0.4073	4.133E-16	2.281E-15	5.8
J	0.4837	3.602E-16	1.988E-15	5.9
J	0.5540	3.153E-16	1.740E-15	6.0
J	0.6197	2.778E-16	1.533E-15	6.1

(a)Units of protons/(MeV•s).
(b)Units of protons/s.
(c)Scale factor obtained from Run 83/07 of Table HEDL-2.3.1 (NUREG/CR-3323, Vol. 1) is 5.519.
(d)Total uncertainty is given at the 1σ level.

TABLE HEDL-16

PROTON-RECOIL REACTION RATES FOR THE NRE EXPOSED
IN VENUS OUTER BAFFLE AT 24°, (X=-29,Y=-12) FOR IRRADIATION 83/07

Neutron Energy (MeV)		Observed Reaction Rate	Reaction Rate Scaled to Reference Run[c]	Total (%) Uncertainty[d]
I[a]	0.4467	2.843E-16	1.569E-15	8.4
I	0.5198	1.830E-16	1.010E-15	8.4
I	0.5877	1.406E-16	7.759E-16	8.9
I	0.6515	1.264E-16	6.978E-16	8.9
I	0.7119	1.149E-16	6.343E-16	10.0
J[b]	0.4073	1.085E-16	5.986E-16	5.8
J	0.4837	8.678E-17	4.789E-16	5.9
J	0.5540	7.391E-17	4.079E-16	6.0
J	0.6197	6.469E-17	3.570E-16	6.1

(a)Units of protons/(MeV•s).
(b)Units of protons/s.
(c)Scale factor obtained from Run 83/07 of Table HEDL-2.3.1 (NUREG/CR-3323, Vol. 1) is 5.519.
(d)Total uncertainty is given at the 1σ level.

TABLE HEDL-17

COMPARISON OF CALCULATED AND OBSERVED PROTON-RECOIL REACTION RATES IN VENUS AT LOCATION V1[a]

Neutron Energy (MeV)		Calculation	Experiment	C/E
I[b]	0.4467	5.72E-15	4.38E-15	1.30
I	0.5198	4.50E-15	3.99E-15	1.13
I	0.5877	3.65E-15	3.54E-15	1.03
I	0.6515	3.15E-15	3.07E-15	1.03
I	0.7119	2.72E-15	2.60E-15	1.05
J[c]	0.4073	2.74E-15	2.63E-15	1.04
J	0.4837	2.33E-15	2.29E-15	1.02
J	0.5540	2.03E-15	2.01E-15	1.01
J	0.6197	1.80E-15	1.78E-15	1.01

[a]Reference run irradiation conditions apply.
[b]Units of protons/(MeV•s).
[c]Units of protons/s.

TABLE HEDL-18

COMPARISON OF CALCULATED AND OBSERVED PROTON-RECOIL REACTION RATES IN VENUS AT LOCATION V3[a]

Neutron Energy (MeV)		Calculation	Experiment	C/E
I[b]	0.4467	4.56E-17	3.79E-17	1.20
I	0.5198	3.47E-17	3.47E-17	1.00
I	0.5877	2.70E-17	3.05E-17	0.89
I	0.6515	2.28E-17	2.56E-17	0.89
I	0.7119	1.92E-17	2.03E-17	0.94
J[c]	0.4073	1.86E-17	1.98E-17	0.94
J	0.4837	1.54E-17	1.69E-17	0.91
J	0.5540	1.31E-17	1.45E-17	0.90
J	0.6197	1.14E-17	1.25E-17	0.91

[a]Reference run irradiation conditions apply.
[b]Units of protons/(MeV•s).
[c]Units of protons/s.

TABLE HEDL-19

COMPARISON OF CALCULATED AND OBSERVED PROTON-RECOIL REACTION RATES IN VENUS BARREL AT 21°, X=-35,Y=-12[a]

Neutron Energy (MeV)		Calculation	Experiment	C/E
I[b]	0.4467	4.62E-16	2.96E-16	1.56
I	0.5198	3.52E-16	2.28E-16	1.54
I	0.5877	2.77E-16	1.75E-16	1.58
I	0.6515	2.36E-16	1.40E-16	1.68
I	0.7119	2.01E-16	1.18E-16	1.70
J[c]	0.4073	1.96E-16	1.40E-16	1.40
J	0.4837	1.64E-16	1.17E-16	1.40
J	0.5540	1.40E-16	1.01E-16	1.39
J	0.6197	1.22E-16	8.98E-17	1.36

(a)Reference run irradiation conditions apply.
(b)Units of protons/(MeV•s).
(c)Units of protons/s.

TABLE HEDL-20

COMPARISON OF CALCULATED AND OBSERVED PROTON-RECOIL REACTION RATES IN VENUS BARREL AT 41°, X=-28,Y=-24[a]

Neutron Energy (MeV)		Calculation	Experiment	C/E
I[b]	0.4467	2.15E-16	1.36E-16	1.58
I	0.5198	1.66E-16	1.22E-16	1.36
I	0.5877	1.32E-16	1.07E-16	1.24
I	0.6515	1.13E-16	9.27E-17	1.22
I	0.7119	9.72E-17	7.94E-17	1.22
J[c]	0.4073	9.72E-17	9.16E-17	1.06
J	0.4837	8.21E-17	8.13E-17	1.01
J	0.5540	7.10E-17	7.27E-17	0.98
J	0.6197	6.26E-17	6.56E-17	0.96

(a)Reference run irradiation conditions apply.
(b)Units of protons/(MeV•s).
(c)Units of protons/s.

TABLE HEDL-21

COMPARISON OF CALCULATED AND OBSERVED PROTON-RECOIL REACTION RATES IN THE VENUS OUTER BAFFLE AT 42°, X=-17,Y=-14[a]

Neutron Energy (MeV)		Calculation	Experiment	C/E
I[b]	0.4467	6.28E-15	3.84E-15	1.64
I	0.5198	4.89E-15	3.53E-15	1.38
I	0.5877	3.89E-15	3.15E-15	1.23
I	0.6515	3.34E-15	2.75E-15	1.21
I	0.7119	2.85E-15	2.36E-15	1.21
J[c]	0.4073	2.78E-15	2.28E-15	1.22
J	0.4837	2.33E-15	1.99E-15	1.17
J	0.5540	2.01E-15	1.74E-15	1.15
J	0.6197	1.76E-15	1.53E-15	1.15

[a]Reference run irradiation conditions apply.
[b]Units of protons/(MeV•s).
[c]Units of protons/s.

TABLE HEDL-22

COMPARISON OF CALCULATED AND OBSERVED PROTON-RECOIL REACTION RATES IN THE VENUS OUTER BAFFLE AT 24°, X=-29,Y=-12[a]

Neutron Energy (MeV)		Calculation	Experiment	C/E
I[b]	0.4467	1.98E-15	1.57E-15	1.26
I	0.5198	1.53E-15	1.01E-15	1.51
I	0.5877	1.22E-15	7.76E-16	1.57
I	0.6515	1.04E-15	6.98E-16	1.50
I	0.7119	8.88E-16	6.34E-16	1.40
J[c]	0.4073	8.68E-16	5.99E-16	1.45
J	0.4837	7.25E-16	4.79E-16	1.51
J	0.5540	6.24E-16	4.08E-16	1.53
J	0.6197	5.46E-16	3.57E-16	1.53

[a]Reference run irradiation conditions apply.
[b]Units of protons/(MeV•s).
[c]Units of protons/s.

in these calculations covers the neutron energy range from 407.6 keV up to 742.7 keV, which corresponds to the entire range of threshold energies used to analyze the NRE proton-recoil data. In contrast, the neutron energy resolution available from NRE varies from roughly 80 keV down to 50 keV (FWHM), with increasing neutron energy in the region from 0.4 MeV up to 1.0 MeV.

In this regard, Table HEDL-23 summarizes the NRE-observed low energy-to-high energy I- and J-reaction rate ratios by location. The I-reaction rate ratio varies from roughly 1.6 up to 2.5, whereas the J-reaction rate ratio varies from about 1.4 up to 1.7. Given these observed variations, calculations using a single energy group to cover the energy range of these observations do not treat the physical processes of neutron transport in sufficient detail to generate a definitive comparison between theory and experiment. Under these conditions, the resulting C/E ratios are probably as good as one has any right to expect.

TABLE HEDL-23

PROTON-RECOIL REACTION RATE RATIOS

Location	I(0.4467)/I(0.7119)	J(0.4073)/J(0.6197)
V1	1.68	1.48
V3	1.87	1.59
Barrel 21°	2.50	1.56
Barrel 41°	1.71	1.40
Outer Baffle 24°	2.47	1.68
Outer Baffle 42°	1.63	1.49

Conclusions

The agreement between calculations and NRE observed absolute proton-recoil reaction rates depends sensitively on location in the VENUS PWR mockup. Adequate agreement is attained near the center of the core. However, as one approaches the edge of the core corner at ∿28° (see Figure HEDL-1), the agreement deteriorates. Comparisons between theory and experiment are limited by the broad energy resolution of the 17-energy group structure used in the calculations.

Expected Future Accomplishments

In future C-to-E comparisons of NRE proton-recoil reaction rates observed in the VENUS PWR benchmark, the effect of a finer energy group structure in the calculations will be investigated. Additional NRE irradiated in VENUS will

be scanned. In particular, proportional counter perturbation effects will be investigated by scanning NRE from VENUS irradiations 83/08 through 83/11 (see Tables HEDL-5 through HEDL-8).

Acknowledgments

We are indebted to A. Fabry and L. Leenders for consultation, review and guidance in the conduct of these NRE experiments. The NRE irradiations in VENUS could not have been carried out without the close collaboration and assistance of the VENUS operating crews. In particular, the assistance of P. Truyens and J. VanDijck is sincerely acknowledged.

B. EVALUATION OF NEUTRON EXPOSURE CONDITIONS FOR THE BUFFALO REACTOR

E. P. Lippincott*, L. S. Kellogg, W. Y. Matsumoto, and W. N. McElroy (HEDL) and C. A. Baldwin (ORNL)

Objective

The objective of this work is to provide an evaluation of neutron exposure conditions for in-core metallurgical irradiations in the Buffalo Reactor using a combination of calculational and measurement techniques.

Summary

A calculation was performed using a neutron transport theory to evaluate the neutron flux-spectrum within the Buffalo Reactor core region. In addition, a dosimetry irradiation was carried out under carefully controlled conditions using a mockup of an actual metallurgical assembly. Comparisons of the calculation and measurements indicate good agreement, and the combination of the two can be used to determine exposure parameter values to accuracies of 10% to 15%. Systematic differences between measurement and calculation, however, indicate the importance of continued dosimetry measurements for accurate flux-fluence evaluation.

Accomplishments and Status

1.0 Introduction

The light water test reactor at the Nuclear Science and Technology Facility of the State University of New York at Buffalo is currently being used to irradiate specimens in in-core positions for NRC-sponsored metallurgical tests. It is important that the neutron exposures for these Buffalo tests be consistent with those determined for related irradiations in the Bulk Shielding Reactor (BSR) and the Oak Ridge Reactor (ORR) at the Oak Ridge National Laboratory (ORNL). Therefore, a dosimetry irradiation, using Hanford Engineering Development Laboratory (HEDL) National Reactor Dosimetry Center (NRDC) dosimetry procedures, and a neutronics calculation, using ORNL calculational procedures, were combined for an evaluation of a typical test condition. Results from this test serve both to accurately characterize the irradiation configuration at the time and to provide a benchmark for an improved basis for analysis of dosimetry measurements in future irradiations.

Although previous calculations and measurements have been made for the Buffalo metallurgical positions, the work reported here was performed with a new measurement block that was positioned as accurately as tolerances would

---

*Current address: Westinghouse-Nuclear Technology Division (W-NTD), P.O. Box 355, Pittsburgh, PA.

allow so that all water gaps would be precisely defined. In addition, the calculational model was based on the reactor conditions recorded at the time of the dosimetry irradiation, including, in so far as possible, all out-of-core structures, in-core experimental locations, and control rod positions.

2.0 Description of Experiment

2.1 Buffalo Reactor Description

The reactor consists of a 6 x 6 array of elements (Figure HEDL-5). Of these elements, 30 are fuel, each containing 25 pins of 6% enriched uranium. The fuel assemblies each initially contained about 14 kg of UO_2. The burnup in MWd/tonne U of each fuel assembly is indicated in Figure HEDL-5 (as of 3/31/83). The assemblies are positioned by an aluminum grid plate 5 in. thick located 3.75 in. below the fuel.

The fuel elements are constructed such that the centerline of the element tube that fits into the grid plate is off center. This permits the elements to be positioned such that there is a 1/2-in. water gap for the control rod shroud and blade to fit between Columns 2 and 3 and Columns 4 and 5.

A control rod shroud is made of two U-shaped aluminum channels that extend from the grid plate to several feet above the top of the core. The control blade moves between the shroud and has a stroke of 26 in. When the rod is fully inserted, its tip is 1 in. below the fuel; when the rod is fully retracted, the tip is 1 in. above the fuel. For the dosimetry irradiation, Rods 1, 2, 3 and 5 were 93% withdrawn (tip of the blade 0.82 in. below the top of the fuel), Rod 4 was 91.82% withdrawn (1.13 in. below the top of fuel), and Rod 6 (pulse rod) was completely out of the core (1.86 in. above the top of fuel). The blade is made of 80% silver, 15% indium, and 5% cadmium and is coated with a 0.003 in. thickness of nickel. The blade dimensions are 4.85 in. x 0.180 in. x 29 in.

The six core locations that do not contain fuel contain the startup source and various experiment locations. Four of these locations are shown as blanks in Figure 1 and consisted mostly of water at the time of the dosimetry irradiation.

The region surrounding the core is mostly water, which was at an average temperature of 116°F in the pool. The core outlet temperature was 127°F. Below the core is the Al grid plate and zircaloy elements; above the core are zircaloy and aluminum components plus the withdrawn control rod blades. Surrounding the core are several experimental tubes filled with water. Next to face A are three steel metallurgical experiments located 2-7/8 in. from the core face.

2.2 Description of Dosimetry Measurement

Two locations in the reactor are used for metallurgical irradiations, namely B-4 and C-2. The dosimetry irradiation was carried out in B-4 and lasted 48 hours. It was immediately adjacent in time to a metallurgical irradiation in the same location for which accurate fluence data were desired.

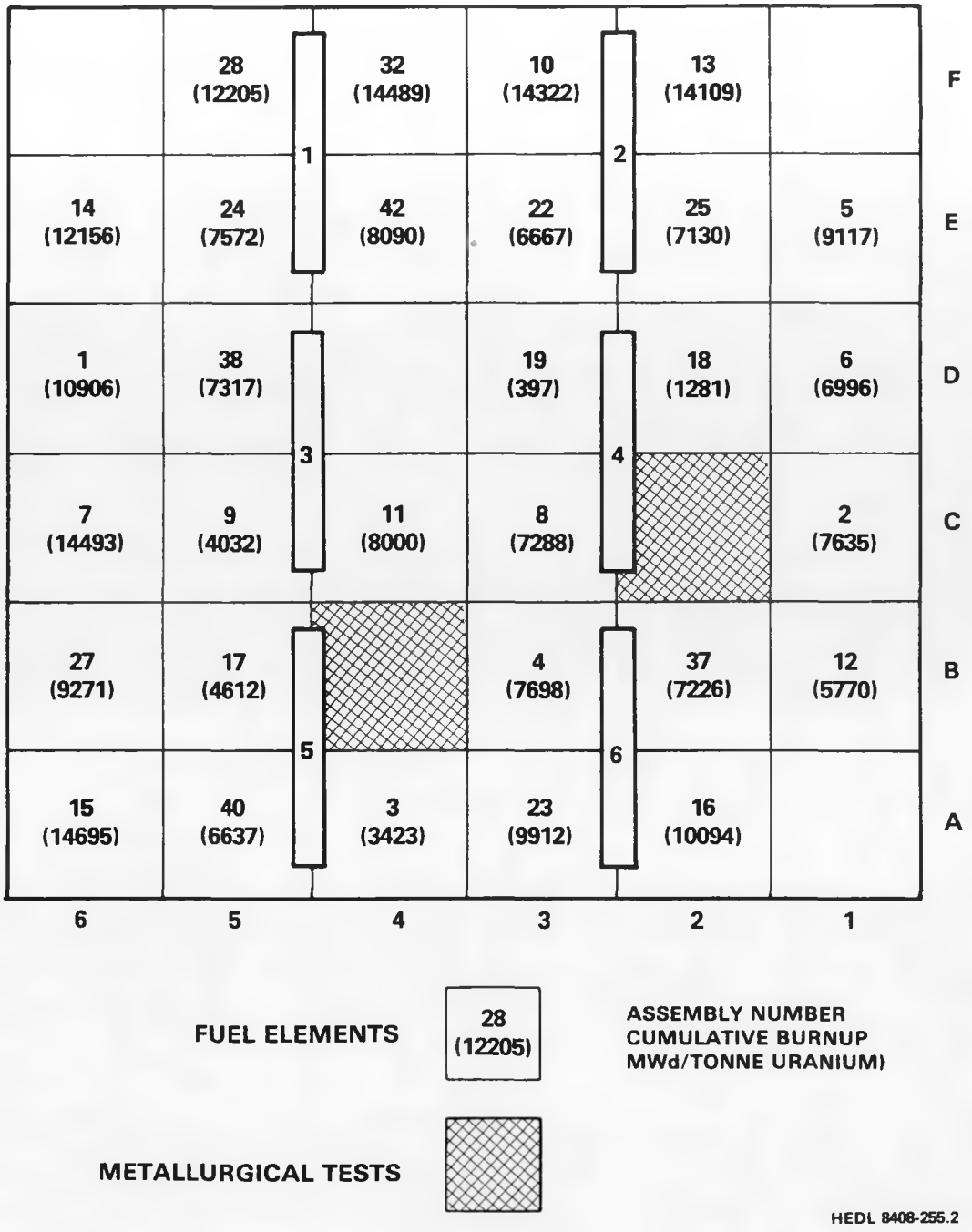

FIGURE HEDL-5. Buffalo Reactor Core Layout. Neg WY09063-2

The metallurgical experiment was irradiated in an ABC block, which consists of three separate steel sections as shown in Figure HEDL-6. Note that the top two sections (A and B) are smaller and have a water gap on one side to allow instrument tubes to carry thermocouple leads from the experiment.

The dosimetry pin was irradiated in a dummy ABC block with a hole down the center to contain the pin. The pin contained three cadmium-covered dosimetry spectral sets (S) positioned at the center of each of the three sections (see Figure HEDL-7). Bare gradient sets (G) were placed near the top and bottom of each section. The dosimeters contained in the spectral sets are listed in Table HEDL-24; the gradient sets contained only the Fe, Co/Al, and Ag/Al materials (0.5 in. long). The remaining space in the dosimetry pin and the pin itself were aluminum.

3.0 Description of the Calculation

The reactor calculation was carried out using the flow path shown in Figure HEDL-8. The CSRL-V cross-section library (Fo82), which is processed from ENDF/B-V, was used. This library was processed using various AMPX modules (Gr78b). A one-dimensional (1-D) slab model was used to collapse the cross sections to course groups. A separate slab model was used to represent the cases of fuel elements located next to other fuel elements and those next to the reflector.

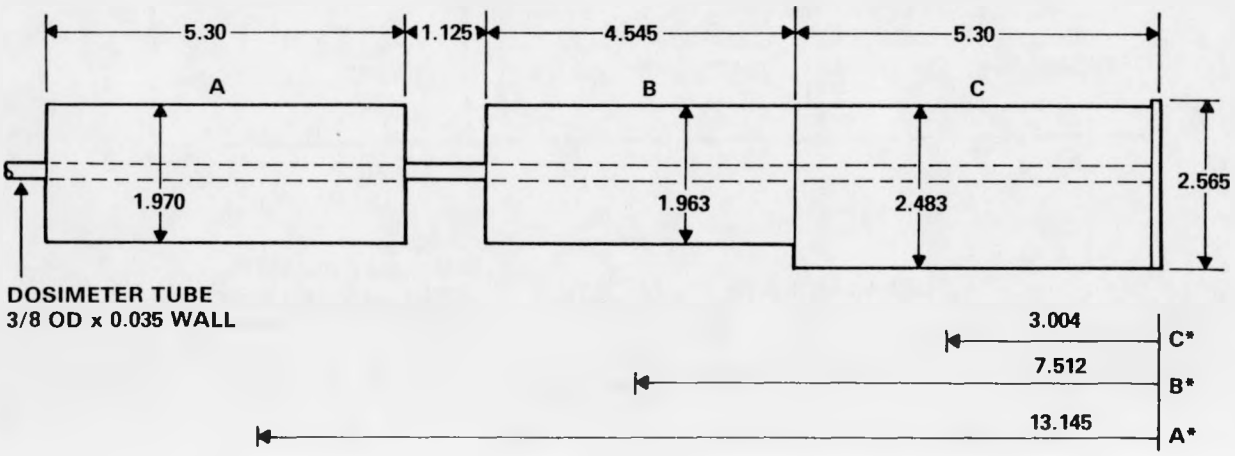

FIGURE HEDL-6. ABC Block. Neg WY09063-3

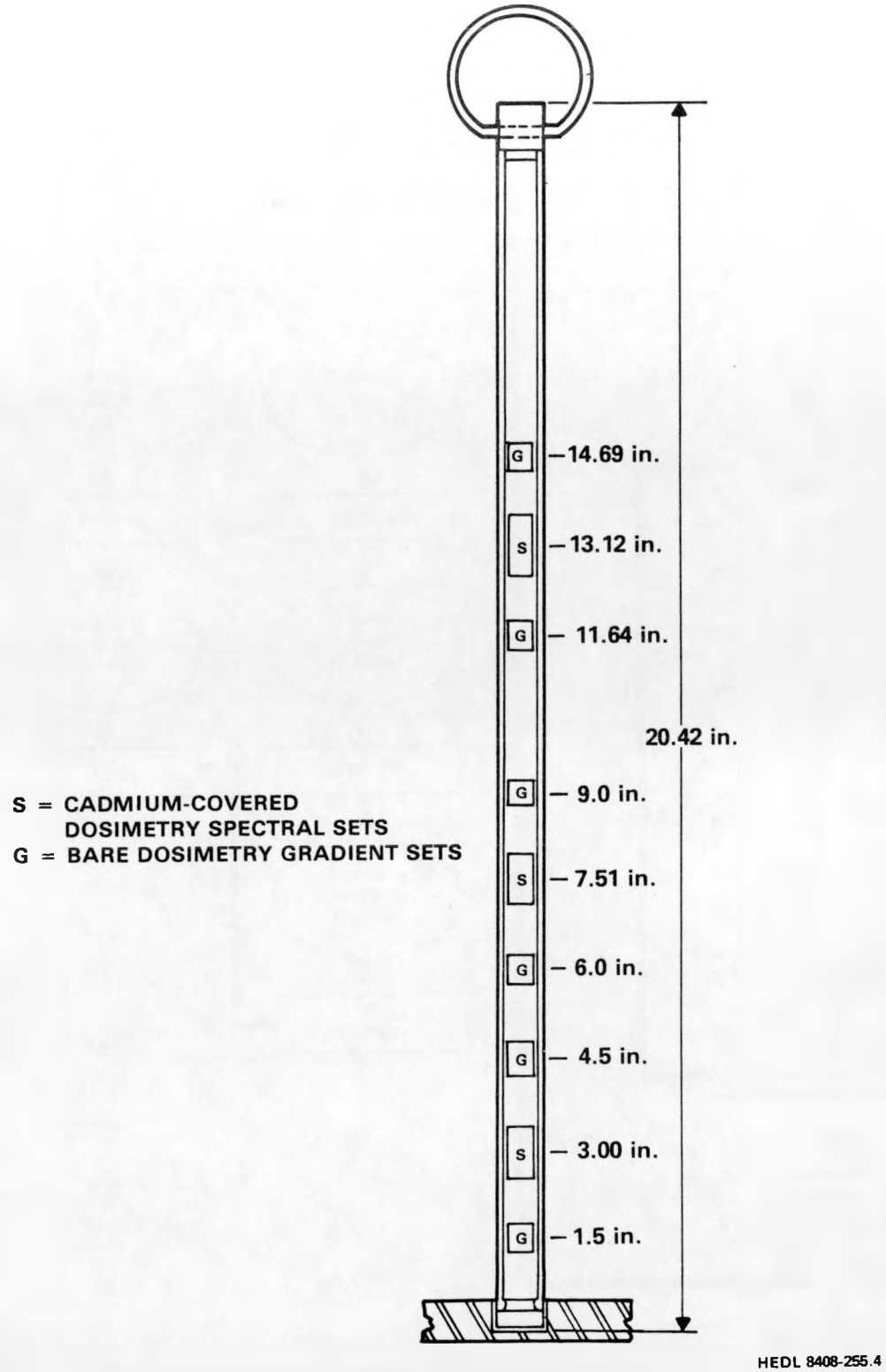

FIGURE HEDL-7. Dosimetry Pin. Neg WY09063-4

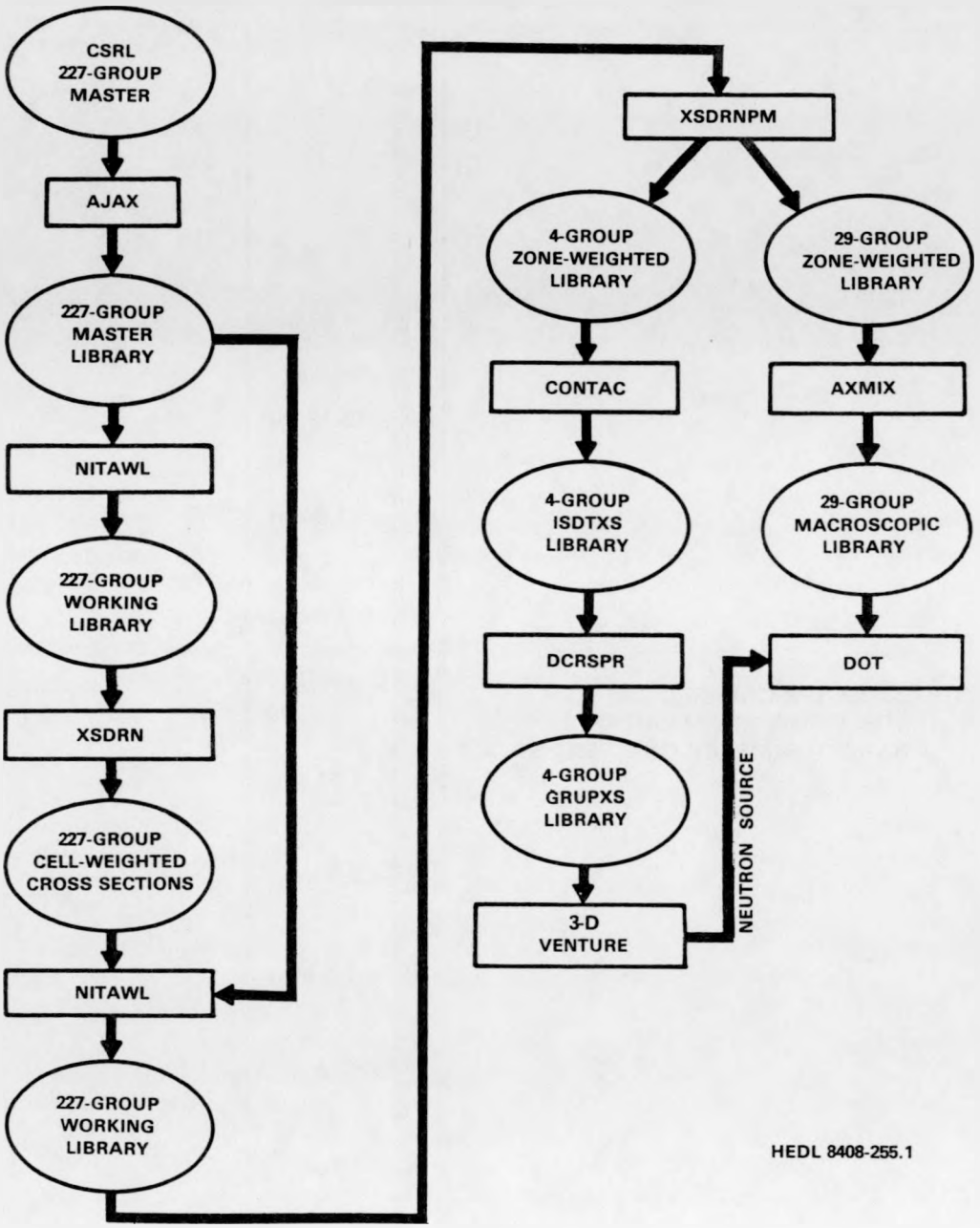

FIGURE HEDL-8. Cross-Section Processing and Calculational Path. Neg WY09063-1.

TABLE HEDL-24

MATERIALS IN DOSIMETRY SETS

Material	Description
0.116% Co/Al	0.020-in. diam x 0.25-in. long Wire
Fe	0.020-in. diam x 0.50-in. long Wire
0.145% Ag/Al	0.020-in. diam x 0.25-in. long Wire
$^{237}NpO_2$ in V	0.280-in. long x 0.035-in. diam Vanadium Capsule
Ti	0.020-in. diam x 1.5-in. long Wire
Ni	0.020-in. diam x 0.2-in. long Wire
Cu	0.020-in. diam x 1.0-in. long Wire
$^{238}UO_2$ in V	0.310-in. long x 0.035-in. diam Vandadium Capsule

A detailed three dimensional (3-D) X-Y-Z model was constructed of the reactor, including approximations of all material within 10 cm of the edge of the reactor core. The model had 41 x 36 x 39 mesh points. Each fuel assembly had heavy element and fission product atom densities calculated according to its burnup. The microscopic cross-section variation with burnup, however, was found to be slight, so cross sections for an average burnup were used. Four different sets of collapsed cross sections were used for the fuel, depending on location (i.e., surrounded by fuel, next to reflector, etc.).

The neutron source was calculated with a 3-D diffusion theory calculation using the code VENTURE (Vo81). A plot of the sources in a typical X-Y plane is shown in Figure HEDL-9. As is evident in this figure, sharp changes in power occur from assembly to assembly because of differences in burnup and details of the reactor configuration.

The final step in the calculation path is the 2-D transport calculation using DOT (Ha76,Rh82). This calculation was made for the X-Y plane through the center of the dosimetry location in the B block. Both the geometry and the source were taken for this plane, not averaged over the core height. The 2-D model was expanded to 49 x 49 mesh points to better model the details of the metallurgical block. The calculation used 29 groups, and the calculated flux-spectrum for the center of the dosimetry location is given in Table HEDL-25. The 29-energy groups were chosen to concentrate on calculation of the flux-spectrum above 0.1 MeV.

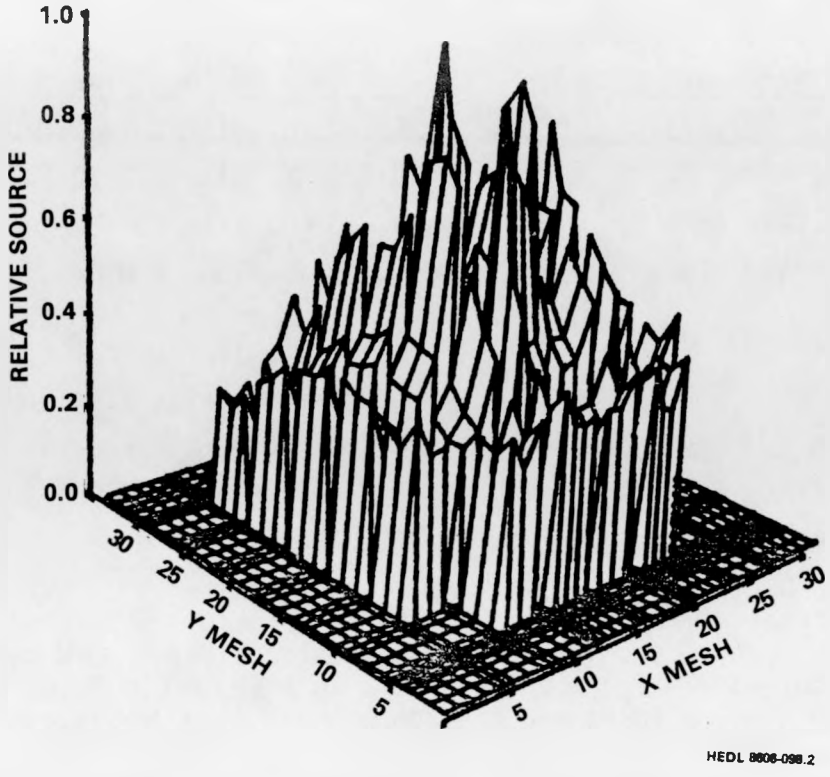

FIGURE HEDL-9. Three-Dimensional Plot of Neutron Source Across the X-1/4 Plane.

4.0 Results and Discussion

The dosimetry pin was irradiated for 48 hours, ending on July 31, 1983. The irradiation was at constant power and a square wave power history was used to correct measured decay rates to reactions per second. In addition, dosimetry was contained in two metallurgy blocks irradiated from June 12, 1983, to July 20 and July 26. The configuration for the metallurgy test was identical to the dosimetry test, except for the substitution of the mockup capsule and the dosimetry pin.

Results for the three sensor sets in the dosimetry pin are given in Table HEDL-26. The measurements included six threshold reactions and three broad-spectrum reactions, which respond to thermal and resonance neutrons. Comparisons of the three sets indicate good consistency for the results. Ratios for the threshold reactions are 0.85 ± 0.01 for A/B and 0.92 ± 0.01 for C/B. The good consistency indicates little axial variation for the fast neutron spectrum.

Results for the six gradient dosimeter sensor sets are presented in Table HEDL-27. These sets are not Cd covered, and the non-threshold reaction rates may be influenced by small differences in position relative to the block and water gaps. Impact of the adjacent spectral set cadmium is expected to be small.

TABLE HEDL-25

29-GROUP DOT SPECTRUM FOR THE B BLOCK DOSIMETRY LOCATION

Energy (MeV)*	Flux ($n/cm^2 \cdot s$)	Energy (MeV)	Flux ($n/cm^2 \cdot s$)
17.33	2.73×10^{7}	1.40	4.66×10^{11}
15.68	9.22×10^{7}	1.356	2.23×10^{11}
14.55	1.85×10^{8}	1.317	1.88×10^{11}
13.84	2.38×10^{8}	1.25	3.50×10^{11}
12.84	6.70×10^{8}	1.20	3.07×10^{11}
10.00	1.01×10^{10}	1.10	6.82×10^{11}
8.19	3.40×10^{10}	1.01	5.47×10^{11}
6.43	1.25×10^{11}	0.92	6.03×10^{11}
4.80	3.78×10^{11}	0.679	2.45×10^{12}
4.30	2.22×10^{11}	0.100	9.34×10^{12}
3.00	1.13×10^{12}	3.74×10^{-3}	3.75×10^{12}
2.48	9.80×10^{11}	6.50×10^{-5}	6.31×10^{12}
2.35	3.35×10^{11}	5.50×10^{-7}	5.58×10^{12}
1.85	1.38×10^{12}	1.0×10^{-10}	4.72×10^{11}**
1.50	1.39×10^{12}		

*Lower bound of the energy group in MeV.
**Calculated with cadmium shield; unshielded value is approximately 3.50×10^{12}.

A plot of the axial fast flux (E > 0.821 MeV) profile calculated by VENTURE is shown in Figure HEDL-10. Also shown are the measured $^{54}Fe(n,p)$ reaction rates normalized to the point at -2 cm. The comparison indicates excellent agreement for the axial flux profile, but a shift of about 1.5 inches is noted between the measurements and calculations. The source of this difference should be investigated. The curve and/or measured points can be used to estimate the axial flux variation in the metallurgical sample. Variation of the fast flux from the midplane value in each block appears to be about 10% or less.

A comparison is made between the dosimetry pin results and the dosimetry in the metallurgical test B block in Table HEDL-28. A similar comparison for the A block is presented in Table HEDL-29. Only small differences are noted for the flux above 1 MeV, but the resonance flux is depressed in the metallurgical block by 10% to 20%. This is probably caused by small differences in geometry between the metallurgical block and the dosimetry mockup.

TABLE HEDL-26

BUFFALO DOSIMETRY TEST SPECTRAL SENSOR RESULTS

Reaction	Reaction Rate* A	B	C
$^{54}Fe(n,p)^{54}Mn$	6.51×10^{-13}	7.58×10^{-13}	6.99×10^{-13}
$^{58}Ni(n,p)^{58}Co$	8.95×10^{-13}	1.05×10^{-12}	9.62×10^{-13}
$^{46}Ti(n,p)^{46}Sc$	8.62×10^{-14}	1.02×10^{-13}	9.34×10^{-14}
$^{63}Cu(n,\alpha)^{60}Co$	4.00×10^{-15}	4.73×10^{-15}	4.27×10^{-15}
$^{238}U(u,f)FP$	3.51×10^{-12}	4.11×10^{-12}	3.74×10^{-12}
$^{237}Np(n,f)FP$	2.12×10^{-11}	2.54×10^{-11}	2.35×10^{-11}
$^{59}Co(n,\gamma)^{60}Co$	8.49×10^{-11}	1.01×10^{-10}	9.28×10^{-11}
$^{109}Ag(n,\gamma)^{110m}Ag$	7.26×10^{-11}	8.60×10^{-11}	7.89×10^{-11}
$^{58}Fe(n,\gamma)^{59}Fe$	1.21×10^{-12}	1.44×10^{-12}	1.33×10^{-12}

*Nominal Locations: A: +8.2 cm; B: -6.0 cm; C: -17.4 cm.
All reactions are Cd covered. Reaction rates are given in reactions per second per nucleus.

TABLE HEDL-27

BUFFALO DOSIMETRY TEST GRADIENT SENSOR RESULTS

Location (cm)	Reaction Rate $^{54}Fe(n,\rho)$	$^{59}Co(n,\gamma)$	$^{109}Ag(n,\gamma)$	$^{58}Fe(n,\gamma)$
+12.2	5.82×10^{-13}	1.79×10^{-10}	7.46×10^{-11}	3.97×10^{-12}
+4.5	7.49×10^{-13}	3.38×10^{-10}	1.11×10^{-10}	8.48×10^{-12}
-2.2	7.82×10^{-13}	2.92×10^{-10}	1.09×10^{-10}	6.89×10^{-12}
-9.8	8.08×10^{-13}	2.53×10^{-10}	1.05×10^{-10}	5.78×10^{-12}
-13.6	7.73×10^{-13}	2.19×10^{-10}	9.88×10^{-11}	4.78×10^{-12}
-21.3	6.91×10^{-13}	2.00×10^{-10}	8.71×10^{-11}	4.46×10^{-12}

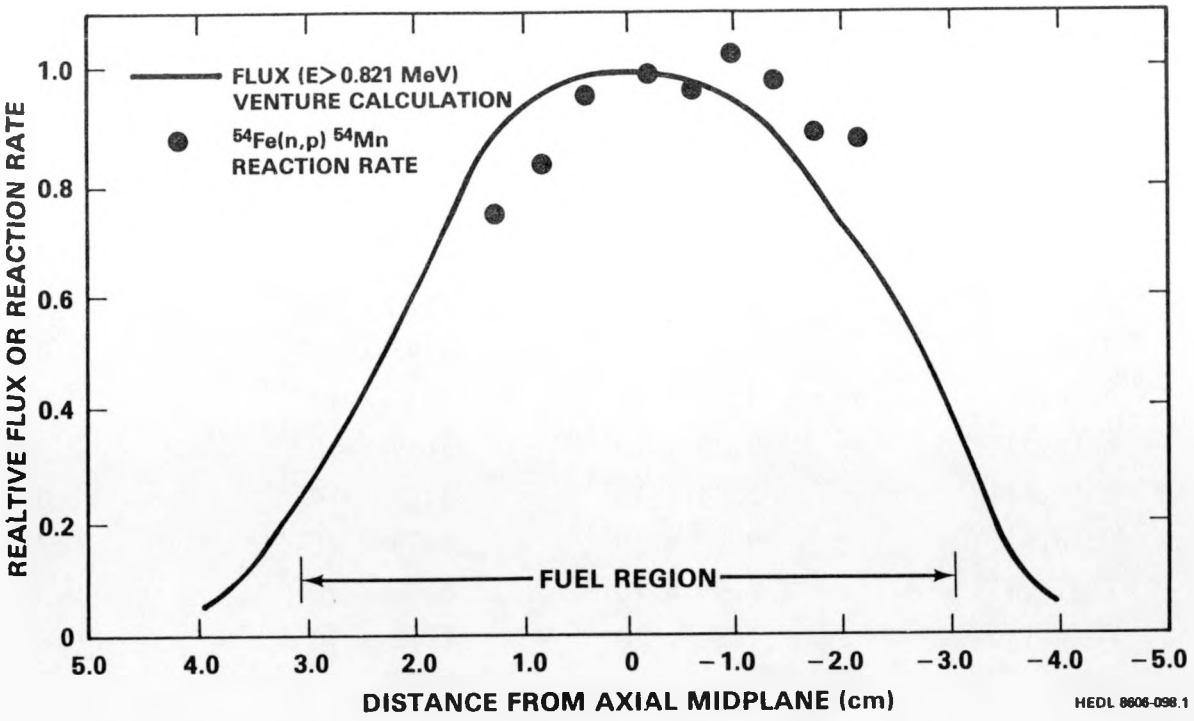

FIGURE HEDL-10. Axial Fast Flux Distribution.

TABLE HEDL-28

COMPARISON OF DOSIMETRY MEASUREMENTS FOR B BLOCK

Reaction	Reaction Rate		
	Dosimetry Pin	Metallurgical Block	Ratio
$^{63}Cu(n,\alpha)^{60}Co$	4.73×10^{-15}	5.04×10^{-15}	1.07
$^{46}Ti(n,p)^{46}Sc$	1.02×10^{-13}	1.07×10^{-13}	1.05
$^{58}Ni(n,p)^{58}Co$	1.05×10^{-12}	1.08×10^{-12}	1.03
$^{54}Fe(n,p)^{54}Mn$	7.58×10^{-13}	7.86×10^{-13}	1.04
$^{238}U(n,f)FP$	4.11×10^{-12}	4.28×10^{-12}	1.04
$^{59}Co(n,\gamma)^{60}Co$	1.01×10^{-10}	8.14×10^{-11}	0.81
$^{109}Ag(n,\gamma)^{110m}Ag$	8.60×10^{-11}	7.97×10^{-11}	0.93
$^{58}Fe(n,\gamma)^{53}Fe$	1.44×10^{-12}	1.31×10^{-12}	0.91

TABLE HEDL-29

COMPARISON OF DOSIMETRY MEASUREMENTS FOR A BLOCK

Reaction	Reaction Rate		
	Dosimetry Pin	Metallurgical Block	Ratio
$^{63}Cu(n,\alpha)^{60}Co$	4.27×10^{-15}	4.38×10^{-15}	1.03
$^{46}Ti(n,p)^{46}Sc$	9.33×10^{-14}	9.43×10^{-14}	1.01
$^{58}Ni(n,p)^{58}Co$	9.62×10^{-13}	9.47×10^{-14}	0.98
$^{54}Fe(n,p)^{54}Mn$	6.99×10^{-13}	6.89×10^{-13}	0.99
$^{238}U(n,f)FP$	3.74×10^{-12}	3.73×10^{-12}	1.00
$^{59}Co(n,\gamma)^{60}Co$	9.28×10^{-11}	6.73×10^{-11}	0.73
$^{109}Ag(n,\gamma)^{110m}Ag$	7.89×10^{-11}	6.82×10^{-11}	0.86
$^{58}Fe(n,\gamma)^{53}Fe$	1.33×10^{-12}	1.13×10^{-12}	0.85

A comparison between the measured and calculated threshold reaction rates for the dosimetry pin is shown in Table HEDL-30. Good agreement between measurement and calculation is indicated for the highest energy neutrons, but neutrons with energies below about 2 MeV are clearly underpredicted. Part of this error could be due to the fact that an average fission spectrum was used, but most of the error is probably due to inaccuracies in iron elastic and inelastic scattering cross sections as well as the amounts of water present. A similar effect was observed in the calculation of the flux in the center hole of the VENUS Mockup (Fe85).

The flux spectrum at the center of the B block was used together with the dosimetry data (Table HEDL-26) as input to the FERRET least-squares adjustment code (Sc79). (The spectrum used was not quite identical to that in Table HEDL-25.) The FERRET code used a 53-group representation of the spectrum and adjusted the group flux values to minimize the deviations (in a least-squares sense) between input data and output calculated values. Large uncertainties were placed on the input flux with the result that all the reaction rates were adjusted to agree to within ±3%. The input and adjusted 53-group spectra and the estimated flux uncertainties are given in Table HEDL-31. The integral FERRET results are given in Table HEDL-32 and are compared with the results of the DOT calculation. The agreement is entirely consistent with the comparisons of reaction rates made in Table HEDL-30.

TABLE HEDL-30

COMPARISON OF CALCULATED AND MEASURED REACTION RATES

Reaction	Reaction Rate		C/E
	Measured (E)	Calculated (C)	
$^{63}Cu(n,\alpha)^{60}Co$	4.73×10^{-15}	4.78×10^{-15}	1.01
$^{46}Ti(n,p)^{46}Sc$	1.02×10^{-13}	9.50×10^{-14}	0.93
$^{54}Fe(n,p)^{54}Mn$	7.58×10^{-13}	7.44×10^{-13}	0.98
$^{58}Ni(n,p)^{54}Co$	1.05×10^{-12}	9.85×10^{-13}	0.94
$^{238}U(n,f)FP$	4.11×10^{-12}	3.43×10^{-12}	0.83
$^{237}Np(n,f)FP$	2.54×10^{-11}	2.12×10^{-11}	0.83

Two previous calculations have been performed for the Buffalo Reactor by Ombrellaro (Om80). These are similar calculations, consisting of an original calculation that used a uniform fuel burnup model, and a revised calculation that used varying fuel burnup. Since the configuration for these earlier calculations was not identical to that used here, it is not expected that results identical to the present calculation should be obtained, but rather that relative results should be close.

Because of the large deviations predicted in the absolute flux values, comparisons of the ratio of flux E > 0.1 to E > 1.0 and spectral-averaged cross sections for Fe(n,p) and Ni(n,p) were made (Table HEDL-33) using each calculated spectrum and ENDF/B-V dosimetry cross sections. It appears that the original and revised Ombrellaro calculations are in good agreement above 1 MeV (and in fact agree with the FERRET result better than the more sophisticated DOT calculation), but show large deviations at lower neutron energies. The FERRET results indicate that derivation of the flux (E > 1) from $^{54}Fe(n,p)$ or $^{58}Ni(n,p)$ dosimetry results gives a reasonably accurate answer.

Conclusions

A recent dosimetry measurement test in the Buffalo Reactor together with a detailed transport calculation have been completed. These data have been used in a least-squares adjustment procedure to determine the flux (E > 1 MeV) at the midplane dosimetry point to an indicated accuracy of 5%. This is a significant improvement over past flux estimates. This experiment also indicates that, with good dosimetry measurements, including calculated spatial gradients, fluences for future metallurgical tests can be determined to accuracies of about 10%. Other exposure parameters can also be determined with only slightly higher uncertainties. It is expected that the results obtained for the Buffalo Reactor can be used as a benchmark for future tests.

TABLE HEDL-31

BUFFALO REACTOR FLUX SPECTRUM NEAR MIDPLANE

Group	Energy (MeV) Lower Bound	DOT Calculated Flux (Arb Norm)	FERRET Adj Flux (n/cm^2-s)	% Uncertainty (1σ)
1	14.92	2.420+8	2.248+8	22
2	13.50	5.465+8	5.023+8	20
3	11.62	2.926+9	2.668+9	18
4	10.00	8.549+9	7.760+9	16
5	8.607	2.337+10	2.124+10	14
6	7.408	5.374+10	4.928+10	12
7	6.065	1.537+11	1.427+11	11
8	4.966	2.894+11	2.730+11	11
9	3.679	7.493+11	7.159+11	10
10	2.865	1.013+12	9.979+11	10
11	2.231	1.566+12	1.638+12	10
12	1.738	1.609+12	1.776+12	11
13	1.353	1.839+12	2.078+12	12
14	1.108	1.615+12	1.814+12	14
15	0.8208	2.266+12	2.574+12	15
16	0.6393	2.320+12	2.651+12	17
17	0.4979	2.077+12	2.374+12	19
18	0.3877	1.770+12	2.013+12	21
19	0.3020	1.504+12	1.696+12	22
20	0.1832	2.357+12	2.627+12	24
21	0.1111	1.748+12	1.923+12	26
22	6.738-2	1.425+12	1.546+12	27
23	4.087-2	1.245+12	1.334+12	28
24	2.554-2	1.075+12	1.139+12	29
25	1.989-2	5.553+11	5.825+11	30
26	1.503-2	6.141+11	6.390+11	30
27	9.119-3	1.073+12	1.110+12	31
28	5.531-3	1.037+12	1.068+12	31
29	3.355-3	9.937+11	1.020+12	31
30	2.839-3	3.209+11	3.285+11	31
31	2.404-3	3.157+11	3.227+11	31
32	2.035-3	3.112+11	3.177+11	31
33	1.234-3	9.081+11	9.267+11	32
34	7.485-4	8.760+11	8.936+11	32
35	4.540-4	8.514+11	8.682+11	32
36	2.754-4	8.342+11	8.506+11	32
37	1.670-4	8.245+11	8.405+11	32
38	1.013-4	8.224+11	8.384+11	32
39	6.144-5	8.276+11	8.437+11	32
40	3.727-5	8.377+11	8.539+11	32
41	2.260-5	8.436+11	8.599+11	32
42	1.371-5	8.332+11	8.492+11	32
43	8.315-6	8.008+11	8.161+11	32
44	5.043-6	7.458+11	7.601+11	32
45	3.059-6	6.685+11	6.812+11	32
46	1.855-6	5.690+11	5.798+11	32
47	1.125-6	4.470+11	4.555+11	32
48	6.826-7	3.028+11	3.085+11	32
49	4.140-7	1.480+11	1.508+11	32
50	2.511-7	5.572+10	5.677+10	32
51	1.523-7	2.290+10	2.333+10	32
52	9.237-8	5.300+10	5.400+10	32
53	1.000-10	3.249+11	3.311+11	32

TABLE HEDL-32

CALCULATED FLUX RESULTS FOR CENTERLINE OF B BLOCK

	DOT Calculation	FERRET Calculation	FERRET Uncertainty
Flux (E > 1 MeV)*	8.83×10^{12}	1.04×10^{13}	5%
Flux (E > 0.1 MeV)	2.13×10^{13}	2.57×10^{13}	11%
Flux (Total)**	4.03×10^{13}	4.76×10^{13}	15%
dpa/s	1.27×10^{-8}	1.50×10^{-8}	6%

*Units of flux are n/cm^2-s.
**Only the threshold reactions were included in the FERRET-SAND II analysis.

TABLE HEDL-33

COMPARISON OF BUFFALO CALCULATIONS

	Reference (Om80) Original	Reference (Om80) Revised	DOT	FERRET*
$\frac{\phi E > 0.1}{\phi E > 1.0}$	2.76	3.56	2.41	2.47
$\sigma Fe(n,p)$ $(10^{-26}\ cm^2)$	1.99	0.94	1.72	1.63
$\sigma Fe(n,p)$ $(E > 1)$ $(10^{-26}\ cm^2)$	7.93	7.06	8.45	7.47
$\sigma Ni(n,p)$ $(10^{-26}\ cm^2)$	2.64	1.27	2.28	2.20
$\sigma Ni(n,p)$ $(E > 1)$ $(10^{-26}\ cm^2)$	10.05	9.57	11.2	10.1

*Least-squares adjusted flux-spectrum using DOT calculation and dosimetry sensor results.

Expected Future Accomplishments

The present scope of this work has been completed.

Acknowledgments

The authors would like to thank Brian Worley (ORNL) for calculating the isotopic changes with burnup and J. M. Ruggles (HEDL) for assisting with the radiometric analysis. Helpful discussions with Mark Williams (LSU) and F. B. K. Kam (ORNL) are also acknowledged. Special thanks are due to J. R. Hawthorne (MEA) for his encouragement, assistance, and help in the planning, design, fabrication, and dosimetry irradiations at the experimental mockup of the MEA metallurgical test assembly. Thanks are also due to Martin Haas (ENSA) and the staff of the SUNY Buffalo Reactor for providing the detailed reactor description and patiently answering our many questions. The encouragement and support provided by C. Z. Serpan and A. Taboada of the Nuclear Regulatory Commission are gratefully acknowledged.

C. ANALYSIS OF PCA AND PSF BENCHMARK DATA

Raymond Gold and W. N. McElroy (HEDL)

Objective

The objective of the present work is to provide a better understanding of the complex radiation-induced embrittlement phenomenon in LWR-PV through an analysis of PCA and PSF benchmark data.

Summary

The existence of some very simple relations are uncovered through a comparative analysis of PCA and PSF benchmark data. Implications of these simple relationships for the description of radiation-induced LWR-PV embrittlement are discussed. It is demonstrated that an exponential representation accurately describes the spatial dependence of neutron exposure in LWR-PV. The coefficients of this exponential representation, α and β, are independent of the chemistry and metallurgical properties of the PV steel. In contrast, on the basis of the six materials studied in the PSF it is shown that the radial dependence of LWR-PV embrittlement is material dependent. The variation of coefficients used in models describing the radial dependence of Charpy shifts observed in these six PSF materials, γ and s, provide a representative magnitude of the material-dependent variation of LWR-PV embrittlement.

Accomplishments and Status

1.0 Introduction

One of the outstanding features of the PSF experiment was the generation of mechanical property data representative of the through-wall behavior in LWR commercial power plants, but under benchmark conditions. Indeed, the PSF experiment is unique in that it represents a real world benchmark. Environmental variables of the PSF irradiations were well controlled and accurately measured. The ORR-PSF facility has been documented in fine detail so that neutron transport calculations can be conducted with the confidence that the geometric and compositional quantities of the environment are accurately known. In this perspective, the PSF experiment represents one of the most important test reactor irradiations conducted to date for the generation of LWR-PVS data.

2.0 Behavior of DPA Within the Simulated Pressure Vessel Capsule (SPVC)

Considerable interlaboratory effort has been expended to quantify exposures attained in the PSF irradiations. Results of these extensive efforts have been documented in the first of four scheduled volumes to be issued on the PSF benchmark (Mc86b). Figures HEDL-11 through HEDL-17 show the behavior of the dpa as a function of location within the PV for the SPVC irradiation. In these figures, interlaboratory consensus dpa values in iron have been used (Li86). Figure HEDL-11 shows the dpa behavior at the center of the capsule, whereas Figures HEDL-12 through HEDL-17 show the dpa variation at the location of the six different materials irradiated in the SPVC.

The smooth curve in each of these figures is a least-squares fit of the dpa data within the PV to an exponential function of the form

$$d = d_0 \exp(-\alpha r) \quad . \qquad (1)$$

Here d represents the dpa within the PV and r is the radial distance (in inches) from the front surface of the PV. The two parameters in Eq. (1), namely d_0 and α, are generated by the least-squares analysis. The computer code FATAL (Sa72) has been used for all the least-squares analyses reported herein.

The adequacy of the fits in all of these figures demonstrates that the dpa variation within the PV can be accurately described by a simple exponential function. The parameter values obtained from these least-squares analyses are given in Table HEDL-34. As could be anticipated from the extensive PSF dosimetry efforts (Mc86b,Mc87c), the value of d_0 varies from lateral location to lateral location in the PV because of the azimuthal and axial variation of the neutron intensity. As a consequence, d_0 values vary by more than 30%, depending on the (x,z) locations of the six different materials irradiated in the SPVC.

In contrast, all values of α agree within uncertainty. In view of this consistency, it is appropriate to use the average of these α-values, namely $\bar{\alpha} = 0.272 \pm 0.0079$, as the single value for the SPVC irradiation. In terms of this simple exponential representation, this single (average) value $\bar{\alpha}$ can be used to characterize the radial dependence of the dpa within the SPVC.

3.0 Behavior of Fluence Within the SPVC

The behavior of fluence within the PV can be examined the same way that the dpa was studied in Section 2.0 above. Figures HEDL-18 through HEDL-24 show the behavior of the fluence of neutrons (having energies >1 MeV) as a function of location within the PV for the SPVC irradiation. In these figures, interlaboratory consensus fluence values have been used (Li86). Figure HEDL-18 shows the fluence behavior at the center of the capsule, whereas Figures HEDL-19 through HEDL-24 show the fluence variation at the location of the six different materials studied in the PSF experiment, respectively.

The smooth curve in each of these figures is a least-squares fit of the fluence data within the PV to an exponential function of the form

$$(\phi t) = (\phi t)_0 \exp(-\beta r) \quad . \qquad (2)$$

Here (ϕt) represents the fluence of neutrons having energy >1 MeV (E > 1) within the PV and r is the radial distance (in inches) from the front surface of the PV. The two parameters in Eq. 2, namely $(\phi t)_0$ and β, are generated by the least-squares analysis.

The adequacy of the fits in Figures HEDL-18 through HEDL-24 demonstrates that the fluence variation within the PV can also be accurately described by a simple exponential function. The parameter values obtained from these least-squares analyses are given in Table HEDL-35. Just as for the dpa analyses given above, the values of $(\phi t)_o$ vary by more than 30% because of the azimuthal and axial dependence of the neutron intensity.

In contrast, all values of β agree within uncertainty. In view of this consistency, it is appropriate to use the average of these β-values, namely $\bar{\beta} = 0.347 \pm 0.0097$, as the single value for the SPVC irradiation. In terms of this simple exponential representation, this single (average) $\bar{\beta}$-value can be used to characterize the radial dependence of the fluence within the SPVC.

Comparison of the fluence and the dpa least-squares results shows that $\bar{\beta}$ is roughly 25% larger than $\bar{\alpha}$, so that the fluence falls off more rapidly with increasing penetration than does the dpa. This behavior can be qualitatively explained by noting that in addition to the intensity fall off, the spectrum softens with increasing penetration further depleting the neutron population above 1 MeV. However, neutrons with energies down to roughly 1 keV and below contribute to displacements, so that the dpa is not expected to fall off as rapidly as the fluence ($E > 1$ MeV).

Recommended (1σ) uncertainties of 9% for individual dpa values and 8% for individual fluence values (Li86) were used in these least-squares analyses. The resulting 1σ uncertainties of the β-values given in Table HEDL-35 range from about 6.5% up to 9%. In contrast, the resulting 1σ uncertainties of the α-values given in Table HEDL-34 range from about 10% to 20%. This uncertainty difference is not reflected in the quality of the fits, since inspection on a (material) location-by-location basis reveals that the least-squares exponential representation provides slightly better fits for the dpa data than the fluence data. Consequently, the uncertainty in individual α- and β-values should not be taken as a measure of the adequacy of the exponential representation.

Much smaller uncertainties of 2.9% and 2.8% have been cited for $\bar{\alpha}$ and $\bar{\beta}$, respectively. These uncertainties are simply the standard deviations from the mean values, $\bar{\alpha}$ and $\bar{\beta}$. It must be recognized that total uncertainties were used for dpa and fluence in these least-squares analyses. However, the largest uncertainty component in the dpa and fluence stems from the uncertainty in the absolute scale of the dosimetry measurements and this uncertainty factor is virtually constant, i.e., independent of r. As a consequence, the standard deviations cited above for $\bar{\alpha}$ and $\bar{\beta}$ are more meaningful measures of the adequacy of a simple exponential representation. In this regard, it is clear that there is no essential distinction in the r-dependence of the dpa and fluence within the SPVC. Both exposure quantities possess the very simple behavior of exponentially decreasing with increasing penetration.

4.0 General Validity of the Simple Exponential Representation

4.1 Configuration Independence α and β

The general validity of the α- and β-values generated in Sections 2.0. and 3.0, respectively, can be tested by comparison with results from the PCA Experiments and Blind Test (Mc81,Mc84i). Comparable interlaboratory dosimetry efforts were expended to characterize the low-power LWR-PV mockups studied in the PCA. Moreover, these investigations include different LWR-PVS configurations and extend to the 3/4-T location in the PV.

Consequently, it is instructive to obtain least-squares analyses for these PCA data that can be compared to the SPVC results. Hence, consensus dpa and fluence values from the NUREG reports on the PCA were used (Li84b) together with the simple exponential representations introduced in Eqs. (1) and (2) for dpa and fluence, respectively.

Figures HEDL-25 through HEDL-27 provide least-squares fits of the dpa data for the 8/7, 12/13, and 4/12 SSC configurations, respectively, that were studied in the PCA. Table HEDL-36 summarizes parameter results obtained from the least squares analyses of the PCA dpa data.

Figures HEDL-28 through HEDL-30 provide least-squares fits of the fluence data for 8/7, 12/13, and 4/12 SSC configurations, respectively, that were studied in the PCA. Table HEDL-37 summarizes parameter results obtained from the least-squares analyses of the PCA fluence data.

These figures demonstrate that a simple exponential description of either dpa or fluence is an excellent representation for all PCA configurations. The inner consistency of the α values in Table HEDL-36 is remarkable. The β-values in Table HEDL-37 also exhibit remarkable consistency. The average value of α from the PCA data is $\langle \alpha \rangle = 0.289 \pm 0.0038$, whereas the average value of β from the PCA data is $\langle \beta \rangle = 0.369 \pm 0.0062$. Here, the quoted uncertainties are simply the standard deviations from the mean values $\langle \alpha \rangle$ and $\langle \beta \rangle$. These standard deviations are $\sim$1.3% and 1.7% for $\langle \alpha \rangle$ and $\langle \beta \rangle$, respectively.

Standard (1σ) uncertainties used in these PCA least-squares analyses were the consensus values recommended in the PCA Experiments and Blind Test work (Li84b). These uncertainties vary slightly with configuration and location, ranging from 6% to 9% for fluence and from 8% to 11% for dpa. Just as has already been noted for the SPVC data, the largest uncertainty component in the dpa and fluence data for the PCA stem from the absolute scale of the dosimeter measurements, which is an uncertainty factor that is essentially independent of r. Hence, just as stressed in Section 3.0, the standard deviations of $\langle \alpha \rangle$ and $\langle \beta \rangle$ are indicative of the adequacy of a simple exponential representation, whereas the individual uncertainties in the α- and β-values given in Tables HEDL-36 and HEDL-37, respectively, are not as meaningful measures of this behavior.

4.2 Comparison of α and β Results from the SPVC and the PCA

PCA and PSF benchmark data compliment each other. PCA results demonstrate that α and β values are configuration independent. PSF results show that α and β are essentially independent of the azimuthal and axial variation of the neutron intensity.

Table HEDL-38 summarizes the average α- and β-values obtained from the SPVC and the PCA. It can be seen that the ratio of the PCA to SPVC values of α and β are virtually identical. In both cases, the PCA result is $\sim$6.3% higher.

Some differences between SPVC and PCA results should be anticipated because of differences that exist in the PV mockup in both benchmarks. In particular, the metallurgical tests in the PSF necessitated temperature control apparatus. As a consequence of this temperature control apparatus, perturbations were introduced into the PSF mockup of the PV. For example, electrical heaters as well as gas and water cooling was employed within the PSF mockup in an effort to maintain constant irradiation temperature. No such apparatus was entailed in the PCA (Ka83).

As a result of addressing different needs, the PCA and PSF benchmarks compliment each other. The PCA is a more faithful mockup of the radiation fields found in LWR-PV environments. The low-power PCA mockup permits use of many radiation metrology methods to carefully characterize the environment. On the other hand, the PSF is a more realistic mockup of a real world power plant in terms of flux, fluence and temperature conditions. In this respect, the PSF was designed to furnish metallurgical and mechanical property radiation data that approximated through-the-PV-wall property data arising in an actual LWR power plant.

The PCA-PSF differences in the average α and β values given in Table HEDL-38 can, therefore, be attributed to the different focus of these two LWR-PV benchmarks. The fact that these two differences are small and identical lends further assurance to the simple exponential description of the radial variation of dpa and fluence within the PV.

Because of the distinction between these two benchmarks, one should use $\bar{\alpha}$ and $\bar{\beta}$ in analyses of the PSF data. For general use, however, it is recommended that $< \alpha >$ and $< \beta >$ be employed to describe the behavior of dpa and fluence, respectively, within LWR-PV.

5.0 Implications of the Simple Exponential Behavior of DPA and Fluence

The simple exponential behavior of dpa and fluence within the PV has far-reaching implications. The nature of these implications depends on the assumptions introduced for the behavior of the nil-ductility temperature shift, ΔT, as a function of penetration distance, r, into the PV; i.e., as measured from the core face of the PV. Perhaps the simplest model that one can assume for the spatial dependence of ΔT is that it qualitatively

possesses the same exponential behavior as dpa and fluence. Under this assumption, one can write

$$\Delta T = (\Delta T)_0 \exp(-\gamma r) \quad , \tag{3}$$

where (ΔT) and γ are the two parameters that comprise this simple exponential representation.

Eq. (1) can be used in Eq. (3) to determine the dependence of ΔT on dpa. One finds

$$\Delta T = (\Delta T)_0 \exp[(\gamma/\alpha)\cdot \ln(d/d_0)] \quad , \tag{4a}$$

which can also be written as

$$\Delta T = (\Delta T)_0 (d/d_0)^{\gamma/\alpha} \quad . \tag{4b}$$

Use of Eq. (2) in Eq. (3) provides the dependence of ΔT on fluence. One has

$$\Delta T = (\Delta T)_0 \exp (\gamma/\beta)\cdot \ln[\phi t/(\phi t)_0] \quad , \tag{5a}$$

which can also be written as

$$\Delta T = (\Delta T)_0 [\phi t/(\phi t)_0]^{\gamma/\beta} \quad . \tag{5b}$$

Eqs. (4) and (5) above are the analytical form of the power law model used by Guthrie (Gu84) and Odette et al. (Pe84) for statistical analyses of temperature shift data from surveillance and test reactor data bases.

The slow spatial variation of ΔT as a function of r in the PSF experiment (Ha84,Ha84a) furnishes the basis for an alternative model. Because of this slow variation, a Taylor series expansion of only a few terms should provide an adequate approximation. Using only the first two terms of such a Taylor series, one has a linear model of the form

$$\Delta T = (\Delta T)_0 - s\cdot r \quad . \tag{6}$$

Here $(\Delta T)_0$ is the intercept at r=0 and s is the slope of the assumed linear variation. To determine the dependence of ΔT on dpa for this linear model, one can use Eq. (1) in Eq. (6). One finds

$$\Delta T = (\Delta)_0 + (s/\alpha) \cdot \ln(d/d_0) \quad . \tag{7}$$

Using Eq. (2) in Eq. (6), one finds for the fluence dependence of ΔT the expression

$$\Delta T = (\Delta T)_0 + (s/\beta) \ln[\phi t/(\phi t)_0] \quad . \tag{8}$$

Eqs. (7) and (8) correspond to the logarithmic trend curve model introduced by McElroy et al. for the analysis of the PSF experiment as well as for analyses of the LWR surveillance data base and the test reactor irradiation data base (Mc86).

Consequently, two very simple assumptions produce trend curve models that are in current use. The power law trend curve model follows from the assumption of an exponential spatial variation of ΔT, namely Eq. (3). On the other hand, the logarithmic trend curve model follows from assuming a linear spatial variation of ΔT, namely Eq. (6).

It must be stressed that in the derivation of both these trend curve models, it has been assumed that ΔT depends solely upon exposure, i.e., dpa or fluence (E > 1), and dependence upon any other environmental variables has been assumed negligible. The validity of this assumption could be limited by the existence of non-negligible systematic effects caused by any of the other environmental variables. The importance of such systematic effects has been emphasized at a recent international symposium [Go86].

6.0 SPVC Tests of Trend Curve Models

Least-squares fits of the spatial variation of ΔT have been performed with the PSF data using both exponential and linear assumptions. The actual ΔT values and uncertainties used here are those developed by McElroy et al., (Mc86) as based on the PSF experimental measurements of Hawthorne (Ha84, Ha84a). Dosimetry values used in these least-squares fits correspond to the group-averaged exposure parameters for a set of Charpy specimens. More specifically, exposure parameters for the notch tip were averaged. Least-squares results for the exponential assumption are shown in Figures HEDL-31 through HEDL-36 for the six materials tested in the PSF. It can be seen that the exponential assumption is an adequate representation for all six materials. Table HEDL-39 summarizes the least-squares parameter results obtained for $(\Delta T)_0$ and γ using the exponential assumption.

As can be seen in Table HEDL-39, there exists a considerable material-dependent variation in both $(\Delta T)_0$ and γ. In fact, the γ-parameter varies from a low of 0.04012 for the EC-material to a high of 0.2084 for the MO-material, which is about a factor of 5.

Least-squares fits obtained from the linear assumption are shown in Figures HEDL-37 through HEDL-42 for all six materials tested in the PSF. These figures confirm that the linear assumption is also an adequate representation for all six materials. Table HEDL-40 summarizes the least-squares parameter results obtained for $(\Delta T)_o$ and s using the linear assumption.

It can be seen that a significant material-dependent variation also exists for the linear assumption. In this case, the slope s varies from a low of 5.9 for the MO-material to a high of 23.48 for the R-material, which is about a factor of 4.

The least-squares parameters from the exponential assumption given in Table HEDL-39 have been used in Eqs. (4a) and (4b) to examine the adequacy of the power law trend-curve model. For these comparisons, it is appropriate to use the average values of α and β obtained from the PSF data analyses given in Sections 2.0 and 3.0, namely $\bar{\alpha} = 0.272$ and $\bar{\beta} = 0.347$.

Figures HEDL-43 through HEDL-48 present the power law trend curves so obtained for the six materials studied in the PSF using the dpa exposure variable. The power law trend curves so obtained using the fluence exposure variable are shown in Figures HEDL-49 through HEDL-54. These figures reveal that the power law trend curve model is an adequate representation of the SPVC data for all six materials. The dpa power law trend curves and the fluence power law trend curves fit the experimental data equally well. Hence no distinction between these two exposure variables is possible on these grounds.

The least-squares parameters from the linear assumption given in Table HEDL-40 have been used in Eqs. (7) and (8) to examine the adequacy of the logarithmic trend curve model. For these comparisons, it is appropriate to use the average values of α and β obtained from the PSF data analyses given in Sections 2.0 and 3.0, namely $\bar{\alpha} = 0.272$ and $\bar{\beta} = 0.347$.

Figures HEDL-55 through HEDL-60 present the logarithmic trend curves so obtained for the six materials studied in the PSF using the dpa exposure variable. The logarithmic trend curves obtained using the fluence exposure variable are shown in Figures HEDL-61 through HEDL-66. These figures reveal that the logarithmic trend curve model is also an adequate representation of the SPVC data for all six materials. Indeed, the quality of these fits to the experimental data is comparable to that obtained with the power law trend-curve model. Hence, no distinction between these two models, i.e., power law or logarithmic, is possible on the basis of the SPVC data. Just as for the power law results, there is essentially no difference in the ability of the logarithmic trend curves to fit the experimental data, whether using dpa or fluence exposure variables.

7.0 Conclusions

1. Exponential Variation of Dpa and Fluence Within the PV -- The spatial variation of dpa and fluence exposure variables can be accurately described by an exponential radial dependence within the PV. More

specifically, the spatial variation of dpa with increasing penetration distance r from the inner PV surface (i.e., the core side of the PV) is given by

$$d = d_0 \exp(-\alpha r) \quad , \tag{9}$$

whereas the fluence variation is given by

$$(\phi t) = (\phi t)_0 \exp(-\beta r) \quad . \tag{10}$$

General values of α and β, which have been derived from the PCA experiments, are $<\alpha> = 0.289$ and $<\beta> = 0.369$. Values of α and β obtained from the SPVC data are slightly lower, namely $\bar{\alpha} = 0.272$ and $\bar{\beta} = 0.347$, and are specific values representative of the PSF experiment only.

2. Derivation of Trend Curve Models -- Specific trend curve models that are currently used to predict PV embrittlement have been derived. The assumption of an exponential spatial variation of the temperature shift, namely

$$\Delta T = (\Delta T)_0 \exp(-\gamma r) \quad , \tag{11}$$

leads to the power law trend curve model. In contrast, assuming a linear spatial variation of the temperature shift

$$\Delta T = (\Delta T)_0 - s \cdot r, \tag{12}$$

leads to the logarithmic trend curve model.

3. Least-Squares Analyses of SPVC Data -- Least-squares analyses show that the exponential and linear assumptions are acceptable representations for the spatial variation of the temperature shift data observed from the SPVC. The quality of the fits obtained using these two assumptions are comparable, so that no distinction between these two assumptions can be made on the basis of the SPVC data.

4. Material Dependence -- Least-squares parameters obtained from analyses of the SPVC data exhibit a significant material dependence. This is true for both cases studied, i.e., for both the exponential and linear assumptions introduced to describe the spatial variation of ΔT. As a consequence, both the power law and logarithmic trend-curve models exhibit a significant material dependence. For example, Table HEDL-41

shows the material dependence of the exponent in the power law trend-curve model as obtained from least-squares analyses of the SPVC data.

5. Spatial Extrapolation Within the PV -- In view of the material dependence of the SPVC data, spatial extrapolation of ΔT from the surface into the body of the PV should be carried out on a material-by-material basis. This material dependence persists, regardless of the assumed spatial variation of ΔT. Rather than extrapolate ΔT directly, it is recommended that the exposure, dpa or fluence, be extrapolated. The dpa or fluence extrapolation can be accurately accomplished using the exponential representations established above. This accurately extrapolated dpa or fluence value can then be used in a material-dependent trend-curve model to produce the extrapolated value of ΔT.

The accuracy of these exposure extrapolations can be estimated in a straightforward manner by applying elementary differential calculus to Eqs. (9) and (10). Using the notation $\sigma(\chi)$ to represent the relative standard deviation of χ, one finds

$$\sigma(d) = \left[\sigma(d_0)^2 + (\alpha r)^2\, \sigma(\alpha)^2\right]^{1/2} \tag{13}$$

and

$$\sigma(\phi t) = \left\{\sigma\left[(\phi t)_0\right]^2 + (\beta r)^2\, \sigma(\beta)^2\right\}^{1/2} . \tag{14}$$

Under idealized conditions, such as in the PCA benchmark [Mc81], the uncertainties in exposure parameters at the surface of the PV, namely $\sigma(d_0)$ and $\sigma[(\phi t)_0]$, range from 5% to 15%. In contrast, $\sigma(\alpha)$ and $\sigma(\beta)$ uncertainty values can be obtained from Table HEDL-36 and HEDL-37 and are 1.3% and 1.7%, respectively.

Using these numerical results in Eqs. (13) and (14), one can determine the radial dependence of the uncertainty in the extrapolated values of dpa and fluence. On this basis, the uncertainty in extrapolated dpa and fluence are presented in Figures HEDL-67 and HEDL-68, respectively, for surface exposure uncertainties of 5, 10 and 15%. It can be seen that this simple extrapolation entails a negligible penalty in increased uncertainty virtually everywhere. The exception to this rule lies in the region defined by large extrapolation, i.e., large r, and most accurate surface exposure determinations, i.e., near 5% for $\sigma(d_0)$ and $\sigma[(\phi t)_0]$. However, even in this region the increase in total uncertainty is modest.

It is important to recognize that through a simple change in the coordinate system, the exponential representation can be used for accurate exposure extrapolation from the cavity side of the PV. In

fact, the quadrature formulas given in Eqs (13) and (14) for the propagated uncertainty are still valid for extrapolation from the cavity side of the PV. In this case, r represents the distance as measured from the cavity surface of the PV.

6. Validity of Trend-Curve Models -- Comparison of the power law and logarithmic trend-curve models with SPVC data reveals that both models provide an adequate representation within the PV. The quality of the fits obtained from these two models are comparable, so that no distinction between these two models is possible on the basis of the SPVC data.

   The general validity of any conclusions concerning trend-curve models based on these analyses of the SPVC data is seriously limited by the following two factors:

   - The restricted range of exposure used in the PSF experiments.
   - Systematic effects have been completely ignored [the importance of systematic effects was stressed at a recent international symposium (Go86,Mc86)].

   Because of these two factors, one can only advance the qualitative conclusion that both the power law and logarithmic trend curve models are plausible representations of the exposure dependence of ΔT.

7. On the Choice of Exposure Variable, DPA or Fluence? -- Based on the analyses and curves presented herein, no distinction can be drawn concerning which exposure variable, dpa or fluence, is better to use for the prediction of radiation damage. However, this conclusion could have been easily anticipated because of the slow variation exhibited by the temperature shifts in the PSF together with the rather restricted range of exposure of the PSF irradiations. Consequently, the PSF experiment is clearly not a suitable experiment to use in appraising any preference between dpa and fluence exposure variables.

   In general, such comparisons depend not only on the specific experiment, but the metallurgical (property change) observable under study. The measurements of nil-ductility temperature shift, which varies slowly with exposure, is therefore not particularly well suited for comparative tests of exposure variables. More sensitive tests can be obtained using different property change observables, especially observables that vary rapidly with exposure.

Expected Future Accomplishments

Extension of this work will be included in the PSF Physics-Dosimetry-Metallurgy Experiments, NUREG/CR-3320, Vol. 4, which is to be issued later in FY-87.

TABLE HEDL-34

PARAMETER RESULTS FROM DPA LEAST-SQUARES ANALYSES

Location	d_o	α
Capsule Centers	0.0768 ± 0.0081	0.282 ± 0.043
R-Material	0.0612 ± 0.0048	0.259 ± 0.026
3PU-Material	0.0582 ± 0.0049	0.273 ± 0.028
F23-Material	0.0644 ± 0.0053	0.268 ± 0.028
EC-Material	0.0627 ± 0.0064	0.268 ± 0.029
K-Material	0.0602 ± 0.0062	0.280 ± 0.030
MO-Material	0.0662 ± 0.0088	0.275 ± 0.057
		Average α = 0.272 ± 0.0079* (2.9%)

*The uncertainty cited for the average value is only the standard deviation from the mean.

TABLE HEDL-35

PARAMETER RESULTS FROM THE FLUENCE LEAST-SQUARES ANALYSES

Location	$(\phi t)_o$	β
Capsule Centers	(5.23 ± 0.44)E+19	0.360 ± 0.032
R-Material	(4.11 ± 0.31)E+19	0.333 ± 0.029
3PU-Material	(3.93 ± 0.30)E+19	0.343 ± 0.026
F23-Material	(4.31 ± 0.32)E+19	0.340 ± 0.027
EC-Material	(4.22 ± 0.37)E+19	0.346 ± 0.024
K-Material	(4.09 ± 0.39)E+19	0.358 ± 0.029
MO-Material	(4.43 ± 0.39)E+19	0.351 ± 0.023
		Average β = 0.347 ± 0.0097* (2.8%)

*The uncertainty cited for the average value is only the standard deviation from the mean.

TABLE HEDL-36

PARAMETER RESULTS FROM LEAST-SQUARES ANALYSES OF THE PCA DPA DATA

Configuration	d_o	α
8/7	(8.98 ± 1.17)E-28	0.293 ± 0.026
12/13	(1.54 ± 0.22)E-29	0.286 ± 0.031
4/12 SSC	(8.52 ± 1.42)E-28	0.287 ± 0.037

Average α = 0.289 ± 0.0038* (1.3%)

*Uncertainty cited for the average value is only the standard deviation from the mean.

TABLE HEDL-37

PARAMETER RESULTS FROM LEAST-SQUARES ANALYSES OF THE PCA FLUENCE DATA

Configuration	$(\phi t)_o$	β
8/7	(6.39 ± 0.68)E-07	0.362 ± 0.024
12/13	(1.18 ± 0.69)E-07	0.371 ± 0.014
4/12 SSC	(6.13 ± 0.74)E-07	0.374 ± 0.027

Average β = 0.369 ± 0.0062* (1.7%)

*Uncertainty cited for the average value is only the standard deviation from the mean.

TABLE HEDL-38

AVERAGE α AND β VALUES FROM THE SPVC AND PCA

SPVC	PCA	Ratio
$\bar{\alpha} = 0.272 \pm 0.0079$	$\langle \alpha \rangle = 0.289 \pm 0.0028$	$\langle \alpha \rangle / \bar{\alpha} = 1.0625$
$\bar{\beta} = 0.347 \pm 0.0097$	$\langle \beta \rangle = 0.369 \pm 0.0062$	$\langle \beta \rangle / \bar{\beta} = 1.0634$

TABLE HEDL-39

PARAMETER RESULTS FROM AN EXPONENTIAL LEAST-SQUARES FIT OF THE PSF TEMPERATURE SHIFT DATA

Material	$(\Delta T)_o$	γ
R	(5.150 ± 0.097) E+02	(+5.123 ± 0.669) E-02
3PU	(1.399 ± 0.116) E+02	(+1.197 ± 0.364) E-01
F23	(1.474 ± 0.083) E+02	(+9.887 ± 2.65) E-02
EC	(2.105 ± 0.169) E+02	(+4.012 ± 2.01) E-02
K	(1.356 ± 0.175) E+02	(+6.470 ± 2.34) E-02
MO	(5.459 ± 1.05) E+01	(+2.084 ± 0.524) E-01

TABLE HEDL-40

PARAMETER RESULTS FROM A LINEAR LEAST-SQUARES
FIT OF THE PSF TEMPERATURE SHIFT DATA

Material	$(\Delta T)_o$	s
R	(5.132 ± 0.112) E+02	(+2.348 ± 0.407) E+01
3Pu	(1.380 ± 0.105) E+02	(+1.317 ± 0.399) E+01
F23	(1.453 ± 0.075) E+02	(+1.176 ± 0.315) E+01
EC	(2.090 ± 0.156) E+02	(+7.400 ± 4.75) E+00
K	(1.337 ± 0.162) E+02	(+7.141 ± 3.46) E+00
Mo	(4.821 ± 0.735) E+01	(+5.900 ± 1.88) E+00

TABLE HEDL-41

EXPONENTS FOR THE POWER LAW TREND CURVE MODEL
DERIVED FROM THE PSF-SPVC DATA

Material	$dpa(\gamma/\bar{\alpha})$	Fluence $(\gamma/\bar{\beta})$
R	0.188	0.148
3Pu	0.440	0.345
F23	0.364	0.285
EC	0.148	0.119
K	0.238	0.187
Mo	0.766	0.601

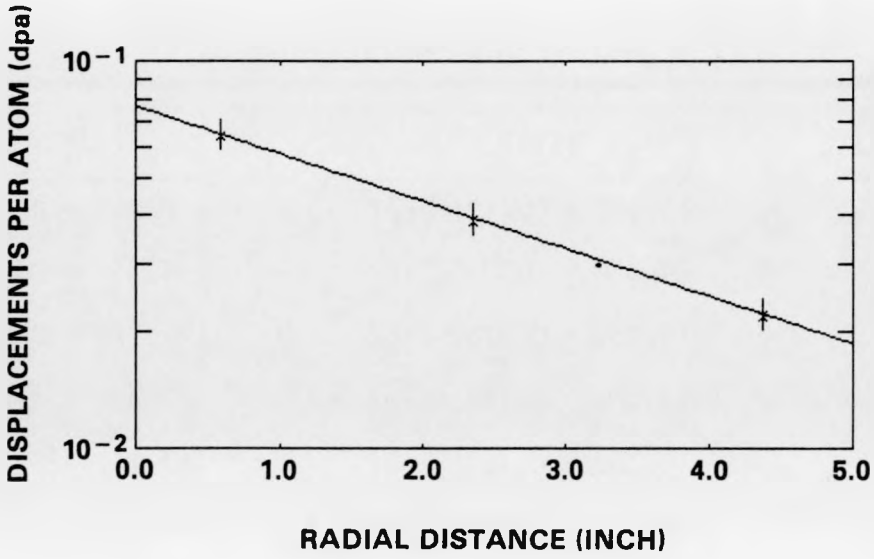

FIGURE HEDL-11. Radial Dependence of the dpa in the SPVC at the Center of the Capsules. The smooth curve is a least-squares fit of the data to a simple exponential function (see text).

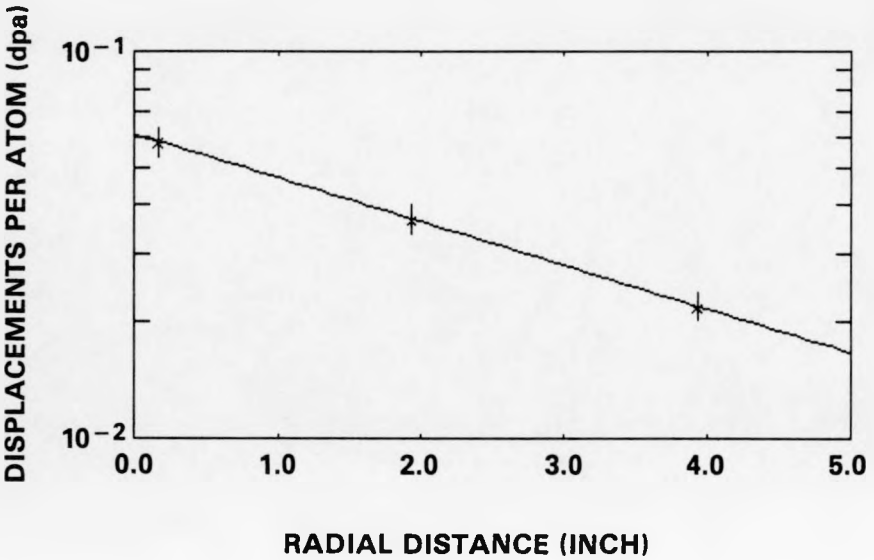

FIGURE HEDL-12. Radial Dependence of the dpa in the SPVC at the R-Material Location. The smooth curve is a least-squares fit of the data to simple exponential function (see text).

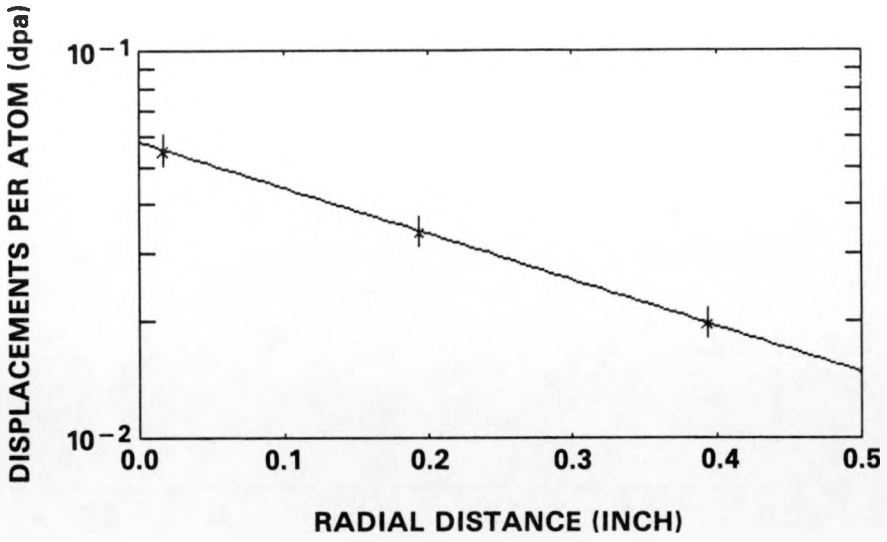

FIGURE HEDL-13. Radial Dependence of the dpa in the SPVC at the 3PU-Material Location. The smooth curve is a least-squares fit of the data to a simple exponential function (see text).

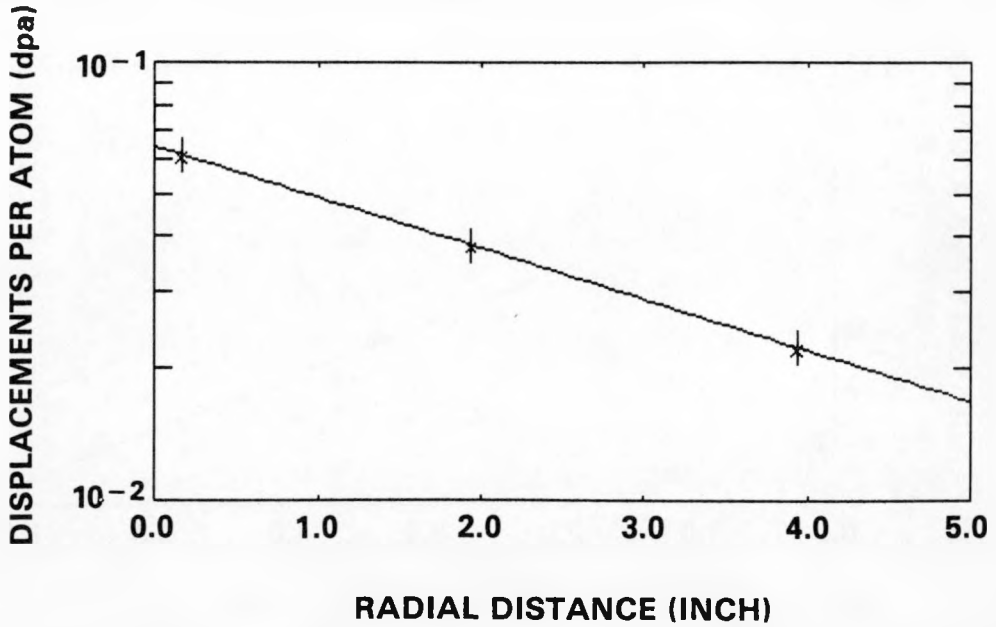

FIGURE HEDL-14. Radial Dependence of the dpa in the SPVC at the F23-Material Location. The smooth curve is a least-squares fit of the data to a simple exponential function (see text).

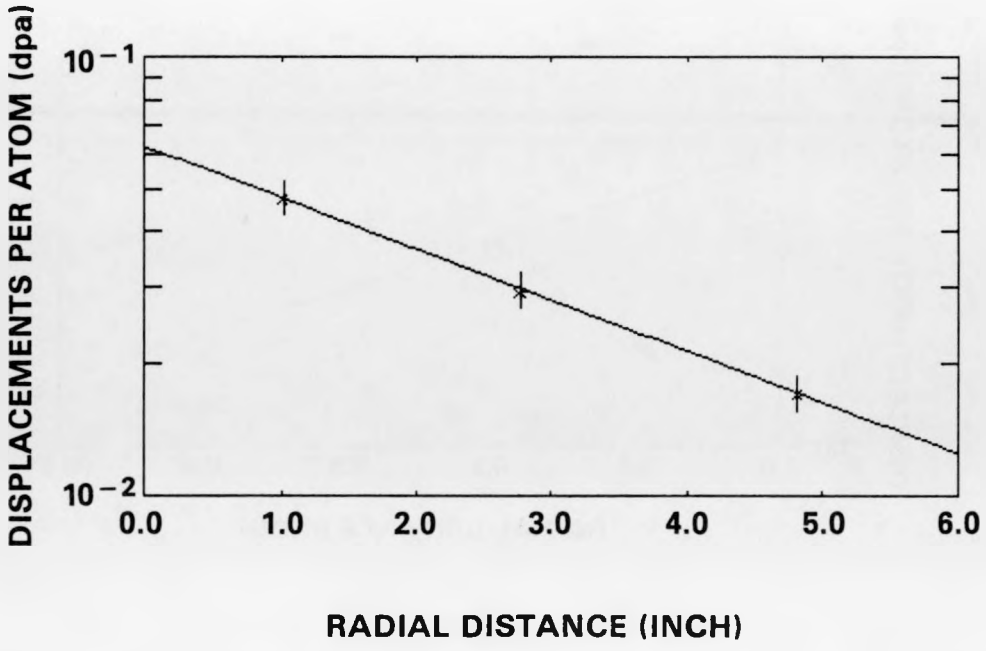

FIGURE HEDL-15. Radial Dependence of the dpa in the SPVC at the EC-Material Location. The smooth curve is a least-squares fit of the data to a simple exponential function (see text).

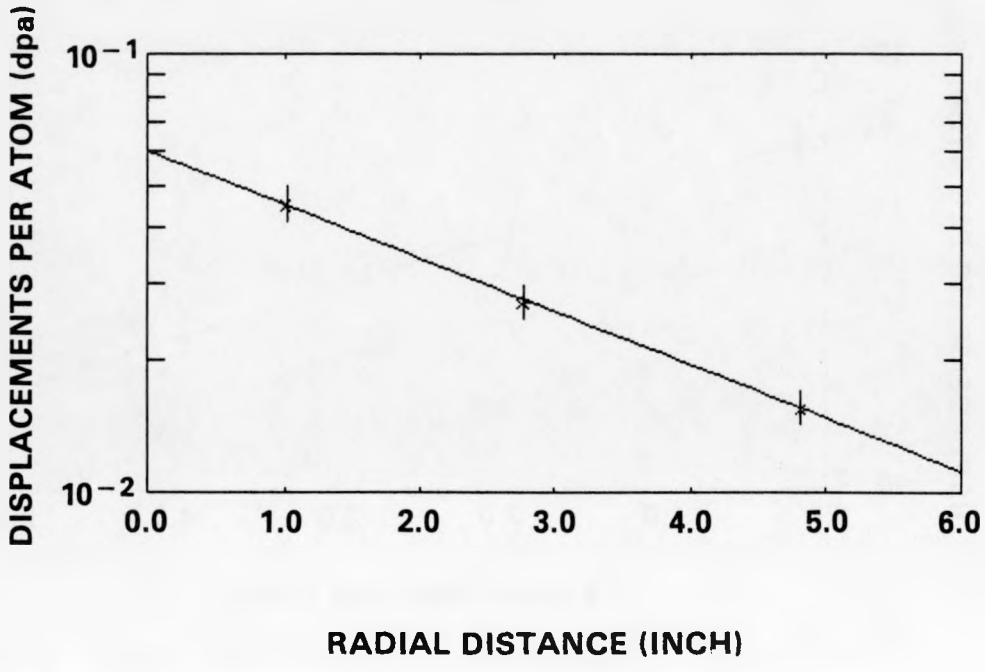

FIGURE HEDL-16. Radial Dependence of the dpa in the SPVC at the K-Material Location. The smooth curve is a least-squares fit of the data to a simple exponential function (see text).

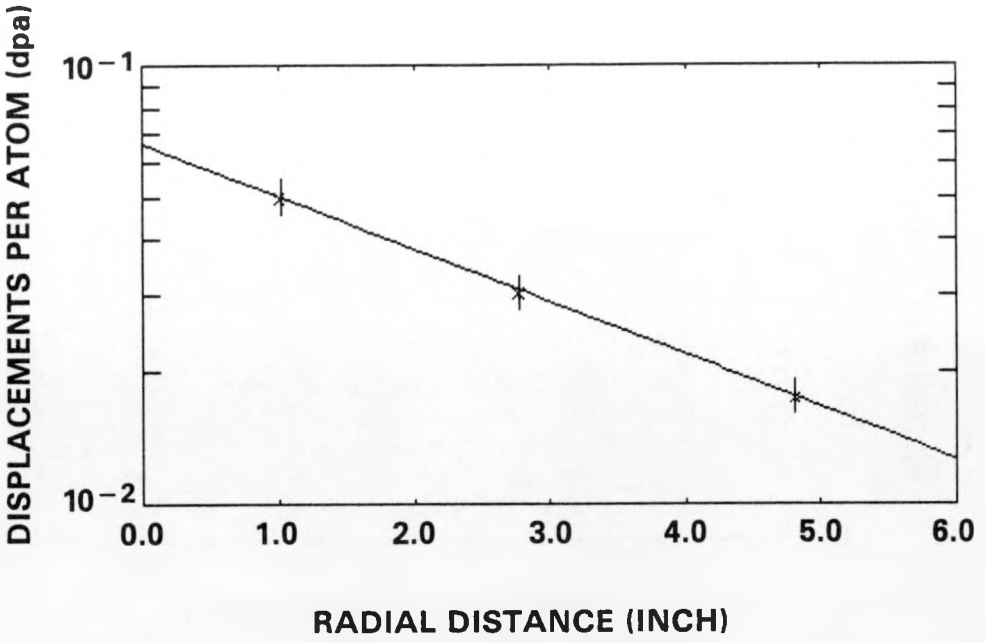

FIGURE HEDL-17. Radial Dependence of the dpa in the SPVC at the MO-Material Location. The smooth curve is a least-squares fit of the data to a simple exponential function (see text).

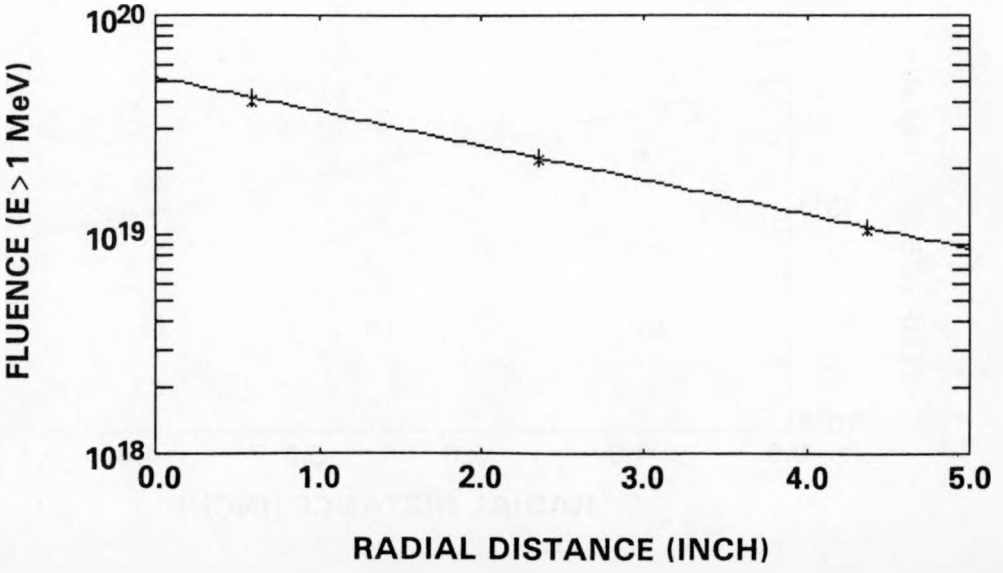

FIGURE HEDL-18. Radial Dependence of the Fluence in the SPVC at the Center of the Capsules. The smooth curve is a least-squares fit of the data to a simple exponential function (see text).

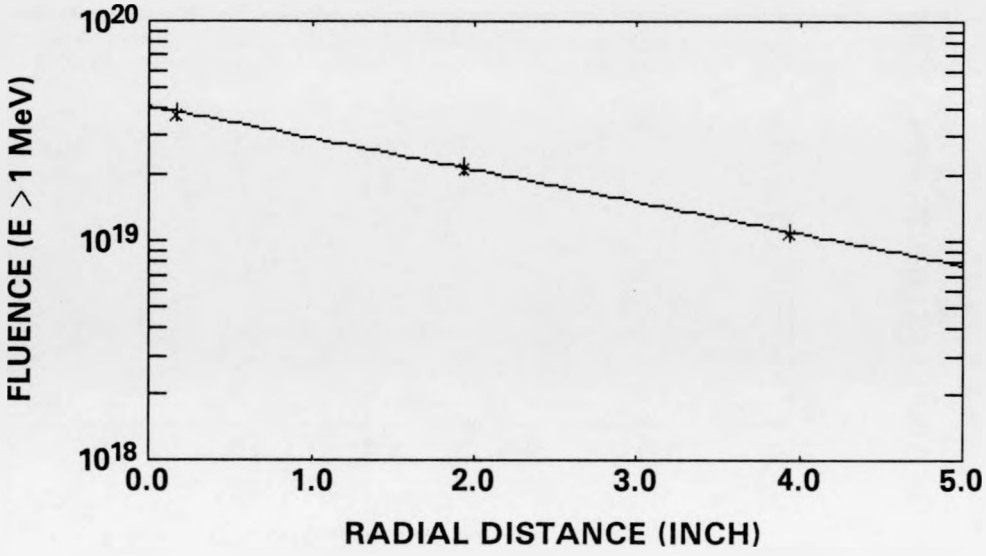

FIGURE HEDL-19. Radial Dependence of the Fluence in the SPVC at the R-Material Location. The smooth curve is a least-squares fit of the data to a simple exponential function (see text).

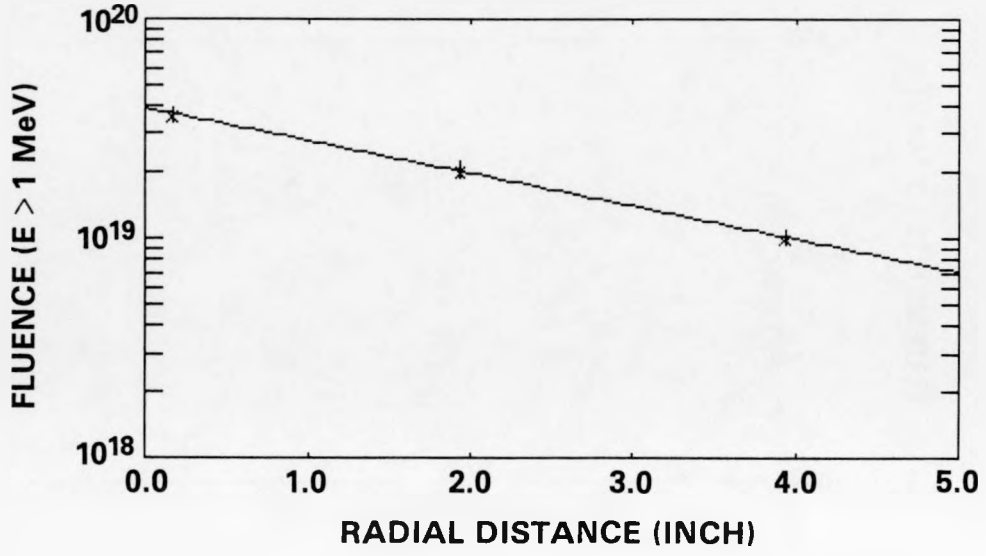

FIGURE HEDL-20. Radial Dependence of the Fluence in the SPVC at the 3PU-Material Location. The smooth curve is a least-squares fit of the data to a simple exponential function (see text).

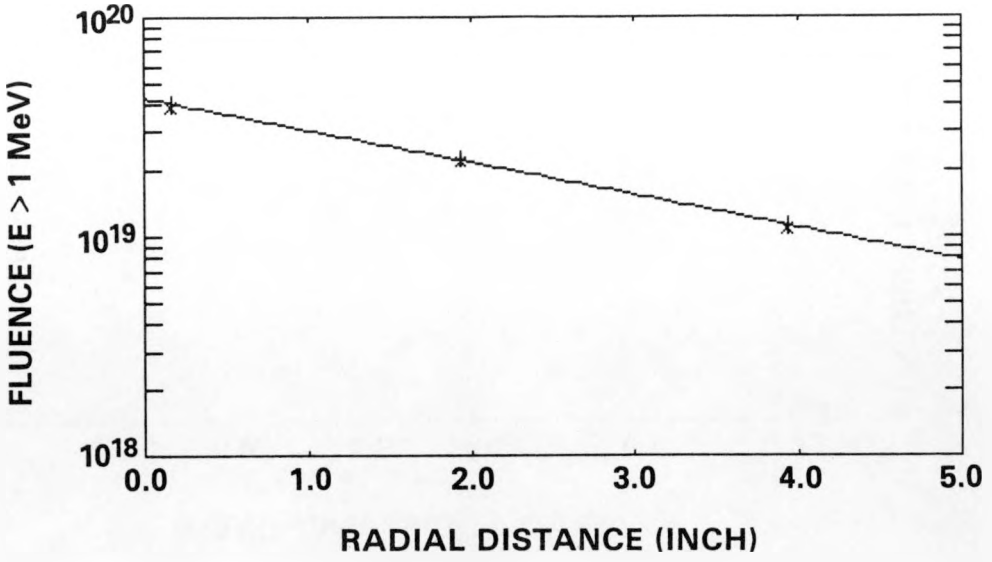

FIGURE HEDL-21. Radial Dependence of the Fluence in the SPVC at the F23-Material location. The smooth curve is a least-squares fit of the data to a simple exponential function (see text).

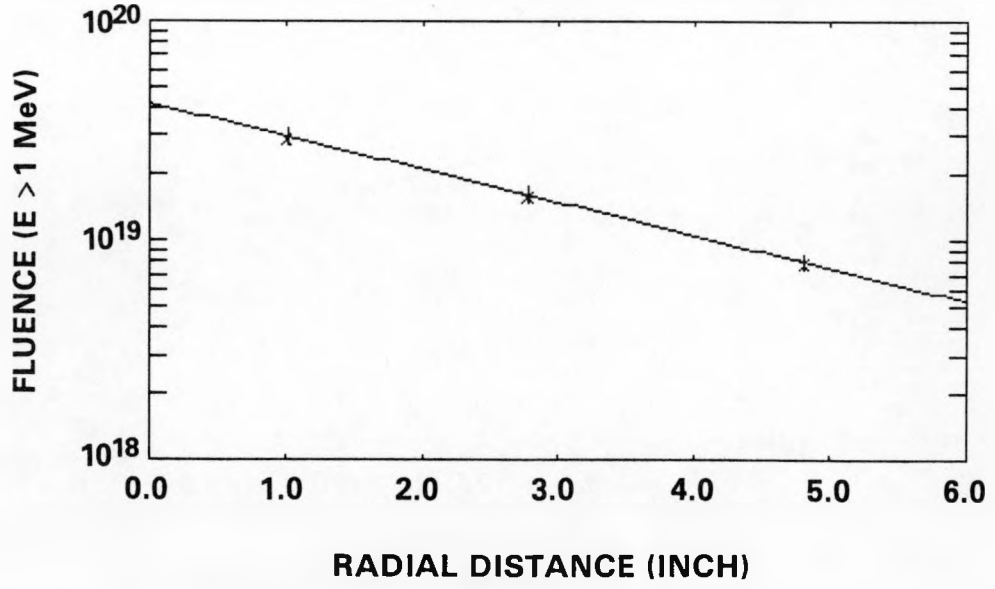

FIGURE HEDL-22. Radial Dependence of the Fluence in the SPVC at the EC-Material Location. The smooth curve is a least-squares fit of the data to a simple exponential function (see text).

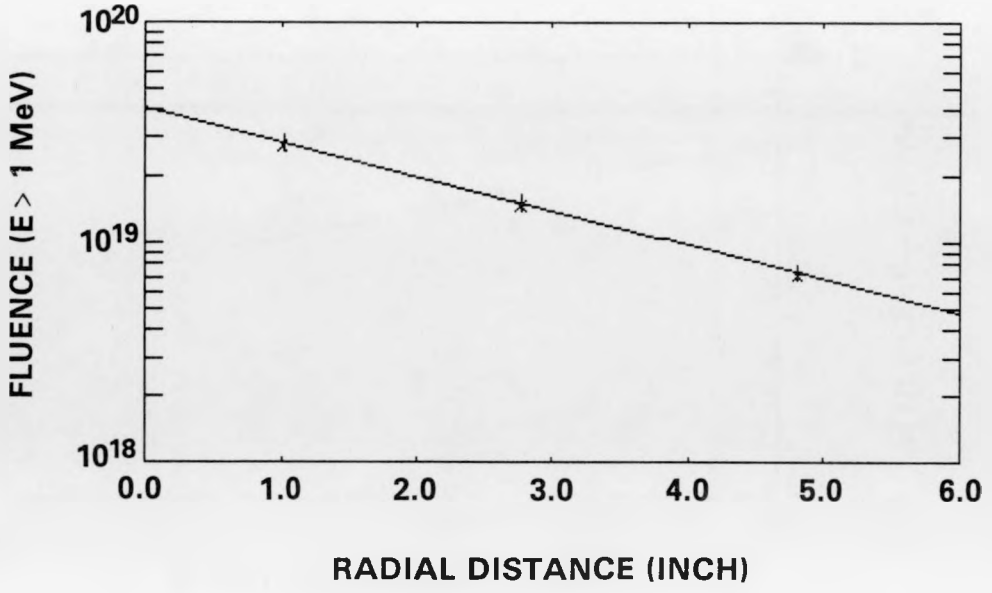

FIGURE HEDL-23. Radial Dependence of the Fluence in the SPVC at the K-Material Location. The smooth curve is a least-squares fit of the data to a simple exponential function (see text).

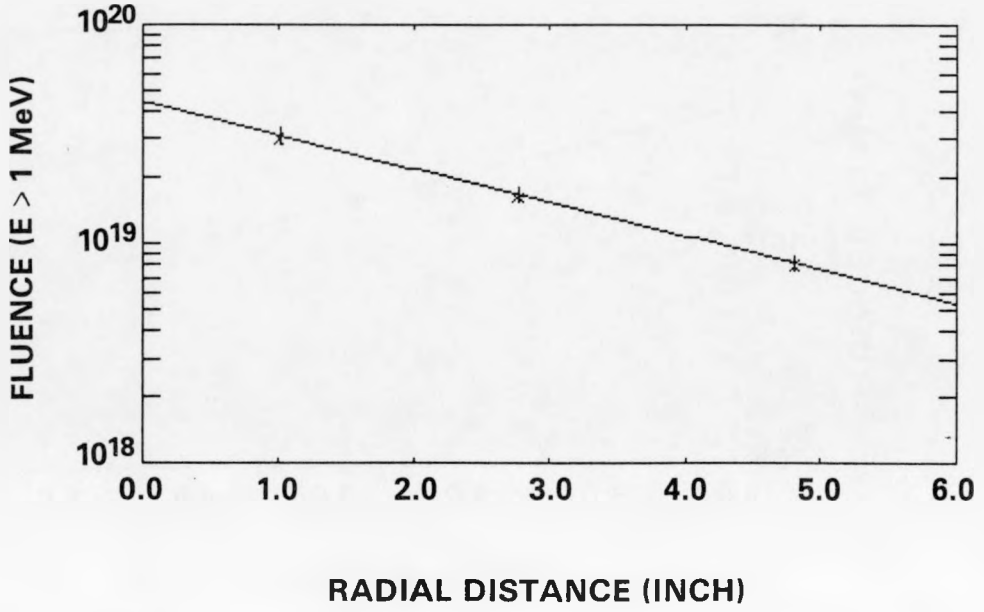

FIGURE HEDL-24. Radial Dependence of the Fluence in the SPVC at the MO-Material Location. The smooth curve is a least-squares fit of the data to a simple exponential function (see text).

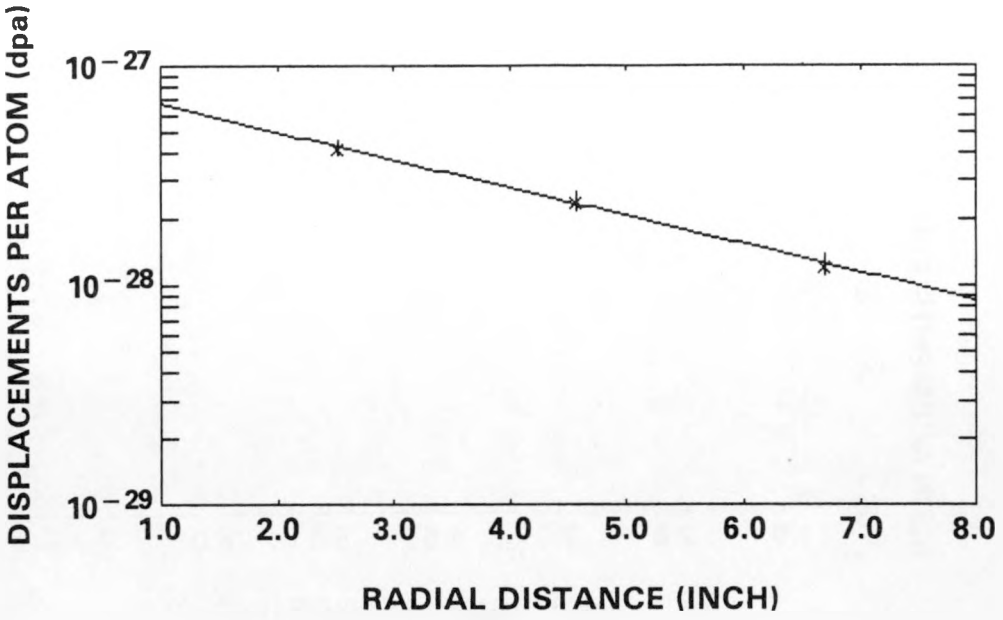

FIGURE HEDL-25. Radial Dependence of the dpa in the PCA for the 8/7 Configuration. The smooth curve is a least-squares fit of the data to a simple exponential function (see text).

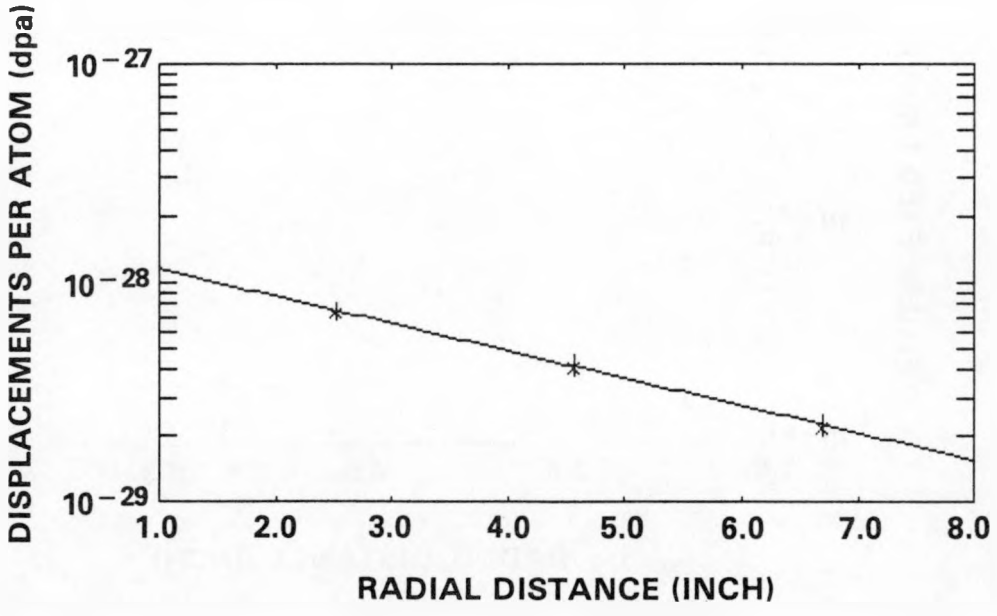

FIGURE HEDL-26. Radial Dependence of the dpa in the PCA for the 12/13 Configuration. The smooth curve is a least-squares fit of the data to a simple exponential function (see text).

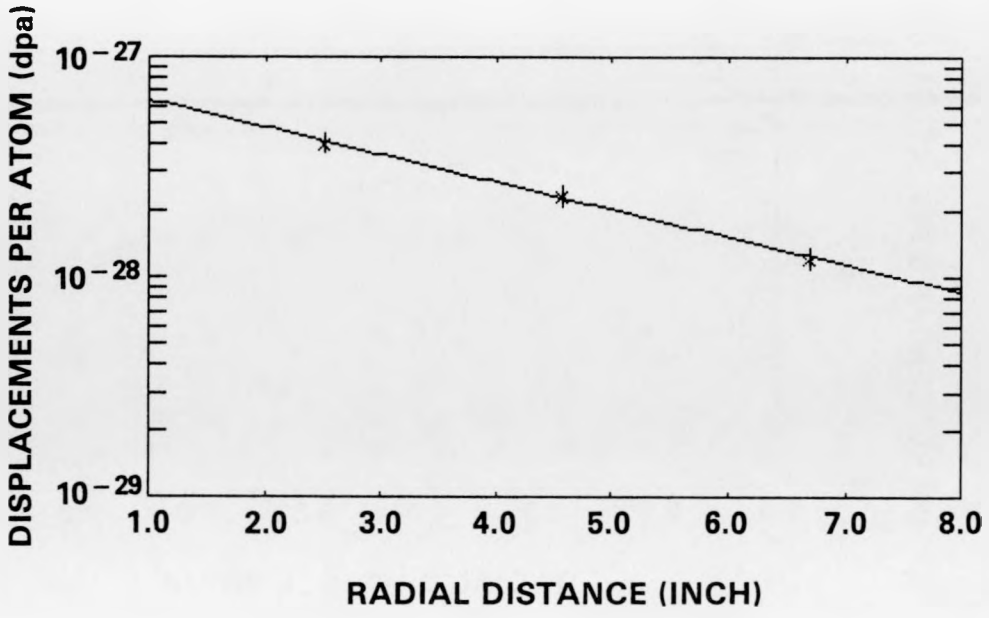

FIGURE HEDL-27. Radial Dependence of the dpa in the PCA for the 4/12 SSC Configuration. The smooth curve is a least-squares fit of the data to a simple exponential function (see text).

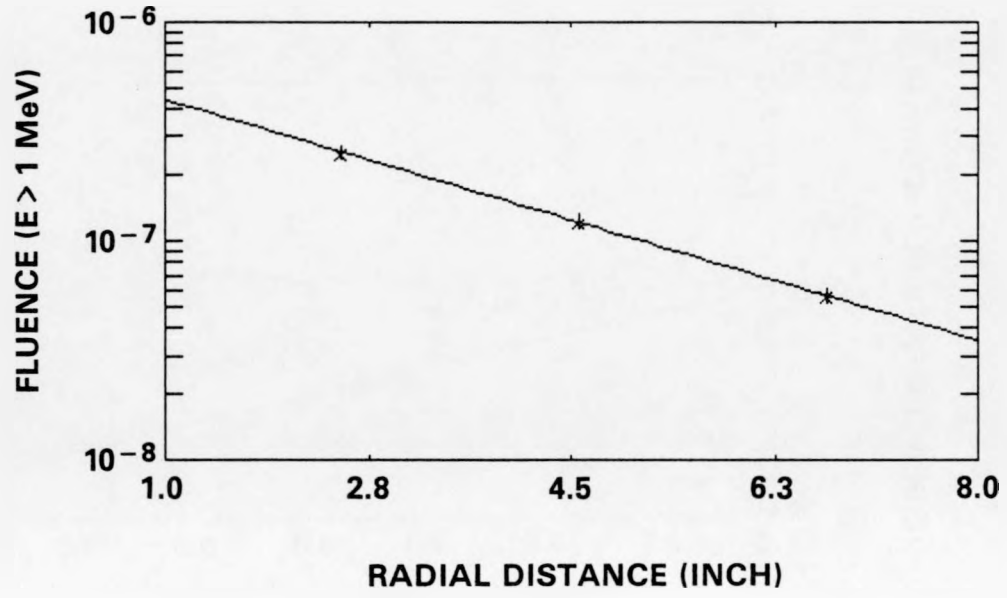

FIGURE HEDL-28. Radial Dependence of the Fluence in the PCA for the 8/7 Configuration. The smooth curve is a least-squares fit of the data to a simple exponential function (see text).

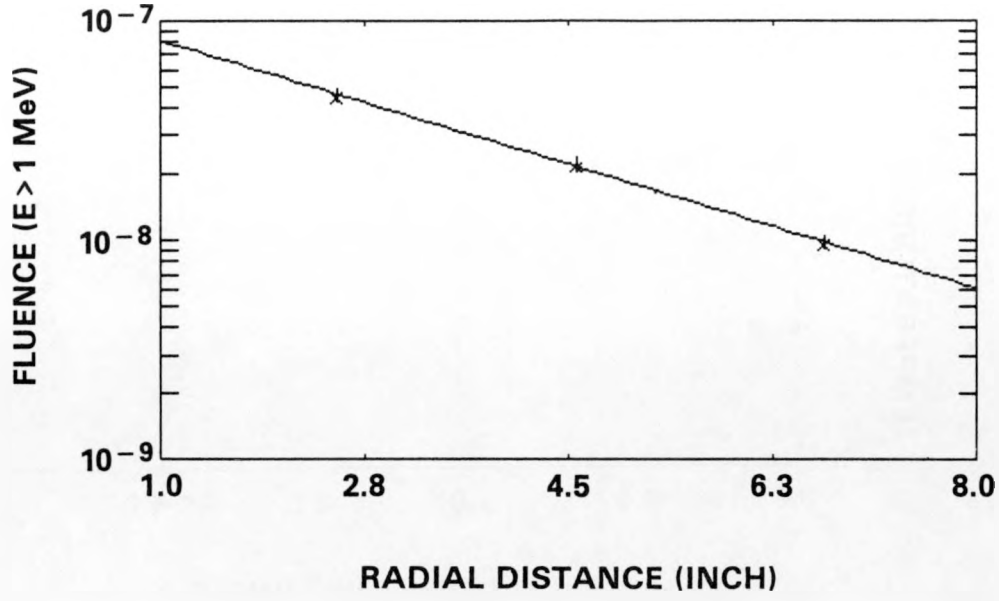

FIGURE HEDL-29. Radial Dependence of the Fluence in the PCA for the 12/13 Configuration. The smooth curve is a least-squares fit of the data to a simple exponential function (see text).

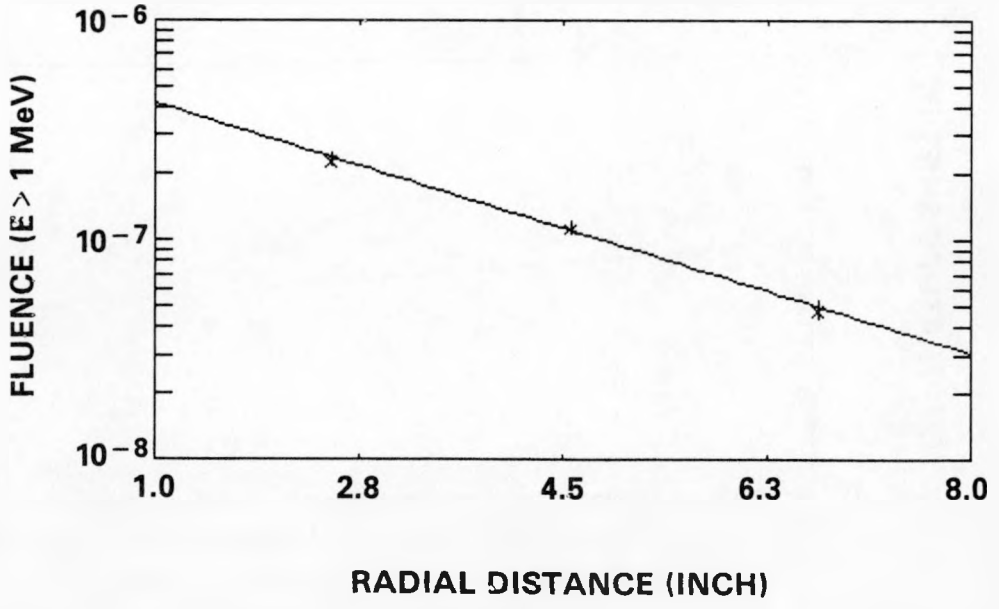

FIGURE HEDL-30. Radial Dependence of the Fluence in the PCA for the 4/12 SSC Configuration. The smooth curve is a least-squares fit of the data to a simple exponential function (see text).

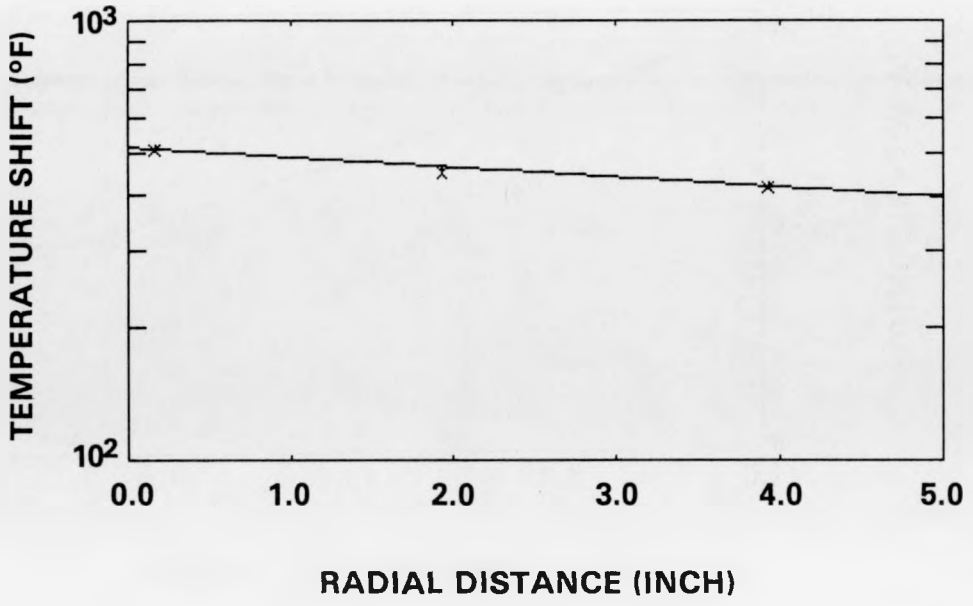

FIGURE HEDL-31. Radial Dependence of the Nil-Ductility Temperature Shift for the R-Material in the SPVC. The smooth curve is a least-squares fit of the data to a simple exponential function (see text).

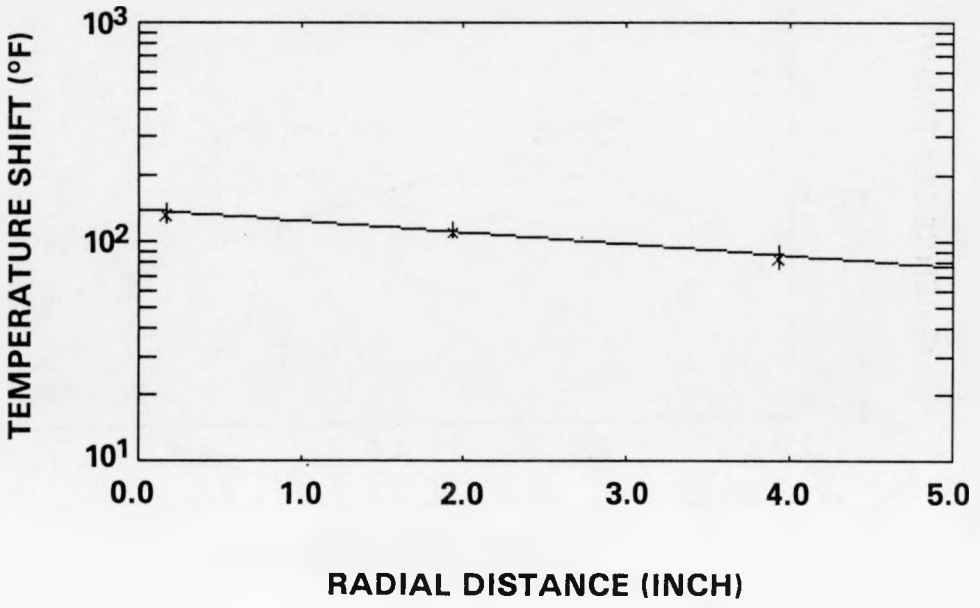

FIGURE HEDL-32. Radial Dependence of the Nil-Ductility Temperature Shift for the 3PU-Material in the SPVC. The smooth curve is a least-squares fit of the data to a simple exponential function (see text).

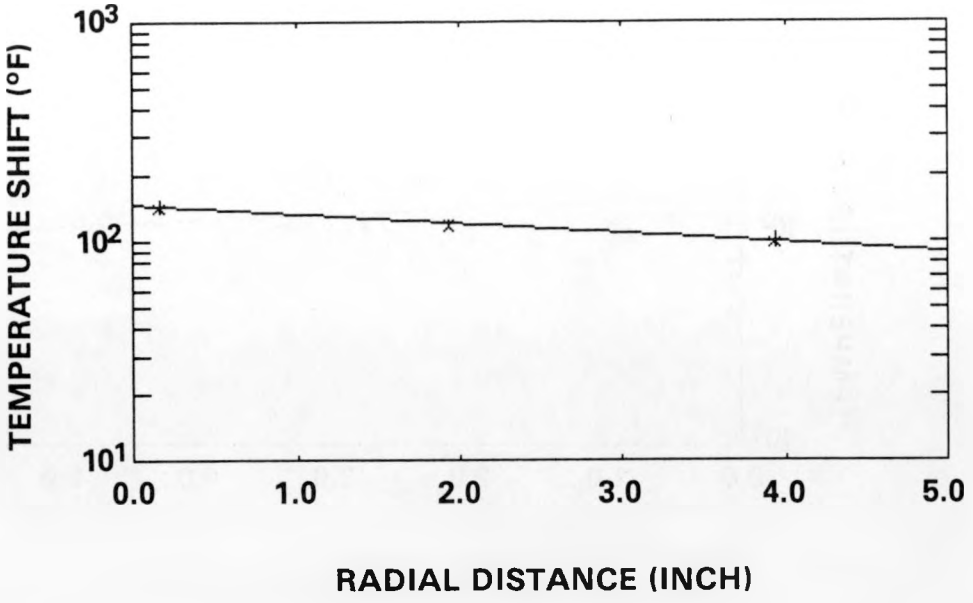

FIGURE HEDL-33. Radial Dependence of the Nil-Ductility Temperature Shift for the F23-Material in the SPVC. The smooth curve is a least-squares fit of the data to a simple exponential function (see text).

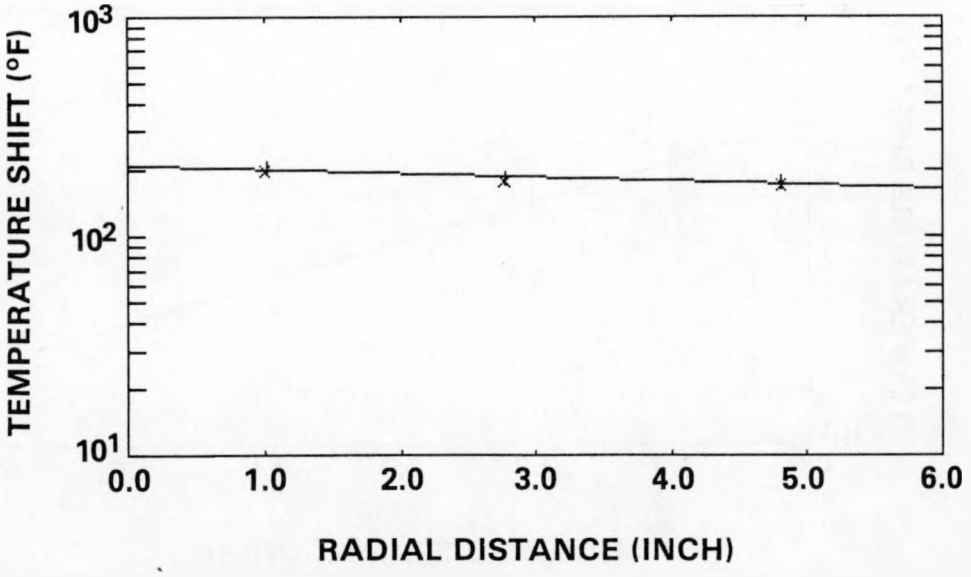

FIGURE HEDL-34. Radial Dependence of the Nil-Ductility Temperature Shift for the EC-Material in the SPVC. The smooth curve is a least-squares fit of the data to a simple exponential function (see text).

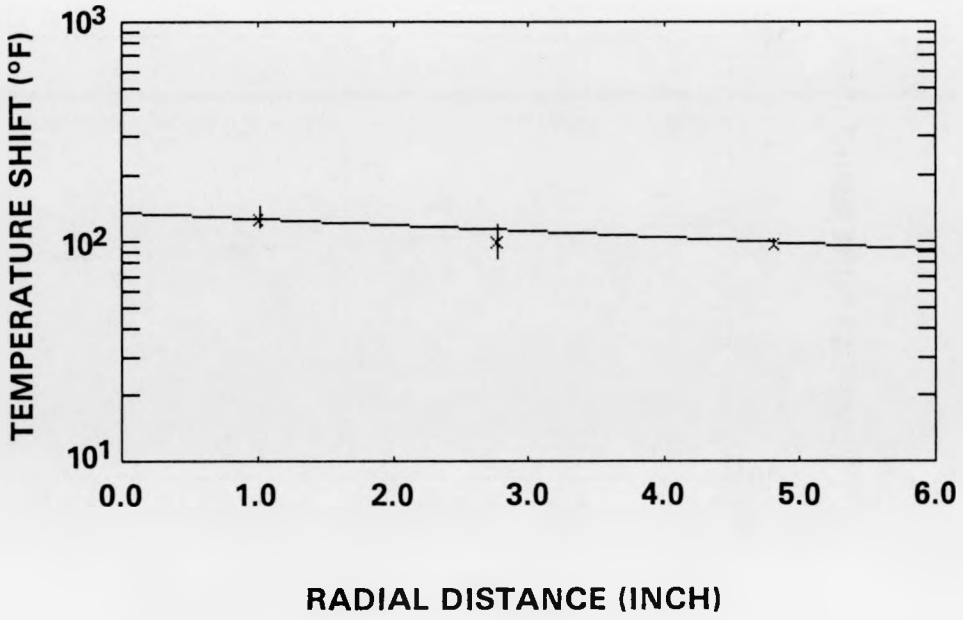

FIGURE HEDL-35. Radial Dependence of the Nil-Ductility Temperature Shift for the K-Material in the SPVC. The smooth curve is a least-squares fit of the data to a simple exponential function (see text).

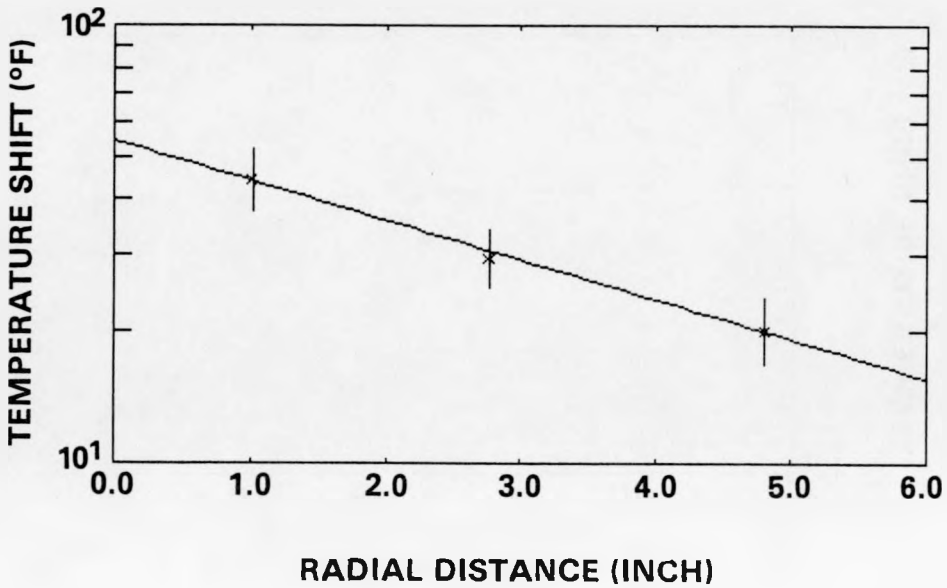

FIGURE HEDL-36. Radial Dependence of the Nil-Ductility Temperature Shift for the MO-Material in the SPVC. The smooth curve is a least-squares fit of the data to a simple exponential function (see text).

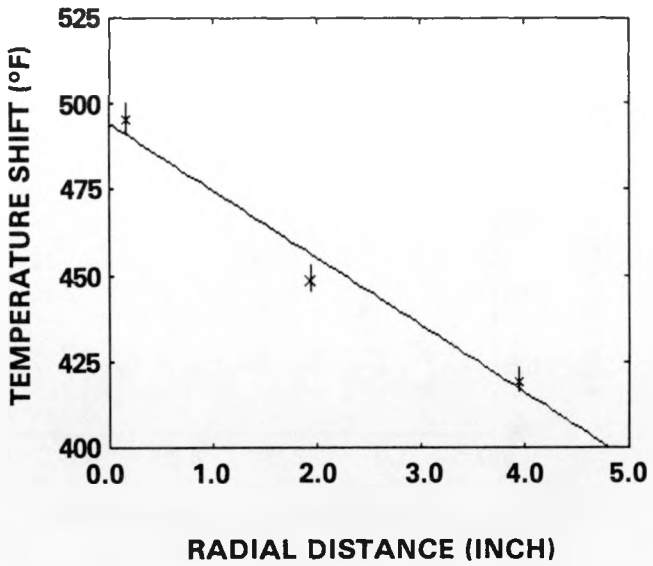

FIGURE HEDL-37. Radial Dependence of the Nil-Ductility Temperature Shift for the R-Material in the SPVC. The smooth curve is a least-squares fit of the data to a simple linear function (see text).

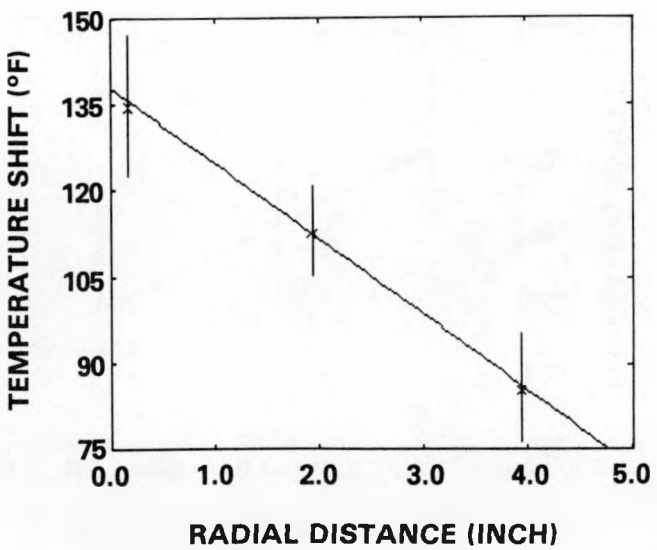

FIGURE HEDL-38. Radial Dependence of the Nil-Ductility Temperature Shift for the 3PU-Material in the SPVC. The smooth curve is a least-squares fit of the data to a simple linear function (see text).

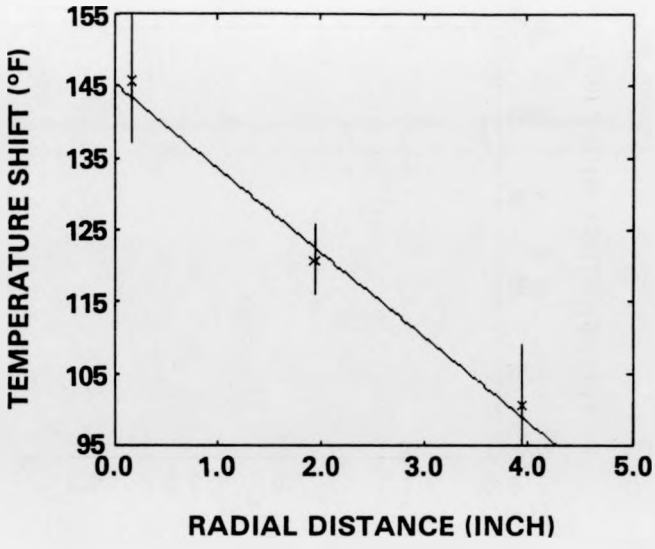

FIGURE HEDL-39. Radial Dependence of the Nil-Ductility Temperature Shift for the F23-Material in the SPVC. The smooth curve is a least-squares fit of the data to a simple linear function (see text).

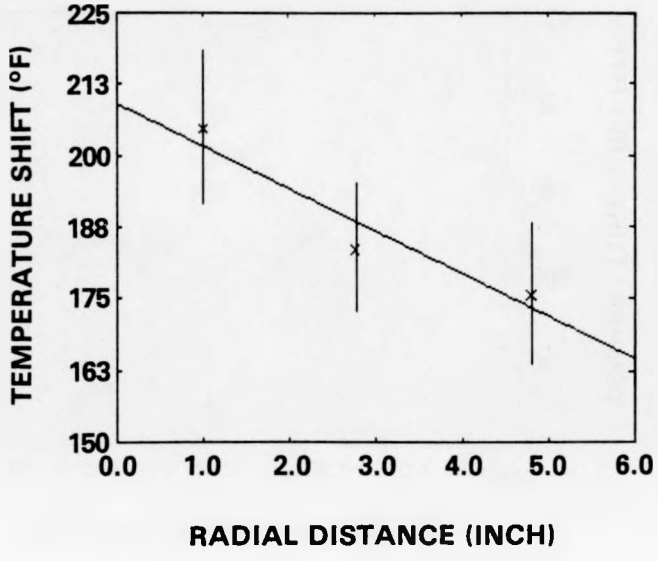

FIGURE HEDL-40. Radial Dependence of the Nil-Ductility Temperature Shift for the EC-Material in the SPVC. The smooth curve is a least-squares fit of the data to a simple linear function (see text).

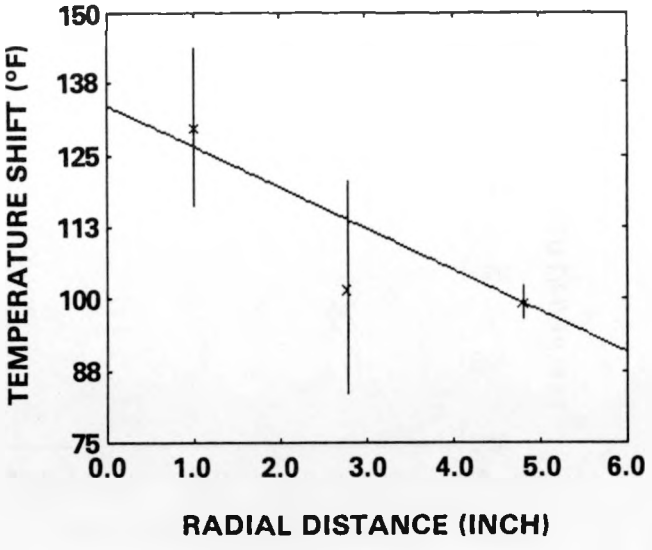

FIGURE HEDL-41. Radial Dependence of the Nil-Ductility Temperature Shift for the K-Material in the SPVC. The smooth curve is a least-squares fit of the data to a simple linear function (see text).

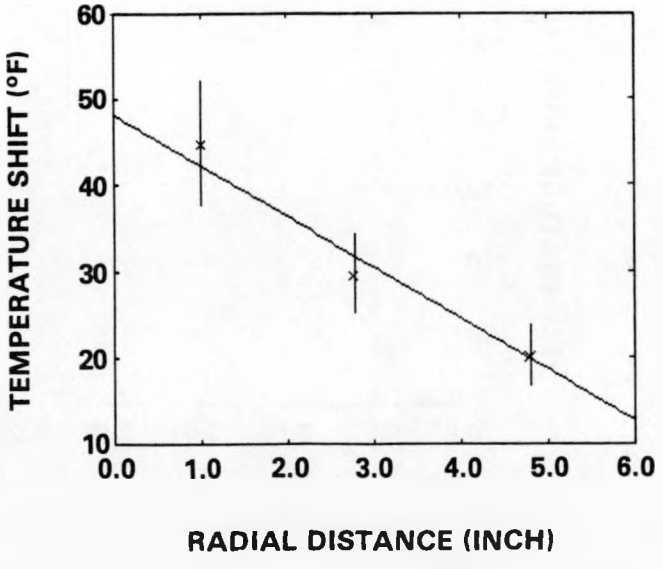

FIGURE HEDL-42. Radial Dependence of the Nil-Ductility Temperature Shift for the MO-Material in the SPVC. The smooth curve is a least-squares fit of the data to a simple linear function (see text).

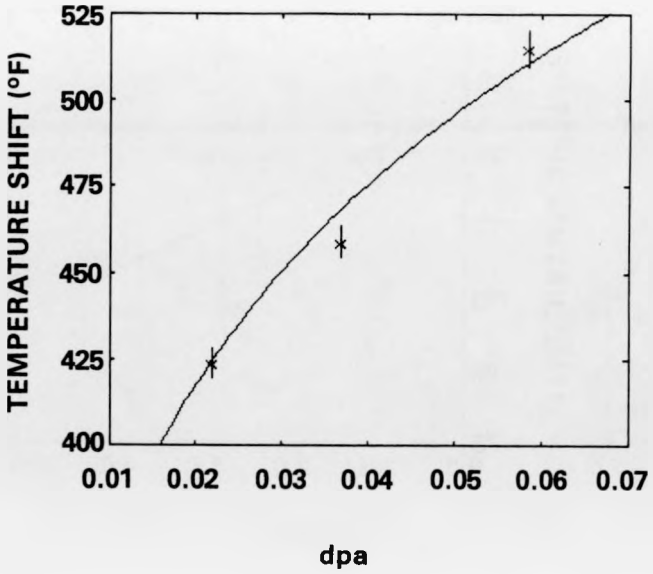

FIGURE HEDL-43. Power Law Trend Curve for the R-Material Using dpa as the Exposure Variable.

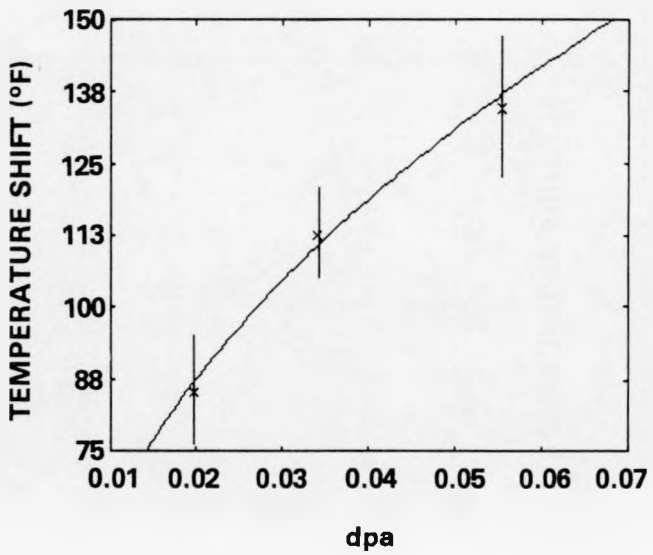

FIGURE HEDL-44. Power Law Trend Curve for the 3PU-Material Using dpa as the Exposure Variable.

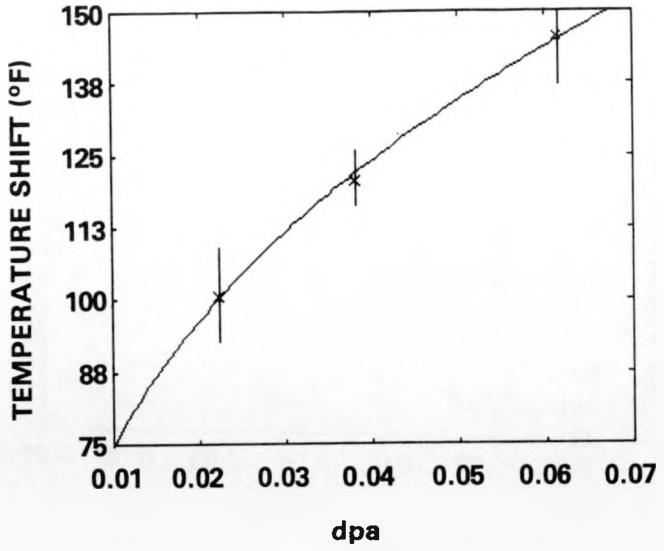

FIGURE HEDL-45. Power Law Trend Curve for the F23-Material Using dpa as the Exposure Variable.

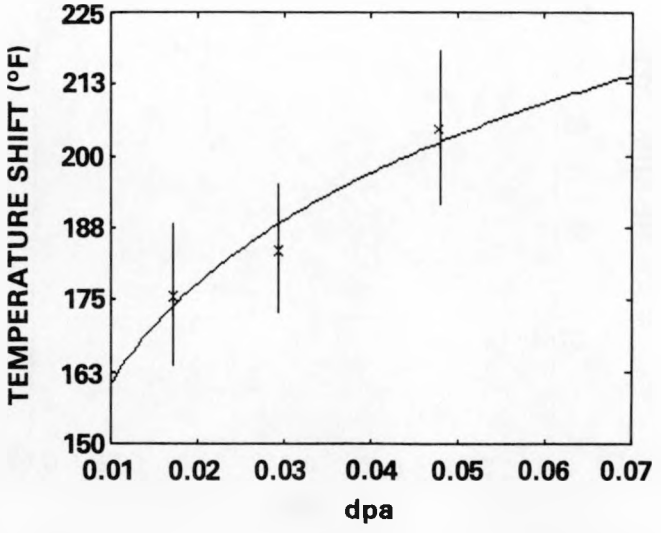

FIGURE HEDL-46. Power Law Trend Curve for the EC-Material Using dpa as the Exposure Variable.

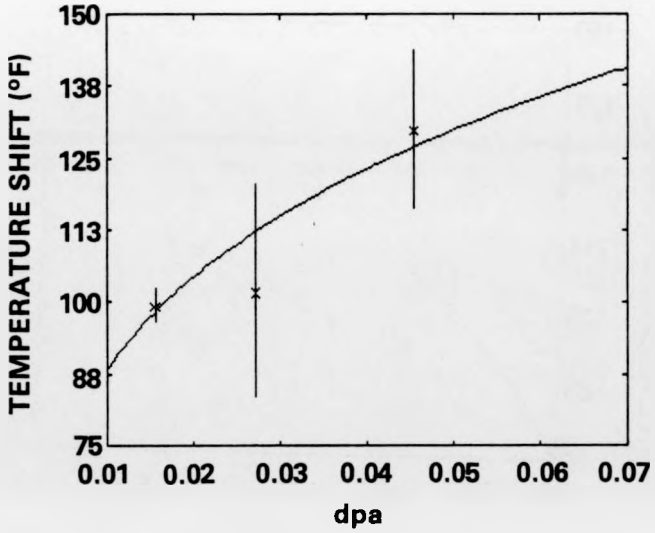

FIGURE HEDL-47. Power Law Trend Curve for the K-Material Using dpa as the Exposure Variable.

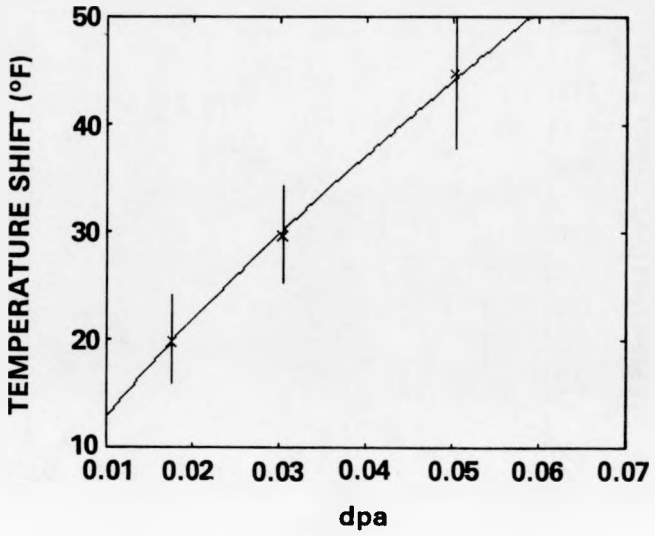

FIGURE HEDL-48. Power Law Trend Curve for the MO-Material Using dpa as the Exposure Variable.

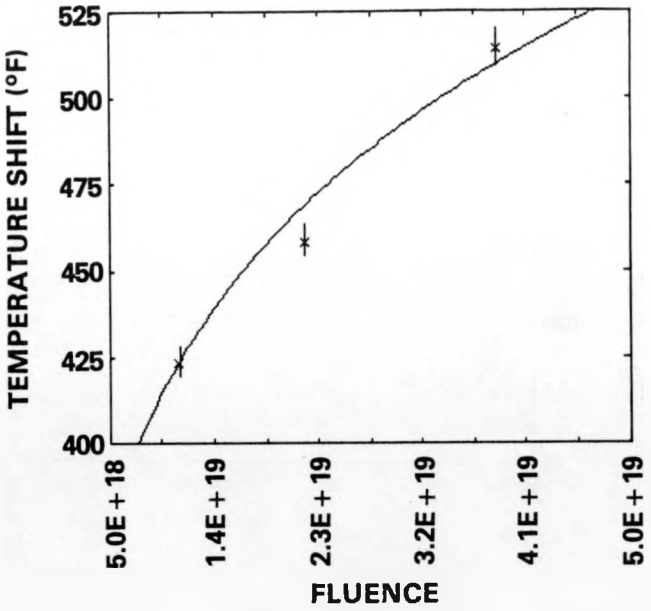

FIGURE HEDL-49. Power Law Trend Curve for the R-Material Using Fluence as the Exposure Variable.

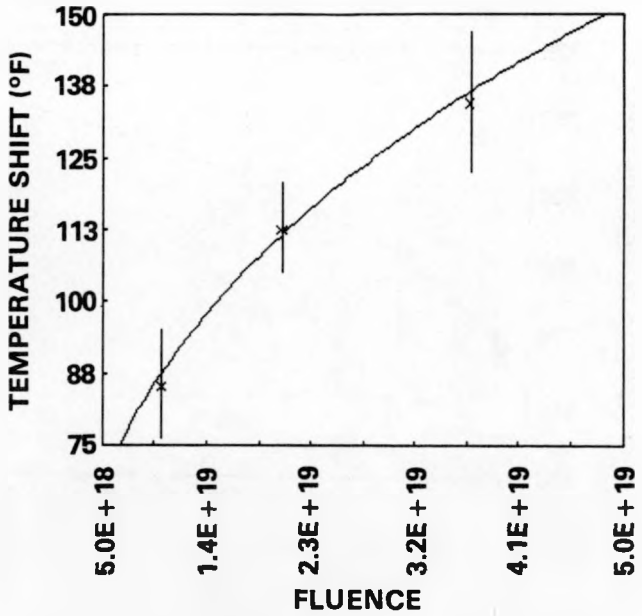

FIGURE HEDL-50. Power Law Trend Curve for the 3PU-Material Using Fluence as the Exposure Variable.

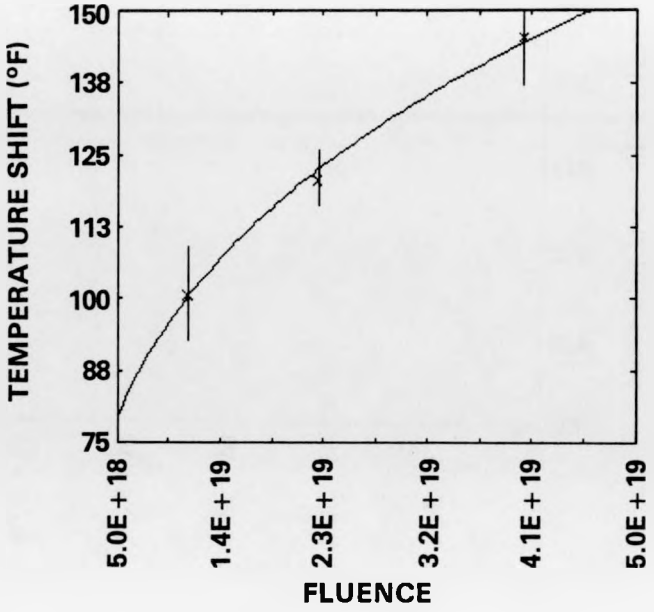

FIGURE HEDL-51. Power Law Trend Curve for the F23-Material Using Fluence as the Exposure Variable.

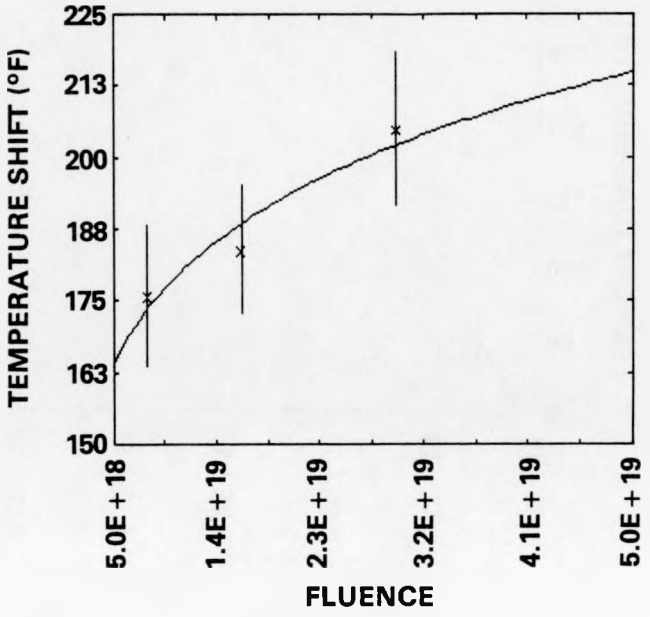

FIGURE HEDL-52. Power Law Trend Curve for the EC-Material Using Fluence as the Exposure Variable.

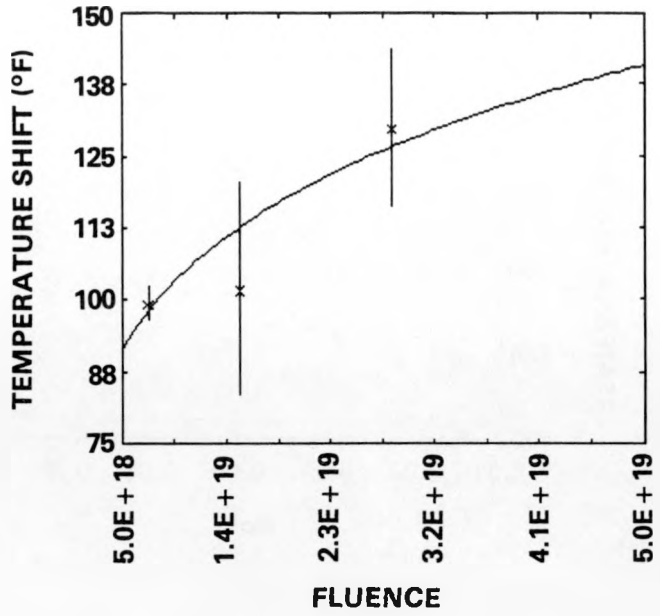

FIGURE HEDL-53. Power Law Trend Curve for the K-Material Using Fluence as the Exposure Variable.

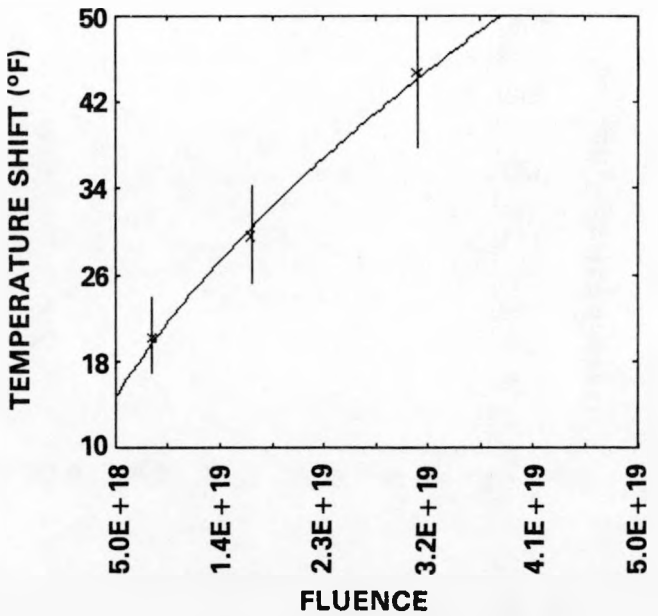

FIGURE HEDL-54. Power Law Trend Curve for the MO-Material Using Fluence as the Exposure Variable.

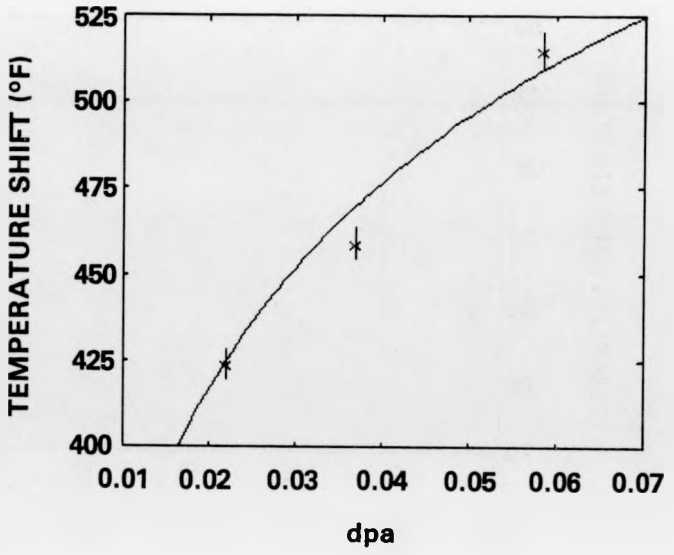

FIGURE HEDL-55. Logarithmic Trend Curve for the R-Material Using dpa as the Exposure Variable.

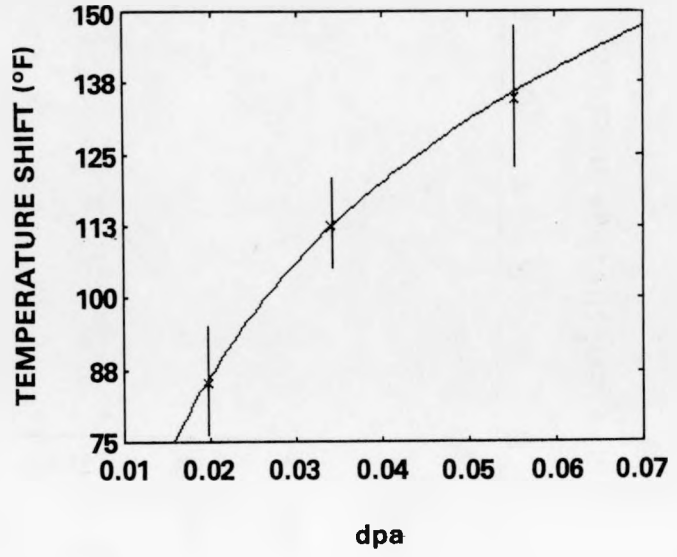

FIGURE HEDL-56. Logarithmic Trend Curve for the 3PU-Material Using dpa as the Exposure Variable.

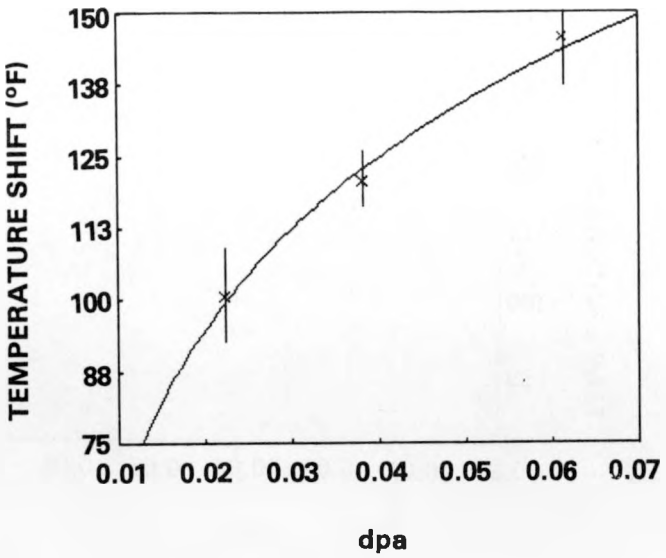

FIGURE HEDL-57. Logarithmic Trend Curve for the F23-Material Using dpa as the Exposure Variable.

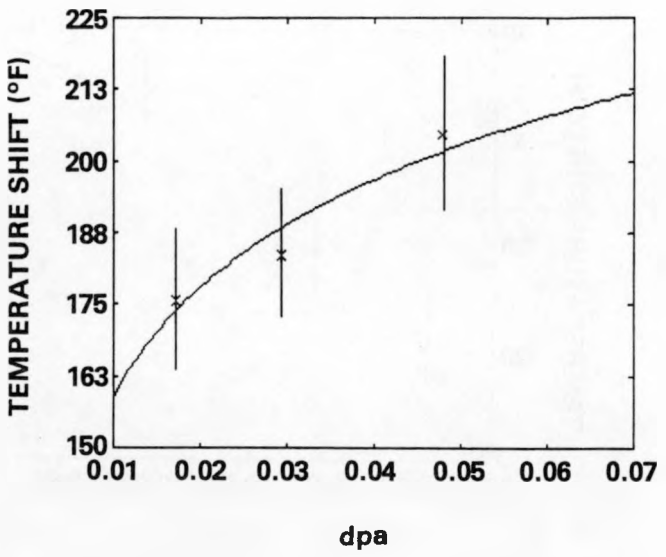

FIGURE HEDL-58. Logarithmic Trend Curve for the EC-Material Using dpa as the Exposure Variable.

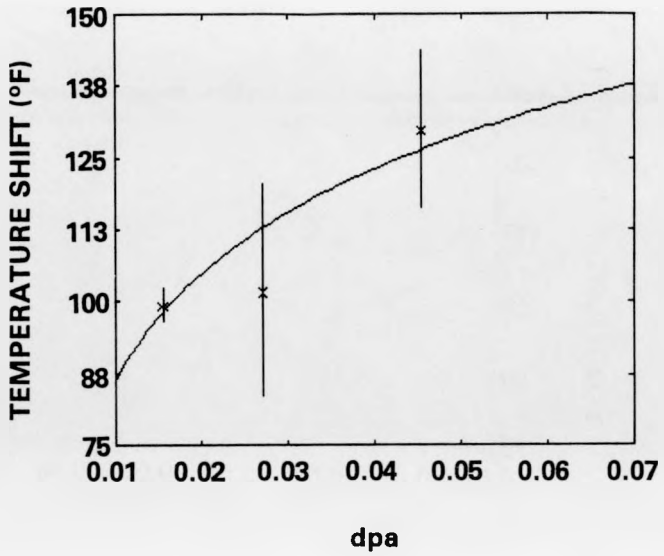

FIGURE HEDL-59. Logarithmic Trend Curve for the K-Material Using dpa as the Exposure Variable.

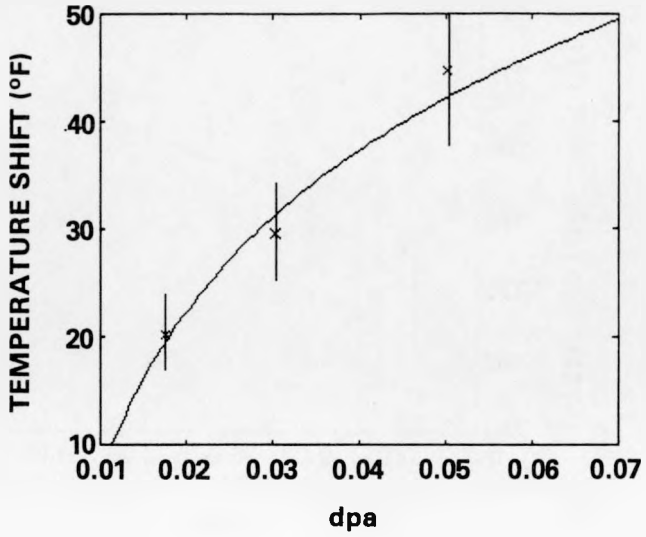

FIGURE HEDL-60. Logarithmic Trend Curve for the MO-Material Using dpa as the Exposure Variable.

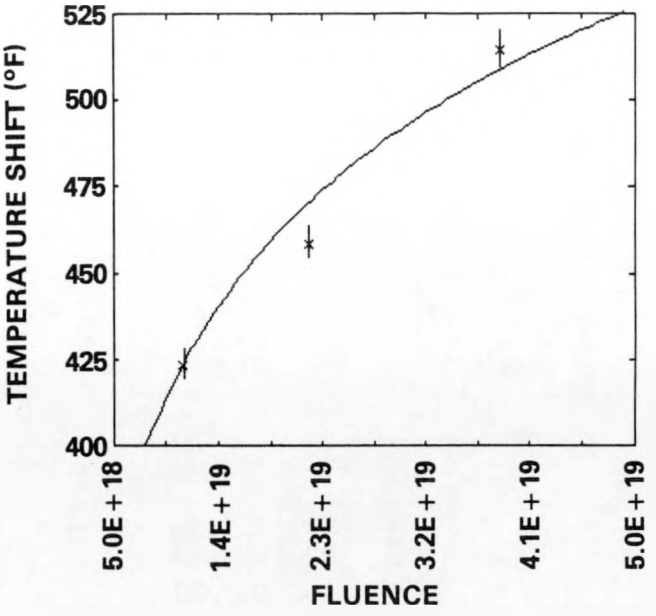

FIGURE HEDL-61. Logarithmic Trend Curve for the R-Material Using Fluence as the Exposure Variable.

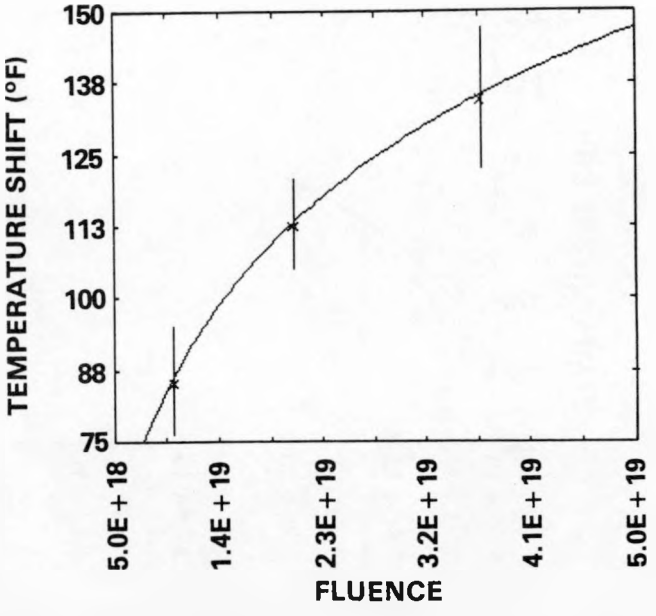

FIGURE HEDL-62. Logarithmic Trend Curve for the 3PU-Material Using Fluence as the Exposure Variable.

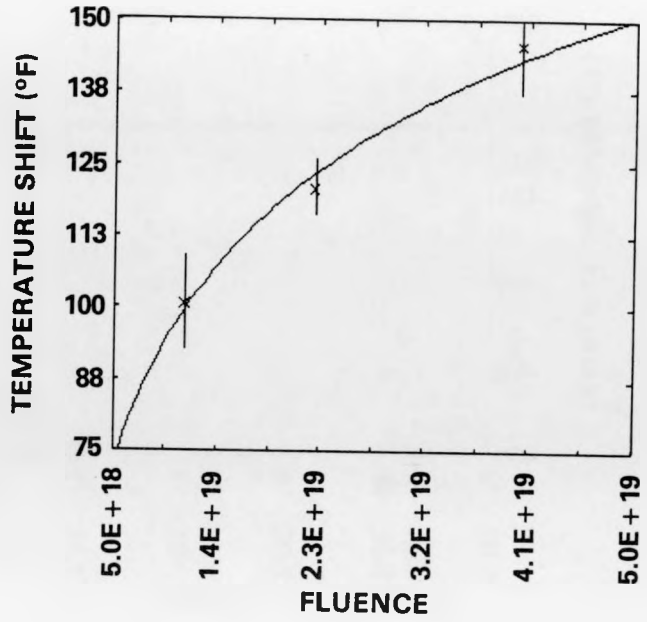

FIGURE HEDL-63. Logarithmic Trend Curve for the F23-Material Using Fluence as the Exposure Variable.

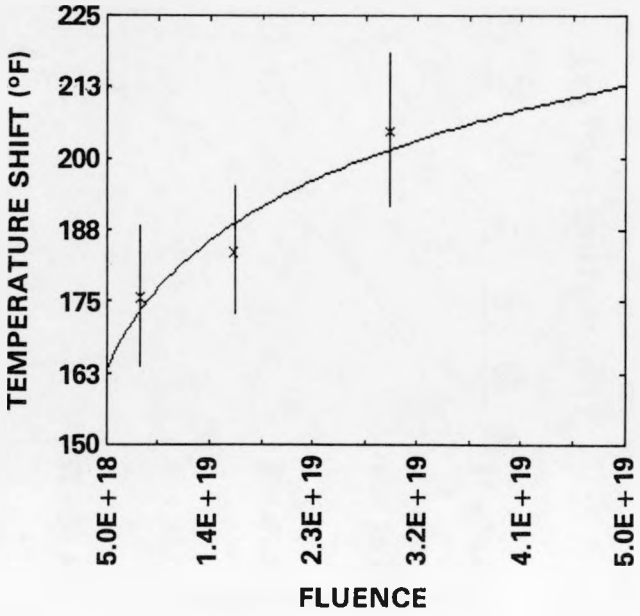

FIGURE HEDL-64. Logarithmic Trend Curve for the EC-Material Using Fluence as the Exposure Variable.

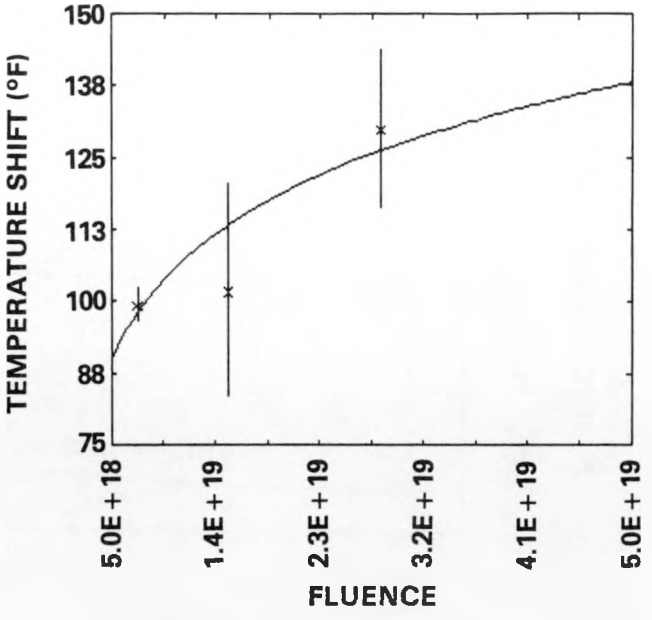

FIGURE HEDL-65. Logarithmic Trend Curve for the K-Material Using Fluence as the Exposure Variable.

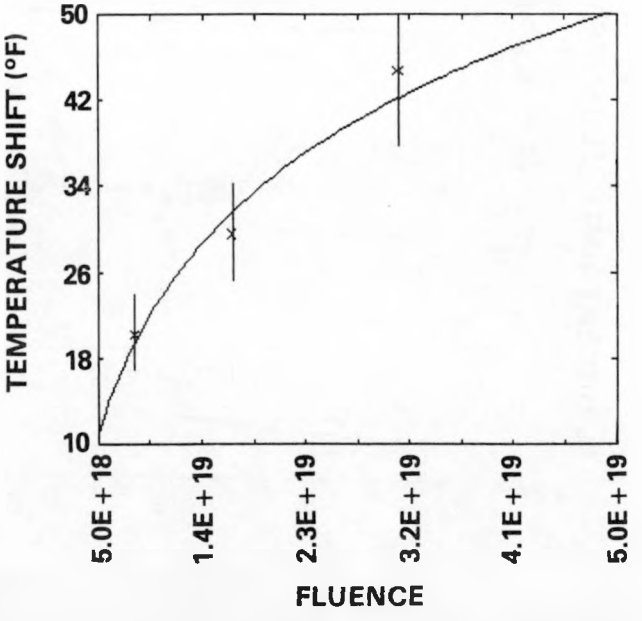

FIGURE HEDL-66. Logarithmic Trend Curve for the MO-Material Using Fluence as the Exposure Variable.

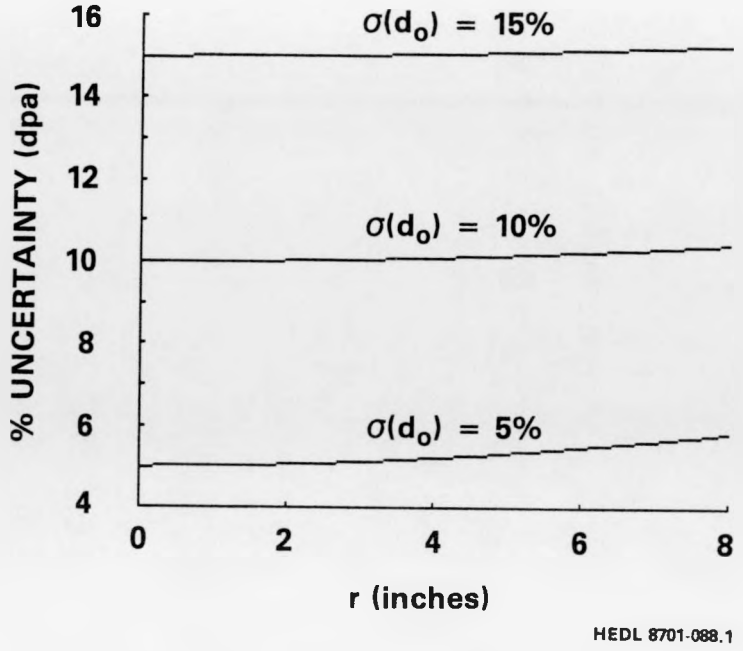

FIGURE HEDL-67. Radial Dependence of the Uncertainty in Extrapolated dpa for Surface Exposure Uncertainties of 5%, 10% and 15%.

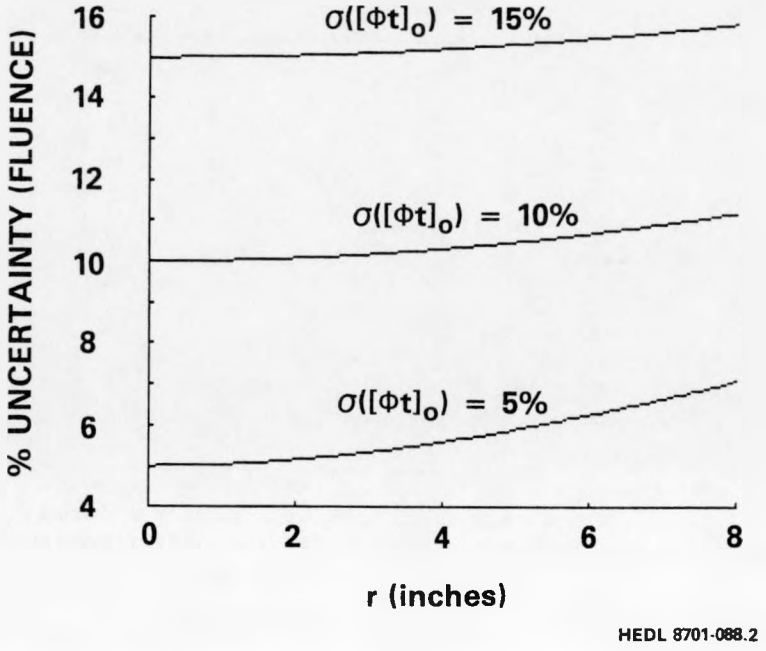

FIGURE HEDL-68. Radial Dependence of the Uncertainty in Extrapolated Fluence for Surface Exposure Uncertainties of 5%, 10% and 15%.

D. STATE-OF-THE-ART OF RADIOMETRIC NEUTRON DOSIMETRY FOR LWR-PV SURVEILLANCE

Raymond Gold, L. S. Kellogg and W. N. McElroy (HEDL) and
A. Fabry (CEN/SCK)

Objective

The objective of this work is to define the current state-of-the-art of radiometric (RM) neutron dosimetry for LWR-PV surveillance.

Summary

International participation in the PSF benchmark has been used to assess the worldwide status of RM neutron dosimetry for LWR-PV surveillance. In the first two of these PSF experiments, involving mainly U.S. laboratories, agreement was generally satisfactory, with nonfissile dosimeter results generally falling with ±5% (1σ) and the fissionable dosimeter results falling within ±10% (1σ). Improved agreement was attained in the third PSF experiment, involving mainly European laboratories, wherein nonfissile RM monitors generally agreed better than 2% (1σ) and fission monitors generally agreed to better than 5% (1σ).

Accomplishments and Status

1.0 Introduction

In LWR-PV work, it is currently accepted that the accuracy goal for reported neutron exposure parameters [flux and fluence ($E < 0.1$ and 1.0 MeV) and dpa] is the 5% to 15% (1σ) range (As82,Mc81,Mc82,Ra77,Ra78). To achieve and maintain this level of accuracy, reactor physics calculational and dosimetry measurement results must routinely be in the same accuracy range or better. It has been shown that this level of accuracy can be obtained, but only through careful standardization, which includes interlaboratory program work using benchmark (verification) facilities and extensive interlaboratory comparisons (Fa77,Gi78,Gr78c,Mc81a). Through these interlaboratory activities, systematic biases that arise at any one laboratory can be recognized and then (hopefully) resolved.

The use of radiometric (RM) neutron dosimetry for measurement of neutron exposure in LWR-PVS work is virtually universal. RM neutron dosimetry has been used since the inception of LWR-PVS programs, and a number of ASTM standards on this subject have existed for sometime. While two more recent passive neutron dosimetry methods have been proposed and possess unique advantages for LWR-PVS work [namely, solid state track recorder (SSTR) and helium accumulation fluence monitor (HAFM) neutron dosimetry], the use of these two methods in LWR-PVS work is extremely limited to date. Standards for both of these newer methods have only recently been issued (As82b,As83a). Equally significant is the fact that the number of laboratories with expertise and special facilities required for these two methods is very limited. As a consequence, RM dosimetry is the primary standard for LWR-PVS work and probably will continue to be so for sometime.

The PSF startup experiments provided a unique set of benchmarks for comparing RM dosimetry results from many laboratories, both nationally and internationally. The geometrical scale and fluence levels of these PSF startup experiments provided benchmarks considerably closer to LWR power plant environments than were heretofore available. Moreover, because of the unique character of the PSF metallurgical tests (Mc86b), many laboratories around the world participated. Hence, these PSF startup experiments afforded an ideal opportunity for intercomparisons of RM dosimetry.

Three PSF startup experiments were used for these RM intercomparisons:

(RM-I) -- The PSF Surveillance Capsule Perturbation Experiment [also known as the Simulated Dosimetry Measurement Facility Experiment 1 (SDMF1)] (Ba84a,To82).

(RM-II) -- The first PSF metallurgical simulated surveillance capsule (SSC-1) experiment (Mc84b).

(RM-III) -- The PSF 18-day high-power irradiation (Fa80a).

Table HEDL-43 identifies laboratories that participated in each of these three (RM-I, RM-II, and RM-III) PSF startup experiments. RM dosimetry aspects of these three PSF irradiations are described in Section 2.0 below. Interlaboratory comparisons are provided in Section 3.0. Conclusions drawn from these intercomparisons are then presented in Section 4.0.

2.0 Description of RM Neutron Dosimetry in PSF Startup Experiment

The PSF startup experiments used for benchmark testing of RM dosimetry in LWR-PVS environments were described at the fourth ASTM-EURATOM Symposium on Reactor Dosimetry, where interlaboratory comparisons of RM results were initially presented (Ke82,To82a). PSF irradiations RM-I, RM-II, and RM-III are described below in Sections 2.1, 2.2, and 2.3, respectively. Special emphasis is given to the RM dosimetry aspects of these PSF startup experiments.

2.1 RM-I -- PSF Surveillance Capsule Perturbation Experiment (SDMF1)

The RM-I experiment was included as a integral part of the PSF Surveillance Capsule Perturbation Experiment (Ba84a,To82). RM dosimeter sets fabricated at HEDL included six replicate samples of each dosimeter and were designed to minimize spatial effects. The design of typical capsules is illustrated in Figures HEDL-69 and HEDL-70. Capsules of similar design but without the gadolinium shield were also used in the first irradiation.

RM dosimeters were placed in the Thermal Shield Back (TSB) and the Pressure Vessel Face (PVF) simulated surveillance capsules. The location of the two capsules are shown in Figure HEDL-71. Figure HEDL-72 shows the dosimetry arrangement in each capsule. Those dosimetry capsules labeled HF and HNF contain the interlaboratory comparison samples. The HF capsules contain bare or Gd-covered fissionable and Co/Al monitors, shown in Figure HEDL-70. The HNF capsules have bare or Gd-covered nonfission wires, as shown in Figure HEDL-69.

TABLE HEDL-42

LABORATORIES PARTICIPATING IN PSF STARTUP EXPERIMENTS

PSF Experiment	Participating Laboratories*
RM-I	B&W, BMI, CE, GE, HEDL, SwRI, W
RM-II	B&W, BMI, CE, GE, HEDL, SwRI, W
RM-III	AEEW, AERE, CEN/SCK, ECN, HEDL, PTB

* AEEW = Atomic Energy Establishment Winfrith (UK)
AERE = Atomic Enger Research Establishment Harwell (UK)
B&W = Babcock and Wilcox (US)
BMI = Battelle Memorial Institute (US)
CEN/SCK = Centre d'Etude de'l Energie Nucleaire/Studiecentrum voor Kernenergie (Belg)
CE = Combustion Engineering (US)
ECN = Netherlands Energy Research Foundation, Petten (Neth)
GE = General Electric (US)
HEDL = Hanford Engineering Development Laboratory (US)
PTB = Physikalisch-Technische Bundesanstalt, Braunschweig (FRG)
SwRI = Southwest Research Institute (US)
W = Westinghouse (US)

2.2 RM-II -- SCC-1 Experiment

The RM-II experiment was included in the first metallurgical simulated surveillance capsule (SSC-1) experiment (Mc84b). Figure HEDL-71 reveals that the 4/12 configuration was used in the SSC-1 experiment. The location of RM dosimeters within the experiment is shown in Figure HEDL-72. The HF comparison samples were placed in Hole B-Block 38 and the HNF samples in Hole D Block 37.

After both the RM-I and RM-II irradiations, the assemblies were dismantled at ORNL and the individual dosimeter capsules shipped to HEDL. The capsules were opened and the individual dosimeters were identified by unloading sequence and dosimeter weight or ID designation. All RM dosimeters were counted at HEDL to determine relative normalization factors between a given RM dosimeter and the corresponding HEDL RM dosimeter. These individual normalization factors could then be used on a dosimeter-by-dosimeter basis to correct for effects that might arise from:

- Gradients in the neutron exposure.
- Self-shielding.
- Uncertainties in dosimeter mass.

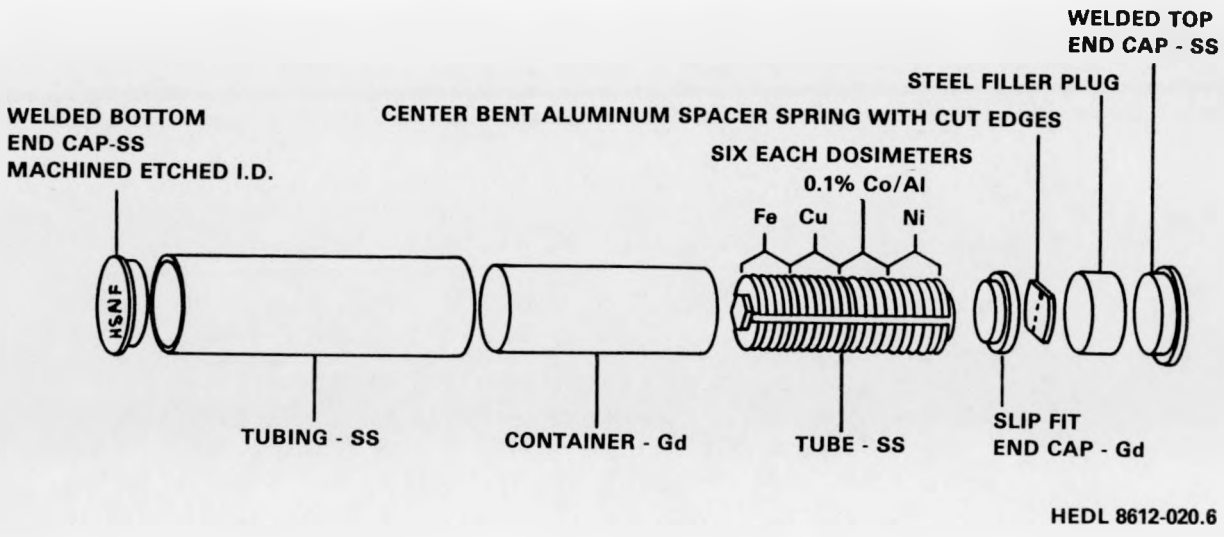

FIGURE HEDL-69. HEDL Surveillance Capsule - Nonfissionable Materials (1 Set HEDL/Vendor/Service Laboratory Counting).

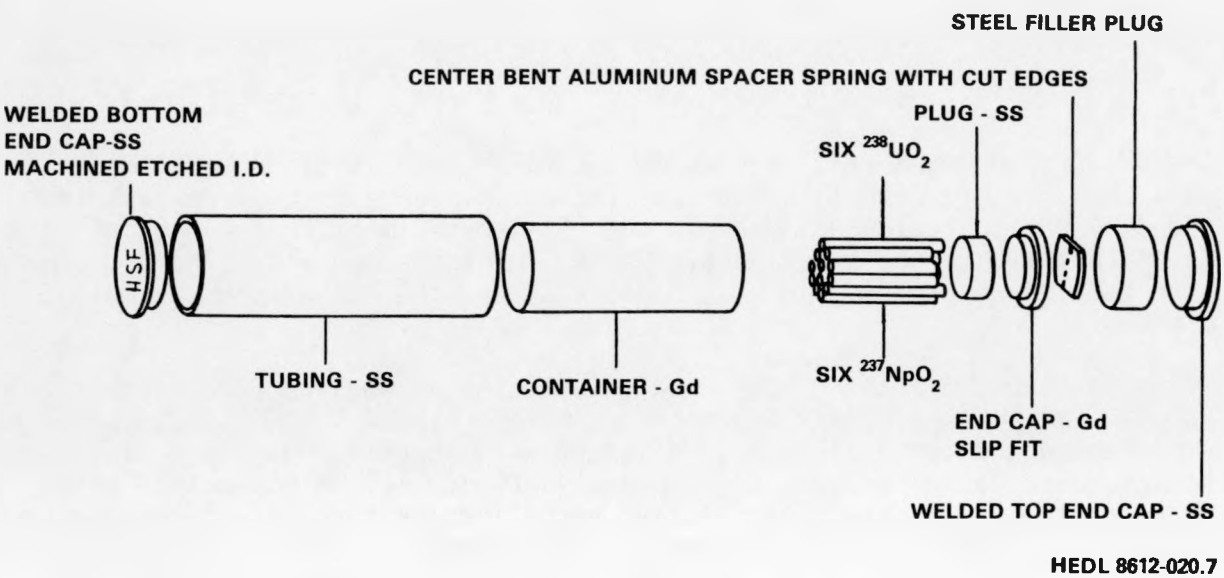

FIGURE HEDL-70. HEDL Surveillance Capsule - Fissionable Materials (1 Set HEDL/Vendor/Service Laboratory Counting).

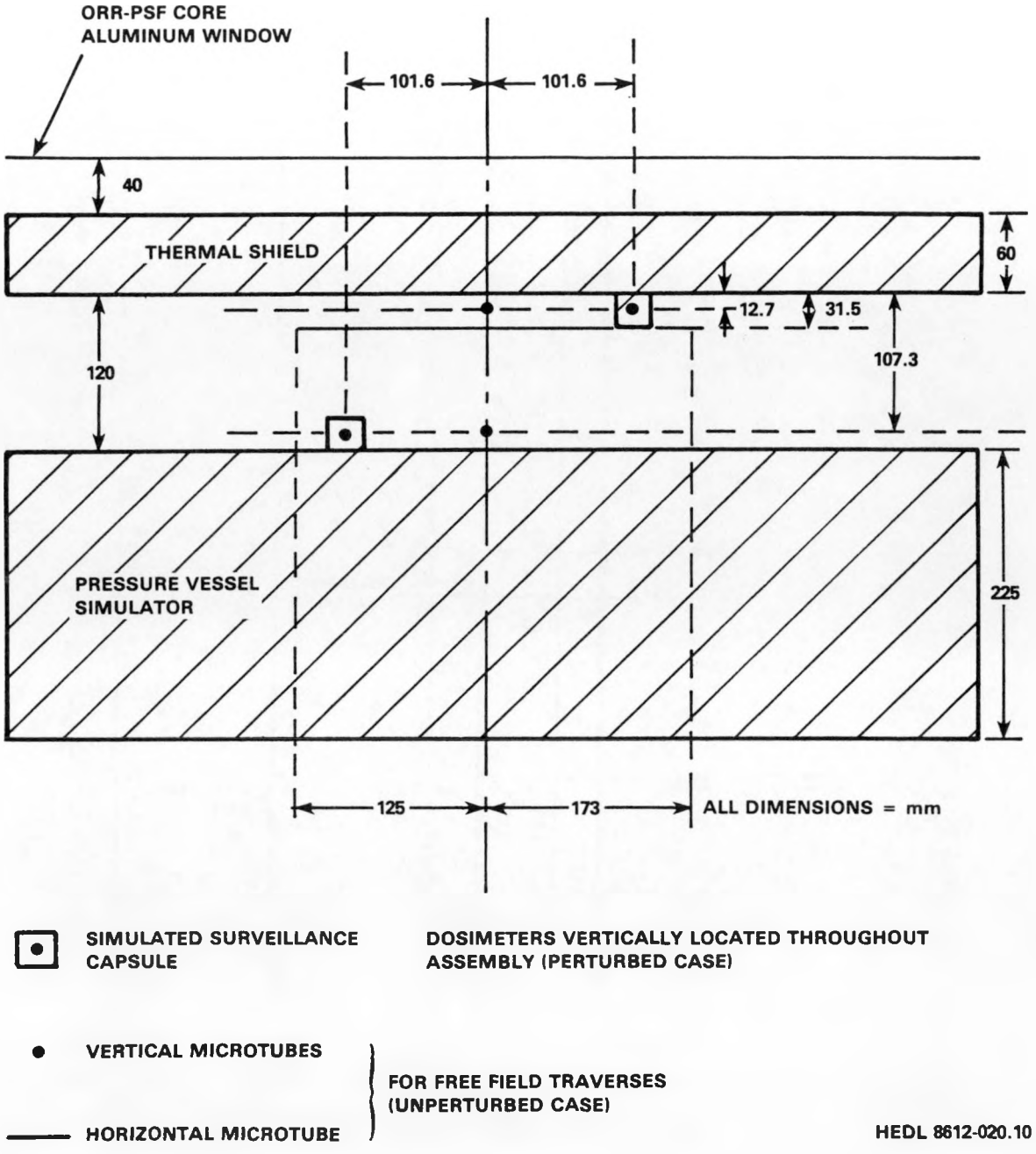

FIGURE HEDL-71. PSF-SDMF Perturbation Test Experimental Configuration (Horizontal Cut at Maximum Axial Flux).

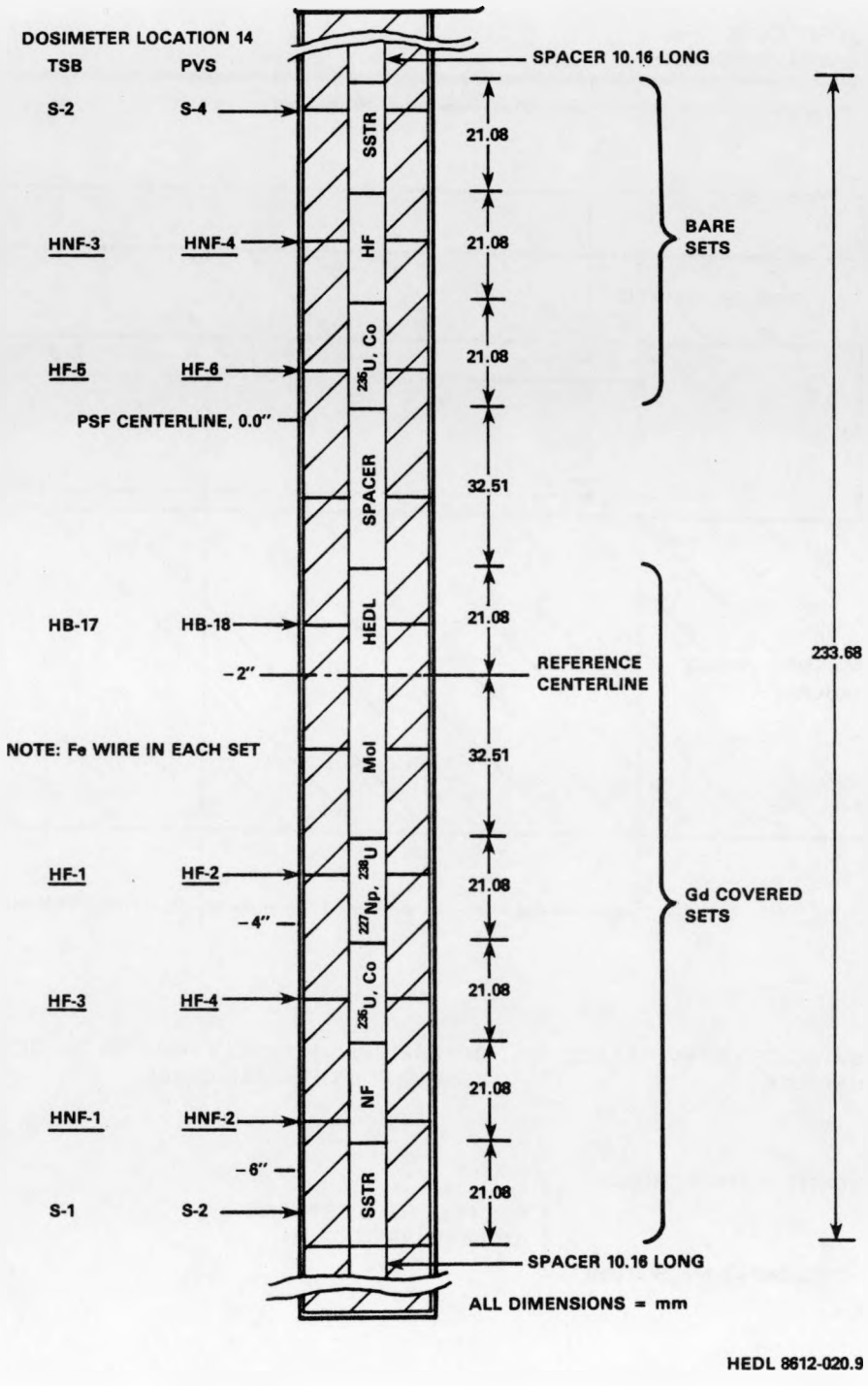

FIGURE HEDL-72. Axial Distribution of Dosimetry Sets in Simulated Surveillance Capsule.

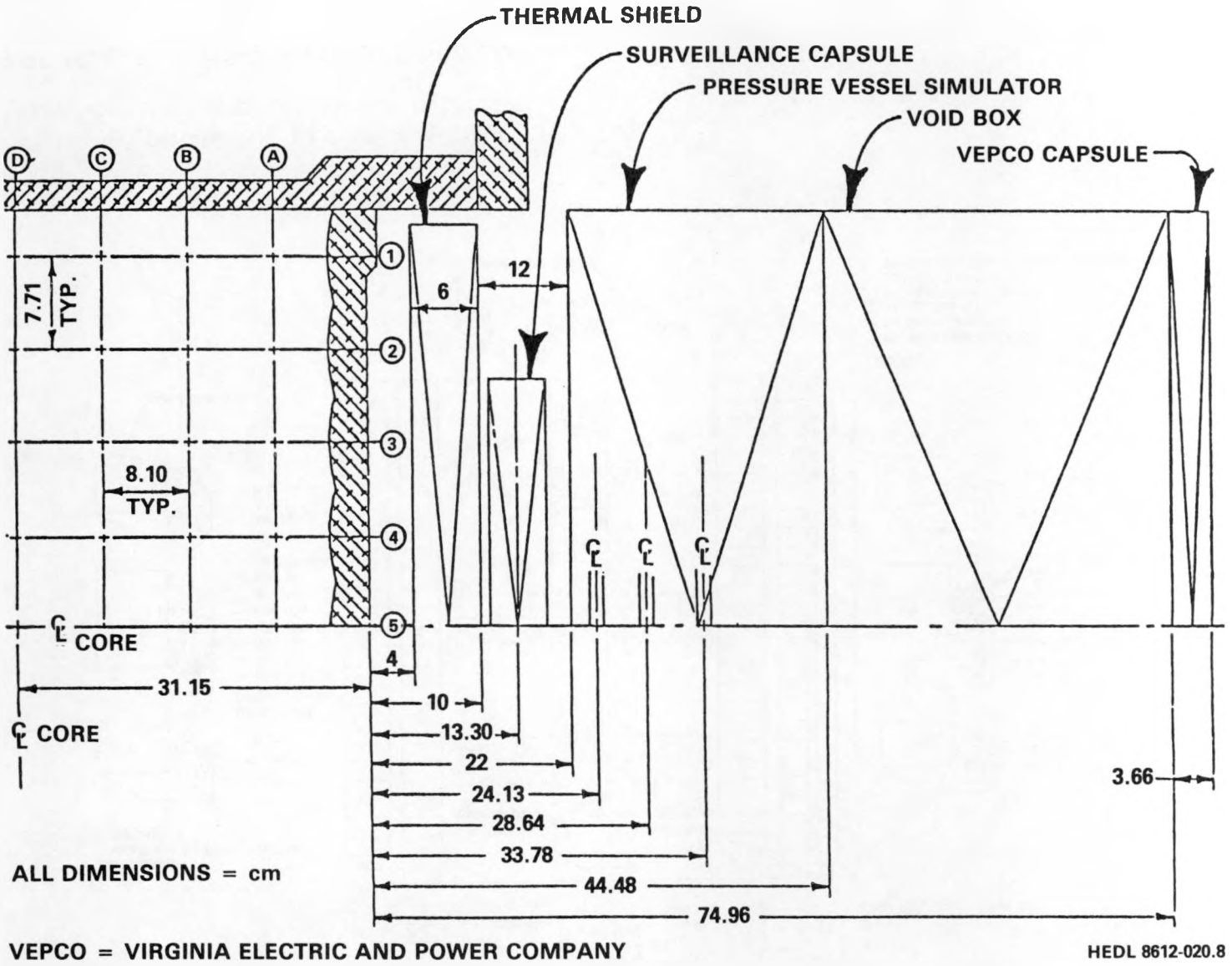

FIGURE HEDL-73. ORR-SDMF 4/12 Configuration (SSC-1).

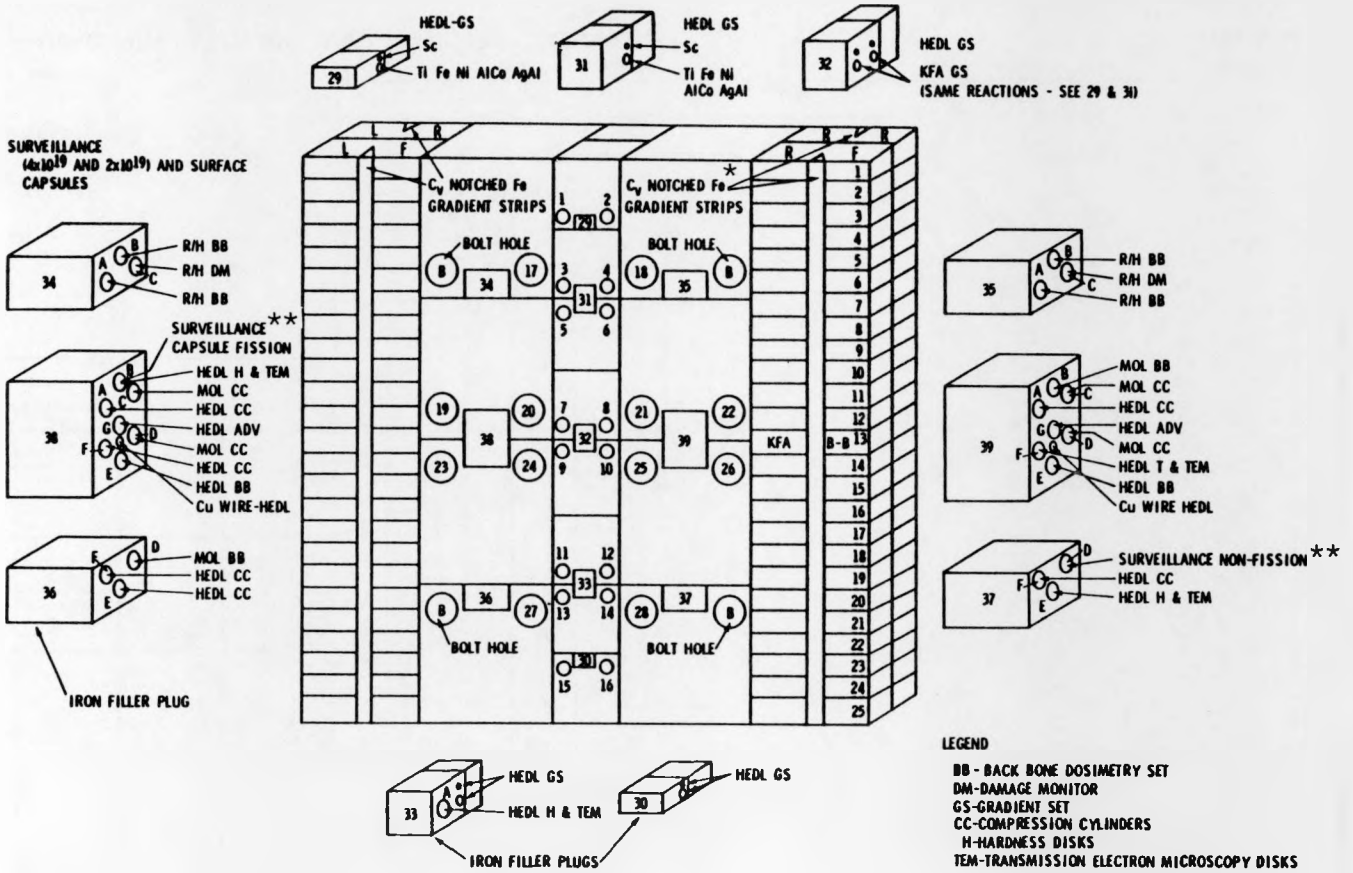

*Fe wire ∿0.010-in. OD placed in ∿0.020 OD SS Tubing.
**Interlaboratory comparison dosimeters.

FIGURE HEDL-74. SSC-1 Specimen Configuration.

These normalization factors were determined to an accuracy of better than 1.5% by counting at HEDL.

In addition to the dosimeter sets, laboratory participants were provided all basic information concerning the dosimetry materials, as well as the irradiation information provided by ORNL to allow calculations of both absolute specific activities and reaction rates. These data included the individual dosimetry "as-built" sheets (describing materials, form, and encapsulation), dosimeter (QA) information (Table HEDL-43), and the individual location and time-history information (Table HEDL-44).

2.3 RM-III -- The 18-Day High-Power Experiment

For the RM-III experiment, different sources of RM materials were employed. AERE and Rolls-Royce and Associates (RR&A, Derby, UK) supplied ORNL with stainless steel capsules containing Fe, Cu, Ti, Ni, Nb, and Co/Al detectors together with some prototype sapphire damage dosimeters. SCK/CEN Mol supplied ORNL with interlaboratory steel and gadolinium capsules and with different sets of foils. The final mounting of the SCK/CEN capsules was done at ORNL. Each capsule contained 6 Ag/Al, 6 Co/Al, 6 Nb, 6 Fe, 6 Ti, 6 Ni, and 2 Cu foils. The gadolinium capsules were filled by ORNL with fission detectors supplied by HEDL.

These AERE/RR&A and SCK/CEN capsules were located in the PSF 4/12 configuration according to the specifications given in Table HEDL-45. Table HEDL-45 considers only those RM capsules that were afterwards used for interlaboratory comparisons by the European laboratories and HEDL.

Table HEDL-46 provides detailed irradiation histories for each RM capsule. Because of loading and unloading procedures, the irradiation interval was somewhat different for RM capsules at these different locations.

After irradiation, the interlaboratory capsules were dismantled at ORNL. Part of the interlaboratory capsule content was sent to SCK/CEN Mol, the remaining part being set to HEDL. SCK/CEN provided afterwards ECN-Petten and PTB-Braunschweig each with a detector set of each irradiation location. All detectors were counted by SCK/CEN before shipment to ECN and PTB.

The AERE/RR&A capsules were dismantled by AERE-Harwell, and RM dosimeters from these capsules were counted at both AERE-Harwell and AEE-Winfrith.

The Cu foils of the interlaboratory capsules were sent by SCK/CEN in a round robin to all European participants.

3.0 Interlaboratory Comparisons of RM Dosimetry

3.1 Comparison of RM Results from Irradiations RM-I and RM-II

In the RM-I and RM-II experiments all participating laboratories used high-resolution Ge or GeLi detectors in conjunction with 2048 to 8196 multichannel analyzer systems for analysis of the dosimeter gamma spectra. A few of the participants also analyzed low-activity reactions [e.g., $^{63}Cu(n,\alpha)$

TABLE HEDL-43

DOSIMETRY FOIL QA DATA

Dosimeter	Form	ρ	Batch	Target Element[a,b] (wt.%)	Isotopic Wt. % [a,b] 233	234	235	236	237	238	239
^{235}U	18.6 mil UO_2 Wire	8.68	264C	87.97	<0.005	0.034(1)	99.89(1)	0.025(1)		0.053(2)	
^{238}U	17.5 mil UO_2 Wire	9.62	ES-Z	87.75	<0.001	<0.001	0.0012(1)	<0.001		99.999(1)	
^{237}Np	19.7 mil NpO_2 Wire	4.92	HP-24	87.4			<0.0005	<0.0005	99.99(1)	≤0.003	≤0.003

The above foils are encapsulated in 0.035" OD vanadium capsules (~40 ppm Ta impurity) wall thickness ~0.006".

Capsule lengths are: ^{235}U - 0.190", ^{238}U - 0.310", ^{237}Np - 0.340".

Dosimeter	Form	Batch	Isotopic	Target Element and Impurity Content (Wt.%) Ni	Fe	Cu	Ti	Co	Al	Ag	Cr	Mg	Si	Mn
Ni[a]	20 mil Wire (0.51 mm)	S.E.	Natural	Balance	<0.0003			<0.0001		<0.0001		<0.0002	<0.0003	
Fe[c]	20 mil Wire	2	"	0.0041	Balance			<0.0058			0.0018			
Cu[a,d]	20 mil Wire	CPO 3054	"			99.999		<0.0003		0.0002		0.0001	0.0001	
Ti[a]	20 mil Wire	139 W	"		0.008	0.001	99.917		0.0001		0.003	0.001	0.005	0.02
Co/Al[a]	20 mil Wire	SRM 953	"					0.116	Balance					

(a) Elemental, isotopic and/or impurity analysis provided by vendor. Assigned errors, i.e. (1), represents value error in the last significant figures.
(b) QA also performed at HEDL. Values supplied by ORNL were confirmed within the error assignments.
(c) Impurity analysis performed at HEDL utilizing activation analysis. Analysis was not made for impurity products with t 1/2 <~2 hr.
(d) Co analysis was made at HEDL by spark source mass spectrometry.

TABLE HEDL-44

IRRADIATION HISTORY AND LOCATION

FIRST ORR-SDMF IRRADIATION
(Perturbation Experiment)

Start of Irradiation	1530 EST	1/31/80
End of Irradiation	1530 EST	2/9/80
Total Duration		9.00 days
Nominal Reactor Power		30 MW

Irradiation can be treated as a square wave function.

Sample Locations

X coordinate: TSB - 101.6 mm South of Core C_L

PVS - 101.6 mm North of Core C_L

Y coordinate: Referenced to ORR Core Al window:

TSB - 112.7 mm

PVS - 207.3 mm

Z coordinate: Approximate location referenced between Reference Core C_L (maximum flux) rather than actual Core C_L and approximate location of mid-point of each replicate sample group. Actual sample position depends on sample location within set and adjustments will be made later if required.

Gadolinium Covered Capsules: HF-1, HF-2, HF-3, HF-4, HNF-1, HNF-2

Bare Capsules: HF-5, HF-6, HNF-3, HNF-4

SECOND ORR-SDMF IRRADIATION
(SSC-1 Experiment)

Inserted	Retracted or ORR Down
April 30, 1980 13:34	May 8, 1980 7:00
May 8, 1980 16:43	May 14, 1980 13:30
May 16, 1980 9:67	May 21, 1980 2:17
May 22, 1980 10:49	June 6, 1980 24:00
June 12, 1980 9:20	June 23, 1980 12:53

(All times Eastern Daylight Time)

Nominal Reactor Power 30MW

Sample Locations

X coordinate: HSF 38B 49.9 mm South of Core C_L

HSNF 37D 47.2 mm North of Core C_L

(individual dosimeter locations vary from this mid point location)

Y coordinate: Referenced to ORR Al window

HSF 38B 133.0 mm

(individual dosimeters may vary by ± 1.1 mm)

HSNF 37D 139.9 mm

Z coordinate: Referenced to Reference Core C_L (maximum flux) rather than actual Core C_L and mid point of each capsule. Actual position of individual HSF samples may vary by ± 1.1 mm

HSF 38B 7.9 mm

HSNF 37D -67.5 mm

TABLE HEDL-45

LOCATION OF RM CAPSULES IN IRRADIATION RM-III

IRRADIATION LOCATION	SAMPLE	AXIAL HEIGHT ABOVE MIDPLANE (mm)
SSC	INTERLABORATORY CAPSULE	- 51
	AERE/RR & A CAPSULE	- 3.5
1/4 T	INTERLABORATORY CAPSULE	- 75
	AERE/RR & A CAPSULE	-122
	FISSION DETECTORS	0
1/2 T	INTERLABORATORY CAPSULE	- 75
	AERE/RR & A CAPSULE	-122
3/4 T	INTERLABORATORY CAPSULE	- 75
	AERE/RR & A CAPSULE	-122

TABLE HEDL-46

IRRADIATION HISTORIES FOR THE 18-DAY HIGH-POWER RUN (RM-III)

LOCATION	BEGIN EXPOSURE (LOCAL TIME)	END EXPOSURE (LOCAL TIME)	TOTAL IRRADIATION TIME (s)	EFFECTIVE IRRADIATION TIME AT 30 MW (s)
SSC	OCT.27,1979 14h26	NOV.14,1979 8h55	$1.5377\ 10^6$	$1.5105\ 10^6$
1/4 T	OCT.27,1979 14h26	NOV.14,1979 8h43	$1.5370\ 10^6$	$1.5097\ 10^6$
1/2 T	OCT.27,1979 21h11	NOV.14,1979 8h55	$1.5134\ 10^6$	$1.4902\ 10^6$
3/4 T	OCT.27,1979 21h18	NOV.14,1979 8h55	$1.5130\ 10^6$	$1.4898\ 10^6$

^{60}Co] using NaI(Tl) detectors. All nonfissile dosimeters were analyzed nondestructively, but some of the participating laboratories destructively analyzed the fissionable dosimeters in accordance with their routine surveillance of the participants (because of the much higher activities of some of the dosimeters than the routine surveillance sample activities normally encountered).

An initial review of the individual preliminary results from RM-I and RM-II was conducted. Outlying values were anticipated, but consistent discrepancies as large as 60% were observed. Individual discussions were held with each laboratory participant concerning these data and the possible discrepancies that existed. Analytical and calibration techniques, nuclear parameters being used, and corrections applied to the observed counting data were reviewed. In almost all cases, one or more problems were identified, though some were relatively insignificant. Some of the more important problems identified, and their effects on the reported RM data, are shown in Table HEDL-47.

Final reported specific activities for the RM-I irradiation calculated to end of irradiation (EOI) are listed in Tables HEDL-48 and -49 (not all participants reported all reaction rates). To determine the range of values that might be expected from the laboratories performing the analysis, the participants' data were first scaled by the individual HEDL normalization factor. The average value of this normalized set of data was obtained. Maximum and minimum values were then determined relative to this average. The maximum-to-minimum ratio is used as a range evaluation and is presented in Table HEDL-50. Since absolute HEDL values are not given in Table HEDL-50, the deviation between individual participant-measured activities and HEDL-measured activities are presented separately in Table HEDL-51.

A comparison of the relative ratios listed in the vertical columns of Table HEDL-51 demonstrates whether a particular laboratory appears to be consistently biased. It would appear that Laboratory B is generally biased low by ∿6% to 10% for nonfissile RM dosimeters. However laboratory C appears to be generally biased high by ∿4% to 7% for nonfissile RM dosimeters, and at the same time Laboratory C appears to be generally biased low by ∿5% to 10% for fissile RM dosimeters. By reading across this table, one can observe whether an apparent bias exists in the analysis of a particular dosimeter reaction. It appears that the HEDL analysis of both the $^{63}Cu(n,\alpha)$ and $^{46}Ti(n,p)$ reactions appear biased low by ∿2% relative to the other participants.

The RM results from participant laboratories from irradiation RM-II are given in Tables HEDL-52 and HEDL-53. Unfortunately, only three of the six participating laboratories reported results. Two separate sets of results are reported by Laboratory C from measurements performed by two different individuals in Laboratory C. Since a difference was observed, both sets of results were reported and are treated separately in the comparisons. It was anticipated that the RM-II test would show improved correlations; and indeed the deviation relative to HEDL (Table HEDL-54) indicate better agreement. All comparisons with two of the three reporting participants fall within ∿±4%. Laboratory C still appears to be biased, though this time a low bias

TABLE HEDL-47

IDENTIFIED PROBLEMS AND ESTIMATED EFFECT

	Problem	Effect on Data
1.	Faulty calibration standards	10% to 100% depending on energy region
2.	Faulty nuclear parameter data	0% to 2%, depending on specific results
3.	No correction for external or self shielding	0% to 4% depending upon reaction and analysis technique
4.	Error in conversion of specific activity to reaction rate	0% on specific activity up to 4% on specific reaction rates
5.	Coincidence loss corrections for high count rate samples not applied	Estimated at up to 6%

is indicated for the nonfissile RM dosimeters, while the RM-I irradiation indicates a high bias.

3.2 Comparison of RM Results from Irradiation RM-III

RM dosimetry results (Fa80a) for irradiation RM-III (specific activities at the end of irradiation) from the participating laboratories are shown in Table HEDL-55. All these RM results have been normalized to the CEN/SCK RM data. In addition, all RM results were corrected for the axial fast neutron intensity gradient.

An empirical correction for this axial gradient was determined using an axial array of Ni RM dosimeters at each of the RM-III irradiation positions, namely the SSC, 1/4-T, 1/2-T, and 3/4-T locations of the 4/12 configuration in the PSF.

These axial Ni RM results were fit by a cosine buckling term of the form $\cos[B(y - C)]$, where y is axial distance in mm from reactor midplane. Table HEDL-56 summarizes the B and C parameters obtained from these fits. The axial distribution becomes flatter when penetrating into the vessel wall, while the axial maximum shifts from negative to positive values.

Small radial flux corrections were applied to the detectors from the RM-III interlaboratory capsules, since the detectors in these capsules were not all positioned on the same vertical axis. Somewhat different decay scheme parameters were used by the RM-III participants. In order to intercompare results, all reported data were rescaled using decay scheme parameters taken from Zijp and Baard (Zi79).

TABLE HEDL-48

INTERLABORATORY COMPARISON OF RADIOMETRIC (RM) DATA
FROM IRRADIATION RM-I
[Nonfission Foil Sets (DPS/mg @ EOI)][a]

Dosimeter Reaction	Set Laboratory	HNF-1 (E+5)		HNF-3 (E+5)		HNF-2 (E+4)		HNF-4 (E+4)	
$^{58}Ni(n,p)$	A	4.60	4.493	4.26	4.170	8.17	7.984	7.73	7.480
	B	4.18	4.497	3.90	4.164	7.30	7.986	6.78	7.470
	C	4.33	4.510	4.04	4.192	7.98	7.968	7.43	7.493
	D	4.58	4.486	4.22	4.163	7.97	8.045	7.50	7.465
	E[b]	4.44	4.512	4.05	4.158	7.79	8.016	7.32	7.472
	F	4.430	4.510	4.187	4.177	8.243	8.027	7.728	7.438
		(E+3)		(E+3)		(E+3)		(E+3)	
$^{46}Ti(n,p)$	A	5.72	5.59[c]	5.43	5.371	1.22	1.154	1.17	1.119
	B	5.00	5.59	4.65	5.40	1.07	1.157	1.11	1.125
	C	5.75	5.55	5.55	5.30	1.24	1.159	1.21	1.122
	D	5.68	5.60	5.49	5.37	1.23	1.163	1.17	1.119
	E[b]	5.56	5.60	5.23	5.343	1.16	1.170	1.11	1.107
	F	5.677	5.557	5.427	5.33	1.206	1.141	1.175	1.130
		(E+1)		(E+1)		(E+1)		(E+1)	
$^{63}Cu(n,\alpha)$	A	8.19	8.048	7.89	7.688	1.90	1.880	1.91	1.825
	B	7.98	8.166	7.63	7.509	1.88	1.854	1.82	1.787
	C	8.56	8.031	8.11	7.870	2.02	1.864	1.90	1.784
	D	8.06	8.069	7.87	7.730	1.92	1.864	1.82	1.814
	E[b]	7.82	8.002	7.56	7.714	1.84	1.851	1.78	1.819
	F	8.444	7.815	7.946	7.789	1.994	1.886	1.935	1.811
		(E+3)		(E+3)		(E+3)		(E+3)	
$^{54}Fe(n,p)$	A	6.86	6.659	6.67	6.633	1.26	1.233	1.23	1.155
	B	6.27	6.692	5.93	6.608	1.15	1.245	1.08	1.168
	C	6.89	6.758	6.58	6.573	1.27	1.248	1.25	1.194
	D	6.79	6.646	6.45	6.600	1.25	1.234	1.20	1.182
	E[b]	6.70	6.674	6.40	6.622	1.21	1.260	1.18	1.172
	F	6.650	6.628	6.289	6.560	1.242	1.239	1.160	1.183
		(E+3)		(E+4)		(E+3)		(E+4)	
$^{58}FE(n,\gamma)$	A	6.45	6.352	6.71	6.688	8.32	8.746	2.29	2.246
	B		6.530		6.630		9.067		2.241
	C		6.569		6.627		9.104		2.240
	D		6.517		6.654		8.950		2.244
	E[b]	6.62	6.542	6.62	6.674	8.78	9.049	2.32	2.247
	F		6.610		6.540		8.948		2.249

(a) The first column under each heading are those data reported by the participants, with any subsequent corrections made by HEDL. The second column of data is the corresponding HEDL analysis. Results are to exponent in parenthesis [e.g., 4.60 (E+5) reads 4.60×10^5].

(b) The participant reported the specific activity as per mg target isotope. For comparison with the other reported values, the reported numbers were multiplied by the atom fraction used by the participant.

(c) Only two absolute counts were made on these sets. All of the samples in these sets were counted on a non-calibrated system for determination of the relative ratios. Correlations were made between those samples counted on both systems and absolute values were than calculated for the remaining samples in the sets.

TABLE HEDL-49

INTERLABORATORY COMPARISON OF RADIOMETRIC (RM) DATA
FROM IRRADIATION RM-I
[Fission Foil Sets (DPS/mg @ EOI)]

Dosimeter Set	Laboratory	$^{235}U(n,f)$ (a) ^{140}Ba (E+5)		^{103}Ru (E+5)		^{95}Zr (E+5)		^{137}Cs (E+3)	$^{59}Co(n,\gamma)$ (E+5)	
HF-3	A	25.2	25.20	51.3	48.73	64.0	63.52		34.0	33.06
	B (b)		25.82		49.71	64.5	64.50		32.3	32.81
	C (b)		24.58	40.9	47.06	53.4	61.73	31.6	35.5	33.04
	D (c)	24.4	25.51	46.9	48.44	67.0	63.81	35.5	31.6	31.26
	E	23.2	24.85	48.1	47.68	60.6	62.37	35.4	33.9	33.29
	F		24.94		47.95		62.92		30.6	30.93
HF-5	A	361	329.8	651	601.3	858	812.0		172	171.9
	B (b)		326.5		588.7	668	780.4		161	173.9
	C (b)		330.9	640	602.6	875	800.6	470	184	173.0
	D (c)	294	324.5	528	580.2	788	770.6	535	168	169.7
	E	321	335.3	605	595.8	787	810.8	462	165	167.7
	F		327.2		586.1		781.9		172	172.9
HF-4	A	3.38	3.409	6.72	6.505	8.49	8.699		4.08	3.989
	B (b)		3.555		6.583	8.50	9.101		3.90	3.973
	C (b)		3.497	6.15	6.521	8.02	9.059	4.57	4.33	4.019
	D (c)	3.32	3.586	6.47	6.641	9.25	9.259	4.69	4.04	3.978
	E	3.37	3.561	6.77	6.562	8.39	9.155	4.87	3.98	3.871
	F		3.670		6.666		9.322		4.110	4.058
HF-6	A	123.	126.7	228	214.3	304	294.7		52.9	51.89
	B (b)		121.9		202.9	267	274.9		48.8	53.75
	C (b)		121.9		204.0	250	277.4	156	58.0	54.33
	D (c)	106	124.4	193	210.2	290	285.6	152	57.2	55.15
	E	111	127.7	215	212.9	278	293.3	167	52.8	53.06
	F		130.3		214.7		296.8		58.8	57.45

Dosimeter Set	Laboratory	$^{237}Np(n,f)$ (E+5)		(E+4)		(E+4)		(E+2)
HF-1	A	11.2	11.08	44.5	43.18	27.1	27.27	
	B (b)		11.80		44.12	30.7	27.76	
	C (b)		11.67	39.6	43.10	24.8	27.26	16.9
	D	11.0	11.75	41.8	43.71	28.8	27.66	18.6
	E	10.3	11.61	43.2	43.60	26.1	27.30	17.6
	F	10.5	11.12	39.7	41.38	25.6	25.98	18.5
HF-2	A	1.35	1.307	5.24	5.033	3.23	3.167	
	B (b)		1.375		5.032	3.41	3.236	
	C (b)		1.406	4.79	5.147	3.16	3.318	2.16
	D	1.31	1.322	5.12	4.975	3.52	3.185	2.00
	E	1.20	1.382	4.99	5.159	3.12	3.210	2.13
	F	1.27	1.310	4.92	5.040	3.18	3.220	2.27

Dosimeter Set	Laboratory	$^{238}U(n,f)$ (E+4)		(E+4)		(E+4)		(E+1)
HF-1	A	17.4	16.90	7.06	6.693	35.5	34.98	
	B (b)		16.98		6.823	35.9	34.99	
	C (b)		17.67	6.71	7.011	34.4	36.52	24.8
	D	16.8	16.46	6.46	6.587	36.3	33.44	23.6
	E	16.0	16.95	6.79	6.759	34.2	35.10	25.8
	F	17.1	17.16	6.51	6.865	34.1	35.64	25.4
HF-2	A	2.79	2.722	1.11	1.070	0.572	0.5812	
	B (b)		2.740		1.056	0.596	0.5708	
	C (b)		2.695	0.922	1.033	0.558	0.5802	3.74
	D	2.65	2.792	1.08	1.057	0.616	0.5847	4.15
	E	2.49	2.679	1.01	1.036	0.530	0.5676	3.81
	F	2.74	2.777	1.04	1.059	0.555	0.5750	4.02

(a) The first column under each heading are those data reported by the participant with any necessary corrections. The second column is the corresponding HEDL data. The value in parens (E+5) is the exponent for the data following it ((E+5) 25.2 should read 25.2×10^5).

(b) Corrections were made for elemental and isotopic composition.

(c) Correction made for Co alloy content

TABLE HEDL-50

RANGE EVALUATION (MAXIMA/MINIMA) OF RESULTS FROM IRRADIATION RM-I

Sensor[b] Set No.	$^{58}Ni(n,p)$ Ratio 1	Ratio 2	Ratio 3	Labs	$^{46}Ti(n,p)$ Ratio 1	Ratio 2	Ratio 3	Labs	$^{63}Cu(n,\alpha)$ Ratio 1	Ratio 2	Ratio 3	Labs	$^{54}Fe(n,p)$ Ratio 1	Ratio 2	Ratio 3	Labs
HNF - 1	1.14 C/B	1.10 D/B	1.06 D/C	6	1.39 C/B	1.16 C/B	1.04 C/E	6	1.11 F/B	---	1.09 F/E	6	1.38 C/B	1.11 C/B	1.04 C/F	6
HNF - 3	1.28 C/B	1.09 A/B	1.05 A/C	6	1.48 C/B	1.21 C/B	1.04 C/A	6	1.05 C/E	1.06 C/F	---	6	1.27 C/B	1.10 A/B	1.04 A/F	6
HNF - 2	1.25 C/B	1.13 F/B	1.06 F/E	6	1.42 C/B	1.19 C/B	1.08 C/E	6	1.06 C/E	1.09 C/E	---	6	1.46 C/B	1.12 A/B	1.06 A/E	6
HNF - 4	1.28 C/B	1.14 F/B	1.06 F/E	6	1.41 C/B	1.09 C/B	1.08 C/E	6	1.08 C/E	1.09 F/E	---	6	1.43 C/B	1.13 C/B	1.04 C/F	6

	$^{58}Fe(n,\gamma)$ Ratio 1	Ratio 2	Ratio 3	Labs
HNF - 1	1.15 C/A	1.03 E/A	1.03 E/A	3[c]
HNF - 3	1.02 C/E	1.02 A/E	1.02 A/E	3
HNF - 2	1.23 C/A	1.04 E/A	1.04 E/A	3
HNF - 4	1.12 C/E	1.01 A/E	1.01 A/E	3

Sensor Set No.	$^{59}Co/Al(n,\gamma)$ Ratio 1	Ratio 2	Ratio 3	Labs
HF - 3	1.15 C/B	1.09 C/B	1.06 C/F	6
HF - 5	1.15 C/B	1.11 C/B	1.04 C/D	6
HF - 4	1.06 F/B	1.09 C/B	1.05 C/F	6
HF - 6	1.23 C/B	1.17 C/B	1.07 C/E	6

	$^{235}U(n,f)^{140}Ba$ Ratio 1	Ratio 2	Ratio 3	Labs	$^{235}U(n,f)^{103}Ru$ Ratio 1	Ratio 2	Ratio 3	Labs	$^{235}U(n,f)^{95}Zr$ Ratio 1	Ratio 2	Ratio 3	Labs	$^{235}U(n,f)^{137}Cs$ Ratio 1	Ratio 2	Ratio 3	Labs
HF - 3	1.06 A/E	---	---	3	1.19 C/D	1.22 A/C	1.08 A/D	4	1.09 D/C	1.22 D/C	1.08 D/E	5	---	1.11 E/C	---	3
HF - 5	1.19 A/D	---	---	3	1.73 C/D	1.19 C/D	1.07 C/E	4	1.51 C/B	1.29 C/B	1.12 C/E	5	---	1.31 C/D	---	3
HF - 4	1.05 A/D	---	---	3	1.30 C/D	1.09 A/C	---	4	1.13 D/C	1.14 D/C	1.07 A/C	5	---	1.05 F/C	---	3
HF - 6	1.13 A/D	---	---	3	1.43 C/D	1.14 A/D	---	4	1.15 C/E	1.11 A/C	1.07 A/B	5	---	1.07 E/D	---	3

	$^{237}Np(n,f)^{140}Ba$ Ratio 1	Ratio 2	Ratio 3	Labs	$^{237}Np(n,f)^{103}Ru$ Ratio 1	Ratio 2	Ratio 3	Labs	$^{237}Np(n,f)^{95}Zr$ Ratio 1	Ratio 2	Ratio 3	Labs	$^{237}U(n,f)^{137}Cs$ Ratio 1	Ratio 2	Ratio 3	Labs
HF - 1	1.10 A/F	---	1.04 A/D	4	1.37 C/F	1.11 A/C	---	5	1.16 A/E	1.21 B/C	1.16 A/E	6	---	1.09 D/C	---	4
HF - 2	1.13 A/E	---	---	4	1.27 C/F	1.12 A/F	---	5	1.14 D/F	---	---	6	---	1.12 F/D	---	4

	$^{238}U(n,f)^{140}Ba$ Ratio 1	Ratio 2	Ratio 3	Labs	$^{238}U(n,f)^{103}Ru$ Ratio 1	Ratio 2	Ratio 3	Labs	$^{238}U(n,f)^{95}Zr$ Ratio 1	Ratio 2	Ratio 3	Labs	$^{238}U(n,f)^{137}Cs$ Ratio 1	Ratio 2	Ratio 3	Labs
HF - 1	1.09 A/D	---	1.04 D/E	4	1.44 C/F	1.11 A/F	---	5	1.16 C/F	1.13 D/C	1.06 B/F	6	---	1.08 E/C	---	4
HF - 2	1.09 A/E	---	---	4	1.27 C/F	1.07 A/E	---	5	1.13 D/E	---	---	6	---	1.06 D/E	---	4

(a) Four vendors and two service laboratories participated in this test. All laboratories remain anonymous for these intercomparisons and are identified only as Laboratories A, B, C, D, E and F.[6] The table evaluation shows the present laboratory-to-laboratory comparative status but also shows the improvement in the data comparisons (Ratios 2 and 3) as a result of interim evaluations and discussions with participants. Ratio 2 was obtained after discussions with participants and subsequent reworking of data by participants. For Ratio 3, and for the case of nonfissile sensors, the results from Laboratory B appeared to be consistently biased low and were, therefore, not used. In the case of the fissile sensors, if a participant appeared to be definitely biased, those results were not used in Ratio 3.

(b) HNF-X and HF-X are sensor set identification numbers for specific perturbed locations in 1-in. x 1-in. stainless steel simulated surveillance capsules for this first PSF-SDMF test.

(c) Results for the $^{58}Fe(n,\gamma)$ reaction were not reported by one laboratory after preliminary recalibration of their counting system.

TABLE HEDL-51

DEVIATIONS OF RM RESULTS FROM IRRADIATION RM-I*

Set ID	Reaction	LABORATORY A	B	C	D	E	F
HNF-1	$^{58}Ni(n,p)$	2.38	- 7.05	-3.99	2.10	-1.60	-1.77
-3		2.16	- 6.34	-3.63	1.37	-2.60	0.24
-2		2.33	- 8.59	0.15	-0.93	-2.82	2.69
-4		3.34	- 9.24	-0.84	0.47	-2.03	3.90
HNF-1	$^{46}Ti(n,p)$	2.33	-10.6	3.60	1.43	-0.71	2.16
-3		1.10	-13.9	4.72	2.23	-2.11	1.82
-2		5.72	-7.52	6.98	5.76	-0.85	5.26
-4		4.56	-1.33	7.84	4.56	0.27	3.98
HNF-1	$^{63}Cu(n,\alpha)$	1.76	-3.38	8.59	-1.12	-2.27	8.05
-3		2.63	1.61	3.05	1.81	-2.00	2.01
-2		1.06	1.40	8.37	3.00	0.59	5.73
-4		4.66	1.85	6.50	2.00	2.14	6.85
HNF-1	$^{54}Fe(n,p)$	3.02	-6.31	1.95	-3.73	0.39	-5.37
-3		0.56	-10.26	0.11	-2.27	-3.35	-4.13
-2		2.19	-7.63	1.76	1.30	-3.96	0.24
-4		6.49	-7.53	4.69	1.52	0.68	-1.94
HNF-1	$^{58}Fe(n,\gamma)$	1.54				1.19	
-3		3.29				0.81	
-2		-4.87				-2.97	
-4		1.96				3.25	
HNF-3	$^{59}Co(n,\gamma)$	2.84	-1.55	7.45	1.09	1.83	-1.07
-5		0.06	-7.42	6.36	-1.00	-1.61	-0.52
-4		2.28	-1.84	7.74	1.56	2.82	1.28
-6		1.95	-9.21	6.76	3.72	-0.49	2.35

Set ID	Reaction	LABORATORY A	B	C	D	E	F
HF-3	$^{235}U(n,f)^{140}Ba$	0.00			- 4.35	- 6.68	
HF-5		9.46			- 9.40	- 4.26	
HF-4		9.39			- 7.42	- 5.36	
HF-6		-2.92			-14.79	-13.08	
HF-3	$^{235}U(n,f)^{103}Ru$	5.27		-13.09	- 3.18	0.88	
HF-5		8.27		6.21	- 9.00	1.54	
HF-4		3.31		- 5.59	- 2.57	3.17	
HF-6		6.39		- 6.37	- 8.18	0.99	
HF-3	$^{235}U(n,f)^{95}Zr$	0.76	0.00	-13.49	4.99	- 2.84	
HF-5		5.67	-14.40	9.29	2.26	- 3.31	
HF-4		-2.40	- 6.49	-11.47	- 0.10	- 8.36	
HF-6		3.16	- 1.78	- 6.99	1.54	- 5.22	
HF-1	$^{237}Np(n,f)^{140}Ba$	1.27			- 6.38	-11.28	-5.58
HF-2		3.29			- 0.91	-13.29	-3.05
HF-1	$^{237}Np(n,f)^{103}Ru$	3.06		-31.26	- 4.37	- 0.92	-4.06
HF-2		4.11		- 6.94	2.91	- 3.28	-2.38
HF-1	$^{237}Np(n,f)^{95}Zr$	-0.22	10.59	- 9.06	4.12	- 4.40	-1.46
HF-2		1.99	5.38	- 4.76	10.83	- 2.80	-1.24
HF-1	$^{238}U(n,f)^{140}Ba$	2.96			- 2.19	- 5.60	-0.35
HF-2		0.65			- 0.40	- 7.05	-1.33
HF-1	$^{238}U(n,f)^{103}Ru$	5.48		- 4.29	- 1.93	0.46	-5.17
HF-2		3.74		1.65	2.08	- 2.51	-1.79
HF-1	$^{238}U(n,f)^{95}Zr$	1.72	2.60	- 5.81	8.55	- 2.56	1.37
HF-2		-1.58	4.41	- 3.83	5.35	- 6.62	-3.48

*The deviation cited is (X/HEDL-1) given in percent, where X represents the participant laboratory RM result and HEDL represents the RM result obtained by HEDL.

TABLE HEDL-52

INTERLABORATORY COMPARISON OF RADIOMETRIC (RM) DATA FROM IRRADIATION RM-II
[Fission Foil Sets (DPS/mg @ EOI)]*

Dosimeter Set	Laboratory	$^{238}U(n,f)$ $^{140}Ba(n,f)$ (E+5)	$^{103}Ru(n,f)$ (E+5)		$^{95}Zr(n,f)$ (E+5)		$^{137}Cs(n,f)$ (E+2)	
HNF-38B	A	3.064	2.05	2.003	1.15	1.159		10.95
	B	3.153		2.053		1.207		10.92
	C-1**	2.863	1.74	1.975	1.01	1.142	9.40	11.30
	C-2		1.80		1.05	(1.16)	9.68	(10.4)
	D	3.093		1.998		1.163	10.3	10.16
	E	3.089		2.034		1.183		10.96
	F	2.989		2.022		1.174		10.50

		$^{237}Np(n,f)$ $^{140}Ba(n,f)$ (E+6)	$^{103}Ru(n,f)$ (E+5)		$^{95}Zr(n,f)$ (E+5)		$^{137}Cs(n,f)$ (E+3)	
HNF-38B	A	2.017	1.36	1.315	9.42	9.571		8.368
	B	1.956		1.287		9.375		8.156
	C-1**	2.097	1.22	1.351	8.72	9.793	7.82	8.484
	C-2		1.21		8.65	(9.24)	7.73	(8.37)
	D	2.005		1.302		9.431	8.31	8.169
	E	2.081		1.310		9.456		8.591
	F	2.088		1.332		9.602		9.308

*The first column under each heading lists data reported by the participants, the second column lists HEDL data. Result exponents are given in parens [e.g., 3.064 (E+5) should read 3.064×10^5].

**Two individuals ran separate analyses for this laboratory and both values are reported. The values in parens are from recent counts.

TABLE HEDL-53

INTERLABORATORY COMPARISON OF RADIOMETRIC (RM) DATA FROM IRRADIATION RM-II
[Nonfission Foil Sets (DPS/mg @ EOI)]*

Dosimeter Set	Laboratory	Reaction					
		$^{58}Ni(n,p)$ (E+6)		$^{63}Cu(n,\alpha)$ (E+2)		$^{54}Fe(n,p)$ (E+4)	
HSNF	A	1.16	1.144	2.41	2.389	2.06	2.020
	B		1.137		2.377		2.016
	C-1**	1.03	1.138	2.31	2.399	1.87	2.019
	C-2	1.06		2.35		1.95	
	D	1.13	1.141	2.43	2.386	2.01	1.995
	E		1.141		2.400		2.011
	F		1.132		2.384		2.003

Dosimeter Set	Laboratory	$^{58}Fe(n,\gamma)$ (E+6)		$^{59}Co(n,\gamma)$ (E+2)	
HSNF	A	1.82	1.818	1.40	1.382
	B		1.825		1.381
	C-1**	1.79	1.836	1.33	1.390
	C-2	1.84		1.37	
	D	1.84	1.801	1.42	1.397
	E		1.828		1.383
	F		1.836		1.834

*The first column under each heading lists data reported by the participants, the second column lists HEDL data. The number in parens is the exponent for those numbers following [e.g., 1.16 (E+6) should read 1.16×10^6].

**Two individuals ran separate analyses for this laboratory and both values are reported.

TABLE HEDL-54

DEVIATIONS OF RM RESULTS FROM IRRADIATION RM-II*

Reaction	Laboratory						
	A	B	C-1	C-2	D	E	F
$^{58}Ni(n,p)$	1.40		-9.57	-6.85	-0.96		
$^{63}Cu(n,\alpha)$	0.88		-3.71	-2.04	1.84		
$^{54}Fe(n,p)$	1.98		-7.38	-3.42	0.75		
$^{58}Fe(n,\gamma)$	0.11		-2.51	0.22	2.17		
$^{59}Co(n,\gamma)$	1.30		-4.32	-1.44	1.65		
$^{237}Np(n,f)^{103}Ru$	3.42		-9.70	-10.4			
^{95}Zr	-1.58		-10.9	-5.6			
^{137}Cs			-7.83	-1.34	1.73		
$^{238}U(n,f)^{103}Ru$	2.09		-11.9	-8.86			
^{95}Zr	-0.78		-11.6	1.58			
^{137}Cs			-16.8	-7.96	1.38		

*The deviation cited is (X/HEDL-1) given in percent, where X represents the participant laboratory RM result and HEDL represents the RM result obtained by HEDL.

TABLE HEDL-55

SPECIFIC ACTIVITIES MEASURED BY THE PARTICIPATING LABORATORIES IN IRRADIATION RM-III

	REACTION	SPECIFIC ACTIVITIES RELATIVE TO SCK/CEN				RECOMMENDED SPECIFIC ACTIVITIES ($Bq\ g^{-1}$)	σ (%)
		INTERLABORATORY CAPSULE		AERE/RR & A CAPSULE (1)			
		ECN	PTB	$(AERE)_1$ (2)	$(AERE)_2$ (2)		
SSC	$^{93}Nb(n,n')$	1.17			1.02	$2.062\ 10^7$	9.0
	$^{58}Ni(n,p)$		1.01	1.09	1.05	$7.242\ 10^8$	3.9
	$^{54}Fe(n,p)$	1.01	1.00	1.07	1.10	$1.103\ 10^7$	4.3
	$^{46}Ti(n,p)$	0.99	1.02	1.12	1.07	$8.508\ 10^6$	5.3
	$^{63}Cu(n,\alpha)$	1.02	1.01	0.99(3) (1.29)	(1.05)	$1.201\ 10^5$	1.4
1/4 T	$^{237}Np(n,f)\ ^{95}Zr$	0.97	0.98			$3.437\ 10^7$	1.6
	$^{237}Np(n,f)\ ^{137}Cs$	0.96	0.98			$2.522\ 10^5$	2.0
	$^{238}U(n,f)\ ^{95}Zr$	0.95	0.98			$3.508\ 10^6$	2.6
	$^{238}U(n,f)\ ^{137}Cs$	0.99	0.97			$2.738\ 10^4$	1.4
	$^{93}Nb(n,n')$				1.00	$1.330\ 10^6$	0.3
	$^{58}Ni(n,p)$	1.00	1.00	1.07	1.03	$4.472\ 10^7$	3.1
	$^{54}Fe(n,p)$	1.00	0.98	1.11	1.09	$6.956\ 10^5$	6.0
	$^{46}Ti(n,p)$	1.00	1.01	1.12	1.04	$5.851\ 10^5$	4.9
	$^{63}Cu(n,\alpha)$	1.01	1.01	1.01(3) (1.15)	(1.08)	$9.206\ 10^3$	0.5
1/2 T	$^{93}Nb(n,n')$				0.85	$6.643\ 10^5$	11.8
	$^{58}Ni(n,p)$	0.99		1.09	1.02	$1.721\ 10^7$	4.4
	$^{54}Fe(n,p)$	0.97	1.00	1.10	1.10	$2.606\ 10^5$	6.0
	$^{46}Ti(n,p)$	0.98	1.02	1.13	1.07	$2.161\ 10^5$	5.8
	$^{63}Cu(n,\alpha)$	1.03	1.02	1.02(3) (1.37)	(1.30)	$3.465\ 10^3$	1.0
3/4 T	$^{93}Nb(n,n')$				0.84	$3.338\ 10^5$	11.9
	$^{58}Ni(n,p)$	1.00	0.99	1.07	1.00	$6.310\ 10^6$	3.3
	$^{54}Fe(n,p)$	1.00	1.00	1.10	1.07	$9.306\ 10^4$	4.7
	$^{46}Ti(n,p)$	0.96	0.98	(0.76)	1.01	$7.566\ 10^4$	2.2
	$^{63}Cu(n,\alpha)$	1.00	1.01	1.02(3) (1.46)	(1.27)	$1.245\ 10^3$	0.9

(1) RR&A: Rolls Royce and Associates.
(2) $(AERE)_1$: Measurements performed at Harwell; $(AERE)_2$: Measurements performed at Winfrith.
(3) Cu foil from interlaboratory capsule.

TABLE HEDL-56

PARAMETERS B AND C OBTAINED FROM FITTING
AXIAL Ni RM DOSIMETRY DATA

IRRADIATION LOCATION	B (mm^{-1})	C (mm)
SSC	$4.42\ 10^{-3}$	- 45.4
1/4 T	$3.34\ 10^{-3}$	- 20.6
1/2 T	$2.82\ 10^{-3}$	- 4.9
3/4 T	$2.80\ 10^{-3}$	3.2

The agreement between SCK/CEN, ECN, and PTB is excellent -- in general, better than 2% for all nonfission detectors and better than 5% for the fission detectors. The agreement between the $(AERE)_1$ and $(AERE)_2$ results is reasonable: the $(AERE)_1$ results are, on the average, 4% to 5% higher than the $(AERE)_2$ results, while the average difference for the Cu detectors is about 10%. The observed differences for $^{93}Nb(n,n')$ are somewhat larger than could be expected, taking into account the results from a recent niobium intercomparison (To82).

The specific activities deduced from the detectors in the AERE/RR&A capsules are systematically higher (except for Nb) than the specific activities deduced from the detectors in the interlaboratory capsules: 5% to 10%, on the average, for the $^{58}Ni(n,p)$, the $^{54}Fe(n,p)$, and the $^{46}Ti(n,p)$ reactions, while a difference of $\sim$25% is noted for $^{63}Cu(n,\alpha)$ reactions. These ^{63}Cu differences are apparently not due to a bias in the calibration of the counting equipment of the participants, since a round robin of Cu detectors of the interlaboratory capsules resulted in an excellent agreement -- better than 3% (see Table HEDL-55). Preliminary investigations indicate also that local fast neutron flux perturbations, created by the dosimetry capsules, can be excluded, so that a major reason for the observed 5% to 10% differences could not be identified. The high specific activities from the $^{63}Cu(n,\alpha)^{60}Co$ reaction in the AERE/RR&A capsules are probably due to Co impurities in the Cu material.

The overall uncertainties on the measured specific activities, as quoted by the different laboratories, are given in Table HEDL-57. The uncertainties are on the order of 1.5% to 3% for most reactions, except 93Nb(n,n').

The recommended specific activities (Table HEDL-55) at the end of the irradiation were calculated by averaging the available results. The Cu results of the AERE/RR&A dosimeter capsules were not considered in the calculation of the recommended specific activities (values given between brackets in Table 55).

TABLE HEDL-57

OVERALL UNCERTAINTIES ON THE MEASURED SPECIFIC ACTIVITIES

REACTION	UNCERTAINTY (1 σ) IN %			
	ECN	PTB	AERE	SCK/CEN
$^{237}Np(n,f)\{^{95}Zr$	2.9	1.7		2.1
$^{237}Np(n,f)\{^{137}Cs$	2.9	1.4		2.0
$^{238}U(n,f)\{^{95}Zr$	2.9	2.5		2.1
$^{238}U(n,f)\{^{137}Cs$	2.9	1.4		2.0
$^{93}Nb(n,n')$	5.6		4.6	4.5
$^{58}Ni(n,p)$	2.6	1.5	3.4	1.9
$^{54}Fe(n,p)$	2.2	1.5	2.4	1.9
$^{46}Ti(n,p)$	2.3	1.5	3.2	1.9
$^{63}Cu(n,\alpha)$	2.7	1.5	3.2	1.9

The results of the thermal dosimeters are not discussed in this paper since they are of less importance to the PCA/PSF program. These thermal RM results were only used to determine minor corrections such as the ^{58}Co and $^{58}Co^{m}$ burnup of the Ni detectors.

4.0 Conclusions

While the agreement among the majority of the laboratories participating in the RM-I and RM-II interlaboratory comparisons is generally satisfactory, with nonfissile dosimeter results generally falling within ±5% and the fissionable dosimeter results falling within ±10%, improvement is still required in order to routinely meet accuracy goals of LWR-PVS surveillance dosimetry. Improved agreement was attained in the RM-III experiment, wherein nonfissile RM monitors generally agreed better than 2% and fission monitors generally agreed to better than 5%. The results obtained from these tests along with the subsequent corrections indicate that a critical review of both analytical and calculational techniques must be conducted on a periodic basis by all of the laboratories. In addition, it is recommended that each laboratory review and utilize, where possible, the appropriate ASTM Standard Methods and Guides, maintain system calibration and/or control documentation, and continue in this or similar programs using existing benchmark facilities for verifications and direct correlations.

In the RM-I and RM-II experiments, intercomparisons of dosimetry results from six service laboratories have provided experimental estimates of measured reaction rates accuracies. Preliminary results were distributed over a range of relative values as large as 60%. Had results from a single laboratory been used to derive surveillance capsule fluence values (often based on only one or two reactions), a bias of 40% or more could easily have been introduced. Following discussions of the preliminary analysis results and identification of existing problems, these biases were generally reduced to below 15%.

In the RM-III experiment, systematic problems were uncovered with Cu and Nb dosimeters. Any Co impurity in the Cu dosimeters can seriously comprise results. As stressed in earlier dosimetry work with Nb [To80], more accurate cross-section data are needed for the ^{93}Nb(n,n') reaction.

An important distinction between the RM-I and RM-II intercomparisons and the RM-III intercomparison must be stressed. The use of HEDL-determined normalization factors reduces the RM-I and RM-II tests to essentially an interlaboratory comparison of absolute gamma-ray counting measurements. However in RM-III, factors that arise in the use of dosimetry materials from different suppliers, such as mass and impurities, were included along with absolute gamma-ray counting measurements. Both types of tests are clearly needed. In fact, interlaboratory RM dosimetry results from the long-term PSF one- and two-year metallurgical irradiations will be used to obtain an addition intercomparison of the type treated here in the RM-III test. This work will be reported in the forthcoming NUREG/CR-3320 Vol. 3 report on the PSF Physics-Dosimetry Program.

Finally, these tests and intercomparisons establish a clear and significant difference in accuracy between fissile and nonfissile RM dosimeters. The important contribution of fast neutrons to PV embrittlement, especially in the region from roughly 0.1 up to 1.0 MeV, makes the use of the threshold fission monitors ^{238}U and ^{237}Np crucial in LWR-PVS dosimetry. The higher uncertainties of fissile RM dosimeters relative to nonfissile RM dosimeters (by about a factor of two) are just barely acceptable given the goal accuracies of LWR-PVS work. Indeed, there is no fundamental reason that fissile RM dosimeters must possess such considerably higher uncertainties. If anything, these two threshold RM fissile dosimeters generally possess as accurate or more accurate integral cross sections in standard neutron fields than do the fast neutron nonfissile RM dosimeters (Fa76,Gi85,Ma82,Ma82b). Consequently, additional work is clearly needed to resolve systematic effects that are adversely impacting the accuracy of RM dosimetry with fissile monitors.

Expected Future Accomplishments

This work will be extended and updated for incorporation in the forthcoming NUREG report on the PSF, namely, The PSF Start-Up Experiments, NUREG/CR-3320, Vol. 2.

E. SYSTEMATIC EFFECTS IN THE PSF DATA BASE

Raymond Gold and W. N. McElroy (HEDL)

Objective

To explain left-right asymmetries observed in material tests of PV steels in the PSF experiment.

Summary

A difference in transition temperature and upper-shelf energy has been reported between specimens irradiated on the left- and right-hand sides of the PSF metallurgical assembly (Ha84,Ha84a). These metallurgical experiments were reviewed to determine whether left/right asymmetries in the irradiation environment could be responsible for the observed left/right differences. This review concludes that environmental variables are, in all probability, responsible for the observed left/right differences. For the transition temperature measurements, differences in the in-situ irradiation temperature exist. In the case of the upper-shelf energy measurements, a systematic variation in exposure underlies the observed asymmetry.

Accomplishments and Status

Adequate dosimetry is the underlying foundation for quantitative investigations of radiation effects in materials. Implicit in such effects is the fact that dosimetry measurements must be properly interpreted. Because of the complexity of such investigations, all environmental variables should be considered in the analysis of experimental results (Go86).

A difference in the transition temperature has been observed between the set of specimens irradiated on the left and right side of the PSF metallurgical assembly. This observed left-right difference is not manifested by all materials used in the PSF experiment (Ha84,Ha84a). This behavior pattern has been attributed to some (unknown) effect of specimen location in the parent plate (Ha84a). At the same time, left-right neutron fluence dissimilarities have been ruled out as a cause (Ha84a). However, Hawthorne also states (Ha84a): "The anomaly is compounded by the fact that the specimens for individual capsules were intentionally randomized within the total specimen complement to avoid introducing any across-plate bias." Consequently, one can surmise that the most likely cause for the existence of these left-right differences may still be left-right asymmetries of the irradiation environment.

To further investigate this effect, metallurgical data reported for the transition temperature upper-shelf energy (USE) and lateral expansion (LE) (Ha84,Ha84a) have been qualitatively examined for left-right asymmetry. Results obtained from visual inspections of these data are summarized in Table HEDL-58. This table contains only those cases where a discernable left-right difference is believed to exist. In a subset of these cases, a left-right asymmetry could not be unambiguously discerned. For these

particular cases, a question mark has been affixed to the asymmetry identified in Table HEDL-58. While the question mark signifies an uncertainty as to whether a left-right difference exists, it nevertheless implies that if such a difference were to exist, the asymmetry is in the direction listed in Table HEDL-58.

It can be seen that asymmetries that do exist in the PSF data have an overwhelming preference for the right group of specimens to possess higher transition temperatures, lower USE values, and higher LE values. Given that material specimens have been randomly placed in these PSF irradiations, one would expect a random result between left-right asymmetries, i.e., a nearly equal frequency in the behavior pattern between the left and right groups. The bias in the behavior pattern that is manifested here implies that this asymmetry effect does not originate in the properties of the material specimens irradiated, but rather lies in differences in the irradiation environment.

The largest left-right asymmetry in the PSF data is that exhibited by the F23 material in the SSC-1 irradiation. While there was no exposure asymmetry for this material in the SSC-1 irradiation, there definitely was a left-right difference in the in-situ irradiation temperature. The thermocouple measurements reveal that the left group of F23 specimens was irradiated at a higher temperature in the SSC1 irradiation. This left-right temperature difference ranges from 1°C up to 7°C, with an average left-right temperature difference of roughly 4°C. Such a temperature difference explains most if not all of the 8°C left-right difference in transition temperature observed for the F23 material in the SSC-1 irradiation. In fact, it has been estimated that the transition temperature increases roughly 0.5 to 1.5 degrees per degree decrease in irradiation temperature (Mc86b).

Some of the other left-right asymmetries observed in the PSF data could also be due to differences in irradiation temperature. Examination of the PSF temperature data reveals that three additional asymmetry cases listed may possibly be explained on the same basis, namely the 3PU material in the SSC-1 irradiation, the 3PU material in the W1 irradiation, and the MO material in the SSC-1 irradiation. However, in these three cases, the asymmetries are smaller and the corresponding left-right differences in irradiation temperature are smaller.

While differences in irradiation fluence have generally been ruled out as a contributing factor to these PSF asymmetries, correlations with irradiation fluence or dpa may still exist because many specimens need be tested to generate a Charpy curve. The 3PU material in the SSC-1 irradiation is a good illustration of this point. Table HEDL-59 shows there was essentially no difference in irradiation dpa between left and right specimen groups. However, as shown in Table HEDL-59, a variation of dpa exposure from about 0.038 down to about 0.034, or roughly 12%, exists within both the left and right specimen groups. Such a variation could affect the shape of the deduced Charpy curve, unless care is exercised in the selection of the test temperatures used with different specimens. Ideally, one should correct

individual specimen results for known differences in irradiation exposure and thereby generate a Charpy curve that corresponds to a specific irradiation dpa (Mc86d).

This kind of inadvertent correlation actually shows up more strongly in the USE data. In fact, Table HEDL-58 reveals that the frequency of left-right asymmetries is slightly higher in the USE as opposed to the transition temperature results. A close inspection of PSF measurements (Ha84,Ha84a) discloses that a left-right difference did exist in the irradiation exposure of specimens tested in USE temperature regions. Although the magnitude of this left-right exposure difference varied from one material to the next, the left group of specimens invariably possessed a higher dpa irradiation. In all materials that exhibit this USE left-right asymmetry, USE values are larger at higher dpa exposure, except for the 3PT material that exhibits the opposite correlation.

Expected Future Accomplishments

This analysis together with any additional studies of the PSF data will be issued in NUREG/CR-3320, Vol. 4, "PSF SSC/SPVC Experiments and Blind Test," which is scheduled for publication in FY-87.

TABLE HEDL-58

LEFT-RIGHT DIFFERENCES IN THE PSF METALLURGICAL DATA

Material	Location	Higher Transition Temperature	Lower USE	Higher LE
F23	SSC-1	Right	Right	Right
	SSC-2	Right?	Right	Right
	W1		Right	
	W2		Right	
	W3		Right	
3PU	SSC-1	Right?	Right	Right?
	W1	Right	Right	Right
	W2	Right?	Right	Right?
3PT	SSC-2		Left?	
	W3		Left?	
MO	SSC-1	Right	Right	
	W3	Right?	Right?	
R	W2	Right	Right	
	W3	Left		Left

TABLE HEDL-59

DPA EXPOSURE OF 3PU SPECIMENS IN THE SSC-1 IRRADIATION

Left Group		Right Group		dpa Left/Right
Specimen No.	(dpa) Left	Specimen No.	(dpa) Right	Ratio
1	0.0383	17	0.0382	0.997
2	0.0377	18	0.0376	0.997
3	0.0361	19	0.0360	0.997
4	0.0352	20	0.0351	0.997
5	0.0342	21	0.0341	0.997

F. NUCLEATION AND GROWTH OF PRECIPITATES

G. L. Guthrie (ORNL)

Objective

The objective of the present work is to study and review various aspects of the problem of the formulation of mathematical models that represent the processes of the nucleation and the growth of precipitates in irradiated LWR PV steels.

Summary

Various mathematical representations of the nucleation and growth of precipitates in irradiated LWR PV steels have been studied and reviewed. Emphasis is placed on nucleation sites and copper-rich clusters and their fluence and flux-level dependencies. The validity of certain assumptions and boundary conditions associated with the mathematical formulation of the problem of developing model equations are addressed. It is concluded that any set of assumptions can be made regarding the nucleation and growth, and in some cases, solutions may be obtained in closed form, but the accuracy will depend on the assumptions. For practical fits of Charpy data, simple formulas involving fluence raised to a power give results that are remarkably in conformity to the more complex realities of the world.

Accomplishments and Status

1.0 Introduction

Nucleation may take place as the aftermath of a single cascade or as the result of migration of debris from a number (two or more) of cascades. If the nucleation arises from individual cascades, without cascade-cascade interactions, then the nucleation critical cluster size will not be flux-rate dependent. If the density of nucleation sites is flux-rate dependent, the rate dependence will arise from the relationship between the density of migrating species and the critical nucleation radius, given by (Ka70)

$$r_c = 2\sigma\overline{V}/(RT \ln \pi) \quad . \tag{1}$$

In Eq. (1), r_c is the critical radius, σ is the energy per unit area of the interface surface, $\overline{V}$ is the molar volume of the precipitate material, and π is the ratio of supersaturation in the matrix. That is,

$$\pi = X/X' \tag{2}$$

where X is the concentration of the solute in the matrix and X' is the equilibrium concentration that would exist near a hypothetical flat interface separating the two pure species. If the formation of copper clusters

proceeds from the formation of vacancy clusters that then capture copper atoms, a high flux level will increase the total number of available vacancies and also decrease the critical radius, increasing the formation rate and density of vacancy clusters. This assumes, again, that nucleation involves monomers from two or more cascades. If the copper-rich clusters nucleate originally as copper clusters rather than vacancy clusters, the critical radius and density of clusters can still be dependent on the flux level, if some of the copper atoms migrate as interstitials remaining from more than a single cascade. Independent of the details of the original nucleation, the surviving number of clusters will be less than the number nucleated because of Ostwald ripening (or coarsening) (La61,Wa61). As the clusters grow, the number of copper monomers will decrease so that the size of the critical radius will increase, allowing the smaller clusters to dissolve.

A simple mathematical approach to the problem of growth is to assume that, at some particular time, all the nucleation is finished and all the nuclei are spherical and are all the same size. A supply of monomers still exists after the nucleation, but the concentration is too small to allow any significant additional nucleation.

The above assumptions are already beyond reality. Gelles (Ge82a), working with PE16 at high doses, has found that precipitates form not only as spheres that could presumably be homogeneously nucleated, but also as conglomerates of other shapes where the nucleation was presumably aided by the presence of grain boundaries, voids, or dislocations. But, reverting to the simple mathematical picture of a population of precipitates of a common size, the next step is to write a differential equation describing the growth.

The easiest approach is to assume that each spherical precipitate is enclosed in a spherical world of total volume 1/n, where n is the volume density of precipitates. This is a spherical simplification of a Wigner Seitz cell. Then the boundary conditions are that $\partial C/\partial r$ is zero at the outer radius of the cell, and C at the surface of the precipitate is equal to the thermodynamic equilibrium value. Unfortunately, the thermodynamic equilibrium value is a function of the radius caused by the existence of a surface energy term that is chemistry dependent. This brings in a complication that is central to the question of nucleation but that has been ignored in most growth discussions of precipitates in an irradiation field. The existence of the surface energy and the relationship between the radius and equilibrium concentration in the matrix is responsible for the need for a minimum radius for nucleation.

Proceeding with or without this last incorporation, we arrive at a differential equation and a set of boundary conditions where the inner boundary condition is that

$$C(r_{p,t}) - C_e(r_p) = 0 \quad , \qquad (3)$$

where r_p is the common radius of the precipitates, given by

$$\frac{4}{3}\pi r_p^3 - \frac{4}{3}\pi r_n^3 = \int_0^t 4\pi r_p^2(t) \cdot \left[\frac{\partial C(r)}{\partial r}\right]_{r=r_p} \cdot D\, dt \cdot V_M \qquad (4)$$

where t is measured from the time of nucleation. In Eq. (4), C is the precipitate monomer concentration, C_e is the copper thermodynamic equilibrium concentration in the matrix at the surface of the precipitate (radius dependent), D is the irradiation-enhanced diffusion coefficient, r_n is the radius at nucleation, and V_M is the volume of a single atom.

Ham (Ha58) has shown that, under certain conditions, the ($\partial C/\partial r = 0$) outer boundary condition can be replaced by setting the distant concentration equal to a constant. In a proper treatment, the total copper content of the solid has to be maintained and this leads to a depletion of the matrix as time proceeds and causes a saturation phenomenon. In the Ham simplification just mentioned, the concentration at the outer boundary would be a decreasing function of total precipitate volume.

In reality, there is a continuous range of precipitate radii and the larger precipitates have a lower value of the equilibrium matrix monomer concentration at the precipitate surface. This determines the concentration of the available copper in the matrix and causes the small particles to shrink.

Nelson, Hudson and Mazey (NHM) (Ne72) have pointed out that cascades occasionally involve existing precipitates, and for large precipitates, the cascades spall atoms off the surface (by various mechanisms) to give a loss rate (dV/dt) that, on a time average, is proportional to r^2 for any given precipitate. The total NHM treatment ignored the role of the surface energy both in nucleation and in growth, and it concluded that the diffusion growth term ($dV/dt \propto -r^2$) will combine to make large precipitates shrink while small ones grow. This is a reverse phenomenon to that predicted by Ostwald ripening theory, where large precipitates grow at the expense of small ones.

NMH then predict that all precipitates will proceed to a common equilibrium radius. This line of thought is not applicable to small copper precipitates in a short time frame. It is incorrect to write a differential equation for dV/dt or dr/dt and to include a term for cascade-induced spalling and treat it as a time-continuous phenomenon contributing to the creation of an equilibrium radius except for long time periods (dpa>1) and large precipitates.

The cascade-induced spalling is a sporadic statistical event that causes discontinuous jumps in the radius value of a particular precipitate. In the case of small precipitates, the encounter between a cascade and a precipitate could destroy the precipitate and not merely cause a loss extending down to a particular depth on the surface. The cascade-interaction phenomenon, if it is important, will not drive all precipitates to an equilibrium radius in a time frame of interest to the operation of a power reactor, but will merely

modify the n(r,t) curve, where n(r,t) gives the distribution of precipitates as a function of radius and time. Large precipitates cannot be viewed as gradually shrinking by this mechanism in a short time frame. For power-reactor conditions, small precipitates will not necessarily grow faster than their slightly larger neighbors, since the surface-energy term changes the equilibrium value of the copper concentration near the precipitate surface; i.e., the very small precipitates in effect spit out atoms caused by the surface-energy term and this decreases the net, if any, inflow. This decrease is more important for the smaller radius particles.

In the case of small copper-rich precipitates in an LWR-PV, the inclusion of the NHM spalling term as a constantly acting term in the differential equation is especially inappropriate when one considers that a fluence of 1×10^{19} $n/cm^2 \cdot s$ ($E > 1.0$ MeV) corresponds to $\sim$0.016 dpa. Over 90% of the atoms have not been directly involved in even a single cascade at end-of-life for the reactor. Also, the size of the cascades (several hundred or up to a few thousand atoms) is not inconsequential compared to the size of the copper precipitate responsible for the dislocation pinning (a 25 Å diameter sphere has approximately 525 atoms), so that an r-squared dependent continuous-loss process is not realistic. Comments on the NHM (Ne72) paper have been published by P. Wilkes (Wi79). Wilkes set up a differential equation where the atoms released by spalling re-appeared uniformly inside each Wigner-Seitz cell. This is questionable, since the spalled-off atoms can only appear in a non-cascade cell by coming in through the outer boundary. Failure to recognize this led Wilkes to the conclusion that irradiation-induced NHM spalling helped stabilize bimodel distributions. Larger particles were aided in stability by the favorable surface energy, and smaller particles were aided by the large-manomer-generating space in the unoccupied volume of the cell, under Wilkes mathematical treatment.

Frost and Russell (Fr81) found that the time constant to approach an NHM average radius is 45 days for an ion bombardment experiment and 120 years for metal in a fast reactor. The NHM average radius condition is not reached in the lifetime of a power reactor. A more complete treatment of the total problem has been given by Baron, Chang, and Bleiberg in a Westinghouse ERDA report.

The paper by Ham (Ha58), though it ignored the surface-energy term, has some interesting points. One comment already mentioned deals with the legitimacy of replacing the ($\partial C/\partial r = 0$) outer boundary by a condition where C = constant at the outer boundary. Ham also dealt with a time-dependent phenomenon in which the initial conditions had a spherical precipitate imbedded in a spherical world, where C(r,t) was a constant independent of r (r is the distance from the center of the cell, and not the radius of the particle) for the initial time (t = 0). Ham showed that the problem could be solved by an expansion in orthoganal functions with a separable partial differential equation, and only the fundamental time constant solution was of importance. Then the growth rate can be calculated at any given time, using a fixed geometry, and the time and space parts of the problem are effectively decoupled.

Odette (Od83a,Pe84) has taken the two points of the Ham paper above and implicitly used them as a starting point for a formal solution of the growth problem. The Odette paper assumed that C(r) was zero at the inner boundary of the cell, assumed that the cell contributing to a particular precipitate was infinite in extent and assumed that the concentration at infinite radius was equal to the average (matrix) copper concentration in the solid. The matrix concentration was adjusted for removal by the precipitates. Under these assumptions, Odette found that

$$\phi t = \phi * 0.38 \left(D_c^* N_p^{2/3}\right)^{-1} * \left\{ \frac{1}{6a} \ln \left[\frac{x^3 - a^3}{(x-a)^3} \right] + \frac{1}{a\sqrt{3}} \arctan - \left(\frac{2x + a}{a\sqrt{3}} \right) \right\} \Bigg|_{x_o}^{x} \qquad (5)$$

where ϕt is the fluence, x is the cube root of the volume fraction of precipitate, x_o is the initial value of x, "a" is the cube root of the copper concentration, D_c^* is the irradiation-enhanced value of the diffusion coefficient for copper, and N_p is the number of copper precipitates per unit volume.

This gave a solution for the precipitate radius as a function of fluence ignoring the NHM spalling phenomenon. Odette combined (1) the stress required to give dislocation glide, (2) the (assumed) common radius of all the precipitates, and (3) the precipitate density per unit volume to obtain numerical values of the plastic flow shear stress for various combinations of the fluence and other input parameters. Odette then assumed that the plastic flow stress requirement caused by the irradiation was proportional to the irradiation-induced increase in the Charpy transition temperature. He thus obtained a relationship between the irradiation-induced increase in the transition temperature and the fluence and other input parameters. The Odette work used the results of Russell and Brown (Ru72) for the relationship between precipitate radius, precipitate density, and effective dislocation pinning.

A less accurate but simpler relation (compared to Russell-Brown) is given by (0176)

$$\sigma_s = 2\ Gb/l \qquad (6)$$

$$l = \frac{1}{\sqrt{2\ rn}} \qquad (7)$$

$$\sigma_s = 2\ Gb\ \sqrt{s\ rn} \qquad (8)$$

which allows some direct insight into the effect of changes in precipitate density. In Eq. (6), (7) and (8), G is the shear modulus, σ_s is the shear stress for dislocation glide, b is the dislocation Burgers vector, r is the precipitate radius (assumed common for all precipitates), and n is the volume density of precipitate sites. For a given total volume of precipitate, V_p, we find that

$$V_p = n \cdot \frac{4}{3} \pi r^3 \tag{9}$$

so that Eq. (9) can be substituted in Eq. (8) to yield

$$\sigma_s = \left(\frac{3n^2}{4} V_p\right)^{1/6} \cdot 2^{3/2} Gb \quad . \tag{10}$$

This shows that for any given total amount of precipitate volume, the required shear stress for plastic flow through the precipitate field is an increasing function of n, the precipitate density.

Any set of assumptions can be made regarding the nucleation and growth, and in some cases, solutions may be obtained in closed form, but the accuracy will depend on the assumptions. In actual practice, Charpy data have often been fitted with laws of the type (Gu85)

$$\Delta T = f(\text{chem}) \cdot (\phi t)^{N(\text{chem, fluence, flux})} \tag{11}$$

or, more simply

$$\Delta T = f(\text{chem}) \cdot (\phi t)^{N(\text{fluence})} \quad . \tag{12}$$

These laws recognize the fact that the log of the Charpy shift is approximately linear in the log of the fluence for any given chemistry. The log ΔT VS log fluence plots are usually slightly concave downward, so that d log (ΔT)/d [log (fluence)] decreases with increasing fluence. In fact, from the simple theoretical considerations given with a fixed amount of precipitate material, it would be expected that ΔT would have an upper limit so that "N" should approach zero at high fluence values. However, the additional dislocation pinning strength contribution from dislocation-dislocation interactions might delay the arrival of saturation.

Thus, although a closed form solution of growth equations might show a complete saturation phenomenon, reality might produce data that show a lack of saturation. In the case of pinning by more than one type of precipitate, the pinning contributions of the individual species could be expected to saturate at different values of the fluence since the problem is so complex. The form of Eq. (12) in many cases fits existing data better than closed form solutions based on simple but incorrect assumptions.

It is possible to set up Wigner-Seitz spherical cells with spherical coordinates and obtain numerical solutions for growth equations for irradiation conditions, using a model involving only a single precipitate. This has been done by Straalsund and Guthrie for the growth of voids (St67,St72a). The calculations gave the growth rates and volume fraction as a function of time and critical radius, for voids and for gas-filled bubbles. Conversion of the technique to copper precipitate and applications is possible but the results would depend on the input assumptions and would still not completely duplicate reality.

Some of the relevant points developed in the above discussion are:

1. For a given amount of precipitate material, the Charpy shift can be expected to increase if there are more (and consequently smaller) precipitates.

2. It is difficult to imagine any mechanism that would make the precipitate number density depend on the flux if the nucleation takes place as a closed item associated with only a single cascade.

3. Closed form treatments that use a fixed value of the concentration as an outer boundary condition of the Wigner-Seitz cell for the growth equation of a single precipitate are in error but the error is small (Ha58).

4. The initial time transient in a spherical growth problem can be ignored for most values of the relevant parameters (Ha58).

5. The NHM (Ne72) argument that all precipitates proceed to a common radius is an oversimplification not particularly applicable to power-reactor problems.

6. Wilkes' correction (Wi79) of NHM contains an oversimplification and does not legitimately produce a bimodal distribution.

7. Arguments involving the growth of small particles should not ignore the surface energy.

8. It is possible to make digital calculations of void or precipitate growth rates, including the effects of surface energy.

9. For practical fits of Charpy data, simple formulas involving fluence raised to a power give results that are remarkably in conformity to the more complex realities of the world.

10. Closed-form laws attempting to model precipitation of a finite amount of solute should contain a depletion term if they are to model saturation.

Expected Future Accomplishments

No definite plans for additional work on this topic exist at the present time.

G. SUMMARY OF ASTM PAPERS

R. Gold and W. N. McElroy (HEDL)

Objective

To provide a listing of abstrasts of HEDL papers prepared for presentation and the proceedings of the 13th ASTM International Symposium on the Effects of Radiation on Materials and the 6th ASTM-EURATOM International Symposium on Reactor Dosimetry.

Summary

See Accomplishments and Status

Accomplishments and Status

1.0 13th ASTM International Symposium

The following papers were presented at the 13th ASTM International Symposium on the Effects of Radiation on Materials, June 23-25, 1986, Seattle, WA and have been accepted for publication in the ASTM proceedings:

- W. N. McElroy, R. Gold, R. L. Simons and J. H. Roberts, "Trend Curve Data Development and Testing"
- R. L. Simons, "Damage Rate and Spectrum Effects on Ferritic Steel ΔNDTT Data"
- R. Gold and W. N. McElroy, "Current Limitations of Trend Curve Analysis for the Prediction of Reactor Pressure Vessel Embrittlement"

2.0 6th ASTM-EURATOM Symposium

The following abstracts have been accepted for presentation at the forthcoming 6th ASTM-EURATOM Symposium on Reactor Dosimetry, Jackson Hole, WY, June 1987:

- R. Gold and W. N. McElroy, "LWR-PV-SDIP: Past Accomplishments, Recent Developments and Future Directions" (Invited)
- R. Gold, C. C. Preston, J. H. Roberts, G. DeLeeuw, A. Fabry and L. Leenders, "Nuclear Research Emulsion Measurements in VENUS-1"
- R. Gold and W. N. McElroy, "Correction of Burn-In Effects in Fission Neutron Dosimeters"
- R. Gold, J. H. Roberts and D. G. Doran, "Determination of Gamma-Ray-Induced Displacement Rates"

3.0 Abstracts

3.1 Trend Curve Data Development and Testing

W. N. McElroy, R. Gold and R. L. Simons (HEDL) and
J. H. Roberts (MC^2)

Existing trend curves do not account for previous and more recently observed test and power reactor flux-level, thermal neutron and γ-ray field-induced effects. Any agreement between measured data and trend curve predictions that does not adequately represent the important neutron environmental and temperature effects as well as the microstructural damage processes, therefore, could be fortuitous. Empirically derived end-of-life (EOL) and life-extension-range (LER) trend curves are presented and discussed in this paper for high temperature [$\sim$288°C (550°F)] irradiation of two weld, two plate, and two forging pressure vessel (PV) steels and low-temperature [$\sim$60°C (140°F)] irradiation of one support structure-type steel.

Preliminary results of a comprehensive study of the effects of environmental variables (neutron spectrum, exposure, exposure rate, and the thermal and γ-ray fluxes associated with surveillance capsules and PV through-wall gradients) were used to develop these trend curves.

Pressurized water reactor (PWR) and boiling water reactor (BWR) plant-specific results together with those of the Poolside Facility (PSF) of the Oak Ridge Research Reactor (ORR) at the Oak Ridge National Laboratory (ORNL) and other research reactor experiments support the existence of a significant material-dependent flux-level effect for PV and support structure steels; i.e., a steel may show a decrease, an increase, or no change in the measured Charpy shift with changes in flux-level. Further, the actual behavior of a material can change significantly as a function of neutron exposure; also, thermal neutron and γ-ray effects can contribute to observed changes in property, especially near steel-water interface positions with high thermal-to-fast-neutron ratios.

3.2 Damage Rate and Spectrum Effects in Ferritic Steel ΔNDTT Data

R. L. Simons (HEDL)

A model was developed for irradiation-induced hardening in PV steels by cascade-induced nucleation and free defect diffusion of copper to coherent copper clusters. The model was used as a functional framework for fitting data on ΔNDTT as a function of damage dose and dose rate. Several defect cross sections were tried; however, dpa exposure was found to give the best overall fit. Another defect cross section for Frenkel pair productions, based on resistivity measurements at 4°C, was found to give a comparable or slightly better fit to the data than dpa. Damage rate is an important parameter to consider in correlation of ΔNDTT data and damage rate can affect the nucleation as well as the growth of the copper precipitation.

3.3 Current Limitations of Trend Curve Analysis for the Prediction of Reactor Pressure Vessel Embrittlement

R. Gold and W. N. McElroy (HEDL)

In operating light water reactor (LWR) commercial power plants, neutron radiation induces embrittlement of the pressure vessel (PV) and its support structures. As a consequence, LWR-PV integrity is a primary safety consideration. LWR-PV integrity is a significant economic consideration since the PV and its support structures are nonreplaceable power plant components and embrittlement of these components can therefore limit the effective operating lifetime of the plant.

To define the effects of neutron radiation damage on LWR pressure-temperature operating limits as well as for fracture toughness assessment of power reactor PV, trend curves for the prediction of PV embrittlement have been developed. These trend curves are very general PV embrittlement curves that are used both to evaluate current PV status as well as to predict the future state of the PV. In such trend curves, the two main measures of radiation damage are the adjusted reference nil-ductility temperature ART_{NDT}(RT_{NDT} initial + ΔRT_{NDT}) and the decrease in upper-shelf energy level determined from Charpy V notch impact tests. Current measures of neutron exposure most commonly used in trend curve analyses are fluence >1 MeV and displacements per atom (dpa) in iron.

Since trend curves play such a crucial role in the assessment of PV embrittlement of operating commercial LWR power plants, a critical appraisal of trend curve analysis is essential. To this end, current limitations in trend curve analysis for the prediction of reactor PV embrittlement are examined. It is concluded that a number of systematic effects can arise because environmental differences exist between test reactors, surveillance capsule locations, and the actual irradiation conditions that accrue within the PV of an operating LWR commercial power plant. An irradiation test program is advanced to investigate these systematic effects and to produce the requisite data needed to correct for such systematic biases in trend curve analysis.

3.4 LWR-PV-SDIP: Past Accomplishments, Recent Developments and Future Directions

Raymond Gold and W. N. McElroy (HEDL)

The integrity of the pressure vessel (PV) of a nuclear power plant is a major safety consideration throughout the life of the power plant. Since the PV is nonreplaceable, radiation embrittlement can limit the serviceable lifetime of the PV and thereby limit the effective operating lifetime of the plant. It can further restrict normal heatup and cooldown reactor operations, with resultant cycle-to-cycle economic implications. In recognition of these safety and economic issues, the U. S. Nuclear Regulatory Commission (NRC) established the light water reactor pressure vessel (LWR-PV) surveillance dosimetry improvement program (SDIP) some ten years ago to improve, maintain and standardize neutron dosimetry, damage correlation, and the associated reactor analysis procedures used for predicting the integrated effect of neutron exposure to LWR-PV.

The LWR-PV-SDIP adopted specific experimental and calculational strategies to meet the challenge of this complex radiation-induced PV embrittlement phenomenon. A vigorous research effort has gone forward worldwide to implement these strategies. The major benefit of this program has been and continues to be a significant improvement in the accuracy of the assessment of the current metallurgical condition and the remaining safe operating lifetime of LWR-PV.

The LWR-PV-SDIP has produced a broad range of technical accomplishments over the last decade and these achievements are reviewed. These earlier LWR-PV-SDIP accomplishments have generated, in turn, a number of significant new developments that are described. A natural outgrowth of LWR-PV-SDIP work is the experience to project future needs of LWR-PV surveillance. On this basis, recommendations for future directions are advanced with special emphasis on plant life extension.

3.5 Nuclear Research Emulsion Measurements in VENUS-1

Raymond Gold and C. C. Preston (HEDL), J. H. Roberts (MC²), and G. DeLeeuw, A. Fabry and L. Leenders (CEN/SCK)

Nuclear research emulsion (NRE) observed I-integral and J-integral reaction rates are reported for VENUS-1. Proton-recoil energy-dependent reaction rates are predicted using CEN/SCK-calculated 17-group neutron energy spectra. These calculated reaction rates are compared with absolute NRE observations at seven different locations in steel and water regions of VENUS-1. The agreement between calculations and NRE-observed absolute proton-recoil reaction rates depends sensitively on location in VENUS-1. Adequate agreement is attained near the center of the core. However, as one approaches the edge of the core corner at approximately 28°, the agreement deteriorates. Comparisons between theory and experiment are limited by the broad energy resolution of the 17-energy-group structure used in the calculations. Nevertheless, these comparisons do suggest that difficulties arise in the calculation of neutron transport as one approaches the edge of the core corner.

In the 1983 dosimetry campaign in VENUS-1, possible perturbations introduced by 4π proton-recoil gas-filled proportional counters were investigated with NRE. Preliminary I-integral and J-integral proton-recoil reaction rates from NRE irradiated in this perturbation study reveal that proportional counters do create non-negligible perturbations in LWR-PV environments.

3.6 Correction of Burn-In Effects in Fission Neutron Dosimeters

Raymond Gold and W. N. McElroy (HEDL)

When fission neutron dosimeters are applied for neutron dosimetry, such as those used in light-water reactor (LWR) pressure vessel surveillance (PVS), higher order actinide isotopes can be produced in the dosimeter by the neutron field. These higher order actinide isotopes can also undergo fission and thereby contribute to the number of fissions or fission rate that is observed with the dosimeter. This so-called "burn-in" effect can be non-negligible especially in fission threshold monitors, such as those used in LWR-PVS.

A novel method for correction of this burn-in effect is advanced. In this new method, two quantities are measured in order to quantify the burn-in contribution, namely the amount of the background fissile isotope that is created and the fissions per unit volume produced in the background fissile isotope. Monitors used to measure these two quantities must experience the very irradiation that the fission neutron dosimeter undergoes, i.e., the same location and flux-time history. Conditions are defined under which the burn-in effect can be delineated in terms of these two observed quantities. Advantages of this correction method are discussed.

3.7 Determination of Gamma-Ray-Induced Displacement Rates

Raymond Gold and D. G. Doran (HEDL) and J. H. Roberts (MC^2)

To define the γ-ray component of the radiation field in light water reactor (LWR) pressure vessel (PV) environments, γ-ray spectrometry experiments were conducted in the low power PV mockup at the poolside critical assembly (PCA) at ORNL. The γ-ray displacement rates can be calculated directly from absolute electron spectra observed with the Janus probe γ-ray spectrometry. The γ-ray displacement results are presented for the 1/4-T, 1/2-T, and 3/4-T locations of the 12/13 and 4/12 simulated surveillance capsule (SSC) configurations. In addition, the γ-ray displacement rate at the SSC location was inferred using thermoluminescent dosimeter (TLD) γ-ray dosimetry results obtained in the 4/12 SSC configuration at the PCA. Compared with neutron-induced displacement rates, the calculated γ-ray-induced displacement rates are small at all these LWR-PV locations. The ratio of γ-ray-induced to neutron-induced displacement rates never exceeds roughly 5×10^{-3}.

Expected Future Accomplishments

The present scope of this work has been completed.

H. PRELIMINARY PCA-PROTON RECOIL PROPORTIONAL COUNTER NEUTRON SPECTROMETRY

J. W. Rogers (INEL)

Objective

To use gas-filled proton-recoil proportional counter neutron spectrometry to characterize the neutron spectrum in the LWR-PV mockup at the PCA.

Summary

By conducting neutron spectrometry at different PCA locations, one obtains the variation of the differential neutron spectrum through the PV, which can be used to validate calculations. This spatial variation is an especially powerful probe for examining trends between theory and experiment, thereby furnishing greater insight into any observed differences.

During the fall 1981 PCA irradiations, proton recoil proportional counter neutron spectrometry was conducted in the 4/12 configuration. Preliminary neutron spectral results have now been obtained for the 1/4-T and VB locations. These preliminary spectra, which are shown in Figures HEDL-75 and HEDL-76 cover the energy region from roughly 0.05 to 2.0 MeV.

Expected Future Accomplishments

When the final results of these neutron spectrometry efforts are obtained, they will be incorporated into the 4/12 configuration data base and least-squares analyses will be performed using FERRET-SAND-II. Such analyses will provide quantitative comparison and evaluation of these proportional counter spectrometry results with already existing neutron dosimetry data for the 4/12 configuration. These final results and analyses will be issued in a forthcoming LWR-PV-SDIP annual progress report.

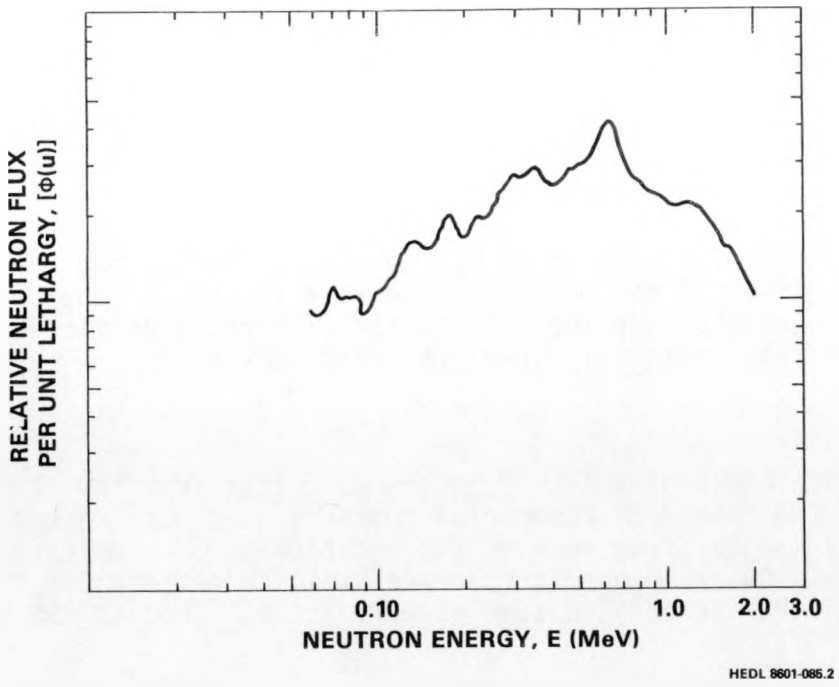

FIGURE HEDL-75. Neutron Spectrum Observed with Proton-Recoil Proportional Counters at the 1/4-T Location of the PCA-PVS 4/12 Configuration.

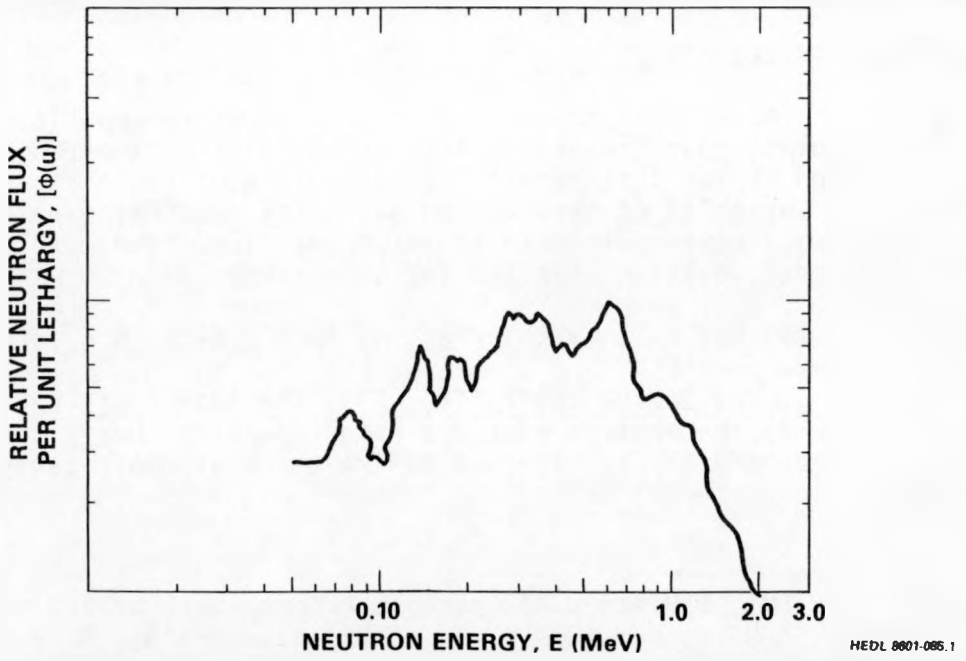

FIGURE HEDL-76. Neutron Spectrum Observed with Proton-Recoil Proportional Counters at the Void Box Location of the PCA-PVS 4/12 Configuration.

I. Measurement of the Boron and Helium Content of Irradiated PV Steels

L. S. Kellogg and W. N. McElroy (HEDL) and B. M. Oliver (RI-RD)

Objective

To measure the boron and helium (B/He) content of irradiated PV steels to help determine the effect of the He generation rate (as one of the contributing environmental variables) in the calculation of plant specific end-of-life and life-extension-range material dependent trend curves.

Summary

Thirteen irradiated samples (six from the PSF, five from the UK DIDO or PLUTO reactors, and two from a US commercial reactor) have been received by HEDL. Two irradiated samples from each of two additional US commercial reactors and specimens from a Gundremmingen trepan are still to be received.* Chemical analyses of the PSF-irradiated samples were accomplished at B&W before shipment to HEDL.

Samples suitable for B/He analysis are being taken from all specimens received. As required, RM (γ-spectrometry) analyses will be made by HEDL on the PSF-irradiated and Gundremmingen trepan samples. Shipment to RI-RD (for B/He analysis) of all available samples will be made by the end of March. (This necessitates the HEDL receipt of samples no later than mid-March 1987.)

Accomplishments and Status

McElroy et al. (Mc86) have reported on the study of an empirical approach for establishing plant specific end-of-life and life-extension-range material dependent trend curves that permit the separation of the effects of the environmental variables of neutron and gamma-ray spectra, exposure, exposure rate, and thermal neutron-induced helium production. The material-dependent trend curve model equation selected for this study was

$$\Delta RT\text{-}NDT = X1 + X2 \ln \dot{He} + X3 \ln \dot{D} + X4 \ln D \qquad (1)$$

where ΔRT-NDT is the Charpy shift (°F); D is the iron dpa** neutron exposure (dpa/0.016); $\dot{D}$ is the neutron exposure rate (dpa/s)**; He is the helium atom production rate; and X1, X2, X3, and X4 are a set of empirically derived constants.

---

*The PSF, UK, BMI, B&W and W-NTD steel specimens were or are being provided by F. B. K. Kam (ORNL), T. J. Williams (RR&A), M. P. Manahan (BMI), A. Lowe (B&W) and S. L. Anderson (W-NTD). The Gundremmingen specimens are being provided by NRC-MEA.

**Including that caused by iron recoil atoms from the Fe (n,γ) reaction and from any γ-ray field-induced displacements in iron.

Measurement of the boron and helium content in selected irradiated PV steels is needed for an initial evaluation of the magnitude of the constant X2 in Eq. (1). Specimens of the following steels have been received by HEDL from ORNL, RR&A and BMI, respectively:

1) Six PSF irradiated Cv steel specimens taken at the O-T position and broken near the 41-J level.

2) Five Cv specimens irradiated in the UK DIDO or PLUTO reactors, with the DIDO/PLUTO results indicating considerably larger shifts than similar specimens irradiated in HERALD.

3) Two Cv specimens irradiated in a US commercial reactor.

4) Still to be received from W-ARD are an additional two Cv specimens irradiated in a US commercial reactor, from B&W two irradiated Cv specimens from a US commercial reactor, and specimens from MEA from a Gundremmingen trepan sample [Mc85g]. Table HEDL-60 describes the materials being analyzed.

The six PSF-irradiated specimens were first shipped to Babcock and Wilcox for chemical analysis (Section HEDL-J) and then to HEDL. All other samples were or are being shipped directly to HEDL. Suitable sized samples are being drilled, from the notch area where possible, and will be shipped to RI-RD for B/He analysis. In addition, samples from the PSF-irradiated specimens and the Gundremmingen trepan samples will undergo RM analysis at HEDL. Considerable delay in the analyses has been encountered because of delay in receipt of all samples. The expense of sampling and sample analyses at RI-RD requires the work to be done in a "batch" rather than individual mode. Rather than incur additional delays, shipment to RI-RD will be made by the end of March, whether all specimens have been received or not.

Expected Future Accomplishments

Results from the analyses of the selected individual Cv and trepan samples will be documented in the appropriate FY-87 LWR-PV-SDIP reports.

TABLE HEDL-60

MATERIALS

Material	Heat Code	Specimen	Supplier	Thickness (mm)	Yield* Strength (MPa)	Heat Treatment
			PSF-Irradiated CV Specimens**			
A533-B (HSST) Plate 03)	3PS, 3PU, 3PT	3PU-22	NRL	305	454	843 to 899°C - 4 h, water quenched 649 to 655°C - 4 h, air cooled 607 to 636°C - 20 h, furnace cooled
A302-B (ASTM Reference Plate)	F23	F23-85	NRL	152	482	899°C - 6 h, water quenched 649°C - 6 h, air cooled
Submerged Arc Weld (Single Vee type, A533-B Base Plate)	R	R-54	RR&A	160	489	920°C ± 15°C - 6 h, water spray quenched 600°C - 6 h, air cooled 600°C - 36 h, air cooled 600°C - 6 h, air cooled
Submerged Arc Weld (Single Vee type, A533-B Base Plate)	EC	EC-16	EPRI	235	456	621 ± 28°C - 50 h, furnace cooled
22NiMoCr37 Forging	K	K414	KFA	295	407	Not reported to MEA or ORNL
A508-3 Forging	MO	MO-14	Mol	238	462	900 to 955°C - 12.8 h, air cooled 630 to 665°C - 14 h, furnace cooled 610 ± 10°C - 24 h, furnace cooled
A537-2 Lukens Steel Base Plate	D0662		CEN-Saclay			885 to 913°C 556 to 593°C

*Ambient temperature strength.
**The six PSF Cv specimens were selected by F. Kam of ORNL.

TABLE HEDL-60 (Cont'd)

Material	Heat Code	Specimen	Supplier	Thickness (mm)	Yield* Strength (MPa)	Heat Treatment
			UK-Irradiated Cv Specimens			
		IPL-21	RR&A			
		IWL-563	RR&A			
		EAO-763	RR&A			
		IWH-463	RR&A			
		IS -258	RR&A			
			US Commercial-Irradiated Cv Specimens			
A302-B Class 1 Leukens Steel Base Plate	H2130	E42	BMI	181	448	Not Reported to BMI.
Submerged Arc Weld in Accordance with CE spec. SAA-33A(3) and MA-339(7) A302-B Base Plate		EJC	BMI	181		Not Reported to BMI.
			B&W			
			B&W			
			W-NTD			
			W-NTD			
		170	MY-BMI			
		37E	MY-BMI			
			Gundremmingen-Irradiated Specimens			
		0 T	MEA			
		1/4 T	MEA			
		1/2 T	MEA			
		3/4 T	MEA			
		Outer Surface	MEA			

*Ambient temperature strength.

J. Babcock & Wilcox Measured Chemistry Results for the Six PSF-Irradiated Steel Materials

A. L. Lowe, Jr. and K. E. Morgan (B&W)

Objective

To provide an independent chemical analysis of six different pressure vessel steel materials irradiated in the PSF metallurgical experiment as part of the investigation of the embrittlement of selected PV steels (Mc86b).

Summary

Six different PSF-irradiated alloy Cv specimens were received by B&W from F. Kam of ORNL. Chemical analysis of the prepared samples was accomplished using emission spectrographic techniques. Equipment calibration was achieved by analysis of NBS SRM low-alloy steel samples. Chemical analysis results for 14 elements are reported.

Accomplishments and Status

Six different alloy Cv specimens provided by NRL, RR&A, EPRI, KFA and MOL (see Table HEDL-60, Section HEDL-I), irradiated in the PSF O-T position and broken near the 41-J level, were selected by Kam (ORNL) and shipped to B&W.

The specimens were cleaned and then buffed on a belt sander using 60-grit paper immediately before analysis using a spark source emission spectrometer (same day analysis is done to preclude possible effects from surface oxidation). Three separate burns were made near the notch area, care being taken not to encroach upon the notch area itself. NBS low-alloy steel reference standards SRM 1261, 1262, 1263, 1264 and 1265 were treated and analyzed in a similar manner at the same time. Analysis of the sample data was made by direct reference to the various element composition curves derived from the reference NBS standards. Average results for 14 elements from the three individual burns are given in Table HEDL-61 along with original reported elemental compositions (Ha84a). Because of the direct reference to the NBS SRM standards, the Mo result for sample K414 is reported as >0.55 wt%, as the observed concentration falls outside of the extrapolation limits of the reference curve.

After analysis the samples were packaged and shipped to HEDL/RI-RD for RM and B/He analysis.

Conclusions

The observed differences in the reported comparative results generally fall within ranges that may be explained by:

- Measurement limits associated with the analytical techniques.
- Level of elemental composition.
- Elemental-sample matrix heterogeniety (Mo85).

- Analytical techniques. Electron microprobe, X-Ray fluorescence, emission spectrometry and wet chemical methods successively analyze increasingly larger sample sizes.

There are some results that raise questions that should be further investigated. In particular, the Cu results in which comparative ratios consistently range from 1.14 to 1.48 with an average of 1.33. It would be of considerable interest to know the analytical techniques used in the initial analysis of the materials.

Expected Future Accomplishments

Provide further documentation of these B&W-measured chemistry results in NUREG/CR-3320, Vol. 4, see Table S-1.

TABLE HEDL-61

PSF ALLOY CHEMICAL COMPOSITIONS (wt%)

Material	Heat Code	B&W Sampler	Supplier	C	Si	Mn	P	S	Cr	Mo	Ni	Al	Cu	Sn	Ti	V	B
A533-B (HSST Plate 03)	3PS, 3PU, 3PT	3PU-22	NRL	0.20[a]	0.25	1.26	0.011	0.018	0.10	0.45	0.56	---	0.12	---	---	---	---
				(0.26)[b]	(0.27)	(1.46)	(0.010)	(0.023)	(0.15)	(0.55)	(0.61)	(0.07)	(0.17)	(0.012)	(0.002)	(0.003)	0.0006
				[1.30][c]	[1.08]	[1.16]	[0.91]	[1.28]	[1.50]	[1.22]	[1.09]	---	[1.42]	---	---	---	---
A302-B (ASTM Ref Plate)	F23	F23-85	NRL	0.24	0.23	1.34	0.011	0.023	0.11	0.51	0.18	0.04	0.20	0.037	0.015	0.001	---
				(0.22)	(0.26)	(1.42)	(0.014)	(0.029)	(0.12)	(0.49)	(0.17)	(0.09)	(0.25)	(0.020)	(0.018)	(0.004)	0.0007
				[0.92]	[1.13]	[1.06]	[1.27]	[1.26]	[1.09]	[0.96]	[0.94]	[2.25]	[1.25]	[0.54]	[1.27]	[4.00]	---
A533-B S/A Weld[d]	R	R-54	RR&A	0.05	0.45	1.54	0.009	0.008	0.12	0.34	1.58	0.01	0.23	0.006	0.003	0.01	---
				(0.05)	(0.40)	(1.58)	(0.009)	(0.014)	(0.13)	(0.35)	(1.57)	(0.024)	(0.33)	(0.007)	(0.002)	(0.006)	0.0006
				[1.00]	[0.89]	[1.03]	[1.00]	[1.75]	[1.08]	[1.03]	[0.99]	[2.40]	[1.43]	[1.17]	[0.67]	[0.50]	---
A533-B S/A Weld[d]	EC	EC-16	EPRI	0.11	0.52	1.57	0.007	0.011	0.02	0.48	0.64	0.008	0.24	0.004	<0.01	0.005	---
				(0.09)	(0.55)	(1.45)	(0.010)	(0.023)	(0.059)	(0.47)	(0.59)	(0.03)	(0.28)	(0.004)	(0.002)	(0.006)	0.0008
				[0.82]	[1.06]	[0.92]	[1.43]	[2.09]	[2.95]	[0.98]	[0.92]	[3.75]	[1.17]	[1.00]	---	[1.20]	---
22NiMoCr37 Forging	K	K-414	KFA	0.18	0.16	0.72	0.009	0.004	0.45	0.63	0.96	0.031	0.12	---	---	---	---
				(0.18)	(0.19)	(0.75)	(0.005)	(0.008)	(0.52)	(>0.55)	(0.94)	(0.09)	(0.15)	(0.010)	(0.002)	(0.003)	<0.0001
				[1.00]	[1.19]	[1.04]	[0.56]	[2.00]	[1.16]	---	[0.98]	[2.90]	[1.25]	---	---	---	---
A508-3 Forging	MO	MO-14	MOL	0.20	0.28	1.43	0.008	0.008	---	0.53	0.75	0.031	0.05	---	---	<0.01	---
				(0.19)	(0.29)	(1.37)	(0.006)	(0.008)	(0.11)	(0.48)	(0.70)	(0.08)	(0.074)	(0.007)	(0.002)	(0.005)	<0.0001
				[0.95]	[1.04]	[0.96]	[0.75]	[1.00]	---	[0.91]	[0.93]	[2.58]	[1.48]	---	---	---	---
	Average Value[c]			[1.00]	[1.07]	[1.03]	[0.99]	[1.56]	[1.56]	[1.02]	[0.98]	[2.80]	[1.33]	[0.90]	[0.97]	[1.90]	

[a]MEA-reported values (Ha84,Ha84a)
[b]B&W-measured and reported values.
[c]Ratio B&W/MEA-reported values.
[d]A533-B base plate & single vee type.

NATIONAL BUREAU OF STANDARDS

A. BENCHMARKED MASSES OF SSTRs USED AT PCA, NESDIP AND VENUS

E. D. McGarry (NBS) and F. H. Ruddy (W-R&D)

Objective

The objective is to validate masses assigned to the solid-state track recorders (SSTRs) used for physics-dosimetry measurements in the PCA, NESDIP and VENUS.

Summary

The masses of 32 SSTR fission deposits belonging to HEDL have been validated by comparison to the known masses of NBS fission deposits. The importance of this mass verification work is that the HEDL SSTRs have been and are being used to characterize the neutron fields in a number of LWR-PV-SDIP benchmark fields, namely PCA, NESDIP, and VENUS.

Accomplishments and Status

The subject fissionable deposits have masses in the range several micrograms to several hundred micrograms. The fissionable material is vacuum-deposited on nickel backings as they undergo rotation. Because of the relatively light weights, accurate determination of the deposit masses requires more sophisticated techniques than weighing. Determinations can be made at the time of fabrication by radioactive spiking and counting, or at a later time by alpha counting, or anytime by counting fissions relative to a known-mass deposit in a suitably constructed fission chamber. When the masses are at the lower end of the mentioned range, or are deposits of a long-lived fissionable material, alpha counting is difficult to do accurately and fission counting is a better method of mass determination or validation.

Because NBS has established a set of deposits with masses in the mentioned range, because these masses are known by a international consensus evaluation to be accurate to $\pm 1.5\%$ (1σ), and because NBS has designed a dual fission chamber in which deposits may be compared (back to back, 0.03 cm apart in the same neutron field), NBS is periodically requested to do mass determinations. For thermally fissionable isotopes, the thermal column at the NBS Reactor provides both external beams and an isotropic neutron field inside a 30-cm diameter cavity in graphite. For fission by higher energy neutrons, ^{252}Cf fission neutron fields are available. Effects, during the irradiations, of geometry and spatial fluence-rate gradients are compensated for by rotating the chamber 180° for about half of the time of the fission-rate measurements.

Table NBS-1 gives a summary of measurements of the masses of 32 fission deposits belonging to Hanford Engineering Development Laboratory (HEDL). The importance of these masses to the NRC's Light Water Reactor Pressure Vessel Surveillance Dosimetry Improvement Program (LWR-PV-SDIP) is that the deposits were used to make the physics-dosimetry measurements that were used

to characterize the neutron fields in the low-powered, pressure vessel simulator (PVS) experiments at the Pool Critical Assembly (PCA) at ORNL, in the VENUS Experiment at CEN/SCK (Mol, Belgium), and in the NESDIP Experiment at Winfrith, UK. Details of the measurement methods results are to be published as a NUREG report in early 1987.

Table NBS-1 lists 34 measurements (two repeats) of deposits that have been identified by markings that HEDL had put on the containers in which they were shipped. The third column of the table gives the deposit masses as determined at NBS by comparing fission rates with the reference deposits listed in the last column of the table. The fourth column of the table specifies the multiplicative correction for the loss of fission fragments in the HEDL deposits. Because the measurements required considerable irradiation time (in excess of 150 hours), measurements in the ^{252}Cf spectrum were accomplished with two fission chambers, each containing two deposits, on either side of the ^{252}Cf source. To provide for a sufficient number of reference deposits with essentially the same masses, extra ratio measurements were made between NBS deposit 37K-05-02 and HEDL deposit 37K-05-04 and then the latter was used as a secondary reference deposit. Consequently, 37K-05-04 is listed on both sides of the table. The additional uncertainty (0.3%) is taken into account in Table NBS-2.

Table NBS-2 provides a summary of the uncertainties that stem primarily from the uncertainties on the masses of the reference deposits and the counting statistics. The deposits were rotated during the irradiation, and the fission rates are determined from the geometric mean of these results. The geometric mean is the square root of the product of the rotated measurements. The order of the deposits is the same in the two tables, and the additional uncertainty because of also using 37K-05-04 as a references is evident in the total uncertainties given in the last column of Table NBS-2.

Expected Future Accomplishments

Details of the measurement method results are to be published as a NUREG report in early 1987.

TABLE NBS-1

SUMMARY OF NBS DETERMINATIONS OF SSTR FISSION DEPOSIT MASSES

No.	Deposit I.D.	Deposit Mass (micrograms)	Fission Fragment Absorption Correction	NBS Reference Deposit
1	35N-65	61.902	1.00337	25A-3-6
2	35N-62	61.630	1.00335	"
3	35N-63	61.898	1.00337	"
4	35N-64	62.236	1.00338	"
5	Rud-55	63.245	1.00344	"
6	35N-76	257.26	1.01399	"
7	35N-77	256.67	1.01396	"
8	35N-78	257.03	1.01398	"
9	35N-52	589.84	1.03208	"
10	35N-53	593.55	1.03228	"
11	35N-54	594.28	1.03232	"
12	35N-55	595.51	1.03238	"
13	37K-1-1	128.56	1.00699	37K-05-02
14	37K-1-2	127.29	1.00692	37K-1-1
15	37K-05-04	69.749	1.00379	37K-05-02
16	37K-1-2	128.01 (repeat)	1.00696	37K-05-04
17	37K-1-3	120.91	1.00658	37K-05-02
18	37K-2-1	255.05	1.01387	"
19	37K-2-2	266.18	1.01448	"
20	37K-2-3	270.84	1.01473	37K-05-04
21	37K-20	238.08	1.01295	"
22	37K-3-1	378.08	1.02056	37K-05-02
23	37K-3-2	392.88	1.02137	37K-05-04
24	37K-3-3	386.52	1.02102	37K-05-02
25	37K-3-4	396.19	1.02155	37K-05-04
26	37K-3-4	394.05 (repeat)	1.02143	37K-05-02
27	37K-31	128.97	1.00710	37K-05-04
28	37K-Ru-133	162.58	1.00884	"
29	37K-Ru-137	168.06	1.00914	37K-05-02
30	37K-Ru-141	173.55	1.00940	37K-05-04
31	37K-Ru-16.6	19.606	1.00107	37K-05-02
32	37K-Ru-17.8	20.943	1.00114	37K-05-04
33	28-U-42.88	42.407	1.00231	28S-2-1
34	28-U-75.97	75.722	1.00412	28HD-5-2

TABLE NBS-2

SUMMARY OF UNCERTAINTIES ON MASSES OF HEDL SSTR FISSION DEPOSITS

No.	I.D.	Statistics on Ratio (%)	Uncertainty on Reference Deposit (%)	Total Uncertainty on Mass (%)
1	35N-65	0.25	0.60	0.65
2	35N-62	0.25	0.60	0.65
3	35N-63	0.25	0.60	0.65
4	35N-64	0.25	0.60	0.65
5	Rud-55	0.25	0.60	0.65
6	35N-76	0.20	0.60	0.63
7	35N-77	0.20	0.60	0.63
8	35N-78	0.20	0.60	0.63
9	35N-52	0.20	0.60	0.63
10	35N-53	0.20	0.60	0.63
11	35N-54	0.20	0.60	0.63
12	35N-55	0.20	0.60	0.63
13	37K-1-1	0.40	1.10	1.17
14	37K-1-2	0.40	1.55	1.50
15	37K-05-04	0.30	1.10	1.14
16	37K-1-2	0.45	1.50	1.57
17	37K-1-3	0.40	1.10	1.14
18	37K-2-1	0.40	1.10	1.14
19	37K-2-2	0.40	1.10	1.14
20	37K-2-3	0.45	1.50	1.57
21	37K-20	0.45	1.50	1.57
22	37K-3-1	0.40	1.10	1.14
23	37K-3-2	0.45	1.50	1.57
24	37K-3-3	0.40	1.10	1.14
25	37K-3-4	0.45	1.50	1.57
26	37K-3-4	0.40	1.10	1.14
27	37K-31	0.45	1.50	1.57
28	37K-Ru-133	0.45	1.50	1.57
29	37K-Ru-137	0.40	1.10	1.14
30	37K-Ru-141	0.40	1.50	1.55
31	37K-Ru-16.6	0.65	1.10	1.28
32	37K-Ru-17.8	0.70	1.50	1.66
33	28-U-42.88	0.50	1.00	1.12
34	28-U-75.97	0.50	1.30	1.40

B. FINAL PHYSICS-DOSIMETRY RESULTS FOR PCA

E. D. McGarry (NBS), F. H. Ruddy (W/R&D), A. Fabry (CEN/SCK),
L. S. Kellogg, C. C. Preston and R. Gold (HEDL), and J. H. Roberts (MC2)

Objective

The objectives are to resolve discrepancies among PCA neutron dosimetry measurements, derive final dosimetry data for the neutronics characterization of the PCA configurations used by LWR-PV-SDIP, assign uncertainties to those results, and then evaluate the data by spectral adjustment techniques so that a reevaluation of the PCA Transport Calculation Blind Test can be made.

Summary

Comparison of SSTR measurements for ^{237}Np and ^{238}U fission rate with corresponding measurements made in the PCA block with the NBS double fission chamber have shown a discrepancy of about 10%. It has been concluded that this is a perturbation effect created by the introduction of the fission chamber into the PV environment. More specifically, the void introduced by the fission chamber during measurements in the PCA block produces approximately a 10% perturbation (increase) in the measured fission rates. Previously published consensus fission rates for ^{238}U and ^{237}Np in the PCA must now be revised. Furthermore, the uncertainty will be reduced but this will depend upon the data set (PCA configuration) under consideration because, for some configurations, considerably more of one type of data exists than for another. These changes in the PCA experimental results have direct bearing on the PCA Blind Test results. The basis for the Blind Test evaluations was the C/E ratios. This change in ^{238}U and ^{237}Np fission rates will increase the averaged C/E ratios by ~5%. FERRET-SAND-II least-squares' analyses will be performed with these revised fission rates.

Accomplishments and Status

Comparisons of PCA SSTR measurements of ^{237}Np and ^{238}U fission rates with corresponding fission-rate measurements made with an NBS double fission chamber (FC) revealed a systematic discrepancy of about 10%. Fission chamber results were always larger and the discrepancy was essentially the same for fission in ^{237}Np and in ^{238}U. The average ratio of 12 sets of PCA measurements of ^{238}U in the PVS block was 0.890 $\pm$ 0.023 with no discernable dependence on PCA configuration or block location. The SSTR/FC ratio for ^{237}Np was 0.906 $\pm$ 0.026 (Mc85g,Mc86c).

On the basis of these results, a direct comparison between SSTR and fission chamber measurements was undertaken to determine the cause of the discrepancy. ^{238}U fission rates were measured with SSTRs inside both the usual SSTR holder and the NBS double fission chamber. Measurements were made in the PCA, PVS block at the 1/4-T location. The SSTR holder consisted of two halves of an iron cylinder with a slight disk-shaped void to hold the SSTR. The fission chamber, which is a larger-volume, gas-filled ionization chamber

(see Figure NBS-1) was also contained inside of an iron cylinder for the PCA measurements. However, the volume of the void that accommodates the fission chamber is more like 5 cm^3 rather than the small 0.2 cm^3 volume in the SSTR holder.

Perturbation measurements were made with both ^{238}U SSTRs and ^{238}U radiometric foils. The ratio of the essentially void-free SSTR measurements to SSTR measurements inside the fission chamber is 0.900 $\pm$ 0.038. Results are tabulated in Table NBS-3. With less accuracy ($\pm$6.4%), the radiometric results were 0.935 $\pm$ 0.06. These results further support the existence of a 10% perturbation.

Table NBS-3 presents the results of four SSTR measurements. Because the void in which the NBS fission chamber resides is not symmetrical with respect to the chamber centerline, fission chamber results are obtained by averaging two measurements for which the chamber orientation differs by 180°. Table NBS-3, and previous results (Mc81,Mc84), show that the orientation causes about a 5% difference. Such orientation averaging is not necessary for the SSTRs, so the PCA-56 and PCA-58 SSTR results indicate the degree of SSTR measurement reproducibility. These two results differ by 4.5%, which is within the 2σ uncertainty band caused by the track counting statistics amassed together with the uncertainty of run-to-run power normalization.

The last column of the table gives the measured SSTR fission rate per atom of deposit thickness divided by the integrated count of a separate fission chamber that was held fixed during the experiment to serve as a run-to-run power monitor. In addition, results in the last column include a multiplicative factor of 1.0126, which is an SSTR efficiency factor. As indicated by the tabulated ratios, and the last footnote, there is good agreement with the mentioned 10% discrepancy observed earlier.

Perturbation-experiment results only provide data for ^{238}U and not for ^{237}Np. This is because of an accident with the NBS fission chamber near the end of the experiment that prevented data necessary for the ^{237}Np comparison from being obtained.

Table NBS-4 provides the revised final fission equivalent fluence rates for ^{237}Np and ^{238}U in the 8/7, 12/13, and 4/12 SSC configurations of the PCA. Table NBS-5 provides fission rates for these same PCA configurations for ^{237}Np, ^{238}U and ^{232}Th. The ^{232}Th data were measured with SSTRs only. Other data are a complex array of fission chamber, SSTR and radiometric results.

Expected Future Accomplishments

FERRET-SAND-II least-squares analyses will be performed using the final physics-dosimetry results for the PCA. Results are expected to be documented in the LWR-PV-SDIP 1987 Annual Report.

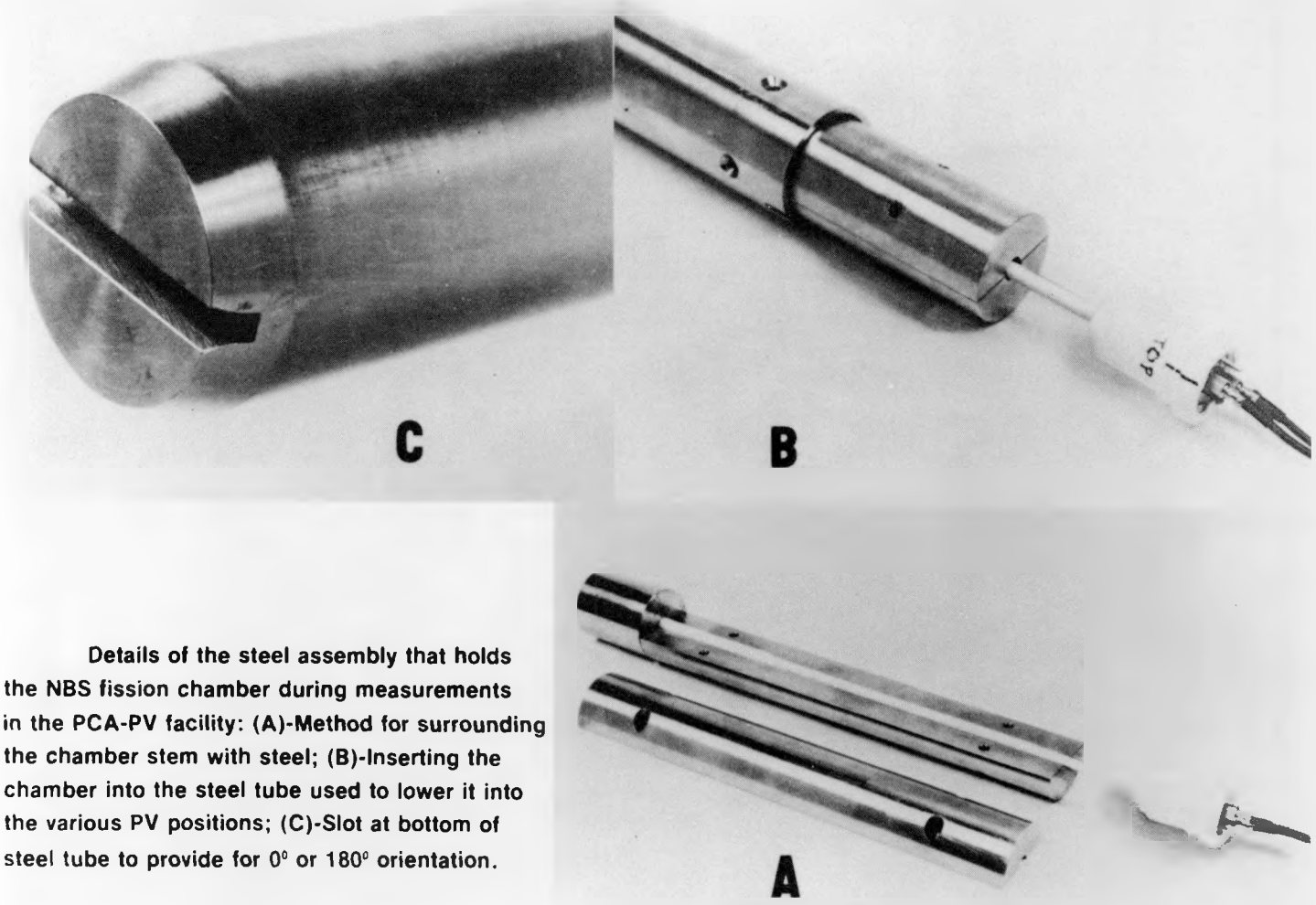

Details of the steel assembly that holds the NBS fission chamber during measurements in the PCA-PV facility: (A)-Method for surrounding the chamber stem with steel; (B)-Inserting the chamber into the steel tube used to lower it into the various PV positions; (C)-Slot at bottom of steel tube to provide for 0° or 180° orientation.

FIGURE NBS-1. Steel Assembly Used to Hold NBS Fission Chamber During Measurements in the PCA-PV.

TABLE NBS-3

PCA FISSION CHAMBER PERTURBATION EXPERIMENT FINAL SSTR RESULTS

Run I.D.	Integrated Power (Mol Fission Chamber Count)	Track Density* (tracks/cm²)	Deposit Thickness** (μg/cm²)	Fission Rate*** (fissions/atom/[FC count])
PCA-55 (FC-0°)	468800	25870 (±1.79%)	34.41 (±0.8%)	6.418×10^{-19} (±2.23%)
PCA-56 (RM-0°)	380100	32260 (±0.78%)	61.36 (±0.5%)	5.536×10^{-19} (±2.14%)
PCA-58 (RM-0°)	135100	11980 (±1.43%)	61.36 (±0.5%)	5.784×10^{-19} (±2.14%)
PCA-59 (FC-180°)	476000	25200 (±1.80%)	34.41 (±0.8%)	6.158×10^{-19} (±2.79%)

Average of the two "void-free" runs (PCA-56 & PCA-58) = 5.660×10^{-19} fiss/a/FC count (±3.10%)

Average of the two fission chamber rotations (PCA-55 & PCA-59) = 6.288×10^{-19} fiss/a/FC count (±2.97%)

$$\frac{\text{(SSTR) "void-free"}}{\text{(SSTR) fission chamber}} = \frac{5.660 \times 10^{-19}}{6.288 \times 10^{-19}} = 0.900\ (\pm 3.6\%)^{****}$$

$$\frac{\text{(SSTR) FC-0°}}{\text{(SSTR) FC-180°}} = 1.042\ (\pm 3.6\%)$$

*Numbers in parentheses indicated agreement between three independent scanners; 3000 tracks were scanned (1σ = 1.83%) by each scanner.

**HEDL deposit calibrations of April 1984.

***Assuming 1% uncertainty on the run-to-run power-level monitor.

****This result is in good agreement with the average value of 0.889 (±2.6%) from 12 SSTR-to-FC, ^{238}U fission-rate ratio measurements from the PCA. Similar results were observed for ^{237}Np at the PCA.

TABLE NBS-4

RECOMMENDED VALUES FOR ^{237}Np AND ^{238}U
(PCA Equivalent Fission Fluxes)

Midplane Location	Distance from Core (cm)	Equivalent Fission Fluxes per PCA Core Neutron (x 10^8) ^{237}Np		^{238}U	
		(8/7 Configuration)			
TSF (A1)	7.9	1460	(±6.2%)*	------	
PVF (A3)	19.7	164	(±6.3%)*	------	
1/4 T (A4)	29.5	53.3	(±6.2%)	29.0	(±4.8%)
1/2 T (A5)	34.7	30.1	(±6.7%)	12.9	(±5.0%)
3/4 T (A6)	40.1	14.6	(±6.1%)	5.3	(±4.8%)
		(12/13 Configuration)			
TSF (A1)	12.0	588	(±5.3%)**	------	
TSB (A2)	23.8	55.1	(±5.3%)**	------	
PVF (A3)	29.7	22.9	(±5.8%)***	19.2	(±5.8%)**
1/4 T (A4)	39.5	8.77	(±5.5%)	5.49	(±4.9%)
1/2 T (A5)	44.7	4.63	(±6.8%)	2.39	(±4.9%)
3/4 T (A6)	50.1	2.47	(±5.3%)***	1.01	(±4.9%)
VB (A7)	59.1	0.72	(±7.3%)***	0.28	(±4.9%)
		(4/12 SSC Configuration)			
SSC (A2)	15.6	631	(±4.8%)**	364.	(±4.8%)**
1/4 T (A4)	30.5	46.7	(±4.8%)	21.0	(±4.8%)
1/2 T (A5)	35.7	25.7	(±4.8%)****	9.61	(±4.8%)****
3/4 T (A6)	41.1	13.2	(±5.7%)*	4.09	(±6.0%)*
VB (A7)	50.1	4.01	(±5.8%)*	1.02	(±5.8%)*

*Only CEN/SCK fission chamber measurements were made at these locations.
**Only HEDL SSTR measurements were made at these locations.
***These measurements were averages of CEN/SCK fission chamber and HEDL SSTR results. No detectable bias existed between the two laboratories' results.
****Only NBS fission chamber measurements were made at these locations. Former (Mc84i) values were reduced by multiplication by 0.90.

TABLE NBS-5

RECOMMENDED VALUES FOR ^{237}Np, ^{238}U, AND ^{232}Th FISSION RATES

Midplane Location	Distance from Core (cm)	Fission Rates per Core Neutron* (fissions/atom/neutron) X10^{33} ^{237}Np	^{238}U	^{232}Th
		(8/7 Configuration)		
TS (A1)	7.9	19500 (±6.2%)	-----	-----
PVF (A3)	19.7	2190 (±6.3%)	-----	-----
1/4 T (A4)	29.5	711 (±6.2%)	89.2 (±4.8%)	21.5 (±4.8%)
1/2 T (A5)	34.7	402 (±6.7%)	39.8 (±5.0%)	9.24 (±4.8%)
3/4 T (A6)	40.1	195 (±6.1%)	16.2 (±4.8%)	3.46 (±4.8%)
VB (A7)	49.1	-----	-----	0.782 (±5.0%)
		(12/13 Configuration)		
TSF (A1)	12.0	7850 (±5.3%)	-----	-----
TSB (A2)	23.8	735 (±5.3%)	-----	-----
PVF (A3)	29.7	305 (±5.8%)	59.1 (±5.8%)	-----
1/4 T (A4)	39.5	117 (±5.5%)	16.9 (±4.9%)	3.56 (±4.9%)
1/2 T (A5)	44.7	61.7 (±6.8%)	7.39 (±4.9%)	1.55 (±5.1%)
3/4 T (A6)	50.1	33.0 (±5.3%)	3.11 (±4.9%)	0.595 (±4.9%)
VB (A7)	59.1	9.6 (±7.3%)	0.867 (±4.9%)	0.132 (±4.7%)
		(4/12 SSC Configuration)		
SSC (A2)	15.6	8420 (±4.8%)	1120 (±4.8%)	-----
1/4 T (A4)	30.5	623 (±4.8%)	64.6 (±4.8%)	-----
1/2 T (A5)	35.7	343 (±4.8%)	29.6 (±4.8%)	-----
3/4 T (A6)	41.1	178 (±5.7%)	12.6 (±6.0%)	-----
VB (A7)	50.1	53.5 (±5.8%)	3.14 (±5.8%)	-----

*The values in this table are related to those in Table NBS-5 by the factors of 1.334 barns for ^{237}Np and 0.308 barns for ^{238}U; additional uncertainties have not been factored in because of this conversion.

C. ASTM STANDARD IIE AND NBS COMPENDIUM

E. D. McGarry and J. A. Grundl (NBS)

Objective

The objectives are to produce a new ASTM Standard Guide for referencing reactor pressure vessel surveillance dosimetry measurements to irradiations in benchmark neutron fields and to provide a compendium of the physical and radiation characteristics of the benchmark fields.

Summary

See Accomplishments and Status.

Accomplishments and Status

1.0 ASTM Standard IIE

In parallel with the development of a compendium and in support of the LWR-PV-SDIP development of engineering types of benchmark fields or facilities, a new ASTM standard guide E706(IIE) entitled "Benchmark Testing of Reactor Vessel Dosimetry" will be reviewed at the ASTM E10.05 meeting in Tampa, FL, January 26-28, 1987.

2.0 Compendium

The 1986 version of the NBS Compendium of Neutron Fields for Benchmarking LWR-PV Surveillance Dosimetry was published as NBSIR-85-3151. The next entry will be the PCA, which will be based on updated integral data, including the recommended fission rate results of Table NBS-2.

Expected Future Accomplishments

Work will continue on the next updated revision of the NBS Compendium and completion of the revision, ballotting and acceptance of the E706(IIE) standard. The schedule for this last effort is provided in Figure S-2.

WESTINGHOUSE - NUCLEAR TECHNOLOGY DIVISION

A. ONE-DIMENSIONAL NEUTRON TRANSPORT ANALYSIS OF THE GUNDREMMINGEN BOILING WATER REACTOR*

S. L. Anderson (W-NTD)

Objective

The objective of the present work was to provide a one-dimensional (1D) discrete ordinates neutron transport analysis of the Gundremmingen boiling water reactor (BWR) geometry. This 1D analysis could be used for scoping evaluations of the neutron field within the reactor for use in the correlation of neutron damage data obtained from materials surveillance capsules as well as from trepans of material removed from the pressure vessel (PV).

Summary

This report was prepared by W-NTD in support of the NRC-sponsored LWR-PV-SDIP. Results are given of a 1D discrete ordinates neutron transport analysis of the Gundremmingen BWR geometry. Neutron exposure parameter values ($E > 1.0$ MeV), ($E > 0.1$ MeV) and dpa in iron are listed for a location one inch from the outer radius of the core shroud as well as at the cladding/vessel wall. Also presented at each location are the ratios of fluence ($E > 0.1$ MeV) and dpa to fluence ($E > 1.0$ MeV). These ratios provide insight into the spectral shift toward lower energies that occurs with penetration into the PV and are an indicator of the different attenuation slopes exhibited by the three exposure parameters. Calculated neutron spectra at six locations within the reactor geometry are also given. These spectra are suitable for use as input to adjustment codes or for direct determination of spectrum-averaged cross sections to be used in dosimetry evaluations for the PV. Since surveillance capsule perturbation effects have not been addressed, caution should be exercised in the use of these data for damage or dosimetry assessments.

Results of a three-dimensional (3D) neutron spectrum analysis performed by IKE (Institut für Kernenergetik und Energiesysteme, Universität Stuttgart) are briefly summarized and are referenced in Section IKE-A.

Accomplishments and Status

1.0 Background

The purpose of this analysis was to provide scoping evaluations of the neutron field within the reactor for use in the correlation of neutron damage data obtained from Gundremmingen materials surveillance capsules as well as from trepans of material removed from the reactor vessel beltline region. In particular, the intent was to investigate the neutron spectral differences that occur between the surveillance locations and positions at the inner diameter and through the thickness of the reactor vessel wall.

---

*Prepared as FSD-RSA-85/2701 under purchase order Y4W-S44-26847 between W-NTD and WHC.

This report provides the results of a 1D discrete ordinates neutron transport analysis of the Gundremmingen boiling water reactor geometry.

2.0 Introduction

Because of limitations inherent in the ID analysis approach, accurate assessment of the absolute magnitude of important exposure parameters such as fluence (E > 1.0 MeV), fluence (E > 0.1 MeV), or iron displacements per atom (dpa) are not possible. Key factors including two-dimensional (2D) effects introduced by core geometry, three-dimensional (3D) variability in reactor power distributions, and local perturbations induced by the presence of surveillance capsules and associated structure cannot be adequately addressed using the 1D approach. However, neutron spectral variations which, on a relative basis, are generally controlled by local rather than global geometries can be evaluated with good accuracy using 1D techniques. The single exception to this rule would occur within a surveillance capsule where even the local geometry is not modelled in the calculations.

Given these limitations in the analytical approach, the direction taken in this report is to provide neutron spectra and exposure parameters relative to a source of 1.0 n/s-cm in the reactor core. In subsequent sections of this report, data are presented for the 0-T, 1/4-T, 1/2-T, 3/4-T, and 1-T positions within the PV wall as well as for a position in the water annulus located between the core shroud and the thermal shield. The vessel data, in particular, should represent a good basis for the evaluation of neutron dosimetry obtained from the trepans and should be valuable in the evaluation of variations in damage rates caused by spectral differences through the thickness of the PV wall. Furthermore, when ultimately normalized to the dosimetry data, these spectral sets will provide a description of the absolute exposure fields within the PV wall.

The additional set of spectral data provided for the downcomer region is intended for illustrative purposes only. Since surveillance capsule materials were not included in the calculation, the data do not include capsule perturbation effects and, as such, do not accurately represent surveillance specimen exposures. The data merely provide an indication of the relative strength of the neutron field in the vicinity of the capsule.

3.0 Method of Analysis

In the analysis of the neutron environment within the Gundremmingen reactor, predictions of the spatial and energy variations of the neutron field were made with the ANISN 1D discrete ordinates code (So70). The analysis employed 47 neutron energy groups and a P_3 expansion of the scattering cross sections. The cross-sections used in the analysis were obtained from the SAILOR cross-section library (OaSa), which was developed specifically for light water reactor (LWR) applications. The neutron energy group structure used in the analysis is listed in Table NTD-1. In the one-dimensional calculation, the angular discretization was approximated with an S_8 order of angular quadrature.

TABLE NTD-1

47-GROUP ENERGY STRUCTURE

Group	Lower Energy (MeV)	Group	Lower Energy (MeV)
1	14.19[a]	25	0.183
2	12.21	26	0.111
3	10.00	27	0.0674
4	8.61	28	0.0409
5	7.41	29	0.0318
6	6.07	30	0.0261
7	4.97	31	0.0242
8	3.68	32	0.0219
9	3.01	33	0.0150
10	2.73	34	7.10×10^{-3}
11	2.47	35	3.36×10^{-3}
12	2.37	36	1.59×10^{-3}
13	2.35	37	4.54×10^{-4}
14	2.23	38	2.14×10^{-4}
15	1.92	39	1.01×10^{-4}
16	1.65	40	3.73×10^{-5}
17	1.35	41	1.07×10^{-5}
18	1.00	42	5.04×10^{-6}
19	0.821	43	1.86×10^{-6}
20	0.743	44	8.76×10^{-7}
21	0.608	45	4.14×10^{-7}
22	0.498	46	1.00×10^{-7}
23	0.369	47	0.00
24	0.298		

[a] The upper energy of group 1 is 17.33 MeV.

The physical dimensions of the Gundremmingen reactor as well as the material compositions were obtained from correspondence.* The model used in the analysis was as follows:

Reactor core outer radius	137.45 cm
Shroud inner radius	147.45 cm
Shroud outer radius	150.45 cm
Thermal shield inner radius	180.45 cm
Thermal shield outer radius	182.99 cm
Vessel clad inner radius	185.53 cm
Vessel inner radius	186.16 cm
Vessel outer radius	199.49 cm
Insulation outer radius	209.49 cm
Shield inner radius	229.49 cm

The model as described is representative of geometric regions located on the reactor core axial midplane. The core region itself has been modelled as an equivalent area cylinder in the 1D computation. No DB^2 corrections to approximate axial leakage from the system were applied to any of the geometric regions in the problem.

As stated earlier, the one-dimensional calculation was normalized to a total source strength of one neutron per second per centimeter of core height. The spatial distribution was taken to be constant with radius and the energy distribution of the source was assumed to be given by the ENDFB-IV Uranium-235 fission spectrum provided with the SAILOR cross-section library.

Strictly speaking, the assumption of a neutron source that remains constant with core radius is not accurate. However, since the purpose of this calculation is to provide spectral variations and not absolute magnitudes, the error introduced by the employment of this assumption is considered to be negligible.

4.0 Results of Analysis

Results of the 1D neutron transport analysis of the Gundremmingen reactor are given in Tables NTD-2 and NTD-3. In Table NTD-2, exposure parameters (E > 1.0 MeV), (E > 0.1 MeV, dpa) are listed at a location one inch from the outer radius of the core shroud as well as at the clad/vessel wall. Also presented at each location are the ratios of fluence (E > 0.1 MeV) and dpa to fluence (E > 1.0 MeV). These ratios provide insight into the spectral shift toward lower energies that occurs with penetration into the PV and are an indicator of the different attenuation slopes exhibited by the three exposure parameters.

---

*Correspondence from Fendler and Preusch, "Auslegung der Abschirmung des Reaktorkernes (1007-237MW KRB)," AEG-6343, Allgemeine Elektricitats Gesellschaft, FRG, January 1964, and "Neutronen-und Gammastrahlungs - messungen im Kernkraftwerk Gundremmingen," Kraftwork Union Aktiengesellschaft, FRG, R315/35/1977, August 1977.

TABLE NTD-2

CALCULATED EXPOSURE PARAMETERS WITHIN THE GUNDREMMINGEN REACTOR GEOMETRY

LOCATION	ϕ(E>1.0MeV)	ϕ(E>0.1MeV)	dPa/sec	$\frac{\phi(E>0.1)}{\phi(E>1.0)}$	$\frac{dPa/sec}{\phi(E>1.0)}$
SURV.	1.61×10^{-6}	4.19×10^{-6}	2.52×10^{-27}	2.60	1.57×10^{-21}
OT	6.66×10^{-8}	1.84×10^{-7}	1.10×10^{-28}	2.76	1.65×10^{-21}
1/4T	4.85×10^{-8}	1.75×10^{-7}	8.89×10^{-29}	3.61	1.83×10^{-21}
1/2T	3.33×10^{-8}	1.54×10^{-7}	6.96×10^{-29}	4.62	2.09×10^{-21}
3/4T	1.85×10^{-8}	1.20×10^{-7}	4.84×10^{-29}	6.49	2.62×10^{-21}
1T	1.23×10^{-8}	9.97×10^{-8}	3.79×10^{-29}	8.11	3.08×10^{-21}

In Table NTD-3, the calculated neutron spectra at the six locations within the reactor geometry are given in the group structure shown in Table NTD-1. The group fluxes listed in Table NTD-2 for the PV locations are suitable for use as a spectrum guess for input to adjustment codes or for direct determination of spectrum-averaged cross sections to be used in dosimetry evaluations for the PV. The fluxes are also suitable for use in establishing damage gradients through the PV wall. Again, since the data for locations near the core shroud do not include capsule perturbation effects, caution should be exercised in the use of these data for damage or dosimetry assessments.

Expected Future Accomplishments

Work on this subject by W-NTD is complete.

TABLE NTD-3

CALCULATED NEUTRON SPECTRA WITHIN THE GUNDREMMINGEN REACTOR

Group	NEUTRON FLUX {n/cm^2-sec}/SOURCE NEUTRON					
	Surv.	0T	1/4T	1/2T	3/4T	1T
1	2.08×10^{-10}	1.97×10^{-11}	1.19×10^{-11}	7.51×10^{-12}	3.81×10^{-12}	2.42×10^{-12}
2	8.06×10^{-10}	7.53×10^{-11}	4.58×10^{-11}	2.89×10^{-11}	1.46×10^{-11}	9.30×10^{-12}
3	3.45×10^{-9}	2.69×10^{-10}	1.60×10^{-10}	9.98×10^{-11}	4.80×10^{-11}	2.98×10^{-11}
4	7.17×10^{-9}	5.08×10^{-10}	2.98×10^{-10}	1.82×10^{-10}	8.70×10^{-11}	5.30×10^{-11}
5	1.37×10^{-8}	8.59×10^{-10}	4.97×10^{-10}	2.98×10^{-10}	1.38×10^{-10}	8.25×10^{-11}
6	3.53×10^{-8}	1.97×10^{-9}	1.13×10^{-9}	6.59×10^{-10}	2.95×10^{-10}	1.72×10^{-10}
7	5.64×10^{-8}	2.74×10^{-9}	1.52×10^{-9}	8.70×10^{-10}	3.77×10^{-10}	2.16×10^{-10}
8	1.24×10^{-7}	5.16×10^{-9}	2.88×10^{-9}	1.65×10^{-9}	7.15×10^{-10}	4.08×10^{-10}
9	1.12×10^{-7}	4.03×10^{-9}	2.38×10^{-9}	1.41×10^{-9}	6.42×10^{-10}	3.77×10^{-10}
10	8.49×10^{-8}	3.17×10^{-9}	1.99×10^{-9}	1.20×10^{-9}	5.63×10^{-10}	3.36×10^{-10}
11	9.79×10^{-8}	3.65×10^{-9}	2.35×10^{-9}	1.44×10^{-9}	6.84×10^{-10}	4.12×10^{-10}
12	4.72×10^{-8}	1.85×10^{-9}	1.20×10^{-9}	7.39×10^{-10}	3.52×10^{-10}	2.13×10^{-10}
13	1.31×10^{-8}	5.25×10^{-10}	3.55×10^{-10}	2.28×10^{-10}	1.14×10^{-10}	7.03×10^{-11}
14	6.31×10^{-8}	2.50×10^{-9}	1.75×10^{-9}	1.13×10^{-9}	5.73×10^{-10}	3.58×10^{-10}
15	1.57×10^{-7}	6.30×10^{-9}	4.48×10^{-9}	2.92×10^{-9}	1.48×10^{-9}	9.31×10^{-10}
16	1.87×10^{-7}	7.03×10^{-9}	5.42×10^{-9}	3.77×10^{-9}	2.09×10^{-9}	1.38×10^{-9}
17	2.64×10^{-7}	1.01×10^{-8}	8.03×10^{-9}	5.71×10^{-9}	3.26×10^{-9}	2.18×10^{-9}
18	4.48×10^{-7}	1.58×10^{-8}	1.41×10^{-8}	1.10×10^{-8}	7.05×10^{-9}	5.08×10^{-9}
19	3.10×10^{-7}	1.04×10^{-8}	9.74×10^{-9}	8.06×10^{-9}	5.64×10^{-9}	4.32×10^{-9}
20	1.61×10^{-7}	5.64×10^{-9}	4.84×10^{-9}	3.83×10^{-9}	2.57×10^{-9}	1.92×10^{-9}
21	3.86×10^{-7}	1.66×10^{-8}	1.90×10^{-8}	1.77×10^{-8}	1.43×10^{-8}	1.19×10^{-8}
22	3.24×10^{-7}	1.27×10^{-8}	1.31×10^{-8}	1.18×10^{-8}	9.52×10^{-9}	7.94×10^{-9}
23	3.50×10^{-7}	1.61×10^{-8}	1.87×10^{-8}	1.80×10^{-8}	1.53×10^{-8}	1.31×10^{-8}
24	3.07×10^{-7}	1.55×10^{-8}	1.97×10^{-8}	2.04×10^{-8}	1.90×10^{-8}	1.70×10^{-8}
25	4.73×10^{-7}	1.97×10^{-8}	1.90×10^{-8}	1.75×10^{-8}	1.48×10^{-8}	1.28×10^{-8}
26	4.17×10^{-7}	2.01×10^{-8}	2.28×10^{-8}	2.28×10^{-8}	2.05×10^{-8}	1.84×10^{-8}
27	3.38×10^{-7}	1.71×10^{-8}	2.04×10^{-8}	2.11×10^{-8}	2.01×10^{-8}	1.82×10^{-8}

TABLE NTD-3 (Cont'd)

Group	NEUTRON FLUX {n/cm^2-sec}/SOURCE NEUTRON					
	Surv.	0T	1/4T	1/2T	3/4T	1T
28	2.88×10^{-7}	1.20×10^{-8}	1.05×10^{-8}	9.73×10^{-9}	8.54×10^{-9}	7.60×10^{-9}
29	1.19×10^{-7}	4.65×10^{-9}	2.83×10^{-9}	2.37×10^{-9}	2.01×10^{-9}	1.77×10^{-9}
30	8.58×10^{-8}	3.53×10^{-9}	1.50×10^{-9}	1.24×10^{-9}	1.05×10^{-9}	9.25×10^{-10}
31	5.99×10^{-8}	5.44×10^{-9}	6.76×10^{-9}	6.74×10^{-9}	6.23×10^{-9}	5.69×10^{-9}
32	6.02×10^{-8}	3.43×10^{-9}	4.03×10^{-9}	4.15×10^{-9}	3.98×10^{-9}	3.70×10^{-9}
33	1.71×10^{-7}	7.46×10^{-9}	6.90×10^{-9}	6.52×10^{-9}	5.87×10^{-9}	5.33×10^{-9}
34	3.14×10^{-7}	1.25×10^{-8}	6.11×10^{-9}	4.10×10^{-9}	2.90×10^{-9}	2.47×10^{-9}
35	3.22×10^{-7}	1.56×10^{-8}	1.25×10^{-8}	9.76×10^{-9}	6.90×10^{-9}	5.61×10^{-9}
36	3.22×10^{-7}	1.48×10^{-8}	1.07×10^{-8}	8.23×10^{-9}	5.71×10^{-9}	4.55×10^{-9}
37	5.27×10^{-7}	2.35×10^{-8}	1.46×10^{-8}	1.01×10^{-8}	6.43×10^{-9}	4.92×10^{-9}
38	3.04×10^{-7}	1.45×10^{-8}	8.27×10^{-9}	5.44×10^{-9}	3.29×10^{-9}	2.47×10^{-9}
39	3.16×10^{-7}	1.52×10^{-8}	9.42×10^{-9}	6.19×10^{-9}	3.57×10^{-9}	2.59×10^{-9}
40	4.27×10^{-7}	2.06×10^{08}	1.33×10^{-8}	8.90×10^{-9}	5.03×10^{-9}	3.53×10^{-9}
41	5.37×10^{-7}	2.61×10^{-8}	1.64×10^{-8}	1.08×10^{-8}	6.00×10^{-9}	4.13×10^{-9}
42	3.21×10^{-7}	1.56×10^{-8}	9.25×10^{-9}	5.93×10^{-9}	3.21×10^{-9}	2.18×10^{-9}
43	4.15×10^{-7}	2.02×10^{-8}	1.06×10^{-8}	6.30×10^{-9}	3.19×10^{-9}	2.09×10^{-9}
44	3.00×10^{-7}	1.45×10^{-8}	6.59×10^{-9}	3.55×10^{-9}	1.64×10^{-9}	1.05×10^{-9}
45	2.85×10^{-7}	1.37×10^{08}	5.11×10^{-9}	2.38×10^{-9}	9.67×10^{-10}	5.87×10^{-10}
46	8.85×10^{-7}	3.96×10^{-8}	7.51×10^{-9}	2.02×10^{-9}	4.97×10^{-10}	2.62×10^{-10}
47	3.76×10^{-6}	1.56×10^{-7}	1.21×10^{-8}	1.30×10^{-9}	1.28×10^{-10}	5.33×10^{-11}

B. EVALUATION OF SURVEILLANCE CAPSULE AND REACTOR CAVITY DOSIMETRY FROM H. B. ROBINSON UNIT 2, CYCLE 9

E. P. Lippincott, T. V. Congedo, S. L. Anderson (W-NTD); W. N. McElroy, L. S. Kellogg, W. Y. Matsumoto, R. Gold (HEDL); B. M. Oliver (RI-RD); J. H. Roberts (MC^2); E. D. McGarry (NBS)

Objective

The objective of the present work is to complete the documentation of H. B. Robinson as a PWR physics-dosimetry benchmark that is linked to the PCA, PSF, VENUS, and NESDIP LWR-PV-SDIP series of benchmarks.

Summary

Neutron dosimetry measurements were made for the H. B. Robinson plant during Cycle 9. The dosimetry was contained both at a replacement physics-dosimetry surveillance capsule location and in the reactor cavity outside the vessel. Excellent experimental results were obtained that can be used to benchmark calculations of neutron transport through the reactor vessel for H. B. Robinson and other similar reactors. Calculations performed by Westinghouse show good agreement with measured flux profiles, but the flux magnitude is underpredicted by 15% to 20% at both the surveillance and reactor cavity measurement locations. Reasonable agreement with measured spectral shape is also attained. By using a combination of the calculations and measurements, the fluence at all points in the reactor vessel can be determined to a high degree of accuracy.

Work will continue to link NESDIP and VENUS into the LWR-PV-SDIP series of benchmarks and place them in context with the studies being or already carried out in PCA, PSF and a selected number of existing PWR and BWR power plants. The establishment of H. B. Robinson as one of the PWR benchmarks is, therefore, an important accomplishment. Detailed results of the H. B. Robinson measurements and calculations are reported in WCAP-11104 (NUREG/CR-4576), Ref (Li85).

Accomplishments and Status

In order to determine neutron exposure levels throughout the reactor vessel geometry with a minimum uncertainty, it is necessary to employ a combination of rigorous analytical techniques and state-of-the-art neutron dosimetry. In particular, neutron transport calculations coupled with neutron sensor sets located in the reactor cavity annulus between the pressure vessel (PV) and the primary biological shield provide a promising approach to the determination of both axial and azimuthal exposure gradients within the PV. In addition, such measurements provide a means to test the veracity of analytically determined through-wall neutron exposure gradients.

As a demonstration of the use of this approach, Carolina Power and Light Company entered into a cooperative venture with the NRC-sponsored LWR Pressure Vessel Surveillance Dosimetry Improvement Program (LWR-PV-SDIP) to perform measurements within the reactor cavity of the H. B. Robinson Unit 2 reactor during the ninth fuel cycle.

This cavity dosimetry program was designed to provide a mapping of the neutron exposure over the entire 12-foot height of the reactor core within an azimuthal sector of 45°. Since the reactor core and internals exhibit 1/8th core symmetry, measurements limited to a 45° sector are representative of a complete azimuthal traverse. During reactor operation, significant deviations from octant symmetry would be detected by the four active power range monitors also located in the reactor cavity. Further limitations placed on core operation with significant quadrant to quadrant power tilts would preclude conditions of asymmetry existing for extended periods.

Coincident with the cavity dosimetry irradiation, an in-vessel dosimetry experiment was also conducted to provide a correlation between the cavity data sets and the measurements obtained at a typical surveillance position. This internal experiment was in part funded by the LWR-PV-SDIP with additional support from the Electric Power Research Institute (EPRI).

The replacement surveillance capsule dosimeter set was designed to be installed in a vacant capsule holder attached to the thermal shield at an azimuthal location of 20° relative to a core cardinal axis. Sensor sets were placed at the center of the replacement surveillance capsule such that measurements could be obtained at the axial core midplane. The azimuthal position of the replacement capsule was chosen so that the internal data were obtained from the same reactor octant as the bulk of the external experimental data.

Having both internal and external measurements using the same state-of-the-art sensor sets irradiated over the same power/time history provides the best available opportunity to demonstrate the adequacy of the sensor sets over a wide range of environmental and neutronic conditions. Also, the data from both measurement locations can be used to test the analytical capability to predict exposure levels at points between the measurement locations, i.e., within the PV itself.

Based on the average of the exposure parameters extrapolated from the measurement locations inside and outside the vessel, the best-estimate neutron flux and dpa/s values at the maximum exposure location on the vessel during the Cycle 9 irradiation are as follows:

Exposure Rate Values	1σ Uncertainty (%)
$(E > 1.0\ MeV) = 3.75 \times 10^{10}\ n/cm^2 \cdot s$	10
$(E > 0.1\ MeV) = 1.00 \times 10^{11}\ n/cm^2 \cdot s$	18
$dpa\ rate = 6.15 \times 10^{-11}\ dpa/s$	15

From a measurement viewpoint, excellent results were achieved at both the surveillance and cavity positions because of the excellent agreement of foil results and the number of reactions available. This experiment serves as an important benchmark experiment for the validation of cavity dosimetry to provide improved data for vessel exposure determination. The experiment also demonstrated the potential application of SSTR and HAFM for surveillance dosimetry.

From an analytical viewpoint, the importance of careful attention to both cavity geometry and core neutron source was highlighted. Improved agreement between exposure parameters extrapolated from the vessel and the cavity was achieved by one-dimensional calculation estimates of effects not included in the two-dimensional transport calculation. These results provide insight to enable more sophisticated calculations to be conducted in the future that can be expected to provide improved agreement.

Expected Future Accomplishments

Work will continue to link the H. B. Robinson benchmark into the series of LWR-PV-SDIP benchmark and ASTM standards.

C. SUMMARY OF NEUTRON AND GAMMA-RAY FLUX CALCULATIONS FOR THE VENUS PWR ENGINEERING MOCKUP

A. H. Fero (W-NTD)

Objective

The objective of this work is to perform transport theory calculations and analysis of the neutron and gamma-ray fluxes in the VENUS PWR engineering mockup benchmark experiment.

Summary

This summary describes the analysis of neutron and gamma-ray fluxes in the VENUS PWR engineering mockup benchmark experiment (SCK/CEN Mol, Belgium). The full report is available as WCAP-11173, NUREG/CR-4827, December 1986. Results will also be included in NUREG/CR-3323 (to be published).

Accomplishments and Status

This VENUS PWR mockup is unique in two ways. It is the first mockup to correctly represent the heterogeneities that exist in the PWR core peripheral fuel assemblies, core baffle, core barrel, and neutron pad. This is accomplished by using low-enrichment (3.3 and 4.0 wt% ^{235}U) fuel pins and a representative PWR fuel assembly geometry (15 x 15) with full-thickness Type 304 stainless steel reactor internals structures located with representative water gap spacing. The VENUS mockup also represents locally the stair-step geometry of the core periphery. Second, the VENUS mockup is extremely well characterized in terms of as-built dimensions, material compositions, and pin-by-pin core power distributions. Engineering details of the mockup as well as nuclear and experimental data will be published in NUREG/CR-3323. Figure NTD-1 is a dimensioned illustration of the VENUS model geometry with the experimental data locations identified.

The analysis of VENUS was performed using the methods and procedures used to analyze commercial PWRs. Specifically, two-dimensional discrete ordinates transport theory calculations were performed using the DOT-IIIW code. Calculations were run in both X-Y and R-theta geometries for a 90 degree sector of the mockup. The finite height (50 cm) of the VENUS mockup was accounted for in the X-Y and R-theta DOT calculations by the use of group- and zone-dependent DB^2 terms derived from axial leakages calculated in a DOT R-Z geometry approximation of the mockup.

Fixed distributed source calculations were run S_8-P_3 using the ENDF-B/V ^{235}U thermal fission neutron spectrum and cross sections from the SAILOR and BUGLE-80 (coupled, 47 neutron, 20 gamma-ray groups) cross-section libraries. Microscopic cross sections for Cr, Mn, Fe, Ni, Zr, and ^{238}U were obtained from the SAILOR cross-section library (Si83). Microscopic cross sections for H, B, O, Si, Mo, Co, Sn and ^{235}U were obtained from the BUGLE-80 cross-section library (Ro80a). Both libraries are derived from the VITAMIN-C (171-N, 36-G) cross-section library (Ro77c). In preparing the SAILOR cross sections for

fuel and steel constituents, the VITAMIN-C cross sections are self-shielded in PWR fuel cell and PWR steel/water downcomer geometries. Note that the VITAMIN-C and SAILOR-coupled libraries do not include delayed fission product gamma-rays and that this component must be included in most reactor gamma-ray calculations. A coupled neutron gamma-ray cross-section set for ^{235}U with both prompt and delayed fission product gamma-ray components is available on the BUGLE-80 library. The delayed fission product gamma-ray data are for ^{235}U thermal fission for 10^{13} seconds. Macroscopic cross sections for the 3/0 and 4/0 fuel regions and for the Pyrex® absorber cells were produced by cell homogenization in ANISN runs. The fast reaction dosimetry cross sections are taken from the SAILOR dosimetry file. These data, in turn, are a processing ENDF/B-IV dosimetry cross sections in a SAND-II Library collapsed over the spectrum at a 1/4-T position in a PWR reactor vessel. The gamma-ray energy deposition response was developed from the kerma factor data (eV-barn/atom) on the BUGLE-80 library, which in turn was obtained from (Go82d). The photofission cross sections were taken from (Ve80). The conversion of reaction rates to equivalent fission fluxes used fission spectrum-averaged reaction cross sections (As85).

Calculated results are taken from both the X-Y and R-theta DOT runs. Calculated values in the center hole, inner baffle, 3/0 fuel, 4/0 fuel, and outer baffle are taken from the X-Y DOT run while calculated values in the core barrel, the water gap between the core barrel and the neutron pad, and the neutron pad are taken from the R-theta DOT run. Values in the water between the outer baffle and the core barrel were obtained from both DOT runs. Tables NTD-4 through 6 present comparisons of calculated and experimental equivalent fission fluxes for fast neutron reactions in ^{237}Np (n,f), ^{238}U (n,f), ^{58}Ni (n,p), and ^{115}In (n,n'). Refer to Figure NTD-1 for the location of the data points in the VENUS geometry. Tables NTD-7 and 8 contain the calculated photoreaction data for the ^{237}Np (γ,f), ^{238}U (γ,f), and ^{115}In (γ,γ') reactions at the same locations used in Tables NTD-4 through 6. Ratios of calculated photoreaction to calculated neutron reaction, and ratios of calculated neutron plus photoreaction to total measured reaction are also provided. Table NTD-9 presents comparisons of a calculated and measured gamma-ray energy deposition rate data in the VENUS steel regions. The measured data presented are the average of three different measurements (made by SCK/CEN using Al_2O_3 TLDs, RRA using ^{7}LiF TLDs, and CEGB using BeO TLDs).

An examination of the comparisons of calculation to measurement for the fast neutron reactions (Tables NTD-4 through 6) shows overall agreement that is generally within $\pm$10%. There is a clear indication of a radial calculation bias, with a tendency to underpredict the measurements farther away from the core (core barrel and water gap II). There is excellent agreement in the prediction of the azimuthal behavior in the system. Any azimuthal bias is not strong enough to be distinguished from the scatter present in the C/E ratios. An examination of Tables NTD-7 and 8 shows that, based on the calculations,

---

®Pyrex is a registered trademark of PUREX Corporation, Lakewood, CA.

photo reactions do not play a major role in the VENUS measurements. Photofission contributions for ^{238}U are on the order of 2 to 6% with ^{237}Np photofission contributions about half of that. Photoreactions in ^{115}In are negligible. The comparison of calculated-to-measured gamma-ray energy deposition in the stainless steel internals structures (Table NTD-9) shows a general underprediction of the measurements (3% in the baffles, 5% in the core barrel, and 20% in the neutron pad) and also shows a radial calculation bias with greater underprediction further from the core.

Expected Future Accomplishments

Publication of the final report (WCAP-11173; NUREG/CR-4827) completes this work. Appropriate parts of this work, however, will be used and incorporated into NUREG/CR-3323 (Vol. 1 and 2), see the Summary section and Table S-1.

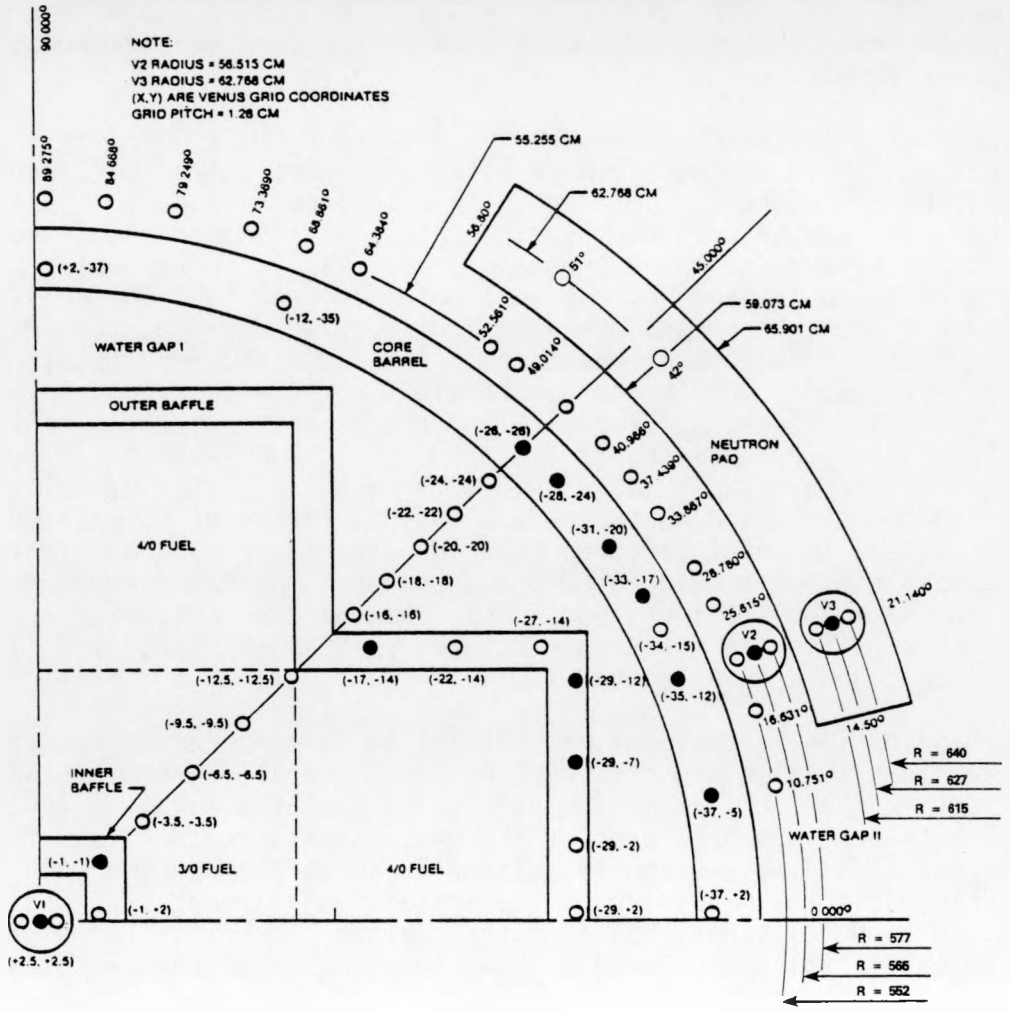

FIGURE NTD-1. VENUS PWR Engineering Mockup Key Dimensions and Location of Experimental Data Points.

TABLE NTD-4

COMPARISON OF CALCULATED AND MEASURED EQUIVALENT FISSION FLUXES IN THE STEEL REGIONS

VENUS LOCATION	Np-237 (n,f) F.P.			U-238 (n,f) F.P.			Ni-58 (n,p) Co-58			In-115 (n,n') In-115m		
	CALC	EXP	C/E	CALC	EXP	C/E	CALC	EXP	C/E	CALC	EXP	C/E
INNER BAFFLE												
(-1, +2) θ = 8.1°	2.58+9	2.52+9	1.02	1.84+9	1.91+9	0.96	1.55+9	1.51+9	1.03	1.88+9	1.90+9	0.99
(-1, -1) θ = 45.0°	3.07+9	2.95+9	1.04	2.22+9	2.28+9	0.97	1.88+9	1.82+9	1.03	2.26+9	2.30+9	0.98
OUTER BAFFLE												
(-29, +2) θ = 0.9°	1.03+9	1.10+9	0.94	7.50+8	7.96+8	0.94	6.43+8	6.38+8	1.01	7.63+8	7.83+8	0.97
(-29, -2) θ = 8.1°	9.78+8	--	--	7.13+8	7.37+8	0.97	6.11+8	6.06+8	1.01	7.25+8	7.37+8	0.98
(-29, -7) θ = 16.8°	7.91+8	8.21+8	0.96	5.75+8	6.12+8	0.94	4.92+8	4.97+8	0.99	5.85+8	5.98+8	0.98
(-29, -12) θ = 24.7°	4.76+8	4.91+8	0.97	3.37+8	--	--	2.84+8	2.93+8	0.97	3.45+8	3.52+8	0.98
(-27, -14) θ = 29.2°	4.95+8	5.08+8	0.97	3.51+8	3.64+8	0.96	2.97+8	3.07+8	0.97	3.59+8	3.64+8	0.99
(-22, -14) θ = 34.0°	9.46+8	9.67+8	0.98	6.82+8	7.26+8	0.94	5.80+8	5.72+8	1.01	6.95+8	7.16+8	0.97
(-17, -14) θ = 40.2°	1.55+9	1.60+9	0.97	1.10+9	1.15+9	0.96	9.34+8	9.31+8	1.00	1.13+9	1.18+9	0.96
CORE BARREL												
(-37, +2) θ = 0.7°	1.16+8	1.21+8	0.96	8.75+7	1.00+8	0.88	7.71+7	9.01+7	0.86	8.77+7	9.72+7	0.90
(-37, -5) θ = 10.8°	1.04+8	1.12+8	0.93	7.52+7	8.72+7	0.86	6.42+7	--	--	7.63+7	--	--
(-35, -12) θ = 21.1°	1.06+8	1.23+8	0.86	7.31+7	8.65+7	0.85	6.09+7	7.46+7	0.82	7.50+7	8.40+7	0.89
(-34, -15) θ = 25.6°	9.30+7	1.08+8	0.86	6.15+7	7.23+7	0.85	5.00+7	--	--	6.37+7	--	--
(-33, -17) θ = 28.8°	8.37+7	9.58+7	0.87	5.53+7	6.76+7	0.82	4.50+7	--	--	5.73+7	--	--
(-31, -20) θ = 33.9°	7.02+7	7.60+7	0.92	4.90+7	6.01+7	0.82	4.16+7	5.47+7	0.76	5.00+7	5.60+7	0.89
(-28, -24) θ = 41.0°	5.44+7	6.26+7	0.87	4.08+7	4.72+7	0.86	3.66+7	--	--	4.09+7	--	--
(-26, -26) θ = 45.0°	5.32+7	6.08+7	0.87	4.05+7	4.75+7	0.85	3.67+7	4.84+7	0.76	4.05+7	4.55+7	0.89
NEUTRON PAD												
(R = 62.8 θ = 21.1°)	9.60+6	--	--	6.32+6	--	--	5.23+6	--	--	6.53+6	8.89+6	0.73
(R = 62.8 θ = 45.0°)	6.75+6	--	--	4.56+6	--	--	3.93+6	--	--	4.66+6	5.95+6	0.78

NOTE: Not adjusted for photoreaction, see also Table NTD-7

Read 2.58+9 as 2.58×10^9

TABLE NTD-5

COMPARISON OF CALCULATED AND MEASURED EQUIVALENT FISSION FLUXES IN THE WATER REGIONS

VENUS LOCATION	Np-237 (n,f) F.P.			U-238 (n,f) F.P.			Ni-58 (n,p) Co-58			In-115 (n,n') In-115m		
	CALC	EXP	C/E	CALC	EXP	C/E	CALC	EXP	C/E	CALC	EXP	C/E
CENTER HOLE												
(+2.5, +2.5)	1.50+9	*	--	1.21+9	1.35+9	0.90	1.13+9	1.13+9	1.00	1.19+9	1.24+9	0.96
WATER GAP I												
(-16, -16)	1.01+9	*	--	7.64+8	8.18+8	0.93	6.85+8	--	--	7.67+8	8.07+8	0.95
(-18, -18)	4.75+8	4.82+8	0.99	3.93+8	--	--	3.74+8	--	--	3.86+8	4.08+8	0.95
(-20, -20)	2.36+8	2.43+8	0.97	2.09+8	2.30+8	0.91	2.08+8	--	--	2.02+8	2.14+8	0.94
(-22, -22)	1.22+8	1.30+8	0.94	1.14+8	--	--	1.18+8	--	--	1.08+8	1.17+8	0.92
(-24, -24)	7.20+7	*	--	6.55+7	7.34+7	0.89	6.71+7	--	--	6.26+7	6.80+7	0.92
WATER GAP II												
(10.75°)	3.05+7	3.64+7	0.84	2.36+7	3.02+7	0.78	2.20+7	--	--	2.34+7	2.85+7	0.82
(16.63°)	3.10+7	3.82+7	0.81	2.34+7	2.90+7	0.81	2.16+7	--	--	2.33+7	2.80+7	0.83
(21.14°)	3.03+7	--	--	2.25+7	2.98+7	0.76	2.05+7	--	--	2.25+7	2.72+7	0.83
(25.62°)	2.81+7	3.33+7	0.84	2.04+7	2.51+7	0.81	1.84+7	--	--	2.05+7	2.46+7	0.83
(28.78°)	2.59+7	3.20+7	0.81	1.89+7	2.38+7	0.79	1.71+7	--	--	1.90+7	2.33+7	0.82
(33.89°)	2.20+7	2.59+7	0.85	1.67+7	2.08+7	0.80	1.55+7	--	--	1.66+7	1.97+7	0.84
(37.44°)	1.98+7	2.44+7	0.81	1.55+7	1.97+7	0.79	1.47+7	--	--	1.52+7	--	--
(40.99°)	1.84+7	*	--	1.47+7	--	--	1.43+7	--	--	1.44+7	1.73+7	0.83
(45.00°)	1.77+7	2.22+7	0.80	1.44+7	1.77+7	0.81	1.40+7	--	--	1.40+7	1.64+7	0.85

NOTE: Not adjusted for photoreaction, see also Table NTD-8

Read 1.50+9 as 1.50×10^9

*-These measurements have been revised, but the new measurements have not yet been released.

TABLE NTD-6

COMPARISON OF CALCULATED AND MEASURED EQUIVALENT FISSION FLUXES ALONG A 45° TRAVERSE

VENUS LOCATION	Np-237 (n,f) F.P.			U-238 (n,f) F.P.			Ni-58 (n,p) Co-58			In-115 (n,n') In-115m		
	CALC	EXP	C/E	CALC	EXP	C/E	CALC	EXP	C/E	CALC	EXP	C/E
CENTER HOLE												
(+2.5, + 2.5)	1.50+9	*	--	1.21+9	1.35+9	0.90	1.13+9	1.13+9	1.00	1.19+9	1.24+9	0.96
INNER BAFFLE												
(-1, -1)	3.07+9	2.95+9	1.04	2.22+9	2.28+9	0.97	1.88+9	1.82+9	1.03	2.26+9	2.30+9	0.98
3/0 FUEL												
(-3.5, -3.5)	4.28+9	4.21+9	1.02	3.67+9	--	--	3.53+9	--	--	3.60+9	--	--
(-6.5, -6.5)	4.56+9	4.59+9	0.99	3.96+9	--	--	3.84+9	--	--	3.88+9	--	--
(-9.5, -9.5)	4.37+9	4.34+9	1.01	3.78+9	--	--	3.66+9	--	--	3.70+9	--	--
(-12.5, -12.5)	3.25+9	3.50+9	0.93	2.70+9	--	--	2.54+9	--	--	2.67+9	--	--
WATER GAP I												
(-16, -16)	1.01+9	*	--	7.64+8	8.18+8	0.93	6.85+8	--	--	7.67+8	8.07+8	0.95
(-18, -18)	4.75+8	4.82+8	0.99	3.93+8	--	--	3.74+8	--	--	3.86+8	4.08+8	0.95
(-20, -20)	2.36+8	2.43+8	0.97	2.09+8	2.30+8	0.91	2.08+8	--	--	2.02+8	2.14+8	0.94
(-22, -22)	1.22+8	1.30+8	0.94	1.14+8	--	--	1.18+8	--	--	1.08+8	1.17+8	0.92
(-24, -24)	7.20+7	*	--	6.55+7	7.37+7	0.89	6.71+7	--	--	6.26+7	6.80+7	0.92
CORE BARREL												
(-26, -26)	5.32+7	6.08+7	0.87	4.05+7	4.75+7	0.85	3.67+7	4.84+7	0.76	4.05+7	4.55+7	0.89
WATER GAP II												
(R=55.255)	1.77+7	2.22+7	0.80	1.44+7	1.77+7	0.81	1.40+7	--	--	1.40+7	1.64+7	0.85
NEUTRON PAD												
(R=62.768)	6.75+6	--	--	4.56+6	--	--	3.93+6	--	--	4.66+6	5.95+6	0.78

NOTE: Not adjusted for photoreaction, see also Tables NTD-7 and -8

Read 1.50+9 as 1.50×10^9

*-These measurements have been revised, but the new measurements have not yet been released.

TABLE NTD-7

GAMMA-RAY DATA IN THE STEEL REGIONS

VENUS LOCATION	Photoreaction Equivalent Fission Fluxes: Np-237 (γ,f) F.P. CALC (γ,f)	RATIO $(\frac{\gamma,f}{n,f})$	C/E $(\frac{n+\gamma,f}{EXP})$	U-238 (γ,f) F.P. CALC (γ,f)	RATIO $(\frac{\gamma,f}{n,f})$	C/E $(\frac{n+\gamma,f}{EXP})$	In-115 (γ,γ') In-115m CALC (γ,γ')	RATIO $(\frac{\gamma,\gamma'}{n,n'})$	C/E $(\frac{n+\gamma,n'+\gamma'}{EXP})$
INNER BAFFLE									
(-1, +2) θ = 8.1°	1.74+7	0.007	1.03 *	2.76+7	0.015	0.98	3.56+6	0.002	0.99
(-1, -1) θ = 45.0°	1.22+7	0.004	1.04	1.94+7	0.009	0.98	2.71+6	0.001	0.98
OUTER BAFFLE									
(-29, +2) θ = 0.9°	5.47+6	0.005	0.94	8.70+6	0.012	0.95	1.16+6	0.002	0.97
(-29, -2) θ = 8.1°	5.23+6	0.005	--	8.33+6	0.012	0.98	1.11+6	0.002	0.98
(-29, -7) θ = 16.8°	4.36+6	0.006	0.96	6.95+6	0.012	0.95	9.16+5	0.002	0.98
(-29, -12) θ = 24.7°	3.35+6	0.007	0.97	5.34+6	0.016	--	6.78+5	0.002	0.98
(-27, -14) θ = 29.2°	3.66+6	0.007	0.98	5.82+6	0.016	0.98	7.50+5	0.002	0.99
(-22, -14) θ = 34.0°	5.80+6	0.006	0.98	9.24+6	0.014	0.95	1.22+6	0.002	0.97
(-17, -14) θ = 40.2°	8.05+6	0.005	0.97	1.28+7	0.012	0.97	1.70+6	0.002	0.96
CORE BARREL									
(-37, +2) θ = 0.7°	2.62+6	0.023	0.98	4.18+6	0.048	0.92	5.18+5	0.006	0.90
(-37, -5) θ = 10.8°	1.98+6	0.019	0.95	3.16+6	0.042	0.90	3.88+5	0.005	--
(-35, -12) θ = 21.1°	1.74+6	0.016	0.88	2.77+6	0.038	0.88	3.38+5	0.005	0.89
(-34, -15) θ = 25.6°	1.45+6	0.016	0.87	2.31+6	0.038	0.88	2.81+5	0.004	--
(-33, -17) θ = 28.8°	1.41+6	0.017	0.89	2.24+6	0.041	0.85	2.74+5	0.005	--
(-31, -20) θ = 33.9°	1.42+6	0.020	0.94	2.26+6	0.046	0.85	2.81+5	0.006	0.89
(-28, -24) θ = 41.0°	1.25+6	0.023	0.89	1.99+6	0.049	0.91	2.56+5	0.006	--
(-26, -26) θ = 45.0°	1.28+6	0.024	0.90	2.04+6	0.050	0.90	2.63+5	0.006	0.89
NEUTRON PAD									
(R = 62.8 θ = 21.1°)	2.15+5	0.022	--	3.42+5	0.054	--	4.17+4	0.006	0.74
(R = 62.8 θ = 45.0°)	1.59+5	0.024	--	2.52+5	0.055	--	3.15+4	0.007	0.78

TABLE NTD-8

GAMMA-RAY DATA IN THE FUEL AND WATER REGIONS

VENUS LOCATION	Photoreaction Equivalent Fission Fluxes: Np-237 (γ,f) F.P. CALC (γ,f)	RATIO $(\frac{\gamma,f}{n,f})$	C/E $(\frac{n+\gamma,f}{EXP})$	U-238 (γ,f) F.P. CALC (γ,f)	RATIO $(\frac{\gamma,f}{n,f})$	C/E $(\frac{n+\gamma,f}{EXP})$	In-115 (γ,γ') In-115m CALC (γ,γ')	RATIO $(\frac{\gamma,\gamma'}{n,n'})$	C/E $(\frac{n+\gamma,n'+\gamma'}{EXP})$
CENTER HOLE									
(+2.5, +2.5)	1.29+7	0.009	--	2.06+7	0.017	0.90	2.96+6	0.002	0.96
3/0 FUEL									
(-3.5, -3.5)	2.40+6	0.0006	1.02	3.74+6	0.001	--	1.80+6	0.0005	--
(-6.5, -6.5)	1.10+6	0.0002	0.99	1.67+6	0.0004	--	1.68+6	0.0004	--
(-9.5, -9.5)	1.18+6	0.0003	1.01	1.80+6	0.0005	--	1.63+6	0.0004	--
(-12.5, -12.5)	3.78+6	0.001	0.93	5.97+6	0.002	--	1.56+6	0.0006	--
WATER GAP I									
(-16, -16)	6.34+6	0.006	--	1.01+7	0.013	0.95	1.42+6	0.002	0.95
(-18, -18)	4.44+6	0.009	0.99	7.06+6	0.018	--	1.08+6	0.003	0.95
(-20, -20)	3.27+6	0.014	0.98	5.21+6	0.025	0.93	8.32+5	0.004	0.94
(-22, -22)	2.67+6	0.021	0.96	4.25+6	0.037	--	6.60+5	0.006	0.92
(-24, -24)	2.48+6	0.034	--	3.95+6	0.060	0.94	5.58+5	0.009	0.92
WATER GAP II									
(10.75°)	7.60+5	0.025	0.86	1.21+6	0.051	0.82	1.55+5	0.007	0.82
(16.63°)	7.65+5	0.025	0.83	1.22+6	0.052	0.85	1.54+5	0.007	0.83
(21.14°)	7.38+5	0.024	-	1.18+6	0.052	0.78	1.48+5	0.007	0.83
(25.62°)	7.12+5	0.025	0.87	1.13+6	0.055	0.86	1.42+5	0.007	0.83
(28.78°)	6.91+5	0.027	0.83	1.10+6	0.058	0.84	1.38+5	0.007'	0.82
(33.89°)	6.35+5	0.029	0.87	1.01+6	0.060	0.85	1.28+5	0.008	0.84
(37.44°)	5.95+5	0.030	0.84	9.47+5	0.061	0.83	1.21+5	0.008	--
(40.99°)	5.75+5	0.031	--	9.16+5	0.062	--	1.18+5	0.008	0.83
(45.00°)	5.68+5	0.032	0.82	9.05+5	0.063	0.86	1.17+5	0.008	0.85

TABLE NTD-9

COMPARISON OF CALCULATED AND MEASURED GAMMA-RAY ENERGY DEPOSITION RATES IN THE STEEL REGIONS

VENUS LOCATION	CALCULATED SS-304 HEAT GENERATION RATE (GRAY/HOUR)	MEASURED THREE LABORATORY AVERAGE (GRAY/HOUR)	C/E
INNER BAFFLE			
(-1, +2) θ = 8.1°	150.8	152.4 ± 14.9 [±9.8%]	0.990
(-1, -1) θ = 45.0°	139.1	147.0 ± 12.8 [±8.7%]	0.947
OUTER BAFFLE			
(-29, +2) θ = 0.9°	51.26	53.89 ± 3.12 [±5.8%]	0.951
(-29, -7) θ = 16.8°	40.10	42.16 ± 1.64 [±3.9%]	0.951
(-29, -12) θ = 24.7°	27.16	29.27 ± 1.68 [±5.7%]	0.928
(-27, -14) θ = 29.2°	30.70	31.77 ± 2.13 [±6.7%]	0.966
(-22, -14) θ = 34.0°	52.81	52.02 ± 1.03 [±2.0%]	1.015
(-17, -14) θ = 40.2°	75.60	73.91 ± 4.88 [±6.6%]	1.023
CORE BARREL			
(-35, -12) θ = 21.1°	12.15	12.83 ± 0.15 [±1.2%]	0.947
(-34, -15) θ = 25.6°	10.14	10.52 ± 0.35 [±3.3%]	0.964
(-33, -17) θ = 28.8°	9.93	10.83 ± 0.80 [±7.4%]	0.916
(-31, -20) θ = 33.9°	10.72	11.50 ± 0.22 [±1.9%]	0.932
(-26, -26) θ = 45.0°	10.96	10.89 ± 0.29 [±2.7%]	1.006
NEUTRON PAD			
R = 61.5 θ = 21.1°	2.236	2.780 ± 0.12 [±4.3%]	0.804
R = 62.8 θ = 21.1°	1.523	1.873 ± 0.02 [±1.1%]	0.813
R = 64.0 θ = 21.1°	1.065	1.410 ± 0.03 [±2.1%]	0.755
R = 62.8 θ = 45.0°	1.245	1.449 ± 0.05 [±3.5%]	0.859

NOTE: 1 watt/gram = 3.6×10^6 Gray/hour

TLD Types: SCK/CEN - Al_2O_3
RRA - ^7LiF
CEGB - BeO

The standard deviation (1σ) of the mean measured energy deposition rate is expressed in both Gray/hour and as a percentage of the mean.

UNIVERSITÄT STUTTGART

INSTITUT FÜR KERNENERGETIK UND
ENERGIESYSTEME (IKE)

A. NEUTRON SPECTRUM CALCULATION FOR THE GUNDREMMINGEN KRB-A REACTOR

G. Prillinger (IKE)

Objective

The objective of this work is to determine the neutron exposure of several trepans taken from the pressure vessel of the nuclear power plant Gundremmingen Block A (KRB-A).

Summary

A three-dimensional (3-D) neutron spectrum analysis was performed by the Institut für Kernenergetik und Energiesysteme, Universität Stuttgart (IKE). The objective of this work is to determine the neutron exposure of several trepans taken from the pressure vessel of the nuclear power plant Gundremmingen Block A (KRB-A). The work, funded by the U.S. NRC*, is part of the KRB-A program analyzing through-vessel-wall embrittlement of a real reactor vessel at the end of operation. This progress report describes the method used, summarizes important input data, and gives first results of fluence ($E > 1.0$ MeV) values.

Calculated and measured ^{54}Mn activities are compared. A detailed analysis of all transport-calculation results, especially neutron spectrum variation within the vessel, is underway. Further comparison with available dosimetry results will be performed.

The final report on this work has been completed and will be available for distribution in March 1987 (Pr86).

Accomplishments and Status

1.0 Introduction

The Boiling Water Reactor KRB-A has a nominal thermal power of 801-MW (250-MW electrical). The reactor was put in operation in November 1966 and, until the last shutdown on January 13th, 1977, generated a total of about 16 TWh of electrical power, with an average availability of 75%.

After decommissioning, 15 trepans have been taken at different axial and azimuthal positions within the 90 to 135 degree octant of the reactor. The axial and azimuthal positions of the trepans named A, B, C, D, E, F, G, K, L, M, N, P, Q, R, T can be seen in Figures IKE-1 and IKE-2. To get accurate assessments of the absolute magnitude of the exposure parameters of interest, such as fast fluence ($E > 1.0$ MeV), fluence ($E > 0.1$ MeV), or dpa, the 3-D flux distribution has to be calculated using the DOT4.2 (Rh79) code. This code solves the Boltzmann transport equation in two-dimensional (2-D) geometry using the discrete ordinates method. Combining the results of a (R,θ) and (RZ) model of the reactor, the neutron spectrum is defined with sufficient accuracy (Pr83a). To perform the transport calculations on an absolute scale, evaluations of the reactor power-time history and of the 3-D burnup distributions at the beginning and the end of each of the reactor cycles were necessary.

---

*Work done under the auspices of Purchase Order Y63-S44-52307 between WHC and IKE.

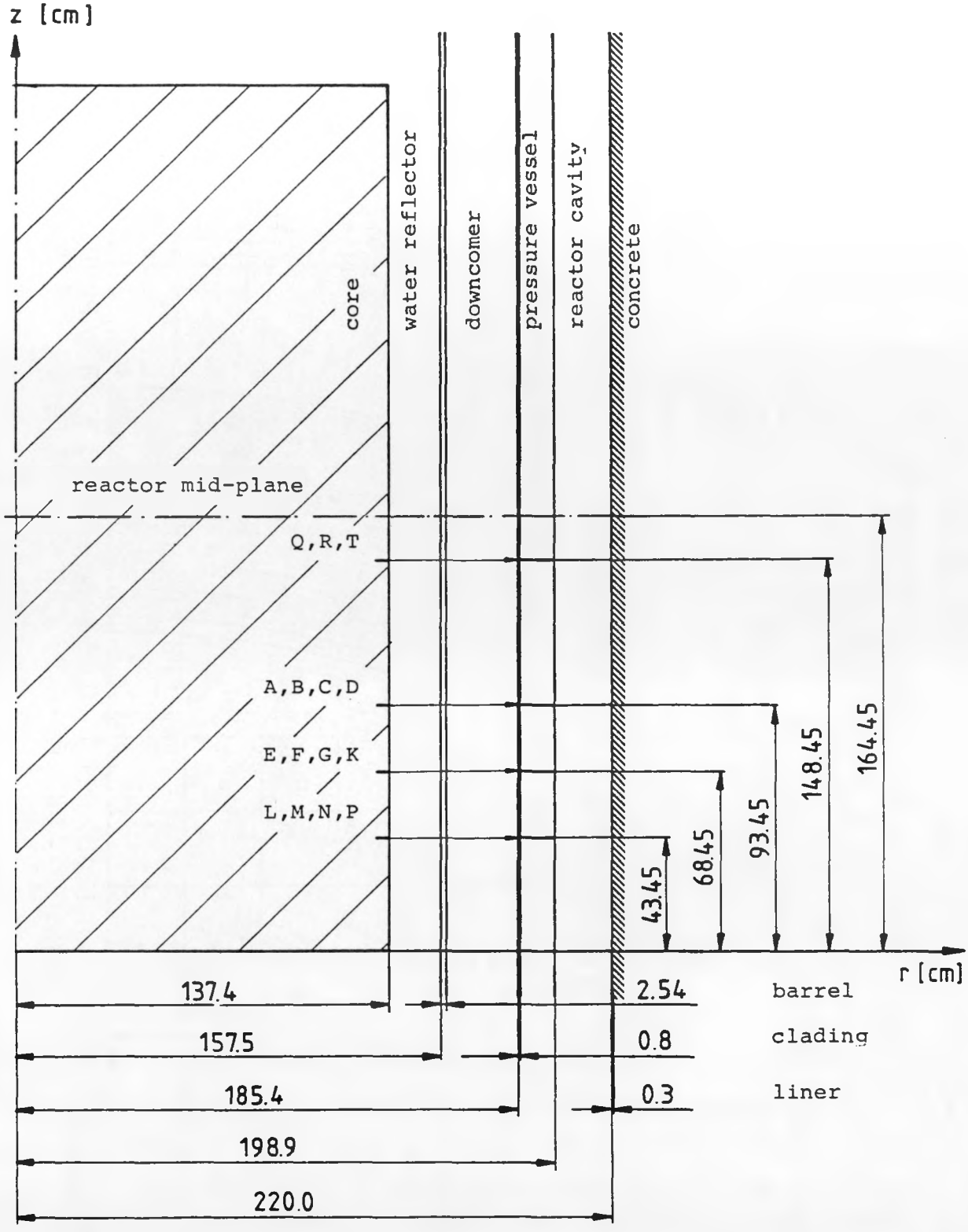

FIGURE IKE-1. (R-Z) Geometry for KRB-A Reactor with Trepan Positions.

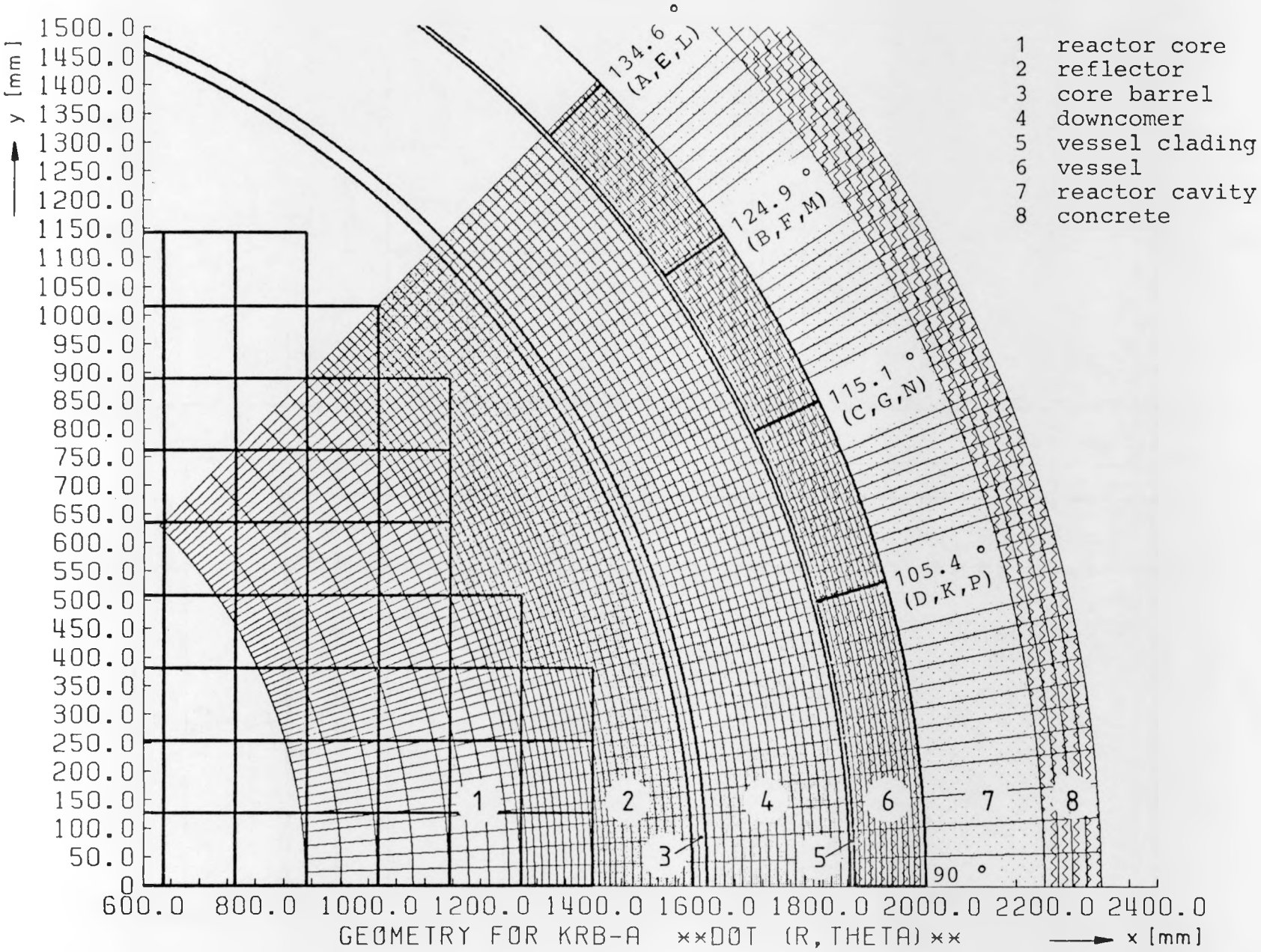

FIGURE IKE-2. (R-θ) Geometry for KRB-A Reactor with Trepan Positions.

2.0 Method of Analysis and Input Data

2.1 3-D Reactor Physics Calculation

In the analysis of the neutron environment outside the reactor core, the 3-D flux distribution has been calculated with the help of a flux synthesis for each energy group G of the form

$$\Phi^G(R,\theta,Z) = \Phi_1^G(R,\theta) \cdot F^G(R,Z)$$

$$F^G(R,Z) = \Phi_2^G(R,Z) \Big/ \Phi_3^G(R)$$

where:

$\Phi^G(R,\theta,Z)$ = Neutron fluence at point R,Z,θ for energy group G

$\Phi_1^G(R,\theta)$ = Solution of (R,Φ) calculation

$\Phi_2^G(R,Z)$ = Solution of (R,Z) calculation

$\Phi_3^G(R)$ = Solution of one-dimensional axial infinite (R) calculation

Φ_1^G, Φ_2^G and Φ_3^G have been calculated with the DOT4.2 code (Rh79) applying an S_8/P_3 approximation. In the (R,θ) model shown in Figure IKE-2, the neutron source is calculated from axial averaged burnup distributions. In the (R,Z) model, axial variation of the burnup as well as moderator density is taken into account. In the (R,Z) analysis, the reactor core is treated as an equivalent volume cylinder with a 137.4-cm radius (Figure IKE-2). To obtain the relative axial variation $F^G(R,Z)$, the radial-axial neutron flux distribution $\Phi_2^G(R,Z)$ must be divided by the one-dimensional (1-D) axial-infinite solution $\Phi_3^G(R)$.

The perturbation of the neutron field by the surveillance capsules is not taken into account. Neutron fluxes have been stored at appropriate R-boundaries for detailed surveillance capsule analysis in the future.

2.2 Material Data

Specific material data for KRB-A are given in Table IKE-1. The atomic compositions of material zones modeled in the transport calculation are summarized in Table IKE-2. For the water temperature in the downcomer and

TABLE IKE-1

MATERIAL DATA

Zone	Shield thickness [cm]	Density [g/cm³]	Comment
core			
reflector	20.1 *)	0.753	water
barrel	2.54	7.86	ASTM-A240, Typ 304 X5CrNi189
downcomer	25.36	0.753	water
clading	0.8	7.8	
vessel	12.7	7.86	20NiMoCr26
reactor cavity	21.1		
liner	0.3	7.85	St34
concrete	129.7		

*) equivalent core radius is 137.4 cm

TABLE IKE-2

MATERIAL COMPOSITIONS (at. $cm^{-3} \cdot 10^{-24}$)

	core	reflector	barrel	downcomer	clading	vessel	liner	concrete
H	2.97E-2	5.03-2	-	5.03-2	-	-	-	9.62E-3
C	-	-	3.15E-4	-	8.99E-5	9.06E-4	6.69E-4	3.81E-3
O	2.71E-2	2.52-2	-	2.52-2	-	-	-	4.65E-2
Al	-	-	-	-	-	-	-	9.75E-4
Si	-	-	-	-	-	-	-	1.47E-2
Ca	-	-	-	-	-	-	-	9.68E-4
Cr	-	-	1.64E-2	-	1.87E-2	3.37E-4	-	-
Mn	-	-	8.62E-4	-	1.01E-3	6.03E-4	-	-
Fe	-	-	5.81E-2	-	5.51E-2	8.18E-2	8.45E-2	1.41E-3
Ni	-	-	9.68E-3	-	9.20E-3	6.37E-4	-	2.60E-6
Zr	3.70E-3	-	-	-	-	-	-	-
Mo	-	-	-	-	-	3.01E-4	-	-
U^{35}	1.49E-4	-	-	-	-	-	-	-
U^{38}	6.01E-3	-	-	-	-	-	-	-

and reflector in front of the trepans, a temperature of 279°C was assumed. The inlet temperature into the reactor core is 265.6°C. For the homogenized core zone data in Table IKE-2, saturated water with a temperature of 285.8°C has been assumed. These core data are only used in the (R,θ) calculations. In the (R,Z)-model, 16 core zones with axial increasing void content have been taken into account.

2.3 Determination of the Neutron Source

The whole time-power history, as well as burnup distributions per fuel element at the beginning and the end of each cycle, are available for the KRB-A reactor. On the basis of these data, total neutron source densities have been calculated taking into account burnup-dependent energy and the number of neutrons per fission. Since the burnup tables are only available per fuel elements, the shape of the power distribution within the outer fuel elements has been determined by means of theoretical curves. The calculated source densities have been transformed finally to the (R,θ) space mesh (shown in Figure IKE-1) conserving the number of neutrons.

For the (R,Z)-transport calculations, the axial-radial dependent source densities have been obtained from axial burnup given at 12 axial modes of the fuel elements around the 120 degree theta direction. An energy spectrum for thermal fission of ^{235}U (Watt-type, ENDF/B-V) has been assumed for the whole core. Only a few plutonium fuel elements situated at inner positions have been used during the whole reactor operation time.

2.4 Cross-Section Data Used

For the 2-D transport calculation, a special library with 35 neutron energy groups has been generated. Energy boundaries are given in Table IKE-3. Group cross section weighting has been performed with fine-group spectra calculated for KRB-A in 1-D geometry.

The fine-group library is based on ENDF/B-IV data (Ma79) and has been compared with the VITAMIN/C (Ro82) library giving equivalent results (Pr83a).

With this procedure, higher accuracy can be achieved compared to the use of the more general libraries like CASK (OaXX) or SAILOR (OaSa). The SAILOR library is specially designed for large Light Water Power reactors of the 1000 MW_{el}-class. Nevertheless, differences should be small if correct treatment of the resonance region, especially in iron, and temperature-corrected thermal cross section are guaranteed.

3.0 Results

The main purpose of the analysis is to define the neutron exposure of the 15 trepans taken from the KRB-A vessel.

Exposure values like total, E > 1 MeV, E > 0.1 MeV, and thermal fluence, and dpa have been determined from the fluence energy spectra.

TABLE IKE-3

35-GROUP ENERGY STRUCTURE

Nr	Energy boundaries	Nr	Energy boundaries
1	10.000 - 14.917 MeV	18	183.16 - 301.97 KeV
2	8.187 - 10.000 MeV	19	111.09 - 183.16 KeV
3	6.703 - 8.187 MeV	20	52.475 - 111.09 KeV
4	6.065 - 6.703 MeV	21	31.829 - 52.475 KeV
5	4.966 - 6.065 MeV	22	26.050 - 31.829 KeV
6	3.679 - 4.966 MeV	23	24.788 - 26.050 KeV
7	3.011 - 3.679 MeV	24	15.034 - 24.788 KeV
8	2.466 - 3.011 MeV	25	5.531 - 15.034 KeV
9	2.346 - 2.466 MeV	26	1.585 - 5.531 KeV
10	2.231 - 2.346 MeV	27	0.454 - 1.585 KeV
11	1.653 - 2.231 MeV	28	101.3 - 454.0 eV
12	1.353 - 1.653 MeV	29	37.267 - 101.3 eV
13	1.003 - 1.353 MeV	30	10.677 - 37.267 eV
14	0.748 - 1.003 MeV	31	5.044 - 10.677 eV
15	550.23 - 747.74 KeV	32	1.855 - 5.044 eV
16	368.83 - 550.23 KeV	33	0.625 - 1.855 eV
17	301.97 - 368.83 KeV	34	0.414 - 0.625 eV
		35	10^{-5} - 0.414 eV

3.1 Fast Fluence (E > 1 MeV)

3.1.1 Azimuthal and Axial Variation

The maximum fluence value at the 0-T vessel position is 5.96×10^{18} n/cm^2 near the axial midplane of KRB-A at Z = 130 cm and 90 degree theta direction. The azimuthal variation of the fluence (E > 1 MeV) is within 55% of the maximum fluence value, as can be seen in Figure IKE-3. The axial shape function as a ratio of the 2-D (R,Z) and 1-D (R) calculation is shown in Figure IKE-4.

3.1.2 Trepan Fluences (E > 1 MeV)

The axial fluence variation for the cylindrical trepans, which is equivalent to the attenuation of the neutrons through the vessel wall, is shown in Figures IKE-5 to IKE-8. Each figure represents one axial level. Z and θ coordinates can be seen in Figures IKE-1 and IKE-2. The radial variation of neutron exposure within one trepan (radius = 5.35 cm) can be neglected. From the curves one can see a maximum fluence value of about 4.5×10^{18} n/cm^2 at the inner vessel surface. The attenuation through the vessel is in the range of 5.5 to 6.5.

3.2 Comparison of Calculated and Measured Activities

3.2.1 ^{54}Mn Activity of Trepans

Two independent measurements of the ^{54}Mn activity (one on May 1, 1984, the other on January 22, 1986) have been made by KFA Jülich (Sc86). The measured activities of drillings taken from trepan A (1984) and trepan A, D, G, L, P (1986) are listed together with their radial position in the vessel measured from the vessel-cladding interface in Table IKE-4.

The calculated specific activity A is determined using the relationship

$$A = A_{sat} \cdot \sum_{m=1}^{n} P_m (1-e^{-\lambda \cdot T_m})(e^{-\lambda t_m}),$$

where:

P_m = Fractional power for the operating period m.

λ = Decay constant for the activation product [d^{-1}]
$\lambda = 2.218 \times 10^{-3}$ for ^{54}Mn.

T_m = Number of operating days for period m.

t_m = Decay time after operating period m (days).

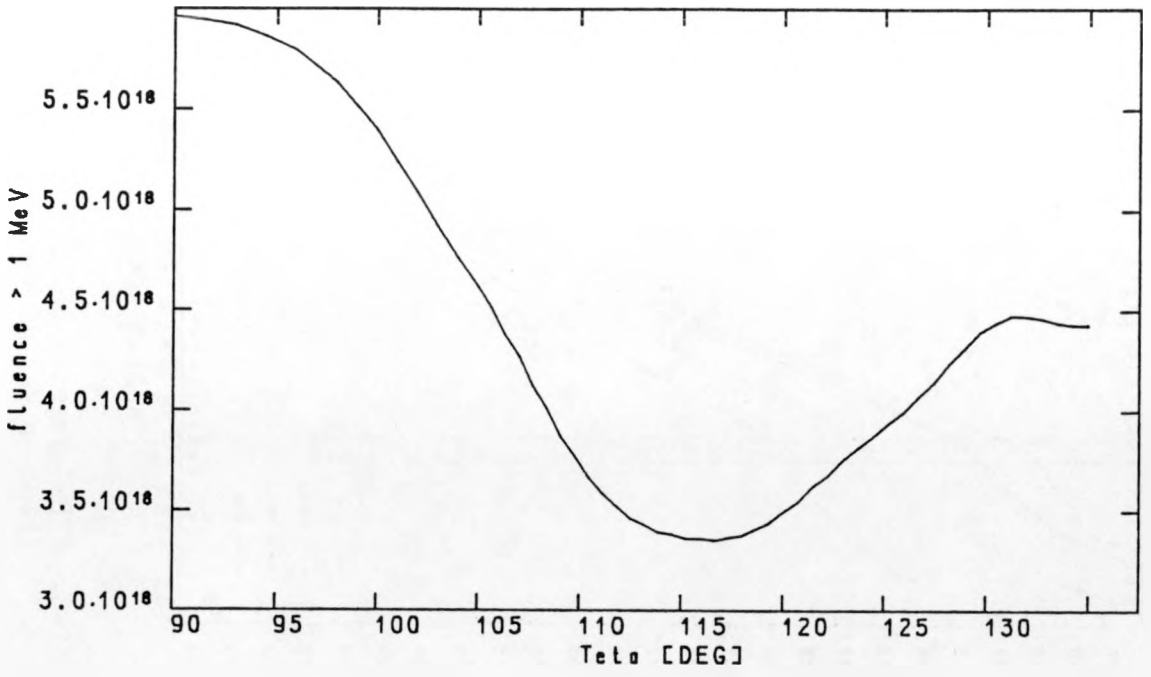

FIGURE IKE-3. KRB-A Azimuthal Fluence Variation (PV-Cladding, Z = 164 cm).

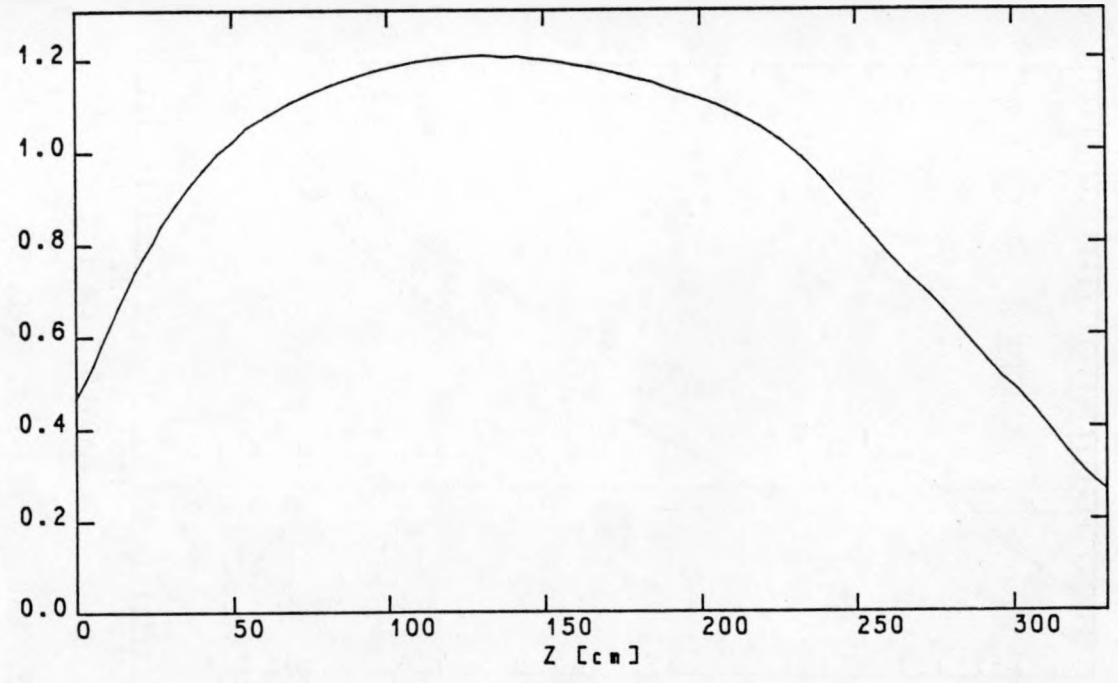

FIGURE IKE-4. Axial Formfactor at Inner Vessel Surface (for Fluence E > 1 MeV).

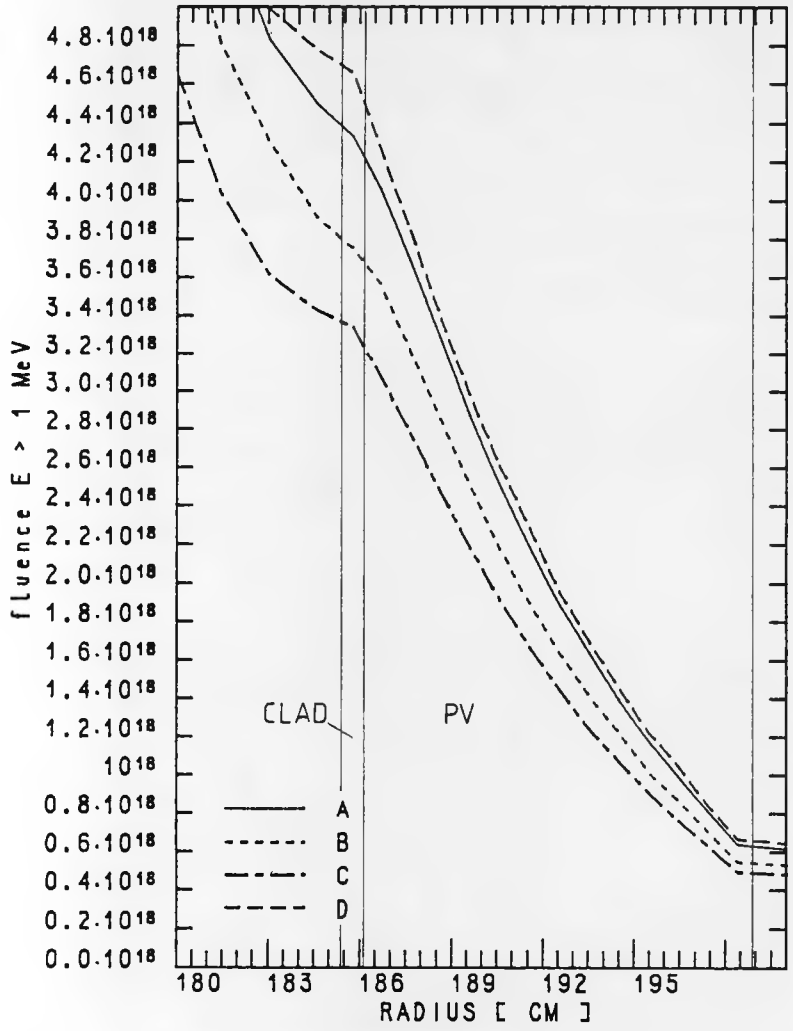

FIGURE IKE-5. KRB-A Trepans A, B, C, D (Fluence Versus Radius).

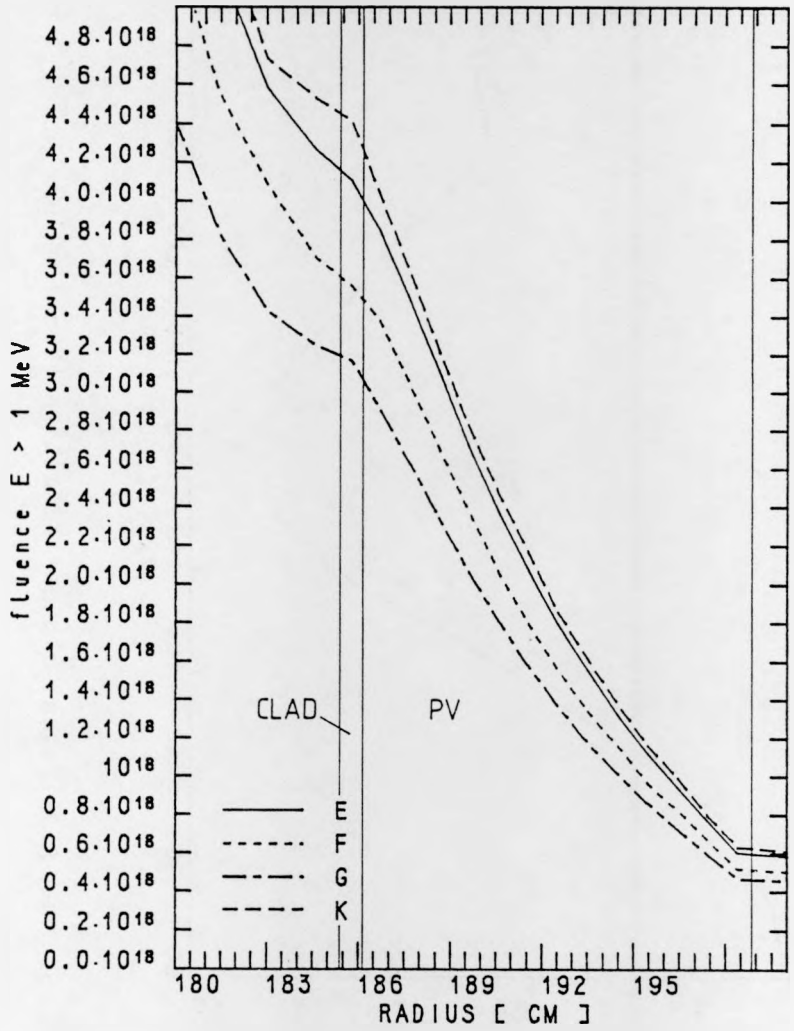

FIGURE IKE-6. KRB-A Trepans E, F, G, K (Fluence Versus Radius).

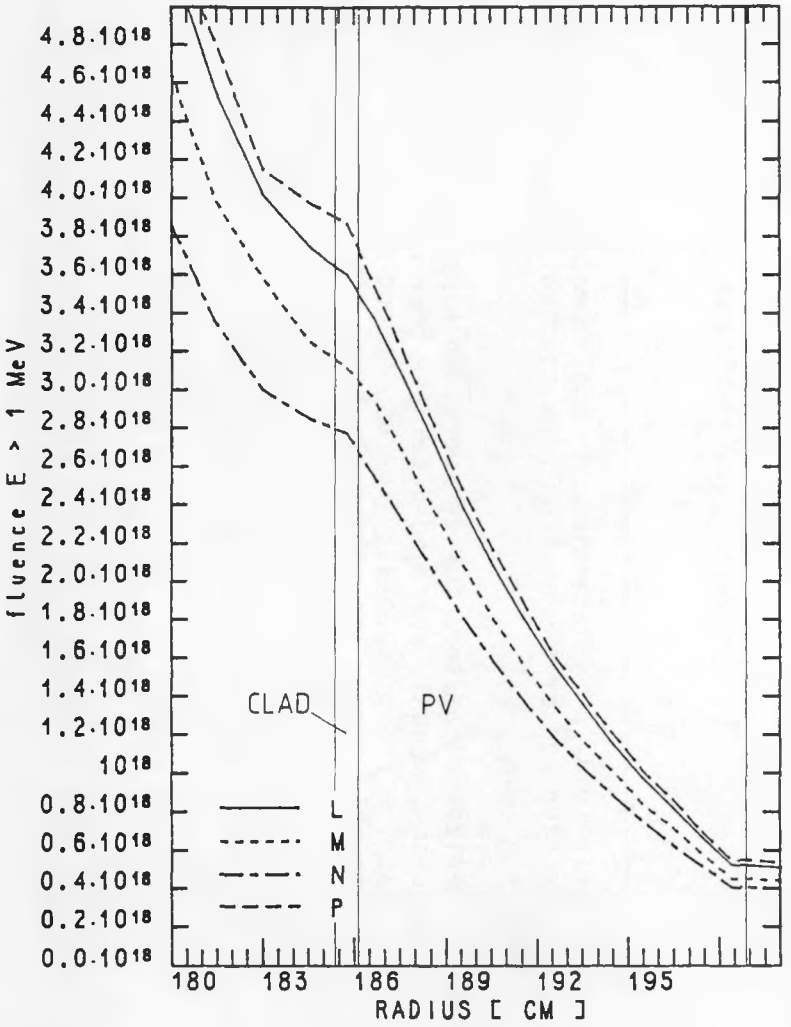

FIGURE IKE-7. KRB-A Trepans L, M, N, P (Fluence Versus Radius).

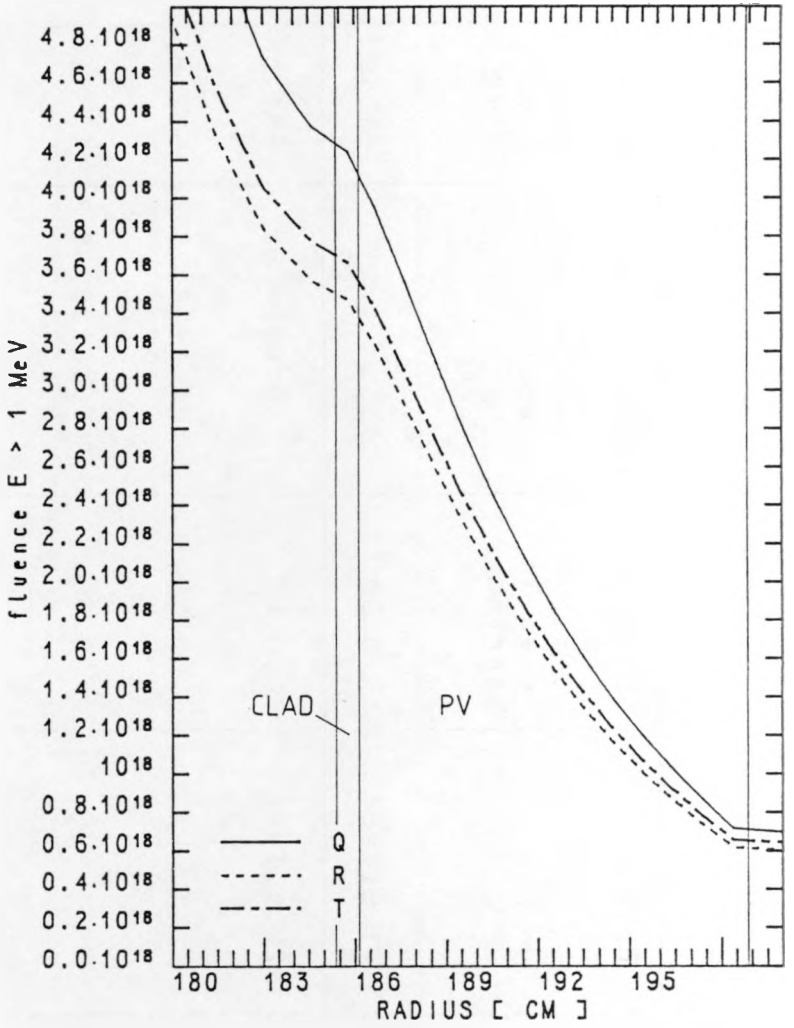

FIGURE IKE-8. KRB-A Trepans Q, R, T (Fluence Versus Radius).

TABLE IKE-4

COMPARISON OF MEASURED AND CALCULATED ^{54}Mn ACTIVITIES OF TREPANS

Trepan	Date of measurement	Distance [cm] from vessel-clad interface	Spec. activity [Bq/g]		C/E
			measured	calculated	
A	1.5.1984	0.30	2035.	2615.0	1.28
A	22.1.1986	0.65	568.8±28.8%	584.8	1.03
D	"	0.55	403.2±36.3%	632.8	1.57
G	"	0.80	405.3±36.0%	437.1	1.08
L	"	0.80	440.2±41,1 %	475.8	1.08
P	"	0.60	429.1±36.5 %	521.5	1.22

The saturated activity A_{sat} is determined by the macroscopic $^{54}Fe(n,p)^{54}Mn$ reaction cross section and by the neutron flux spectra at appropriate space mesh intervals.

Table IKE-5 summarizes parameters for 14 operation time periods. For the activity calculations, monthly averaged data have been used. Considering the high statistical errors, especially for the second measurement, the agreement is reasonable good. The relatively large discrepancy for trepan D should be investigated further.*

Additional evaluations for dosimetry results obtained from the surveillance capsule 128, which was irradiated during the whole reactor operation time, will be performed.

---

*In the mean time, the azimuthal trepan positions have been corrected, resulting in better agreement of the calculated and measured values (Pr86).

TABLE IKE-5

PARAMETERS USED FOR ACTIVITY CALCULATION

	Operation period	T_m	t_m *)	Fractional power
1	15.11.66-15.07.67	242	6132	0.403
2	15.09.67-15.01.68	123	5948	0.826
3	15,02.68-15.05.68	90	5827	0.859
4	01.06.68-30.09.68	122	5689	0.506
5	25.11.68-31.05.69	188	5447	0.559
6	25.08.69-31.05.70	280	5082	0.969
7	27.07.70-15.06.71	324	4702	0.986
8	15.07.71-30.04.72	290	4383	0.987
9	01.07.72-05.05.73	309	4013	0.988
10	15.06.73-15.10.73	123	3850	0.974
11	15.11.73-04.05.74	171	3649	0.962
12	15.06.74-11.05.75	331	3277	0.971
13	15.06.75-07.05.76	327	2915	0.955
14	02.10.76-13.01.77	104	2664	0.952

*) for date of measurement 1st May, 1984

Expected Future Accomplishments

The final report on this work is to be completed and submitted to HEDL on or before September 30, 1986. See (Pr86).

BIBLIOGRAPHY

(As82) ASTM E706-81a, "Master Matrix for LWR Pressure Vessel Surveillance Standards," 1982 Annual Book of ASTM Standards, American Society for Testing and Materials, Philadelphia, PA, Part 45, 1982. (See most recent version of ASTM E706, Annual Book of ASTM Standards, Section 12, Volume 12.02, current edition.)

(As82b) ASTM E854-81, "Standard Method for Application and Analysis of Solid-State Track Recorder (SSTR) Monitors for Reactor Vessel Surveillance," 1982 Annual Book of ASTM Standards, American Society for Testing and Materials, Philadelphia, PA, Part 45, 1982.

(As83a) ASTM E910-82, "Standard Method for Application and Analysis of Helium Accumulation Fluence Monitors for Reactor Vessel Surveillance," 1983 Annual Book of ASTM Standards, American Society for Testing and Materials, Philadelphia, PA, Section 12, Volume 12.02, pp. 761-774, 1983.

(As85) ASTM E706-(IIE), "Standard Guide for Benchmark Testing of Reactor Vessel Dosimetry," in ASTM E706, in Annual Book of ASTM Standards, American Society for Testing and Materials, Philadelphia, PA, current edition.

(Ba63) W. H. Barkas, "Techniques and Theories," Nuclear Research Emulsions, Vol. I, Academic Press, New York, NY, 1963.

(Ba73) W. H. Barkas, Nuclear Research Emulsions, Vol. II, Academic Press, New York, NY, p. 252, 1973.

(Ba84a) C. A. Baldwin and F. B. K. Kam, "ORR-Surveillance Dosimetry Measurement Facility (ORR-SDMF) Simulated Surveillance Capsule Perturbation Experiment," LWR-PV-SDIP: Quarterly Progress Report, April 1983 - June 1983, NUREG/CR-3391, Vol. 2, HEDL-TME 93-22, pp. ORNL-9 - ORNL-25, April 1984.

(Be67b) S. Berg and W. N. McElroy, A Computer Automated Iterative Method for Neutron Flux Spectra Determination by Foil Activation, AFWL-TR-67-41, Vol. 1, Air Force Weapons Laboratory, Kirkland AFB, NM, July 1967.

(Cf83) Code of Federal Regulations, 10CFR50, "Domestic Licensing of Production and Utilization Facilities," "General Design Criteria for Nuclear Power Plants," Appendix A; "Fracture Toughness Requirements," Appendix G; "Reactor Vessel Material Surveillance Program Requirements," Appendix H; US Government Printing Office, Washington, DC, current edition.

(Cu79) Current Status of Neutron Spectrum Unfolding, IAEA-TECDOC-221, International Atomic Energy Agency, Vienna, Austria, August 1979.

(Fa76) A. Fabry et al., "Review of Microscopic Integral Cross Section Data in Fundamental Dosimetry Benchmark Neutron Fields," Neutron Cross Sections for Reactor Dosimetry, IAEA-208, Vol. 1, International Atomic Energy Agency, Vienna, Austria, p. 233, November 1976.

(Fa77) A. Fabry, H. Ceulemans, P. Vandeplas, W. N. McElroy and E. P. Lippincott, "Reactor Dosimetry Integral Reaction Rate Data in LMFBR Benchmark and Standard Neutron Fields: Status, Accuracy and Implications," Proc. of the 1st ASTM-EURATOM Symposium on Reactor Dosimetry, Petten, The Netherlands, September 22-26, 1975, EUR 5667, Vol. II, Commission of the European Communities, pp. 112-130, 1977.

(Fa80a) A. Fabry et al., "Results and Implications of the Initial Neutronic Characterization of Two HSST Irradiation Capsules and the PSF Simulated LWR Pressure Vessel Irradiation Facility," Proc. of the 8th WRSR Information Meeting, Gaithersburg, MD, October 27-31, 1980, NUREG/CP-0023, NRC, Washington, DC, March 1982.

(Fe85) A. H. Fero, "Neutron and Gamma-Ray Flux Calculations for the Venus PWR Engineering Mockup," Proc. of the 5th Symposium on Reactor Dosimetry - Reactor Dosimetry: Dosimetry Methods for Fuels, Cladding and Structural Materials, GKSS Research Centre, Geesthacht, FRG, September 24-28, 1984, Vols. 1 and 2, D. Reidel Publishing Company, Dordrecht, The Netherlands, EUR 9869, for the Commission of the European Communities, 1985.

(Fo82) W. E. Ford et al., CSRL-V: Processed ENDF/B-V 227-Neutron Group and Pointwise Cross-Section Libraries for Criticality Safety, Reactor and Shielding Studies, NUREG/CR-2306, NRC, Washington, DC, June 1982.

(Fr81) H. J. Frost and K. C. Russel, "Recoil Resolution and Particle Stability Under Irradiation," J. Nucl. Mater. 104, pp. 1427-1432, 1981.

(Ga61) J. L. Gammel, Fast Neutron Physics, Part II, J. B. Marion and J. L. Fowler, Eds., Wiley & Sons (Interscience), New York, NY, 1961.

(Ge82a) D. S. Gelles, "Precipitation During Irradiation, An Experimental Example," Proc. of the International Conference on Solid-State Phase Transformations, Pittsburgh, PA, August 1981, H. I. Aaranson, D. E. Laughlin, R. F. Sekerka and C. M. Wayman, Eds., AIME, Warrendale, PA, pp. 293-298, 1982.

(Gi78) D. M. Gilliam et al., "Reference and Standard Benchmark Field Consensus Fission Yields for U.S. Reactor Dosimetry Programs," Proc. of the 2nd ASTM-EURATOM Symposium on Reactor Dosimetry, Palo Alto, CA, October 3-7, 1977, NUREG/CP-0004, NRC, Washington, DC, p. 1507, 1978.

(Gi85) D. M. Gilliam, J. A. Grundl, G. P. Lamaze, E. D. McGarry, and A. Fabry, "Cross Section Measurements in the ^{235}U Fission Spectrum Neutron Field," Proc. of the 5th ASTM-EURATOM Symposium on Reactor Dosimetry, Geesthacht, Federal Republic of Germany, September 24-28, 1984, EUR 9869, Commission of the European Communities, 1985.

(Go77c) R. Gold, "Neutron Spectrometry for Reactor Applications: Status Limitations and Future Directions," Proc. of the 1st ASTM-EURATOM Symposium on Reactor Dosimetry, Petten, The Netherlands, September 22-26, 1975, EUR 5667, Vol. I, Commission of the European Communities, pp. 119-147, 1977.

(Go81) R. Gold and J. H. Roberts, "Nuclear Emulsion Neutron Spectrometry in the FFTF," Trans. Am. Nucl. Soc. 39, p. 896, December 1981.

(Go81d) R. Gold, J. H. Roberts, F. H. Ruddy, C. C. Preston and C. A. Hendricks, "Proton-Recoil Emulsion Observations for Integral Neutron Dosimetry," Proc. of the IAEA Advisory Group Meeting on Nuclear Data for Radiation Damage Assessment and Related Safety Aspects, Vienna, October 12-18, 1981, IAEA-TECDOC-263, International Atomic Energy Agency, Vienna, Austria, pp. 115-121, 1982.

(Go81e) R. Gold, J. H. Roberts, C. C. Preston and F. H. Ruddy, "Neutron Spectrometry with Nuclear Research Emulsions," LWR-PV-SDIP: PCA Experiments and Blind Test, NUREG/CR-1861, HEDL-TME 80-87, NRC, Washington, DC, Sec. 3.3, July 1981.

(Go82d) Y. Gohar and M. A. Abdou, MACKLIB-IV-82: 171 Neutron, 36 Gamma-Ray Group Nuclear Response Function Library Calculated with MACK-IV from Cross-Section Data in ENDF/B-IV, RSIC-DLC-60, ORNL Radiation Shielding Information Center, Oak Ridge, TN, January 15, 1982.

(Go83) R. Gold, J. H. Roberts, C. C. Preston, F. H. Ruddy, C. S. Cooper, C. A. Hendricks, D. T. Johnson, J. P. McNeece, G. W. Main, T. E. Michaels, N. E. Spence, H. J. Svoboda and G. F. Vargo Jr, "Interactive System for Scanning Tracks in Nuclear Research Emulsions," Rev. Sci. Instrum. 54, pp. 183-192, 1983.

(Go84d) R. Gold, J. P. McNeece, B. J. Kaiser, T. A. Lewis, P. J. H. Heffer and M. D. Carter, "Janus Probe Perturbation Factors," LWR-PV-SDIP: PCA Experiments, Blind Test, and Physics-Dosimetry Support for the PSF Experiments, NUREG/CR-3318, HEDL-TME 84-1, NRC, Washington, DC, Section 4.4, September 1984.

(Go86) R. Gold and W. N. McElroy, "Current Limitations of Trend Curve Analysis for the Prediction of Reactor Pressure Vessel Embrittlement," HEDL-SA-3390, Proc. of the 13th International Symposium on Effects of Radiation on Materials, June 23-25, 1986, Seattle, WA, Hanford Engineering Development Laboratory, Richland, WA, September 1986.

(Gr78b) N. M. Greene, W. E. Ford III, J. L. Lucius, J. E. White, L. M. Petrie and R. Q. Wright, AMPX-II: A Modular Code System for Generating Coupled Multigroup Neutron-Gamma-Ray Cross-Section Libraries from Data in ENDF Format, ORNL/TM-3706, Oak Ridge National Laboratory, Oak Ridge, TN, December 1978.

(Gr78c) R. C. Greenwood, R. G. Helmer, J. W. Rogers, R. J. Potek, R. R. Heinrich, N. D. Dudey, L. S. Kellogg, and W. H. Zimmer, "Radiometric Reactor Rate Measurements in CFRMF and BIG-10," Proc. of the 2nd ASTM-EURATOM Symposium on Reactor Dosimetry, Palo Alto, CA, October 3-7, 1977, NUREG/CP-0004, Vol. 3, NRC, Washington, DC, p. 1207, 1978.

(Gu84) G. L. Guthrie, "Charpy Trend Curves Based on 177 PWR Data Points," LWR-PV-SDIP: Quarterly Progress Report, April 1983 - June 1983, NUREG/CR-3391, Vol. 2, HEDL-TME 83-22, NRC, Washington, DC, pp. HEDL-3 - HEDL-15, April 1984.

(Gu85) G. L. Guthrie, "HEDL Analysis of the Poolside Facility Experiment," LWR-PV-SDIP: Semiannual Progress Report, April 1984 - September 1984, NUREG/CR-3746, Vol. 2, HEDL-TME 84-21, NRC, Washington, DC, pp. HEDL-28 - HEDL-52, March 1985.

(Ha58) F. S. Ham, "Theory of Diffusion-Limited Precipitation," J. Phys. Chem. Solids 6, Pergamon Press, pp. 335-351, 1958.

(Ha76) G. C. Haynes, The AXMIX Program for Cross-Section Mixing and Library Arrangement, RSIC-PSR-75, Oak Ridge National Laboratory, Oak Ridge, TN, June 1976.

(Ha84) J. R. Hawthorne, B. H. Menke and A. L. Hiser, LWR-PV-SDIP: Notch Ductility and Fracture Toughness Degradation of A302-B and A533-B Reference Plates from PSF Simulated Surveillance and Through-Wall Irradiation Capsules, NUREG/CR-3295, MEA-2017, Vol. 1, NRC, Washington, DC, April 1984.

(Ha84a) J. R. Hawthorne and B. H. Menke, LWR-PV-SDIP: Postirradiation Notch Ductility and Tensile Strength Determinations for PSF Simulated Surveillance and Through-Wall Specimen Capsules, NUREG/CR-3295, MEA-2017, Vol. 2, NRC, Washington, DC, April 1984.

(Ka70) M. Kahlweit, "Precipitation and Aging," Physical Chemistry: An Advanced Treatise 10 (11), H. Eyring, D. Henderson and W. Jost, Eds., p. 719, Academic Press, 1970.

(Ka83) F. B. K. Kam, F. W. Stallmann, R. E. Maerker and M. L. Williams, "LWR-PV Benchmark Facilities (PCA, ORR-PSF, ORR-SDMF) at ORNL," LWR-PV-SDIP: Quarterly Progress Report, April 1982 - June 1982, NUREG/CR-2805, Vol. 2, HEDL-TME 82-19, Hanford Engineering Development Laboratory, Richland, WA, January 1983.

(Ke82) L. S. Kellogg and E. P. Lippincott, "PSF Interlaboratory Comparison," Proc. of the 4th ASTM-EURATOM Symposium on Reactor Dosimetry, Gaithersburg, MD, March 22-26, 1982, NUREG/CP-0029, Vol. 2, CONF-820321/V2, NRC, Washington, DC, pp. 929-945, July 1982.

(Li61) I. M. Lifshitz and V. V. Slyozov, "The Kinetics of Precipitation from Supersaturated Solid Solutions," J. Phys. Chem. Solids 19 (1-2), Pergamon Press, pp. 35-50, 1961.

(Li84b) E. P. Lippincott, F. W. Stallmann and A. F. Thomas, "Derived Exposure Parameters," LWR-PV-SDIP: PCA Experiments, Blind Test, and Physics-Dosimetry Support for the PSF Experiments, Sec. 7.2, NUREG/CR-3318, HEDL-TME 84-1, NRC, Washington, DC, September 1984.

(Li85) E. P. Lippingcott et al., Evaluation of Surveillance Capsule and Reactor Cavity Dosimetry from H. B. Robinson Unit 2, Cycle 9, WCAP-11104, NUREG/CR-4576, Westinghouse-Nuclear Technology Division, Pittsburgh, PA, April 1986.

(Li86) E. P. Lippincott and R. L. Simons, "HEDL-Recommended Exposure Parameter Values for the PSF Blind Test," Appendix B, LWR-PV-SDIP: PSF Experiments Summary and Blind Test Results, NUREG/CR-3320, Vol. 1, HEDL-TME 86-8, NRC, Washington, DC, July 1986.

(Ma79) M. Mattes, EURLIB-4, A Coupled Neutron and Gamma Multigroup Cross-Section Library Based on ENDF/B-IV/V, IKE6-121, Institut für Kernenergetic und Energiesysteme, Stüttgart, FRG, 1979.

(Ma82) N. Maene, R. Menil, G. Minsart and L. Ghoos, "Gamma Dosimetry and Calculations," Proc. of the 4th ASTM-EURATOM Symposium on Reactor Dosimetry, Gaithersburg, MD, March 22-26, 1982, NUREG/CP-0029, Vol. 1, NRC, Washington, DC, pp. 355-363, July 1982.

(Ma82b) P. Mas and R. Perdreau, "Caracterisation d' Emplacements d'Irradiation en Spectres Neutroniques et en Dommages," Proc. of the 4th ASTM-EURATOM Symposium on Reactor Dosimetry, Gaithersburg, MD, March 22-26, 1982, NUREG/CP-0029, Vol. 2, NRC, Washington, DC, pp. 847-854, July 1982.

(Mc81) W. N. McElroy, Ed., LWR-PV-SDIP: PCA Experiments and Blind Test, NUREG/CR-1861, HEDL-TME 80-87, NRC, Washington, DC, July 1981.

(Mc81a) W. N. McElroy et al., LWR-PV-SDIP: 1980 Annual Report, NUREG/CR-1747, HEDL-TME 80-73, NRC, Washington, DC, April 1981.

(Mc82) W. N. McElroy et al., "Surveillance Dosimetry of Operating Power Plants," Proc. of the 4th ASTM-EURATOM Symposium on Reactor Dosimetry, Gaithersburg, MD, March 22-26, 1982, NUREG/CP-0029, NRC, Washington, DC, pp. 3-43, July 1982. (LWR-PV-SDIP 1981 Annual Report.)

(Mc82c) P. McConnell et al., Irradiated Nuclear Pressure Vessel Steel Data Base, EPRI NP-2428, RP1240-01, Electric Power Research Institute, Palo Alto, CA, June 1982.

(Mc84b) W. N. McElroy and F. B. K. Kam, Eds., PSF Blind Test SSC, SPVC, and SVBC Physics-Dosimetry-Metallurgy Data Packages, HEDL-7449, Hanford Engineering Development Laboratory, Richland, WA, February 1984.

(Mc84) W. N. McElroy et al., LWR-PV-SDIP: 1983 Annual Report, NUREG/CR-3391, Vol. 3, HEDL-TME 83-23, NRC, Washington, DC, January 1984.

(Mc84i) W. N. McElroy, LWR-PV-SDIP: PCA Experiments, Blind Test, and Physics-Dosimetry Support for the PSF Experiments, NUREG/CR-3318, HEDL-TME 84-1, NRC, Washington, DC, September 1984.

(Mc85g) W. N. McElroy et al., Minutes of the 15th LWR-PV-SDIP Meeting in Gaithersburg, MD on October 21-24, 1985 and NESDIP/VENUS/PWR Workshop at Raleigh, NC on September 15-18, 1986, HEDL-7587, Hanford Engineering Development Laboratory, Richland, WA, November 1986.

(Mc86) W. N. McElroy et al., Trend Curve Data Development and Testing, MC2-TR-86-10, HEDL-7591, Metrology Control Corporation and Hanford Engineering Development Laboratory, Richland, WA, March 1986 and HEDL-SA-3400, Proc. of the 13th International Symposium on the Effects of Radiation on Materials, June 23-25, 1986, Seattle, WA, Metrology Control Corporation and Hanford Engineering Development Laboratory, Richland, WA, September 1986.

(Mc86b) W. N. McElroy, Ed., LWR-PV-SDIP: PSF Experiments Summary and Blind Test Results, NUREG/CR-3320, Vol. 1, HEDL-TME 86-8, NRC, Washington, DC, July 1986.

(Mc86c) E. D. McGarry, "PCA Experimental Results," Minutes of the 15th LWR-PV-SDIP Meeting in Gaithersburg, MD on October 21-24, 1985 and NESDIP/VENUS/PWR Workshop at Raleigh, NC on September 15-18, 1986, HEDL-7587, Section 4.2.1, Hanford Engineering Development Laboratory, Richland, WA, November 1986.

(Mc86d) J. J. McGowan and R. K. Nanstad (ORNL), "A Statistical Analysis of Fracture Toughness of Irradiated Low-Alloy Steel, Plate and Welds," paper presented at the 13th International Symposium on the Effects of Irradiation on Materials, June 23-25, 1986, Seattle, WA.

(Ne72) R. S. Nelson, J. A. Hudson and D. J. Mazey, "The Stability of Precipitates in an Irradiation Environment," J. Nucl. Mater. 44, pp. 318-330, 1972.

(OaSa) SAILOR - Coupled, Self-Shielded, 47 Neutron, 29 Gamma-Ray, P_3, Cross-Section Library for LWRs, RSIC-DLC-76, Radiation Shielding Information Center, Oak Ridge, TN.

(OaXX) CASK-40-Group Coupled Neutron and Gamma-Ray Cross-Section Data, RSIC-DLC-23, Radiation Shielding Information Center, Oak Ridge, TN.

(Od83a) G. R. Odette, "On the Dominant Mechanism of Irradiation Embrittlement of Reactor Pressure Vessel Steels," Scripta Met. 17, pp. 1183-1188, 1983.

(Ol76) D. R. Olander, Fundamental Aspects of Nuclear Reactor Fuel Elements, TID-26711-P1, National Technical Information Service, US Department of Commerce, Springfield, VA, 1976.

(Om80) P. A. Ombrellaro, R. A. Bennett, E. P. Lippincott and C. L. Long, "Buffalo Light Water Reactor Calculations," Dosimetry Methods for Fuels Cladding and Structural Materials: Proc of the 3rd ASTM-EURATOM Symposium on Reactor Dosimetry, Ispra, Italy, October 1-5, 1979, EUR 6813, Vol. I, p. 589, 1980.

(Pe84) J. S. Perrin, R. A. Wullaert, G. R. Odette and M. P. Lombroso, Physically Based Regression Correlations of Embrittlement Data from Reactor Pressure Vessel Surveillance Programs, EPRI NP-3319, Final Report, RP1240-01, Electric Power Research Institute, Palo Alto, CA, January 1984.

(Pr83a) G. Prillinger and G. Pfister, "Necessity of Detailed Multidimensional Transport Calculations in LWR Pressure Vessel Surveillance and for MTR Irradiation," presented at 6th International Conference on Radiation Shielding (ICRS), Tokyo, Japan, May 16-20, 1983.

(Pr86) G. Prillinger, Neutron Spectrum Calculation for the Gundremmingen KRB-A Reactor, IKE 6-FB-35, Institut für Kernenergetic und Energiesysteme, IKE-Stuttgart, FRG, July 1986.

(Ra77) F. J. Rahn, K. E. Stahlkopf, T. V. Marston, R. Gold, and J. H. Roberts, "Standards for Dosimetry Beyond the Core," Proc. of the International Specialists Symposium on Neutron Standards and Applications, Gaithersburg, MD, March 28-31, 1977, NBS SP 493, Government Printing Office, Washington, DC, pp. 137-145, 1977.

(Ra78) F. J. Rahn, C. Z. Serpan, A. Fabry, W. N. McElroy, J. A. Grundl, and J. Debrue, "Trends in Light Water Reactor Dosimetry Programs," Proc. of the 2nd ASTM-EURATOM Symposium on Reactor Dosimetry, Palo Alto, CA, October 3-7, 1977, NUREG/CP-0004, Vol. 3, NRC, Washington, DC, p. 1064, 1978.

(Rh79) W. A. Rhoades, D. B. Simpson, R. L. Childs and W. E. Engle, The DOT-IV Two-Dimensional Discrete Ordinates Transport Code with Space-Dependent Mesh and Quadrature, ORNL/TM-6529, Oak Ridge National Laboratory, Oak Ridge, TN, 1979.

(Rh82) W. A. Rhoads and R. L. Childs, An Updated Version of the DOT-IV One- and Two-Dimension Neutron/Photon Transport Code, ORNL-5851, Oak Ridge National Laboratory, Oak Ridge, TN, July 1982.

(Ro53) L. Rosen, "Nuclear Emulsion Techniques for the Measurement of Neutron Energy Spectra," Nucleonics 11, p. 32, and 12, p. 38, 1953.

(Ro57) J. H. Roberts, "Absolute Flux Measurements of Anisotropic Neutron Spectra with Proton Recoil Tracks in Nuclear Emulsions," Rev. Sci. Instrum. 28, p. 667, 1957.

(Ro68) J. H. Roberts and A. N. Behkami, "Measurement of Anisotropic Fast Neutron Spectra with Nuclear Emulsion Techniques," Nucl. Technol. 4, p. 182, 1968.

(Ro77c) R. W. Roussin et al., WITAMIN-C: 171 Neutron, 36 Gamma-Ray Group Cross Sections in AMPX and CCC Interface Format for Fusion and LMFBR Neutronics, RSIC-DLC-41, ORNL Radiation Shielding Information Center, Oak Ridge, TN, September 23, 1977.

(Ro80a) R. W. Roussin, BUGLE-80: Coupled, 47 Neutron, 20 Gamma-Ray, P_3 Cross-Section Library for LWR Shielding Calculations, RSIC-DLC-75, ORNL Radiation Shielding Information Center, Oak Ridge, TN, June 1980.

(Ro81) J. H. Roberts, R. Gold, C. C. Preston, C. A. Hendricks, J. P. McNeece and F. H. Ruddy, Neutron Spectrometry in the Fast Test Reactor with Nuclear Research Emulsions: Observation of Angular Anisotrophy, HEDL-TC-1977, Addendum, Hanford Engineering Development Laboratory, Richland, WA, August 1981.

(Ro82) R. W. Roussin et al., VITAMIN-C: 171 Neutron, 36 Gamma-Ray Group Cross-Sections in AMPX and CCCC Interface Formats for Fusion and LMFBR Neutronics, ORNL/RSIC-37, Radiation Shielding Information Center, Oak Ridge, TN, 1982.

(Ro83b) J. H. Roberts, R. Gold, F. H. Ruddy, C. C. Preston and J. P. McNeece, "Fast Neutron Fluence-Spectra and Integral Reaction Rates Determined with Nuclear Research Emulsions," Proc. of the 12th International Conference on Solid-State Nuclear Track Detectors, Acapulco, Mexico, September 4-10, 1983.

(Ru72) K. C. Russell and L. M. Brown, "A Dispersion Strengthing Model Based on Differing Elastic Module Applied to the Iron-Copper System," Acta Met. 20, July 1972.

(Sa72) L. Salmon and D. V. Booker, FATAL - A General Purpose Computer Program for Fitting Experimental Data to Any Required Function, AERE-R-7129, Atomic Energy Research Establishment, Harwell, UK, 1972.

(Sc79) F. A. Schmittroth, FERRET Data Analysis Code, HEDL-TME 79-40, Hanford Engineering Development Laboratory, Richland, WA, September 1979.

(Sc86) R. Schröder, Gammaspektroskopische Untersuchung von Bohrspänen aus den Bohrkernen A, D, G, L und P des RDB Gundremmingen, KFA-Jülich, IRW-TN-24/86, February 1986.

(Si83) G. L. Simons and R. Roussin, SAILOR - Coupled, Self-Shielded, 47 Neutron, 29 Gamma-Ray, P_3, Cross-Section Library for LWRs, RSIC-DLC-76, Radiation Shielding Information Center, Oak Ridge, TN, 1983 [same as (OaSa)].

(So70) R. G. Sopltesz, R. K. Disney, J. Jedruch and S. L. Ziegler, "Nuclear Rocket Shielding Methods, Modification, Updating and Input Data," Two-Dimensional Discrete Ordinates Transport Technique, WANL-PR(LL)-034, Vol. 5, Westinghouse Electric Corp., Pittsburgh, PA, August 1970.

(St67) J. L. Straalsund and G. L. Guthrie, "An Analysis of the Effects of Hydrostatic Stress on Swelling," Nucl. Tech. 16, pp. 36-44, October 1967.

(St72a) J. L. Straalsund and G. L. Guthrie, Computer Calculations of Growth Rates of Voids in Stainless Steel During Neutron Irradiation, HEDL-TME 72-35, Hanford Engineering Development Laboratory, Richland, WA, April 1972.

(To82) H. Tourwé and G. Minsart, "Surveillance Capsule Perturbation Studies in the PSF 4/12 Configuration," Proc. of the 4th ASTM-EURATOM Symposium on Reactor Dosimetry, Gaithersburg, MD, March 22-26, 1982, NUREG/CP-0029, Vol. 1, NRC, Washington, DC, pp. 471-480, July 1982.

(To82a) H. Tourwé et al., "Interlaboratory Comparison of Fluence Neutron Dosimeters in the Frame of the PSF Start-Up Measurement Programme," Proc. of the 4th ASTM-EURATOM Symposium on Reactor Dosimetry, Gaithersburg, MD, March 22-26, 1982, NUREG/CP-0029, Vol. 1, NRC, Washington, DC, pp. 159-168, July 1982.

(Ve80) V. V. Verbinski, C. G. Cassapakis, W. K. Hagen and G. L. Simmons, "Photointerference Corrections in Neutron Dosimetry for Reactor Pressure Vessel Lifetime Studies," Nucl. Sci. & Eng. 75, p. 159, 1980.

(Vo81) D. R. Vondy, T. B. Fowler and G. W. Cunningham, The Bold VENTURE Computation System for Nuclear Reactor Core Analysis, Version III, ORNL-5711, Oak Ridge National Laboratory, Oak Ridge, TN, 1981.

(Wa61) C. Wagner, "Theory Concerning Aging of Precipitates of Re-Solution," Zeitschrift für Elektrochem. 65, p. 581, 1961.

(Wi79) P. Wilkes, "Phase Stability Under Irradiation - A Review of Theory and Experiment," J. Nucl. Mater. 83, pp. 166-175, 1979.

(Zi79) W. L. Zijp and J. H. Baard, Nuclear Data Guide for Reactor Neutron Metrology, EUR 7167, Parts I and II, Energieonderzoek Centrum Nederland (Energy Research Center Netherlands), Petten, The Netherlands, August 1979.

DISTRIBUTION FOR LWR-PV-SDIP

DOE-HQ/Office of Asst Secy
for Nuclear Energy
NE-1
Washington DC

AD Rossin, Asst Secy

DOE-HQ/Office of Deputy Asst Secy
For Reactor Deployment
Office of LWR Safety & Technology
NE-42
Washington, DC 20545

DJ McGoff, Manager

DOE-HQ/Office of Advanced
Reactor Programs (2)
NE-53
Washington, DC 20545

FX Gavigan JD Nulton

DOE-HQ/Office of Technology
Support Programs (4)
Division of Advanced Tech Develop
NE-542
Washington, DC 20545

RJ Neuhold, Director JW Lewellen
PB Hemmig A. Van Echo

DOE-RL/AMF
Site & Laboratory Management Division
Laboratory Management & Technology
Services Branch
P.O. Box 550, FED/210
Richland, WA 99352

DK Jones, Chief

American Society for Testing & Materials
1916 Race Street
Philadelphia, PA 19103

M. Lieff

Ames Laboratory
Iowa State University
Ames, IA 50010

MS Wechsler

APTECH Engineering Services
795 San Antonio Road
Palo Alto, CA 94303

PD Hedgecock

Argonne National Laboratory-East (3)
9700 South Cass Avenue
Argonne, IL

RJ Armani RR Heinrich, Bldg 316
LR Greenwood

Arizona State University (2)
College of Eng & Applied Science
Tempe, AZ 85287

JW McKlveen G. Stewart

Arkansas Power and Light
P.O. Box 551
Little Rock, AK 72203

O. Cypret

Babcock & Wilcox Co
Lynchburg Research Center (6)
P.O. Box 11165
Lynchburg, VA 24506-1165

LL Collins DA Nitti
SQ King N. Snidow
AL Lowe Jr F. Walters

DISTRIBUTION FOR LWR-PV-SDIP (Cont'd)

Baltimore Gas & Electric Co
Lexington and Liberty Streets
P.O. Box 1475
Baltimore, MD 21203

E. Titland

Battelle
Pacific Northwest Laboratory (8)
P.O. Box 999
Richland, WA 99352

A. Burtron
TT Claudson
B. Johnson
WC Morgan
JT Roberts
LC Schmid
EP Simonen
J. Straalsund

Battelle Memorial Institute
Office of Nuclear Waste Isolation (2)
505 King Avenue
Columbus, OH 43201

MP Manahan
J. Perrin

Bechtel Power Corporation
15740 Shady Grove Road
Gaithersburg, MD 20760

WC Hopkins

Brookhaven National Laboratory
Upton, Long Island, NY 11973

J. Carew

Carolina Power & Light Co
P.O. Box 1551
Raleigh, NC 27602

SP Grant

(CEGB-Berkeley)
Central Electricity Generating Board (4)
Research Division
Berkeley Nuclear Laboratories
Berkeley, Gloucestershire GL13 9PB, UK

BJ Darlaston
TE Lewis
PJ Heffer
J. Young

Centre d'Etude de l'Energie Nucleaire
Studiecentrum voor Kernenergie (7)
Boeretang 200
B-2400 Mol, Belgium

J. Debrue
G. DeLeeuw
S. DeLeeuw
PJ D'hondt
A. Fabry
G. Minsart
Ph. Van Asbroeck

CNEA
DPTO de Materiales, C.A.C.
Avda del Libertador 8250
1429 Buenos Aires, Argentina

M. Mondino

Combustion Engineering, Inc (2)
1000 Prospect Hill Road
Windsor, CT 06095

S. Byrne
G. Cavanaugh

Comitato Nazional per l'Energia Nuclere
Centro di Studi Nucleari Della Casaccia
Casella Postale 2400
I-00060 Santa Maria di Galeria
Rome, Italy

M. Petille

DISTRIBUTION FOR LWR-PV-SDIP (Cont'd)

Commissariat a l'Energie Atomique
Centre d'Etudes Nucleaires de Saclay (2)
Boite Postale 2
91190 Gif-sur-Yvette, France

AA Alberman P. Soulat

Commissariat a l'Energie Atomique
Centre d'Etudes Nucleaires de Cadarache
13115 St Paul Lez Durance, France

JP Genthon

Commissariat a l'Energie Atomique
Service des Transfers Thermiques
38401 Grenoble, France

P. Mas

Commonwealth Edison
P.O. Box 767
Chicago, IL 60690

E. Steeve

Consolidated Edison of NY
4 Irving Place
Room 1515S
New York, NY 10003

S. Rothstein

Consumers Power
1945 W. Parnall Road
Jackson, MI 49201

H. Slager

EG&G Idaho, Inc (2)
P.O. Box 1625
Idaho Falls, ID 83415

CW Frank JW Rogers

Electric Power Research Institute (4)
3412 Hillview Avenue
P.O. Box 10412
Palo Alto, CA 94304

T. Griesbach O. Ozer
TU Marston JJ Taylor

Energieonderzoek Centrum Nederland (2)
Netherlands Energy Research Foundation
Westerdionweg 3
Postfach 1
NL-1755 ZG, Petten, The Netherlands

H. Rottger WL Zijp

Ente Nazionale Energia Elettica
Italian Atomic Power Authority
National Electric Energy Agency (2)
Viale Regina Margherita 137
Rome, Italy

M. Galliani F. Remondino

EURATOM
European Atomic Energy Community
Materials Science Division
Joint Research Center Ispra
I-21020 Ispra, Varese, Italy

R. Dierckx

Florida Power & Light (2)
9250 W. Flager Street
P.O. Box 52100
Miami, FL 33152

S. Collard JB Sun

DISTRIBUTION FOR LWR-PV-SDIP (Cont'd)

GKSS-Forschungszentrum Geesthacht GmbH (3)
Max-Planck-Strasse
Postfach 1160
D-2054 Geesthacht,
Federal Republic of Germany

J. Ahlf W. Spalthoff
GM Richter

General Electric Co
Vallecitos Nuclear Center-103
P.O. Box 460
Vallecitos Road
Pleasanton, CA 94566

GC Martin

General Public Utilities
100 Interpace Parkway
Parsippany, NJ 07054

AP Rochina

Grove Engineering
P.O. Box 720
Washington Grove, MD 20880

CA Negin

Helgeson Scientific Services
5587 Sunol Blvd
Pleasanton, CA 94566

WH Zimmer

IKE-Stuttgart
Institut für Kernenergetik
und Energiesysteme (2)
Pfaffenwaldring 31
Postfach 801140
D-7000 Stuttgart 80 (Vaihingen),
Federal Republic of Germany

G. Hehn G. Prillinger

International Atomic Energy Agency (3)
Wagramerstrasse 5, Postfach 100
A-1400 Vienna, Austria

A. Sinev JJ Schmidt
NA Titkov

IRT Corporation (2)
P.O. Box 80817
San Diego, CA 92183

NL Lurie WE Selph

Japan Atomic Energy Research Institute (2)
Tokai Research Establishment
Tokai-mura, Naka-gun,
Ibaraki-ken, 319-11 Japan

S. Mizazono K. Sakurai

Institut für Festkorperforschung der
Kernforschungsanlage Jülich GmbH (3)
Postfach 1913
D-517 Jülich 1,
Federal Republic of Germany

D. Pachur L. Weise
W. Schneider

Kraftwerk Union Aktiengesellschaft (3)
Postfach 3220
D-8520 Erlangen,
Federal Republic of Germany

A. Gerscha C. Leitz
J. Koban

La Societe FRAMATOME
Tour Fiat-Cedex 16
92084 Paris La Defense, France

C. Buchalet

DISTRIBUTION FOR LWR-PV-SDIP (Cont'd)

Lawrence Livermore National Laboratory (2)
P.O. Box 808
Livermore, CA 94550

M. Guinan R. Van Konynenburg

Los Alamos National Laboratory (2)
P.O. Box 1663
Los Alamos, NM 87545

GE Hansen L. Stewart

Maine Yankee Atomic Power Company
Edison Drive
Augusta, ME 04336

HF Jones

Materials Engineering Associates, Inc (2)
111 Mel-Mara Drive
Oxen Hill, MD 20745

JR Hawthorne FJ Loss

Max-Planck-Institüt
für Plasma Physik
The NET Team
D-8046 Garching bei München,
Federal Republic of Germany

DR Harries, Technology

Metrology Control Corporation
P.O. Box 944
Richland, WA 99352

JH Roberts

National Bureau of Standards (3)
Gaithersburg, MD 20899

JA Grundl ED McGarry
G. Lamaze

Naval Research Laboratory
Engineering Materials Division
Thermostructural Materials Branch
Code 6390
Washington, DC 20375

LE Steele

Northeast Utilities Service Co (3)
P.O. Box 270
Hartford, CT 06101

MF Ahern M. Kupinski
JF Ely

Northern States Power
414 Nicollet Mall
Minneapolis, MN 55401

G. Neils

Nuclear Regulatory Commission
Office of Nuclear Regulatory Research (7)
Division of Engineering Technology
Materials Engineering Branch
NL-5650
Washington, DC 20555

R. Alexander CZ Serpan, Chief
W. Hazelton A. Taboada
L. Lois M. Vagin
PN Randall

Nuclear Regulatory Commission
Office of Nuclear Reactor Regulation
Division of Safety Review and Oversight
Engineering Issues Branch
Washington, DC 20555

RE Johnson

DISTRIBUTION FOR LWR-PV-SDIP (Cont'd)

Oak Ridge National Laboratory (4)
P.O. Box X
Oak Ridge, TN 37831-6151

FBK Kam SK Iskander
RE Maerker FW Stallmann

Omaha Public Power District
1623 Harney Street
Omaha, NE 68102

J. Gasper

RACAH Institute of Physics
The Hebrew University
91904 Jeruselum, Israel

JJ Wagschal

Radiation Research Associates
4425 W. Vickery Street
Fort Worth, TX 76107-6221

MB Wells

Rochester Gas & Electric Corp
Supervisor of Material Engineering
89 East Avenue
Rochester, NY 14649

AE Curtiss III

Rockwell International
Rocketdyne Division (2)
6633 Canoga Avenue
Canoga Park, CA 91304

H. Farrar BM Oliver

Rolls-Royce & Associates Ltd (4)
P.O. Box 31
Derby DE2 8BJ, UK

M. Austin AF Thomas
R. Squires TJ Williams

Royal Naval College
Dept of Nucl Science & Tech
Greenwich, London SE10 9NN, UK

JRA Lakey

S.A. Cockerill-Ougree
Recherches et Developments
Division de la Construction Mecanique
B-4100 Serraing, Belgium

J. Widart

Sandia National Laboratory
P.O. Box 5800, MS-6446
Albuquerque, NM 87059

L. Bustard

Science Applications, Inc
P.O. Box 2351
La Jolla, CA 92037

GL Simmons

Ship Research Institute
Tokai Branch Office
Tokai-mura, Naka-gun
Ibaraki-ken, Japan

K. Takeuchi

Southwest Research Institute
8500 Calebra Road
P.O. Box 28510
San Antonio, TX 78284

PK Nair

Swiss Federal Institute
for Reactor Research
CH-5303 Wuerenlingen, Switzerland

F. Hegedus

DISTRIBUTION FOR LWR-PV-SDIP (Cont'd)

United Kingdom Atomic Energy Authority
Atomic Energy Research Establishment (2)
Harwell, Oxon OX11 ORA, UK

LM Davies AJ Fudge

United Kingdom Atomic Energy Authority
Atomic Energy Establishment (5)
Winfrith, Dorchester, Dorset, UK

J. Butler P. Miller
MD Carter A. Packwood
I. Curl

United Kingdom
Nuclear Installations Inspectorate
Health and Safety Executive
Thames House North
Millbank, London SWIP 4QJ, UK

T. Currie

University of Arkansas (2)
Dept of Mechanical Engineering
Fayetteville, AK 72701

CO Cogburn L. West

University of California
at Santa Barbara (2)
Dept of Chem & Nucl Eng
Santa Barbara, CA 93106

G. Lucas GR Odette

University of Illinois
Urbana, IL 61801

JG Williams

University of London Research Center
Silwood Park
Sunnyhill, Ascot,
Berkshire SL5 7PY, UK

JA Mason

University of Tokyo
Dept of Nuclear Engineering
7-3-1, Hongo,
Bunkyo-ku, Tokyo, 113 Japan

M. Nakazawa

University of Virginia
Dept of Nuclear Engineering
Dept of Material Science
Charlottesville, VA 22901

TG Williamson

Virginia Power and Light
P.O. Box 26666
Richmond, VA 23261

D. Hostetler

Westinghouse
Nuclear Energy Systems (6)
P.O. Box 355
Pittsburgh, PA 15230

SL Anderson F. Lau
AH Fero TR Mager
EP Lippincott SE Yanichko

Westinghouse
Research and Development Center
1310 Beulah Road
Pittsburgh, PA 15235

FH Ruddy

DISTRIBUTION FOR LWR-PV-SDIP (Cont'd)

Yankee Atomic Electric Co
1671 Worchester Road
Framingham, MA 01701

E. Biemiller

HEDL (38)

HJ Anderson	W/C-28		
LD Blackburn	W/A-40	WN McElroy (20)	W/C-39
JM Dahlke	W/C-115	JA Rawlins	W/C-39
DG Doran	W/A-57	WF Sheely	W/C-44
R. Gold	W/C-39	FR Shober	W/E-3
GL Guthrie	W/A-40	RL Simons	W/A-57
LS Kellogg	W/C-39	HH Yoshikawa	W/C-44
NE Kenny	W/C-115	Central Files	W/C-110
RL Knecht	W/A-40	Documentation (3)	W/C-123

NRC FORM 335 (2-84) NRCM 1102, 3201, 3202

U.S. NUCLEAR REGULATORY COMMISSION

BIBLIOGRAPHIC DATA SHEET

SEE INSTRUCTIONS ON THE REVERSE

1. REPORT NUMBER (Assigned by TIDC, add Vol No., if any)

NUREG/CR-4307, VOL. 3
HEDL-TME 86-2

2. TITLE AND SUBTITLE

LWR Pressure Vessel Surveillance Dosimetry Improvement Program: 1986 Annual Report October 1985-September 1986

3. LEAVE BLANK

4. DATE REPORT COMPLETED

MONTH	YEAR
February	1987

5. AUTHOR(S)

W. N. McElroy

6. DATE REPORT ISSUED

MONTH	YEAR
April	1987

7. PERFORMING ORGANIZATION NAME AND MAILING ADDRESS (Include Zip Code)

Hanford Engineering Development Laboratory
P. O. Box 1970
Richland, WA 99352

8. PROJECT/TASK/WORK UNIT NUMBER

9. FIN OR GRANT NUMBER

B5988

10. SPONSORING ORGANIZATION NAME AND MAILING ADDRESS (Include Zip Code)

Division of Engineering Technology
Office of Nuclear Regulatory Research
U.S. Nuclear Regulatory Commission
Washington, DC 20555

11a. TYPE OF REPORT

Technical

b. PERIOD COVERED (Inclusive dates)

October 1985-September 1986

12. SUPPLEMENTARY NOTES

13. ABSTRACT (200 words or less)

The Light Water Reactor Pressure Vessel Surveillance Dosimetry Improvement Program (LWR-PV-SDIP) has been established by the U.S. Nuclear Regulatory Commission (NRC) to improve, test, verify, and standardize the physics-dosimetry-metallurgy, damage correlation, and associated reactor analysis methods, procedures and data used to predict the integrated effect of neutron exposure to LWR pressure vessels and their support structures. A vigorous research effort attacking the same measurement and analysis problems exists worldwide, and strong cooperative links between the U.S. NRC-supported activities at HEDL, ORNL, NBS, and MEA and those supported by CEN/SCK (Mol, Belgium), EPRI (Palo Alto, USA), KFA (Jülich, Germany), and several United Kingdom laboratories have been extended to a number of other countries and laboratories. These cooperative links are strengthened by the active membership of the scientific staff from many participating countries and laboratories in the ASTM E10 Committee on Nuclear Technology and Applications. Several subcommittees of ASTM E10 are responsible for the preparation of LWR surveillance standards. Results of FY-86 research by a number of LWR-PV-SDIP participants are reported in this progress report.

14. DOCUMENT ANALYSIS – a. KEYWORDS/DESCRIPTORS

Light Water Reactor Pressure Vessel Surveillance Dosimetry Improvement Program (LWR-PV-SDIP)

b. IDENTIFIERS/OPEN-ENDED TERMS

15. AVAILABILITY STATEMENT

Unlimited

16. SECURITY CLASSIFICATION

(This page) Unclassified

(This report) Unclassified

17. NUMBER OF PAGES

18. PRICE